GLOBAL SIMULATION OF NITRATE AND AMMONIUM AEROSOLS AND THEIR RADIATIVE EFFECTS

AND

COMPARISON OF SATELLITE-BASED AND MODELED AEROSOL INDIRECT FORCING

by

Li Xu

A dissertation submitted in partial fulfillment
of the requirements for the degree of
Doctor of Philosophy
(Atmospheric and Space Sciences)
in The University of Michigan
2012

Doctoral Committee:

Professor Joyce E. Penner, Co-Chair
Assistant Professor Xianglei Huang, Co-Chair
Associate Professor Christopher J. Poulsen
Assistant Professor Derek J. Posselt

ACKNOWLEDGEMENTS

I wish to express my sincere gratitude to my advisor, Professor Joyce Penner, for her insightful guidance and continuous encouragement, which motivate and inspire me to conduct and finish this research work. I felt very fortunate just to be around her all these years, observing how she thinks, how she approaches the problem and solves it, and how she dedicates to science. It really helps me grow intellectually. I am sure I am going to benefit from this in my future career. I would like to thank my co-advisor, Assistant Professor Xianglei Huang, for sharing his own research experience and for his numerous help and enthusiastic encouragements towards the completion of this dissertation. I also wish to thank all committee members, collaborators, group members, and friends who helped me and encouraged me during the accomplishment of this dissertation. Finally, I am grateful of countless support from my family.

TABLE OF CONTENTS

ACKNOWLEDGEMENTS ……..ii

LIST OF FIGURES ……...vi

LIST OF TABLES……xiv

CHAPTER

I. INTRODUCTION 1

1.1 Global climate system and climate change.....1
1.1.1 Energy budget in the Earth system 1
1.1.2 Climate change and radiative forcing 4
1.2 Atmospheric aerosols and their effects on climate 8
1.2.1 An overview of atmospheric aerosols.....8
1.2.2 Aerosol direct effect.....11
1.2.3 Aerosol indirect effect.....11
1.2.4 Global observed and modeled aerosol effects 13
1.2.5 Modeling semi-volatile inorganic aerosols.....18
1.3 Overview of the dissertation 19

II. A COMPARISON OF INORGANIC AEROSOL THERMODYNAMIC PROPERTIES PREDICTED BY EQSAM4 AND EQUISOLV II ……22

2.1 Introduction.....22
2.2 Description of two thermodynamic equilibrium models 25
2.3 Comparison of simulation results 33
2.3.1 Aerosol water 39
2.3.2 Total particulate matter 40
2.3.3 Particulate nitrate 45
2.3.4 Particulate ammonium 50
2.3.5 Particulate chloride 51
2.3.6 Potential of hydrogen.....51
2.3.7 Dominant solid PM compounds.....52
2.3.8 Hygroscopic growth factor (HGF).....56

2.4 Comparison with MINOS observations....58
2.5 Discussion and conclusions....68

III. BOX MODEL SIMULATIONS OF NITRATE AND AMMONIUM AEROSOLS ……73

3.1 Introduction....73
3.2 Methods....78
3.2.1 Aerosol thermodynamic module....78
3.2.2 Diffusion-limited mass transfer....80
3.2.3 Hybrid dynamic method....84
3.2.4 Simple kinetic-limited equilibrium method....92
3.2.5 Aerosol mixing state....98
3.3 Results....105
3.3.1 Nitrate treatment using EM and IM....105
3.3.2 Nitrate treatment using KEQ and HDYN....114
3.4 Discussion and conclusions....118

IV. GLOBAL SIMULATIONS OF NITRATE AND AMMONIUM AEROSOLS AND THIR RADIATIVE EFFECTS……..122

4.1 Introduction....122
4.2 Model descriptions....129
4.2.1 Global aerosol and chemistry transport model....129
4.2.2 Nitrogen chemistry....134
4.2.3 Treatment of nitrate and ammonium....135
4.2.4 Emission Scenarios....138
4.3 Present-day global aerosol concentration fields....143
4.3.1 Sulfate....143
4.3.2 Nitric acid and nitrate....144
4.3.3 Ammonia and ammonium....149
4.3.4 Aerosol water....152
4.3.5 Zonal average mixing ratios....153
4.4 Global budgets....156
4.4 Aerosol optical properties....168
4.6 Radiative forcing of nitrate and ammonium....172
4.6.1 Direct forcing of nitrate and ammonium....173
4.6.2 Indirect forcing of nitrate and ammonium....179
4.7 Summary and discussion....195

V. COMPARISON O SATELLITE-BASED AND MODELED AEROSOL INDIRECT FORCING……201

5.1 Introduction....201
5.2 Methods....209
5.2.1 The coupled IMPACT/CAM model....209
5.2.2 Calculation of cloud droplet number concentration and the first aerosol indirect forcing....211
5.2.3 Calculation of aerosol optical properties....214

5.3 Empirical measures of aerosol-cloud interactions 215
5.3.1 Aerosol-cloud interaction relationships based on theory....215
5.3.2 Statistical relationship following satellite-based method ..220
5.4 Global aerosol mass budgets in PD and PI simulations.....223
5.5 Results of PD and PI simulations.....224
5.5.1 Statistical relationship between CDNC and AOD/AI.....224
5.5.2 Sensitivity study of CCN activation with the change of aerosol concentration 230
5.5.3 Cloud droplet number concentration and cloud effective radius.....237
5.5.4 Aerosol optical depth and aerosol index.....241
5.5.5 Aerosol indirect forcing.....243
5.6 Discussion and conclusions 249

VI. SUMMARY AND FUTURE WORK 253

6.1 Summary.....253
6.2 Future work.....264

BIBLIOGRAPHY ……..267

LIST OF FIGURES

Figure

1.1 The global annual mean Earth's energy budget for the March 2000 to May 2004 period (W m^{-2}). The broad arrows indicated schematic flow of energy in proportion to their importance. Source: Trenberth et al. (2009).....3

1.2 Global mean temperature and CO_2 concentration from 1880 to 2009. Source: National Climatic Data Center…….……...5

1.3 Comparison of outgoing shortwave radiation flux anomalies (in W m^{-2}, calculated relative to the entire time period from 1984 to 1999) from several models in the MMD archive at PCMDI (colored lines) with ERBE satellite data (black with starts) and ISCCP flux data set (black with squares). Source: Intergovernmental Panels on Climate Change (IPCC), 2007……6

1.4 Global mean radiative forcing from human activities and natural processes for the year 2005 relative to the pre-industrial era (about 1750). Colored bars represent the best estimates of radiative forcing of respective agents and processes. Red and blue bars represent positive forcing (warming) and negative forcing (cooling) respectively. The think black line attached to each colored bar represents the range of uncertainty. Source: Intergovernmental Panels on Climate Change (IPCC), 2007……7

1.5 Key processes that aerosols influence climate and must be accurately represented in future generations of climate models. Source: Ghan and Schwartz (2007)……10

1.6 Radiative forcing due to the cloud albedo effect, in the context of liquid water clouds from the global climate models. The labels next to the bars correspond to the published study. Top panel: results from models that consider a limit number of species, primarily anthropogenic sulfate (S). Bottom panel: results from studies that include a variety of aerosol compositions and mixtures; the estimates here cover a larger range than those in the top panel. Source: Intergovernmental Panels on Climate Change (IPCC), 2007……..17

2.1 Scatter plots of aerosol water ($H_2O_{(aq)}$), total particulate matter (PM), particulate NO_3^- ($[NO_3^-]_p$), particulate NH_4^+ ($[NH_4^+]_p$), particulate Cl^- ($[Cl^-]_p$), and potential of hydrogen (pH) predicted by EQSAM4 and EQUISOLV II based on the 200 initial conditions specified in Table 2.3 at a temperature of 298.15K. The black diagonal lines are the 1:2, 1:1, 2:1 lines, respectively. The units are μg m^{-3}. The concentration is shown using a logarithmic scale……...38

2.2 Aerosol water predicted by EQSAM4 and EQUISOLV II for all 20 cases listed in Table 2.3.....……..40

2.3 Total particulate matter predicted by EQSAM4 and EQUISOLV II for all 20 cases listed in Table 2.3.....……43

2.4 Particulate nitrate predicted by EQSAM4 and EQUISOLV II for all 20 cases listed in Table 2.3……...….46

2.5 Mean binary activity coefficients of NH_4NO_3 and NH_4Cl as a function of molality (a) and molality for several electrolytes at a temperature 298.15 K as a function of water activity (b) (i.e. RH with a 0-1 scale)……...……49

2.6 Concentrations of major solid compounds predicted by EQSAM4 and EQUISOLV II at an RH of 30% and a temperature of 298.15 K for the 20 cases listed in Table 2.2……54

2.7 Relative difference in the growth factor between EQSAM4 and EQUISOLV II for all 200 conditions in Table 2.3 as a function of RH at a temperature 298.15 K. The error bars indicate the range of values for different cases……...…….57

2.8 Time series by EQSAM4 and EQUISOLV II and observations for NH_4^+(p), NH_3(g), tNH_4, NO_3^-(p), HNO_3(g), tNO_3 during the MINOS campaign. The red lines in the panels at the right represent the linear fits to the data. The NO_3^-(p) within the range (10^{-3}-10^1 μg m^{-3}) in the panel (f) and (h) are plotted…….62

2.9 Time series by EQSAM4 and EQUISOLV II for aerosol water (μg m^{-3}) during the MINOS campaign. The temperature and relative humidity during the campaign are shown. The correlation coefficient (r) between EQSAM4 and EQUISOLV II on the prediction of aerosol water is shown at the top of figure…….63

2.10 The difference between the modeled and observed concentrations of NO_3^- as a function of temperature, RH, SO_4^{2-} concentration, and the molar ratio of tNH_4 to SO_4^{2-} during the MINOS campaign...……...64

2.11 The difference between the modeled and observed concentrations of NH_4^+ as a function of temperature, RH, SO_4^{2-} concentration, and the molar ratio of tNH_4 to SO_4^{2-} during the MINOS campaign……..……66

2.12 Error distributions of aerosol nitrate assuming different equilibrium states (deliquescence vs. efflorescence) of the particles during the MINOS campaign. Errors are calculated as the predicted minus the observed values of aerosol nitrate. The number of samples was 183……...67

3.1 Diagram of size growth factor of $(NH_4)_2SO_4$ particles as a function of relative humidity. D_{p0} is the diameter of the particle at 0% RH……80

3.2 A schematic illustration of the implementation of the hybrid dynamic method into the aerosol thermodynamics module assuming all pre-existing aerosols are internally mixed. ΔT and δt are the model (operator) time step (i.e., ΔT = 3600 s) and the internal time interval in solving mass transfer equations, respectively. $C_{g,i}, C_{a,i,j}, C^{eq}_{g,i,j}$ are the concentration of bulk gas-phase, aqueous-phase and the equilibrium concentration over the particle surface, respectively. *i* and *j* are index for aerosol species (*i* = HNO_3, NH_3 and N_2O_5) and aerosol size bins (*j* = 1, 2, 3, and 4)……...……92

3.3 The kinetic limited gas fraction as a function of aerosol radius for HNO_3 gas.....97

3.4 Two aerosol mixing state: external mixing (left) and internal mixing (right).....100

3.5 A schematic illustration of the implementation of the hybrid dynamic method in the aerosol thermodynamics module for externally mixed three size distributions. ΔT and δt are the model (operator) time step (i.e., ΔT = 3600 s) and the internal time interval in solving mass transfer equations, respectively. $C_{g,i}, C_{a,i,j}, C^{eq}_{g,i,j}$ are the concentration of bulk gas-phase, aqueous-phase and the equilibrium concentration over the particle surface, respectively. *i* and *j* are index for aerosol species (*i* = HNO_3, NH_3 and N_2O_5) and aerosol size bins (*j* = 1, 2, 3, and 4) given size distribution (d = SU, DU, SS).……...104

3.6 The simulated gaseous and size-segregated aerosol concentrations for nitrate and ammonium using the hybrid dynamic method (HDYN) by treating aerosols internally mixed (IM) and externally mixed (EM) in each size bin, varying as a function of time during the establishment of the thermodynamic equilibrium for the continental case……...…….107

3.7 Comparison of the box-model simulated gaseous and size-segregated aerosol concentrations of nitrate and ammonium using the hybrid dynamic method (HDYN) by treating aerosols internally mixed (IntMix) and externally mixed (ExtMix) in each size bin after 1 hour (left) and after 12 hours (right) of diffusion for the continental case..……..108

3.8 As for Figure 3.6, but for the marine case.....110

3.9 As for Figure 3.7, but for the marine case listed in Table 3.4…….112

3.10 The simulated aerosol concentration of nitrate in the first size bin using the loop order of SU1-DU2-SS3 (top left panel) and of SU1-SS2-DU3 (top right panel) for the mix case shown in Table 3.4, respectively, varying with aerosol concentrations of sea salt and dust. The bottom two panels give the absolute difference as well as relative difference of top two panels……...……..113

3.11 Comparison of the box-model simulated gaseous and size-segregated aerosol concentrations of nitrate and ammonium using the hybrid dynamic method (HDYN) and the kinetic limited equilibrium (KEQ) method by treating aerosols internally mixed (IM) in each size bin after 1 hour (left) and after 12 hours (right) of diffusion for the continental case…..……..114

3.12 The calculated distance from the particle to where the kinetic regime applies (Δ), Knudsen number (Kn) as well as fraction (frac) kinetically allowed to condense onto aerosol particles for gaseous HNO_3 and NH_3 for each size bin…….……...116

3.13 As for Figure 3.11, but for the marine case listed in Table 3.4……...118

4.1 Predicted mixing ratios (pptv) of pure sulfate and coated sulfate in the surface layer averaged for January and July. The pressure level of the surface layer together with the average mixing ratio for that layer is indicated above each panel……....144

4.2 Predicted mixing ratios (pptv) of gaseous HNO_3 (left) and NH_3 (right) in the surface layer averaged for January and July. The pressure level of the surface layer together with the average mixing ratio for that layer is indicated above each panel..……..145

4.3 Predicted mixing ratios (pptv) of nitrate associated with each aerosol type and for total nitrate in aerosols (bottom right) in the surface layer averaged for January and July. The pressure level of the surface layer together with the average mixing ratio for that layer is indicated above each panel..……146

4.4 Fraction of the fine mode nitrate to total aerosol nitrate (left): [NO_3^- ($D < 1.25$ μm)]/[NO_3^- ($D < 1.25$ μm) + NO_3^- ($D > 1.25$ μm)] and fraction of total nitrate (gas HNO_3 + aerosol NO_3^-) predicted to occur as aerosol NO_3^- (right) in the surface layer (i.e., 994 mb) averaged for January and July…….147

4.5 Molar ratio of total ammonium to total sulfate (top) and gas ratio (bottom) in the the surface layer averaged for January and July. See text for the definition of the gas ratio..……...149

4.6 Predicted mixing ratios (pptv) of ammonium associated with each aerosol type and for the total ammonium aerosols (bottom right) in the surface layer averaged for January and July. The pressure level of the surface layer together with the average mixing ratio for that layer is indicated at each panel…..……...……..150

4.7 Fraction of the fine mode ammonium to total aerosol ammonium (left): [NH_4^+ (D < 1.25 μm)]/[NH_4^+ (D < 1.25 μm) + NH_4^+ (D > 1.25 μm)] and fraction of total ammonia (gas NH_3 + aerosol NH_4^+) predicted to occur as aerosol NH_4^+ (right) in the surface layer (994 mb) averaged for January and July…..……...……152

4.8 Predicted mixing ratios (pptv) of aerosol water associated with each aerosol type and for the total aerosol water (bottom right) in the surface layer averaged for January and July. The pressure level of the surface layer together with the average mixing ratio for that layer is indicated above each panel..……..153

4.9 Zonal mean mixing ratio of NO_3^-, HNO_3, NH_4^+, NH_3, SO_4^{2-} and H_2O(aq) averaged for January and July. Above each panel, the unit is indicated..……155

4.10 Schematic diagram of the global and annual budgets of nitric acid and nitrate aerosol calculated in this work. Burden and lifetime of HNO_3 gas and aerosol NO_3^- are shown in the boxes. Arrows indicate emission, deposition fluxes and net conversion rates in Tg N per year. The values in parentheses refer to the results simulated using the framework of Feng and Penner (2007) that assumes the internal mixing state of pre-exisiting aerosols..……156

4.11 Schematic diagram of the global and annual budgets of ammonia and ammonium calculated in this work. Burden and lifetime of gas NH_3 and aerosol NH_4^+ are shown in the boxes. Arrows indicate emission, deposition fluxes and net conversion rates in Tg N per year. The values in parentheses refer to the simulated results based on the framework of Feng and Penner (2007) assumes the internal mixing state of pre-exisiting aerosols..……..161

4.12 Global annual mean distribution of modeled aerosol optical depth (AOD) and observed AOD from MODIS satellite for the year 2001 at 550 nm.....……..170

4.13 Global annual mean distribution of modeled aerosol single-scattering albedo at 550 nm...……..171

4.14 Annual mean distribution of the simulated radiative effects of nitrate and ammonium at the top of atmosphere (TOA) and at the surface for full-sky and clear-sky conditions for the PD simulation..……...175

4.15 Global annual mean distribution of the difference in column-integrated aerosol optical depth at 550 nm between the simulations with and without ammonium and nitrate aerosols for the PD (left) and PI (right) scenario....……..175

4.16 Annual mean distribution of the simulated radiative effects of nitrate and ammonium at the top of atmosphere (TOA) and at the surface for full-sky and clear-sky conditions for the PI simulation....……..176

4.17 Annual mean anthropogenic forcing of nitrate and ammonium from the PI to PD scenario...……..177

4.18 Present day zonal annual-average cloud droplet number (CDN) concentration for three cases...……...182

4.19 Present day annual average cloud top droplet number (CDN) concentration for three cases...……....183

4.20 The absolute difference of present day annual average cloud droplet number concentration activated from each aerosol type and the total cloud droplet number near 930 mb (the third model level) between the case PN and NN...…….....186

4.21 The absolute difference of present day annual average cloud droplet number concentration activated from each aerosol type and the total cloud droplet number near 930 mb (the third model level) between the case TN and NN...187

4.22 The percentage change in zonal annual-average cloud droplet number for the case PN and the case TN compared with the baseline case NN near 930 mb (the third model level)…...……..187

4.23 The spatial distribution of change in droplet effect radius (left) and the first aerosol indirect forcing (right) for the TN case...……...189

4.24 The first aerosol indirect effect of nitrate and ammonium aerosols for the PD (top), PI (middle) simulation and the first anthropogenic aerosol indirect forcing of nitrate and ammonium (bottom) at the TOA. The mean forcing value is indicated in each panel...…….193

4.25 The first aerosol indirect forcing at the top of atmosphere over five regions for three cases (AER: PN-NN; GAS: TN-PN; TOT: TN-NN). GLB, NH, SH, LND and OCN stand for the global average, average over the northern and southern hemisphere, average over the land and ocean, respectively...……194

4.26 The first aerosol indirect forcing calculated for the three cases listed in Table 4.10 calculated using monthly average, daily average and hourly average aerosol concentration fields…….....194

5.1 Diagram showing the processes included in the estimation of the first aerosol indirect effect (Wang and Penner, 2009).....……..213

5.2 Choice of the fourteen different regions (Quaas et al., 2008)...……..221

5.3 Scatter plot of the slope ln(N_d) vs ln(AOD) and ln(Nd) vs ln(AI) for North America (NAM) in JJA and DJF and for Asia (ASI) in MAM. The linear regressions for both the PD and PI simulation are shown. The black line shows the fit computed using the difference in the average of PD and PI values (i.e., Eqn. (5.9) and Eqn. (5.10)) (Figure 3, Penner et al, 2011) ……....226

5.4 Slope of the regression between ln(N_d) and τ_a (i.e., AOD) (a) and ln(AI) (b) for the PD simulations for all seasons for the 14 regions in the analysis of Quaas et al. (2008)……...……..228

5.5 The slope calculated from the difference in the average values of ln(N_d) and ln(AOD) (top) and ln(AI) (bottom) between the PD and PI simulations for all seasons for the 14 region in the analysis of of Quaas et al. (2008)…….229

5.6 Cloud droplet number concentrations activated as a function of updraft velocity for two base aerosol concentrations: lowAODhighNd (solid line) and highAODlowNd (dash line) in the Asia (ASI) during the season (MAM). The colored lines are corresponding to the runs with doubling specific aerosol component indicated in the legend. "2xSO_4m1" and "2xSO_4m2" stands for the run with doubling pure sulfate at the aiken and accumulation mode, respectively while "2xSO4-FFOMBC", "2xSO_4-BBOMBC", "2xSO_4-Dust" and "2xSO_4-Sslt" represent the runs with doubling fossil fuel, biomass burning, dust and sea salt aerosols based on the base case...……..233

5.7 Aerosol optical depth for two base aerosol concentrations in ASI during the season MAM……...……233

5.8 Same as in Figure 5.6, but for the Europe (EUR) during the season (MAM)……...…….235

5.9 Same as in Figure 5.7, but for the Europe (EUR) during the season (MAM) (left panel); maximum supersaturation as a function of updraft velocity for the Europe (EUR) during the season (MAM) (right panel)……..236

5.10 Annual averaged cloud droplet number concentration at cloud top for PD and PI condition (top two panels), for the derived PI using the statistical relationship between CDNC and AOD (left in the bottom panel) and using the statistical relationship between CDNC and AI (right in the bottom panel) and the CDNC ratio between the derived PI and the true PI (bottom two panels)……...……..237

5.11 Annual averaged cloud droplet number concentration ratio at cloud top between the derived PI and the true PI condition ……..239

5.12 Annual zonal mean cloud droplet number concentration at cloud top. The case labels are same as in Figure 5.6……..239

5.13 Annual averaged cloud effective radius at cloud top. The case labels are same as in Figure 5.6……...……240

5.14 Annual averaged cloud top effective radius ratio between the derived PI and the true PI condition. The case labels are same as in Figure 5.6……241

5.15 Annual averaged aerosol optical depth (top), Ångström exponent (middle) and aerosol index (bottom) for the PD (left) and PI (right) simulation....…….242

5.16 Shortwave indirect forcing from the PD and PI values of Nd (top), from the PD value of Nd and the estimate of the PI Nd based on the regression between Nd and AOD (middle), and from the PD value of Nd and the estimate of the PI Nd based on the regression between Nd and AI (bottom). The satellite estimates of forcing do not include the forcing outside the region from 60S to 60N. If the true model forcing is restricted to this region, the total forcing is -1.56 W m^{-2}……..244

5.17 Annual averaged 1st aerosol AIE at the top of atmosphere over 19 regions for three cases (PD-PI, PD-PI_AOD, and PD-PI_AI). GLB stands for the region average within 60°S and 60°N, NH and SH are average over the northern and southern hemisphere, LAD and OCN are average over the land and ocean, and the rest of 14 regions are same as that defined in Figure 5.2…….....……..246

5.18 Same as in Figure 5.17 from the coupled CAM/IMPACT inline model……247

LIST OF TABLES

Table

2.1 Description of the parameterization and methods in EQUISOLV II and EQSAM4…….…….28

2.2 List of solubility and corresponding DRH of major solid compounds in EQSAM4 at a temperature 298K that deviate from EQSAM3……..……..34

2.3 List of 20 sets of conditions applied in the model simulations…….37

2.4 Relative difference as well as linear regression slope with the 95% confidence interval of total particulate matter (PM), aerosol water (AW) and pH between EQSAM4 and EQUISOLV II for the three sulfate regimes at 298.15 K under all RH conditions shown in Figure 2.1…….42

2.5 Total Particulate matter (PM) concentration predicted at 298.15 K and RH 30% under all conditions……..44

2.6 Comparison between modeled and observed concentrations of gas and particulate phase ammonium, nitrate and chloride by EQSAM4 (EQ4) and EQUISOLV II (EQ2) as well as the model predicted concentrations of total particulate matter, solid particulate matter and aerosol associated water...….65

3.1 Molecular velocities, diffusivity and mean free path of HNO_3, NH_3 and N_2O_5 at the surface (temperature: 298K; pressure: 1000 hPa) and at the upper troposphere (temperature: 258 K; pressure: 300 hPa)…….....84

3.2 Distribution and constituents and size bins applied for each distribution considered...……101

3.3 List of chemical compositions resolved in each distribution of Table 3.2.….102

3.4 Initial aerosol and gas concentrations ($\mu g\ m^{-3}$)……...106

4.1 Size distribution parameters for non-sulfate aerosols...……..130

4.2 Constitute composition simulated for each aerosol type……136

4.3 Global annual emission for preindustrial and present-day scenarios...……...142

4.4 Global annual budgets of HNO_3(g) and nitrate (NO_3^-) for present-day and preindustrial scenarios...…....……....……165

4.5 Global Annual budgets of NH_3(g) and ammonium (NH_4^+) for present-day and preindustrial scenarios……...……..166

4.6 The calculated nitrate burden, total, wet and dry removal rate coefficient (k, k_{wet} and k_{dry}) as well as the percentage of wet removal rate coefficient for each size bin and all bins. The size range is indicated in the first row…….……...167

4.7 Comparison of model predicted single scattering albedo at 550 nm with annual average measurements…….....……....……..172

4.8 Comparison of direct radiative effect and anthropogenic forcing (W m^{-2}) of nitrate and ammonium with other studies……...…177

4.9 The calculated nitrate and ammonium direct effects (W m^{-2}) for the PD and PI simulation and the anthropogenic forcing (W m^{-2}) (PD-PI) at the top of atmosphere (TOA) and at surface (SFC) using monthly average (M), daily average (D) and hourly average (H) aerosol fields...…...……...178

4.10 Descriptions of experiments for the radiative calculations of the first aerosol indirect forcing…….....……..181

4.11 Global annual-average cloud droplet number concentration at the cloud top in the PD (PI) simulation, cloud top effective radius in the PD (PI) simulation, cloud optical thickness in the PD (PI) simulation, absolute (percentage) change in cloud top droplet number concentration, cloud top effective radius and cloud optical thickness from anthropogenic emission, and 1st AIE for all three cases and the difference of the case NN and TN at the top of atmosphere (at surface)…….....……...192

5.1 Size distribution parameters for non-sulfate aerosols...……..209

5.2 Hygroscopicity, density and refractive index for each aerosol component....213

5.3 ACI values reported in literatures……...219

5.4 Abbreviations for regions and seasons (Quaas et al., 2008)……...222

5.5 Aerosol emissions and burdens in the present day and preindustrial simulations used in this study……....……224

5.6 Forcing (W/m^2) based on PD and true PI model results for droplet number concentrations as well as for PI estimates using the regression of ACI_N(AOD) and of ACI_N(AI)…….248

CHAPTER I

INTRODUCTION

1.1 Global climate system and climate change

The earth climate system is composed of five "spheres", including atmosphere, hydrosphere, biosphere, lithosphere and cryosphere. These components are intertwined through many dynamic, physical, chemical and biological processes. Momentum, moisture and energy are interactively exchanged among them. Climate refers to the mean behavior of weather and its variability over a certain period and a certain area. Typically, the time scale of climate change has the order of decades to centuries. Both weather and climate on the earth are affected by any change in these five components. This research focuses on the atmosphere, where most of the weather and climate phenomena occur.

1.1.1 Energy budget in the Earth system

Solar radiation powers the climate system. A schematic description of the earth's annual global mean energy budget (Trenberth et al., 2009) is shown in Figure 1.1, which is updated in the light of new observations and analysis based on the previous study (Kiehl and Trenberth, 1997). The amount of solar radiation reaching the top of Earth's atmosphere averaged over the entire planet is about 341 W m^{-2}. About 31% of incoming

solar radiation (102 W m^{-2}) is reflected back to space. About 77% of this reflectivity is due to clouds and small particles suspended in the atmosphere known as 'aerosols' while about 23% of the sunlight is reflected by light-colored surface areas on the Earth such as snow, ice and deserts. The remaining incoming solar radiation is absorbed by atmosphere (78 W m^{-2}) and surface (161 W m^{-2}). In order to balance this portion of solar energy not reflected back to space (i.e., 239 W m^{-2}), the Earth (396 W m^{-2}) and its atmosphere/clouds (199 W m^{-2}) emit radiation at long wavelengths. Note that the Earth-Atmosphere would have to have a temperature around -19 °C in order to emit the heat energy of 239 W m^{-2}, which is actually close to the temperature at 5 km above the surface. Due to the presence of greenhouse gases such as water vapor and carbon dioxide and clouds acting as a partial blanket, only a small portion of thermal radiation (40 W m^{-2}) passes directly to space without intermediate absorption and re-emission through atmospheric window. About 333 W m^{-2} long wave radiation is trapped by greenhouse gases to warm the surface of the Earth. This so-called greenhouse effect maintains a global mean surface temperature at about 14 °C, which is 33°C higher than the effective radiating temperature from the Earth-Atmosphere system. In summary, the role of greenhouse gases is to trap the outgoing longwave radiation and warm the Earth-Atmosphere system while aerosols and clouds exert net cooling on a global basis.

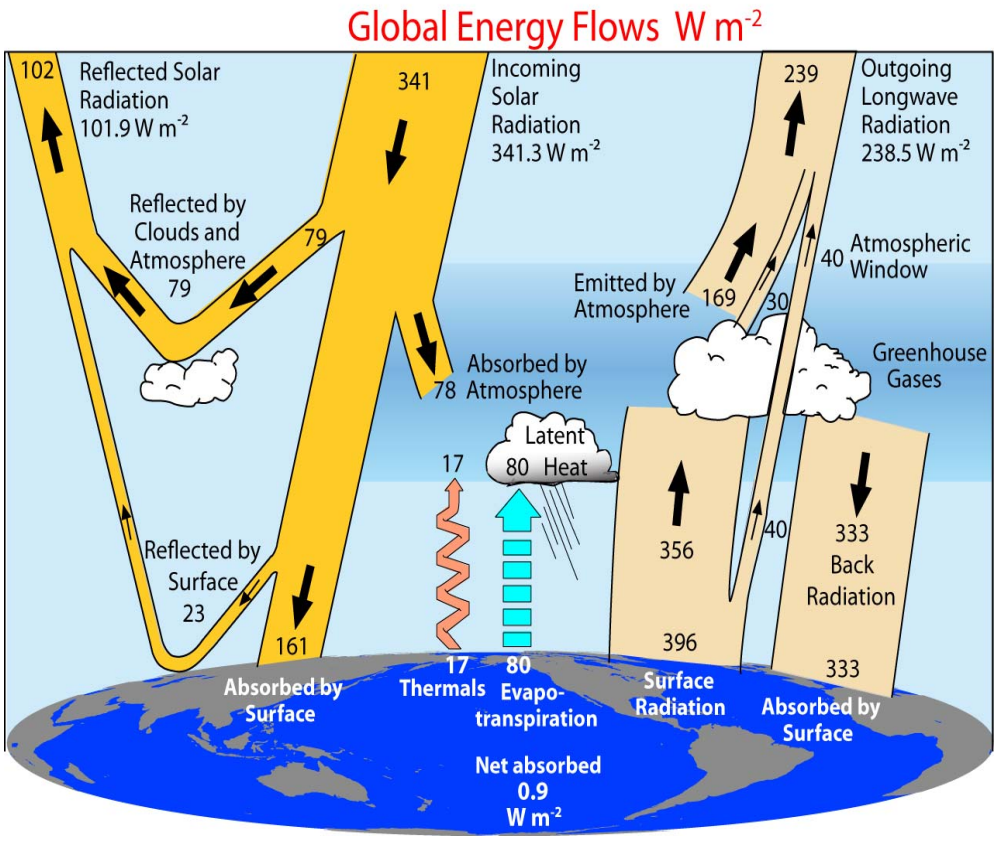

Figure 1.1: The global annual mean Earth's energy budget for the March 2000 to May 2004 period (W m^{-2}). The broad arrows indicated schematic flow of energy in proportion to their importance. Source: Trenberth et al. (2009).

The absorbed solar radiation on the earth varies geographically. Basically, more solar energy is absorbed in the Tropics than that in the polar regions, resulting in temperature gradients between the tropics and polar regions. The temperature gradient drives a general circulation in the atmosphere and ocean. Energy is transported by wind and ocean currents and by releasing latent and sensible heat. The averaged net radiation at the top of atmosphere must be zero in order to maintain an equilibrium state. Any perturbation in either shortwave or longwave radiation can introduce a radiative imbalance to the Earth-Atmosphere system.

1.1.2 Climate change and radiative forcing

Climate change is statistically significant variation in weather pattern, persisting from decades to millions of years. Climate change can be caused by natural variability, e.g., changes in the incoming solar radiation, or induced by human activities, e.g., changes in the chemical compositions in the atmosphere. The continuing increase of greenhouse gases (GHGs), such as carbon dioxide (CO_2) in the atmosphere from fossil fuel combustion, biomass burning and other human activities, is identified as a cause of the rising surface temperature shown in Figure 1.2. On the other hand, decreasing reflective aerosols or clouds over time is indicated from satellite observations of changes in top-of-atmosphere outgoing shortwave radiation flux illustrated in Figure 1.3. This may also contribute to the warming planet since the net effect of both aerosols and clouds tends to cool the atmosphere.

As described earlier, any natural or human-induced perturbations can introduce a radiative imbalance to the Earth-Atmosphere system. The term 'radiative forcing' has been employed to denote an imposed perturbation by different radiative forcing agents (e.g., greenhouse gases, aerosols, clouds, solar activity, volcanic eruption, etc) in the radiative energy budget of the Earth's climate system. The climate sensitivity parameter (λ) expresses the change in the mean surface temperature (ΔT_s) as a function of radiative forcing (ΔF) as follows:

$$\Delta T_s = \lambda \Delta F \ . \qquad (1.1)$$

This simple linear relationship allows us to compare estimates of climate response to different forcing agents by avoiding the use of surface mean temperature change (ΔT_s) since the calculation of ΔT_s may require a decade simulation of a general circulation

model (e.g. 35-year simulation, (Shine et al., 2003)) owing to the high thermal inertia of the oceans and natural variability while that of ΔF may only need a few years simulation (e.g., 5-year simulation (Shine et al., 2003)) in order to have a statistically significant change.

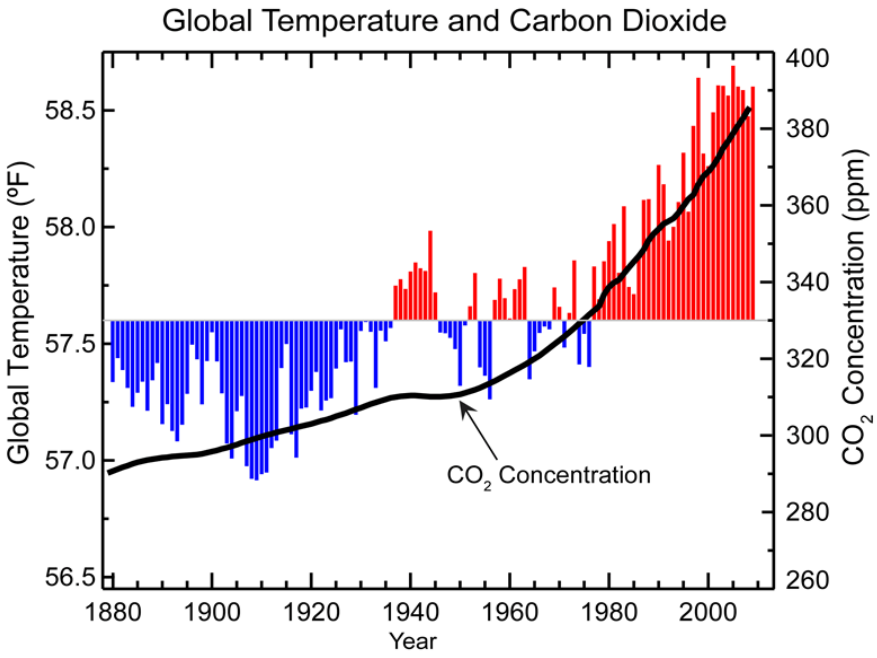

Figure 1.2: Global mean temperature and CO_2 concentration from 1880 to 2009. Source: National Climatic Data Center.

Figure 1.4 shows the estimated radiative forcing between 1750 and 2005 for a variety of radiative forcing agents which include both natural and human activities related changes (IPCC, 2007). Natural forcing due to changes in solar irradiance contributes a positive radiative forcing of 0.12±0.06 W m^{-2}, smaller than forcings induced by human activities. The GHGs have the largest positive forcing with a magnitude of 2.64±0.24 W m^{-2} with a high degree of accuracy because their long life times allow instrumental observation to record their effects. In contrast to the warming effect of the GHGs, total aerosols exert a negative radiative forcing of -1.2 W m^{-2} with a range from -0.2 to -2.3 W

m^{-2}. Overall, the warming due to greenhouse gases and cooling due to aerosols along with other agents (e.g., stratospheric water vapor, land use, aircraft produced contrails) lead to the combined net radiative forcings due to all anthropogenic drivers of 1.6 W m^{-2} with confidence range of 0.6 to 2.4 W m^{-2}. Although the cooling effect due to aerosols could, to some extent, offset warming induced by the GHGs, the uncertainties (shown in error bars) associated with aerosol forcing are still very large. Reducing these uncertainties is of great importance for understanding present climate change.

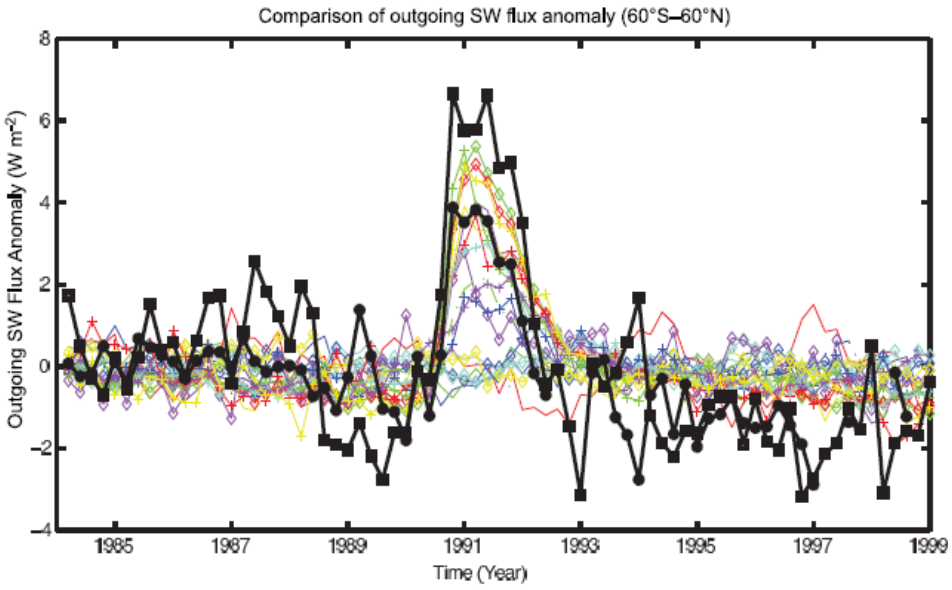

Figure 1.3: Comparison of outgoing shortwave radiation flux anomalies (in W m^{-2}, calculated relative to the entire time period from 1984 to 1999) from several models in the MMD archive at PCMDI (colored lines) with ERBE satellite data (black with starts) and ISCCP flux data set (black with squares). Source: Intergovernmental Panels on Climate Change (IPCC), 2007.

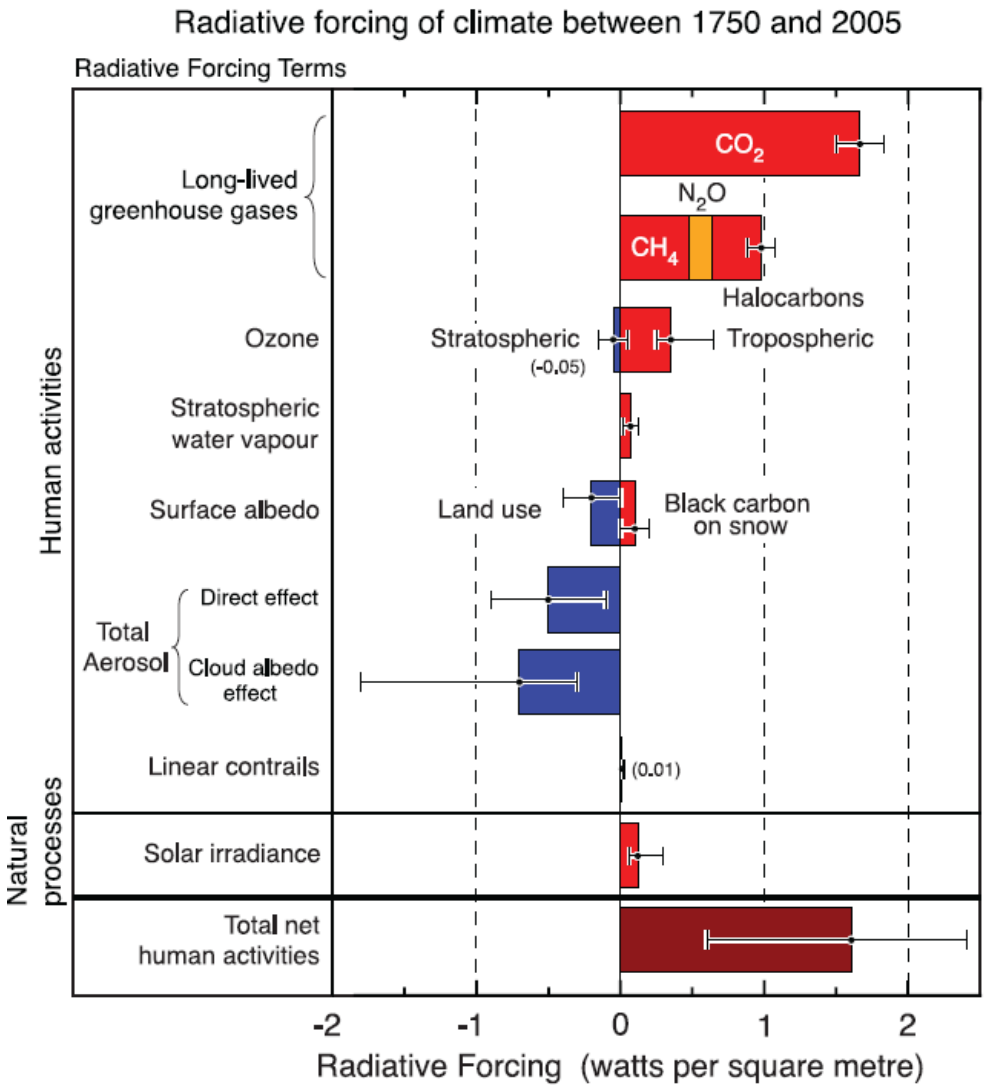

Figure 1.4: Global mean radiative forcing from human activities and natural processes for the year 2005 relative to the pre-industrial era (about 1750). Colored bars represent the best estimates of radiative forcing of respective agents and processes. Red and blue bars represent positive forcing (warming) and negative forcing (cooling) respectively. The think black line attached to each colored bar represents the range of uncertainty. Source: Intergovernmental Panels on Climate Change (IPCC), 2007.

1.2 Atmospheric aerosol and their effects on climate

1.2.1 An overview of atmospheric aerosols

Aerosols are liquid or solid particles suspended in the atmosphere. They come in many different forms, either from natural sources such as windborne dust, sea spray, and volcano eruptions, or from anthropogenic sources such as fossil fuel and biomass burning associated with deforestation. Atmospheric aerosols are classified into two groups according to the mechanism of formation. Those directly emitted from their sources, such as fly ash from industrial activities, sea salt particles emitted at the ocean surface, or mineral dust particles by the effects of wind erosion on arid land, are termed "primary aerosol". Secondary aerosols are those secondarily formed in the atmosphere by oxidation of emitted gaseous precursors and include sulfate, nitrate, ammonium, some organic and carbonaceous substances formed from terpenes and isoprene emitted by vegetation, etc. Once emitted or formed in the atmosphere, aerosols may undergo complex physical processes and chemical reactions (shown in Figure 1.5) and mix with each other either internally (in which each particle has a uniform chemical composition) or externally (in which each particle contains distinct chemical compositions). For example, the oxidation of gaseous sulfuric acid results in new particle formation of sulfate aerosols and condensation onto existing particles (such as dust and sea salt). Particles may age as a result of surface chemistry, coagulation as well as condensation. Aqueous phase chemical reactions within cloud droplets may add additional mass to pre-existing aerosols. Aerosols may grow by uptaking surrounding water vapor with increasing relative humidity while they may effloresce to the dry state when water is evaporated with decreasing relative humidity. During cloud formation, some fractions of

aerosol particles become activated by serving as cloud condensation nuclei. Within clouds, particles can attach to cloud droplets by diffusion or become combined when cloud droplets collide and coalesce. Eventually, atmospheric aerosols are removed from the atmosphere by impacting with the surface of the Earth (dry deposition), or via in-cloud scavenging process and by washing out in precipitation clouds (wet deposition).

Compared to long-lived gases in the atmosphere, aerosol particles have a shorter lifetime on the order of several days. However, small particles released or elevated at high altitudes such as carbonaceous and volcano erupted particles may stay in the atmosphere longer, up to several months, and undergo transport to regions far from their sources. Hence aerosol concentrations have significant spatial and temporal variations, varying from roughly 10^2 cm^{-3} in remote marine regions to as high as 10^7 to 10^8 cm^{-3} in heavily polluted urban regions. The diameters of aerosol particles span over five orders of magnitude, from a few nanometers to around 100 micrometers. In general, for the primary aerosols, combustion-generated particles, such as those from automobiles, power generation, and wood burning can be as small as a few nanometers and as large as 1 micrometer while wind-blown dust, pollens, plant fragments, and sea salt are larger than 1 micrometer. Most secondary aerosol particles are smaller than 1 micrometer. The chemical composition of atmospheric aerosols differs by region. For example, sea salt particles in remote marine regions are mainly composed of sodium chloride; sulfate, nitrate, ammonium and some carbonaceous aerosols are often dominant over industrial areas; soil dust aerosols are found to be composed of calcium carbonate, metal oxides and silicates, etc. Due to their diverse particle size distributions, various types, chemical compositions and mixing states, atmospheric aerosols affect on climate in different ways.

Aerosols mainly influence climate by affecting Earth's energy budget through absorption and scattering of radiation (the direct effects) and by modifying reflectance and lifetime of clouds (the indirect effect). In addition, aerosols particles also exert effects on important processes in the climate system, for instance, fertilizing land and ocean by the deposition of nitrates, iron, and other nutrients, acidifying lakes and forests by the deposition of sulfates and nitrates, reducing the albedo of snow and ice with the deposition of the black carbon, and weakening the South Asia summer monsoon (Bollasina et al., 2011).

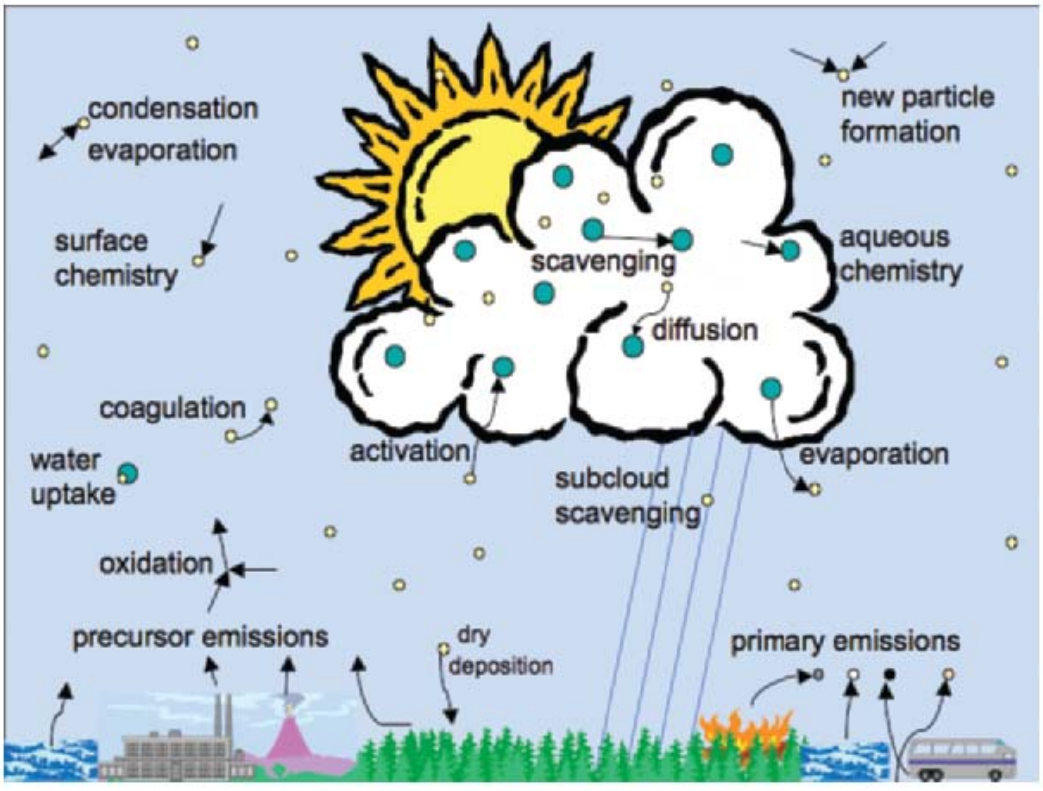

Figure 1.5: Key processes that aerosols influence climate and must be accurately represented in future generations of climate models. Source: Ghan and Schwartz (2007).

1.2.2 Aerosol direct effect

Aerosols can alter the Earth's radiation budget directly by scattering and absorbing solar and thermal infrared radiation. This is the aerosol direct radiative effect. Sulfate and nitrate aerosols, either emitted from fossil fuel combustions or formed through gas-to-particle conversion processes, mainly scatter incoming solar radiation due to their small sizes. Carbonaceous particles, such as organic matter from fossil fuel and biomass burning, participate in the scattering of solar radiation (Penner et al., 1992; Penner et al., 1998). Black carbon (or soot) warms the atmosphere and hence cools the surface by absorbing solar radiation and changing the thermodynamics in the atmosphere. Dust aerosols not only scatter and absorb incoming solar radiation but also scatter thermal infrared radiation emitted from the surface owing to their larger sizes. The IPCC AR4 (Forster., 2007) estimates the combined aerosol direct radiative forcing to be -0.5 W m^{-2} with an overall 90% confidence interval uncertainty of 0.4 W m^{-2}.

1.2.3 Aerosol indirect effect

Aerosol particles also indirectly affect the climate by modifying cloud microphysical properties by acting as cloud condensation nuclei (CCN) or ice nuclei (IN), which is termed as aerosol indirect effect. Clouds serve as a regulator of the climate system. They not only reflect incoming solar radiation and lead to cooling, but also trap outgoing infrared longwave radiation and cause warming. This so-called blanketing effect similar to that of the greenhouse gases is offset by their reflectivity. In sum, clouds have a net cooling effect on climate. A small change in cloud amount will have a large influence on the climate. Increased aerosol concentration may lead to an increase of cloud droplet number concentration at constant liquid water path, resulting in smaller cloud droplet

effect radii and larger cloud albedo (Twomey, 1974). This process is referred to as the "first aerosol indirect effect" or "cloud albedo effect". The deduction of cloud effective radii may further enhance the cloud lifetime and liquid water content by lowering the collision/coalescence rate (Albrecht, 1989). This process is referred to as the "second aerosol indirect effect" or "cloud lifetime effect". For instance, smoke aerosols from burning vegetation (Rosenfeld 1999; Andreae et al., 2004; Koren et al., 2008) and aerosols from urban and industrial air pollution (Rosenfeld, 200l; Rosenfeld et al., 2002) can reduce cloud droplet sizes as well as drop coalescence and thereby delay the onset of precipitation. Desert dust was also found to suppress precipitation in thin low-altitude clouds (Rosenfeld 2001; Mahowald and Kiehl, 2003). Moreover, absorbing aerosols such as black carbon can heat the atmosphere and thus reduce large-scale cloud cover in terms as "semi-direct effect" (Hansen et al., 1997; Koren et al., 2004; Kaufman and Koren, 2006). Additionally, aerosols are found to cause mixed-phase cloud to glaciate, thereby adding the release of latent heat (in going from the liquid to the ice phase) to the atmosphere. The glaciation effect refers to rapid glaciation of super-cooled liquid water cloud due to an increase in the ice nuclei and the difference in vapor pressure over ice versus water (Lohmann 2002; Menon and Del Genio, 2007). Unlike cloud droplets, these ice crystals grow in an environmental of high super-saturation with respect to ice, rapidly reaching precipitation size, which potentially turn a non-precipitating cloud into a precipitating cloud. The thermodynamic effect refers to a delay in freezing by smaller droplets causing super-cooled clouds to extend to colder temperatures (Rosenfeld, 1999; Rosenfeld and Woodley, 2000; Khain et al., 2005). Besides, aerosols affect cirrus clouds that are pure ice clouds at temperature below 235 K by acting as the ice nuclei. The

presence of these ice nuclei can facilitate the formation cirrus clouds, leading to changes in ice crystal number concentration, cloud albedo and ice water content. The magnitude of these effects has not yet been fully established (Penner et al., 2009). Furthermore, aerosols affect changes in the large–scale (Kristjansson et al., 2005; Takemura et al., 2005) and regional circulation (Menon et al., 2002; Wang, 2004).

1.2.4 Global observed and modeled aerosol effects

Two approaches are generally used for estimating aerosol effects on climate. One is to use satellite observations owing to the advantage of their global coverage and their basis in observations. The other is to use the global climate models. Both methods have their own merits and deficiencies, which are discussed in detail below.

Aerosols have been monitored from space for over three decades (King et al., 1999). Early satellite aerosol-monitoring products included data from sensors that were designed for other purposes. For instance, Advanced Very High Resolution Radiometer (AVHRR) is intended as a weather satellite and Total Ozone Mapping Spectrometer (TOMS) is intended for ozone monitoring. However, both have proven to be successful in providing aerosol optical depth over ocean and monitoring dust and biomass burning aerosols, respectively. These products have significantly advanced our understanding of aerosol regional and global distributions. With the developments of increasingly sophisticated retrievals as well as remote sensing techniques in recent years, satellites provide not only aerosol optical depth at one wavelength, but also spectral optical depth, particle size over land and ocean as well as aerosol types. However, the use of current broadband satellite measurements is practically limited by their coarse spatial resolution (e.g., ERBE had a footprint size of 40 km, and CERES/TRMM had a resolution of 20 km at nadir), which

makes it difficult to screen sub footprint-scale clouds from the analysis (Loeb and Kato, 2002). Another major limitation is the conversion of satellite radiances to fluxes. This is a source of uncertainty for all radiance-based approaches (Loeb and Kato, 2002). Moreover, satellite retrievals for aerosols over bright surface (e.g., desert, snow, or ice surfaces) or at high latitudes (polewards of 60°) may not be reliable because the large surface reflectance of snow/ice/desert tends to cause a large bias. Furthermore, satellite measurements have been used recently to determine the relationships between aerosol and cloud properties owing to their extensive coverage, although satellite measurements cannot unambiguously distinguish natural from anthropogenic aerosols.

Global climate models are also capable of providing estimates of aerosol effects based on numerical representations of aerosol sources, sinks, transport processes as well as involved physical and chemical processes. The uncertainties in global model estimates of aerosol direct effect come from different sources: one may be the quantification of emissions, transport and depositions; the other is the representation of aerosol physical and chemical properties involved in aerosol size distribution, chemical composition and mixing state as well as the simulation of aerosol growth under ambient environment; another large source of uncertainties is the poor knowledge of the amount of distribution of anthropogenic aerosols used in the model simulations, particularly for pre-industrial conditions.

As discussed above, large uncertainties exist in current estimates of aerosol forcings due to incomplete knowledge about the composition, distribution, physical and chemical properties of aerosols as well as aerosol-cloud interactions. The uncertainty for the aerosol direct forcing is about a factor of 2 with respect to its mean whereas that for the

indirect forcing is much larger and more difficult to quantify (IPCC, 2007). Compared to estimates from global aerosol models, the observation-based estimates tend to have more negative radiative forcing for the aerosol direct effect but have less negative forcing for the cloud albedo effect.

Specifically, for the aerosol direct effect, the IPCC AR4 provides a best estimate of -0.5 W m^{-2} with the uncertainty of -0.4 W m^{-2}. The range of estimates is -0.9 to -0.1 W m^{-2}. This uncertainty, however, is found to be largely due to differences between estimates from global aerosol models and observation-based estimates (Myhre, 2009). The gap between model-based and observation based approaches on the estimates of the aerosol direct effect shrinks in the study by Myhre (2009) and a global annual mean radiative forcing of -0.3 W m^{-2} is reported. It demonstrates the consistency between a global aerosol model and adjustment to an observation-based method. The relative larger increase of anthropogenic black carbon (absorbing aerosols) than the overall increase in the anthropogenic abundance of aerosols is ascribed to earlier discrepancy in the IPCC AR4 (Myhre, 2009). On the other hand, the discrepancy may also be caused due to "missing" aerosol components in most global models included in the IPCC AR4, for example, nitrate and ammonium.

For the aerosol indirect forcing, the IPCC AR4 provides a best estimate for the cloud albedo radiative forcing of -0.7 W m^{-2} with a 5% to 95% confidence interval range of -0.3 to -1.8 W m^{-2}. This uncertainty is also largely due to the differences between estimates from global aerosol models and from modeled estimates constrained by satellite observations shown in Figure 1.6. By using the relationships (e.g. the log of cloud droplet number versus the log of aerosol optical depth) or constraining model with satellite

deduced relationships, some studies (Dufresne et al., 2005; Quaas and Boucher, 2005; Quaas et al., 2008) suggest lower estimates of the cloud albedo effect than those from global models. These lower estimates may result from satellite-related deficiencies including the low spatial and temporal resolution of some of satellite data, the absence of coincident aerosol and cloud properties, or from the assumption in the satellite-based methods that the aerosol optical depth can be linked to the aerosol loadings below the cloud. There was a large difference in radiative forcing estimates from global models and satellite observations according to the reported values in the IPCC AR4, especially for the aerosol indirect forcing. The modeled aerosol indirect forcing constrained by satellite observations (Dufresne et al., 2005; Quaas and Boucher, 2005) ranges from -0.22 to -0.5 W m^{-2} while the estimates from global aerosol models varies from -0.52 W m^{-2} to -1.85 W m^{-2}. The observed aerosol indirect forcing is even smaller. Quaas et al. (2008) suggests an estimate of -0.2±0.1 W m^{-2} for the cloud albedo effect. One focus of this dissertation is to understand the discrepancy existing in current estimates of aerosol indirect forcing between model and observations.

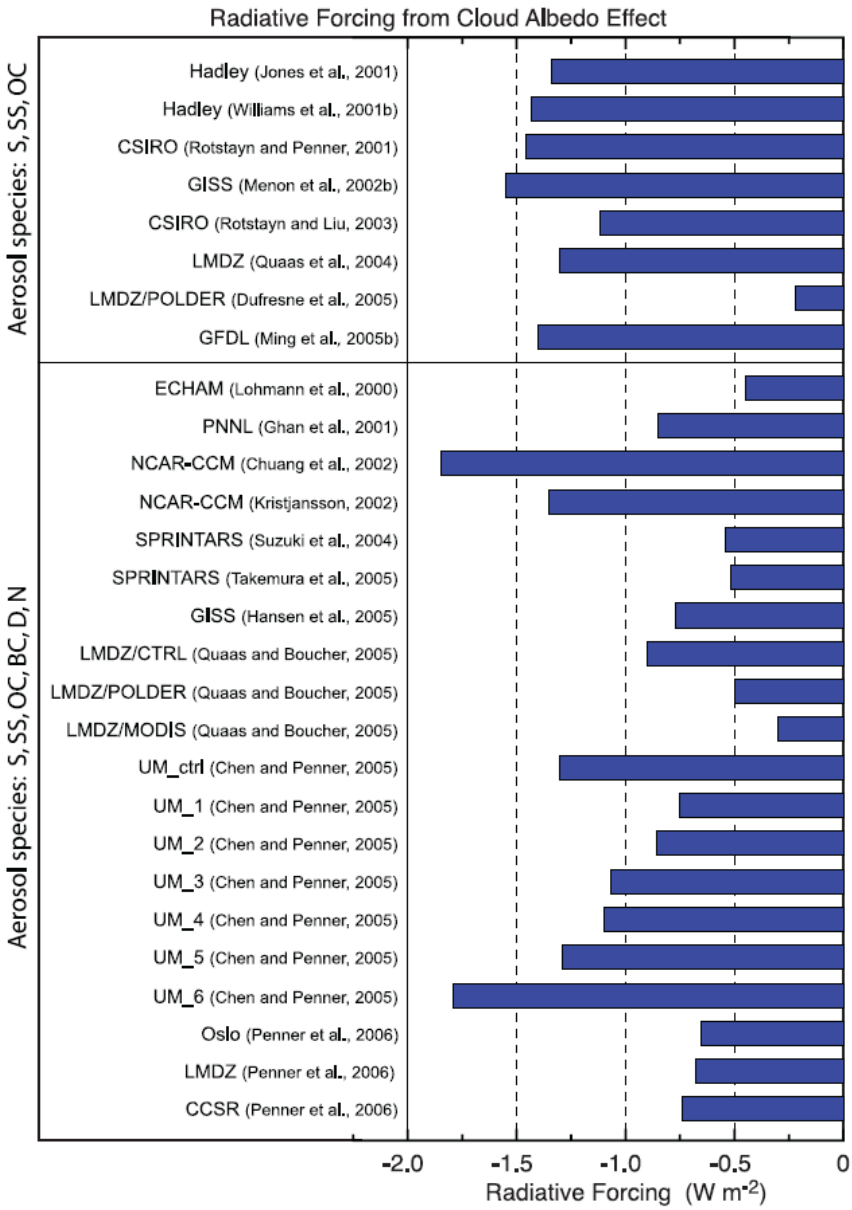

Figure 1.6: Radiative forcing due to the cloud albedo effect, in the context of liquid water clouds from the global climate models. The labels next to the bars correspond to the published study. Top panel: results from models that consider a limit number of species, primarily anthropogenic sulfate (S). Bottom panel: results from studies that include a variety of aerosol compositions and mixtures; the estimates here cover a larger range than those in the top panel. Source: Intergovernmental Panels on Climate Change (IPCC), 2007.

1.2.5 Modeling semi-volatile inorganic aerosols

As stated earlier, most global aerosol models included in the IPCC 2007 do not include aerosol nitrate and ammonium. Ammonium nitrate aerosols have been found to play a significant role in total aerosol mass, especially in polluted continental areas (Adams et al., 1999). A limited number of global models are devoted to study nitrate and ammonium aerosols concentrations (Adams et al., 1999; Metzger et al., 2002b; Liao et al., 2003; Rodriguez and Dabdub, 2004; Bauer et al., 2007; Pringle et al., 2010) as well as their radiative effects (van Doland et al., 1997; Adams et al., 2001; Jacobson, 2001; Liao et al., 2004; Bauer et al., 2007). Most global aerosol models included in the AeroCom exercise exclude ammonium and nitrate aerosols when the direct aerosol radiative forcing is assessed (Schulz et al., 2006; Textor et al., 2006; Kinne et al., 2006). Major nitrate salts (e.g., ammonium nitrate, sodium nitrate) have lower deliquescence relative humidity (DRH) than corresponding sulfate salts (e.g. ammonium sulfate, sodium sulfate). Nitrate aerosols are highly hygroscopic and can affect aerosol optical properties and further radiative forcing by changing the amount of aerosol water as well as wet refractive indexes. The IPCC AR4 (Forster et al., 2007) gives the best estimates of the direct radiative forcing for nitrate to be -0.10±0.10 W m^{-2} at the top of atmosphere for the first time. However, the uncertainty with respect to this estimate is very large because a relatively small number of studies have been conducted (Forster et al., 2007). No estimates regarding indirect forcing of nitrate are given in any modeling studies. Moreover, Feng and Penner (2007) found that different treatments to represent the formation of nitrate and ammonium in fine and coarse modes could either underestimate or overestimate nitrate burden, which may cause either underestimate or overestimate of

their radiative effects dependent upon the fraction of nitrate present in the fine mode with aerosol diameter roughly less than 1 μm. They also suggest that more accurate representation of the formation of nitrate and ammonium by using a hybrid dynamic method needs to be taken into account when calculating burden of aerosol nitrate and ammonium and estimating their direct effects in the global chemical transport model. Furthermore, a number of studies (Kulmala et al., 1993, 1998) show that the condensation of nitric acid on aerosol particles contributes soluble material to the particle surface and hence enhances the water uptake and growth of aerosol particles, leading to increase aerosol activation to cloud. Thus, nitrate and ammonium coated on pre-existing aerosol particles may have influence on altering cloud optical properties and then changing reflectivity of clouds. Therefore, full consideration of aerosol ammonium and nitrate in the global model would be vital in the estimation of both aerosol direct and indirect forcing. This is another focus of this dissertation.

1.3 Overview of this dissertation

As discussed above, two major themes of this dissertation are

1. To study the global distribution of nitrate and ammonium aerosols and their radiative effects;

2. To understand why satellite-based estimates of aerosol indirect forcing are generally smaller than model-based ones.

In Chapter II, a comprehensive comparison for various relative humidities and chemical compositions has been conducted under the assumption of thermodynamic equilibrium over the fine mode with particle diameter less than 1.25 μm between EQUISOLV II and EQSAM4. EQUISOLV II is one of the most reliable and widely used

equilibrium models while EQSAM4 is based on parameterizations that improve computational efficiency. The performance of these two models under realistic atmospheric conditions has also been evaluated during the Mediterranean Intensive Oxidant Study (MINOS) campaign in Crete during the period from 27 July to 25 August 2001. Our objective is to gain an improved understanding of the similarities and differences between these two models for the representation of the gas/liquid/solid partitioning of the aerosols under various thermodynamic regimes.

In Chapter III, the effects of two different treatments of aerosol mixing state for pre-existing aerosol particles (i.e., internally mixing versus externally/partial internally mixing) are examined by using a gas-aerosol thermodynamic equilibrium box model, EQUISOLV II. The objective is to gain some insights on the future implementation of an external mixing treatment (with partially internally mixed sulfate) along with aerosol thermodynamic module into a global aerosol model. In addition, a hybrid dynamic method and a simplified kinetic-limited equilibrium method (Pringle et al., 2010) accounting for the mass transport limitation between the gas and aerosol phases for the formation of ammonium and nitrate aerosols over the surface of larger aerosol particles are evaluated. The purpose of this examination is to understand the discrepancy between these two methods on the prediction of semi-volatile nitrate and ammonium aerosols.

In Chapter IV, a global simulation of nitrate and ammonium aerosols is conducted. The simulated global results are presented for aerosol concentrations and global budgets with the integrated model. Global nitrate and ammonium budgets are compared with those from previous studies. One sensitivity test is performed to investigate the effects on global distribution of nitrate and its size distribution subject to modeling gas-to-particle

conversion with consideration of mixing state of pre-existing aerosols. The aerosol direct and indirect effects of nitrate aerosols are studied. Finally, major results and conclusions from this study are summarized.

In Chapter V, the satellite-based method described in Quaas et al. (2008) is employed in a radiation transfer model to estimate aerosol first indirect effect. The slope of cloud droplet number concentration (N_d) versus aerosol optical depth (AOD) or aerosol index (AI) (i.e., log(N_d) vs log(AOD) or log(AI)) under present day condition is compared to that based on the aerosol and cloud properties evolved from pre-industrial to present day condition. This is followed by the global aerosol mass budgets in the present day and pre-industrial simulations. Statistical relationship between cloud droplet number concentration and aerosol optical depth or aerosol index and global annual distribution of cloud droplet number, cloud effective radius, aerosol optical depth and aerosol index for present day and pre-industrial simulations along with global and regional aerosol indirect forcing are present. The sensitivity of cloud condensation nuclei (CCN) activation varying with aerosol loadings is also investigated. Finally, discussions and conclusions are addressed.

In Chapter VI, the dissertation presents a summary of major results from Chapter II-V and an outlook for future work.

CHAPTER II

A COMPARISON OF INORGANIC AEROSOL THERMODYNAMIC PROPERTIES PREDICTED BY EQSAM4 AND EQUISOLV II

2.1 Introduction

Atmospheric aerosols are important as they affect human health, air quality, visibility as well as climate. Aerosols impact the earth's radiation balance directly through reflecting and absorbing incoming solar radiation back to space and indirectly through changing cloud microphysical properties by acting as cloud condensation nuclei. Accurate methods that are applicable to global modeling are needed to quantify these effects and to study the underlying physical and chemical processes. Sulfate, nitrate, ammonium, chloride and sodium are among the most important inorganic aerosol species in the atmosphere. Some compounds are hygroscopic and absorb water under almost all ambient environmental conditions. The uptake of water alters the aerosol size, and causes water to become the constituent with the largest atmospheric aerosol mass, especially when the aerosols grow into fog, haze or clouds (Metzger and Lelieveld, 2007). The

uptake of water impacts the wavelength dependent refractive indices, since the refractive index of water is lower than that of other aerosol species. Thus, water plays a central role in determining the particle properties and the radiative forcing of aerosols.

Penner *et al.* (1998) showed that increasing the RH from 90% to 99% increases the calculated aerosol direct radiative forcing by 50%. Adams *et al.* (1999) also showed that the amount of water taken up by the aerosol above 95% relative humidity (RH) could increase the total aerosol radiative forcing by about 60%. In a sensitivity study of the direct forcing to various parameters, Pilinis *et al.* (1995) found that the aerosol radiative forcing is most sensitive to changes in relative humidity and the corresponding water content of the aerosol. In addition, the water content of the aerosol is strongly dependent on the chemical composition of the aerosol particles. In the atmosphere, semivolatile species such as HNO_3(g) and NH_3(g) can condense onto low-volatile sulfate particles to form ionic sulfate (SO_4^{2-}), nitrate (NO_3^-), ammonium (NH_4^+) and protons (H^+) that take up the surrounding water concurrently, thus controlling the hygroscopic growth of aerosols. In addition, nitrate and ammonium aerosols can affect tropospheric chemistry by providing additional particle surface for scattering incoming solar radiation (Liao *et al.*, 2003), thus altering photolysis frequencies and photochemical oxidant formation. To more accurately represent the radiative effects of aerosol particles, the prediction of the partitioning of the semi-volatile inorganic aerosol components between the gas and aerosol phases (ammonia and ammonium, nitric acid and nitrate, etc), including that of water, is of great importance in the development of atmospheric chemistry and climate models. This, however, requires numerically efficient approaches based on accurate parameterizations as e.g. used in this comparison work.

In the past two decades, many thermodynamic equilibrium models have been developed to predict the phase partitioning of multi-component aerosols and their gas-phase precursors in the atmosphere, for instance, EQUIL (Bassett and Seinfeld, 1983), KEQUIL (Bassett and Seinfeld, 1984), MARS (Saxena *et al.*, 1986), SEQUILIB (Pilinis and Seinfeld, 1987), SCAPE and SCAPE2 (Kim *et al.*, 1993a, b; Kim and Seinfeld, 1995; Meng *et al.*, 1995), EQUISOLV and EQUISOLV II (Jacobson *et al.*, 1996; Jacobson 1999), AIM and AIM2 (Wexler and Seinfeld, 1990, 1991; Clegg *et al.*, 1992, 1994, 1995, 1998a,b; Wexler and Clegg, 2002), ISORROPIA and ISORROPIA II (Nenes *et al.*, 1998, 1999; Fountoukis and Nenes, 2007), GFEMN (Ansari and Pandis, 1999a,b), EQSAM, EQSAM2, EQSAM3 and EQSAM4 (Metzger *et al.*, 2002; Metzger *et al.*, 2006; Metzger and Lelieveld, 2007; Metzger *et al.*, 2011a; Metzger *et al.*, 2011b), HETV (Makar *et al.*, 2003), ADDEM (Topping *et al.*, 2005), MESA (Zaveri *et al.*, 2005a) and UHAERO (Amundson *et al.*, 2006). Most equilibrium models are computationally expensive since they require iterations to reach equilibrium, including EQUISOLV II which has been adopted in the current version of the UMICH-IMPACT-nitrate model (Feng and Penner, 2007). However, both accuracy and computational efficiency are essential objectives in the development of thermodynamic equilibrium models for chemical transport calculations.

In this study, we conduct a comprehensive comparison for various relative humidities and chemical compositions between EQUISOLV II, one of the most reliable and widely used equilibrium models, and EQSAM4 which is based on parameterizations that strongly improves computational efficiency and flexibility regarding the large number of aerosol species that can be considered (currently 100 compounds per solid or liquid phase

per aerosol mode or size bin). In addition, we evaluate the performance of these two models under realistic atmospheric conditions during the Mediterranean Intensive Oxidant Study (MINOS) campaign in Crete during the period from 27 July to 25 August 2001 (Lelieveld *et al.*, 2002 and Salisbury *et al.*, 2003) by using the same observational data as used in Metzger *et al. (*2006) and Metzger and Lelieveld (2007). Our objective is to gain an improved understanding of the similarities and differences between these two models for representation of the gas/liquid/solid partitioning of the aerosols under various thermodynamic regimes.

A description of EQUISOLV II and EQSAM4 is presented in Section 2.2, which is followed by a comprehensive comparison of the simulation results from 20 different sets of initial compositions in Section 2.3. A brief description of the MINOS campaign and a comparison of the model simulations and the observations during this campaign are presented in Section 2.4. Section 2.5 presents a discussion and our conclusions, while EQSAM4 is described in the companion manuscript (Metzger *et al.*, 2011b).

2.2 Description of two thermodynamic equilibrium models

A comparison of the methods used as well as the system solved in EQUISOLV II and EQSAM4 is listed in Table 2.1. In EQUISOLV II, the equilibrium concentrations of each species are calculated by numerically solving the equilibrium equation for each species separately, accounting for each chemical reaction. The equation for each species is solved in turn and the resulting concentration is used to solve the remaining equations. This sequence is repeated in an iterative manner until the concentrations of all species converge. EQUISOLV II is positive-definite, mass-conserving, and charge-conserving at any point along the iteration procedure (Jacobson, 1999). Bromley's mixing rule

(Bromley, 1973) is used to calculate the mean mixed activity coefficients while the mean binary activity coefficient of an electrolyte is parameterized using a number of measurements (Table B.9, Jacobson, 2005) and Pitzer's method (Pitzer and Mayorga, 1973) at 298.15K. Zaveri et al. (2005b) suggest that Bromley's mixing rule is reasonably accurate for subsaturated solutions and its applicability for saturated and supersaturated multicomponent solutions is limited by the maximum ionic strengths up to which the mean binary activity coefficient parameterizations are valid. Because of its simplicity and reasonably good accuracy, Bromley's mixing rule has been widely adopted in aerosol models (Bassett and Seinfeld, 1983; Saxena et al., 1986, Kim et al., 1993a; Pilinis et al., 1987; Jacobson, 1996, 1999; Nenes et al., 1998; Fountoukis and Nenes, 2007). Harned and Owen's (1958) method is adopted to account for the temperature dependency of mean binary solute activity coefficients. The aerosol water content at equilibrium is determined using the (semi-empirical) Zdanovskii-Stokes-Robinson (ZSR) method (Stokes and Robinson, 1966), by considering the deliquescence relative humidity (DRH) and the crystallization relative humidity (CRH) for single solutes in binary or multi-component mixture (Jacobson, 1999) with temperature dependent but tabulated DRH and CRH. Jacobson (1996, 1999) described that the liquid water content in EQUISOLV II is formulated as a function of the molality of the electrolyte pair in the solution at the ambient RH (Eq. 4 in Jacobson, 1999). Moreover, the molality of the electrolyte pair in the solution is fitted to polynomials as a function of the water activity. The polynomial coefficients are listed in detail in Appendix Table B.10 of Jacobson (2005) and Table 8 of Meng et al. (1995). As discussed above, in EQUISOLV II, the equilibrium concentration of each species, including the liquid water content, is calculated by numerically solving

the equilibrium equation for each species separately, accounting for each chemical reaction. The solute activity coefficients and water contents are updated once the local convergence criterion is met (i.e., the level-2 and -3 iterations are completed). All equilibrium reactions and temperature dependent rate coefficients are listed in Jacobson (2005). The partitioning of ions to relevant solutes (H_2SO_4, $(NH_4)_2SO_4$, NH_4HSO_4, $(NH_4)_3H(SO_4)_2$) can be inferred by solving the solid-liquid equilibrium reactions as a function of temperature and relative humidity. The advantage of EQUISOLV II is that its open architecture makes it easy to incorporate new reactions and species but the shortcoming is that because of the general nature of the solution algorithm it is computationally quite slow even though the analytical equilibrium iteration (AEI) method adopted in EQUISOLV II resulted in a speed up of 13-48 times that of an older version of EQUISOLV (Jacobson, 1999).

EQSAM4 is a solubility-based gas/aerosol equilibrium model and a major revision of EQSAM3 with many improvements, although the overall analytical concept is unchanged. In contrast to EQUISOLV II and all other thermodynamic gas/aerosol equilibrium models, no iterations are required to solve the entire set of equilibrium reactions and the gas-liquid-solid partitioning. Within EQSAM4, all relevant non-ideal solution properties such as aerosol activities (including activity coefficients for (semi-volatile, aerosol water and the DRH and CRH of either binary or multi-component aerosol mixtures) are, at a specific RH and temperature, only analytical functions (parameterizations) of the chemical compound's effective solubility.

Table 2.1: Description of the parameterization and methods in EQUISOLV II and EQSAM4.

	EQUISOLV II	EQSAM4
Binary activity coefficients	A number of measurements, Pitzer's method and Harned and Owen's method[a]	Parameterization of T, RH and effective solubility of chemical compounds[b]
Multi-component activity coefficients	Bromley (Bromley, 1973)	N/A
Water activity	ZSR[c]	Parameterization of T, RH and effective solubility of chemical compounds
DRH/CRH	Prescribed based on a number of laboratory measurements for electrolytes at 298K	Parameterization of T, RH and effective solubility of chemical compounds, or prescribed RHD and T-coefficients.
MDRH	N/A[d]	Mean RHD, or prescribed MRHD
Solution method	Iterative chemical equilibrium and mass-flux iteration techniques	Analytical solution according to the solutes precipitation order (non- iterative)
System solved in this study	H^+-NH_4^+-Na^+-Ca^{2+}-Mg^{2+}-K^+-OH^--NO_3^--SO_4^{2-}-Cl^--CO_3^{2-}	H^+-NH_4^+-Na^+-Ca^{2+}-Mg^{2+}-K^+-OH^--NO_3^-- SO_4^{2-}-Cl^--CO_3^{2-}
Reference	Jacobson *et al.*, 1996; Jacobson 1999	Metzger *et al.*, 2011b

[a]Pitzer's method (Pitzer and Mayorga, 1973) and a number of measurements (Table B.9, Jacobson, 2005) are adopted to predict the mean binary solute activity coefficients at 298.15K while the temperature dependence of the coefficients is predicted using the Harned and Owen (1958) method.

[b]Mean ion-pair activity coefficients are needed only for volatile compounds (i.e., NH_4NO_3 and NH_4Cl) in EQSAM4.

[c]EQUISOLV II and EQSAM4 applied the so-called Zdanovskii-Stokes-Robinson (ZSR, Stokes and Robison, 1966) mixing rule to estimate the liquid water content at equilibrium; EQSAM4 optionally allows to apply instead a mixing rule based on parameterizations that simply uses mean values of the coefficients used for the single solute solutions (see Metzger *et al.*, 2011b).

[d]The MDRH in EQUISOLV II is not a function of chemical composition and temperature but can be inferred by solving the solid-liquid equilibrium reactions at various RH (Zaveri *et al.*, 2005a).

In EQSAM4, the equilibrium concentrations of each species are calculated by analytically solving the neutralization reaction for each species separately, assuming chemical equilibrium. The equation for each species is solved analytically based on cation-anion ratios and the resulting concentration is used in turn to solve the remaining equations. This sequence is repeated in a non-iterative manner until all neutralization reactions of all species are solved. The order for the neutralization reactions can be either prescribed according to an adopted Hofmeister series (same as used in EQSAM3), or automatically determined based on the solute's T-dependent deliquescence relative humidities (DRH) or the crystallization relative humidities (CRH). The Hofmeister series (Hofmeister, 1988) accounts for the order and degree to which ions bind water (i.e., the so-called salting-out effect).

For the T-dependent order, the neutralization order is automatically determined given the temperature and the (effective) solubility of the electrolytes. The electrolyte with the lowest solubility precipitates out first from the solution system so that the solute ions (which form the precipitating compound) are not available for further reactions. Then partitioning between solid and liquid phase is computed based on the mixed DRH/CRH of the solutes present in solution. The concentration of residual gases is deduced from conservation of mass. On the other hand, if the reaction order is prescribed, it is assumed that the precipitation of neutralized compounds follows the ability of the ions of the single solutes to neutralize the mixture, in which the ions to the left are neutralized preferentially:

For anions: $SO_4^{2-} > HSO_4^- > NO_3^- > Cl^- > CO_3^{2-}$

For cations: $Mg^{2+} > Ca^{2+} > Na^+ > K^+ > NH_4^+ > H^+$.

This increases the effective concentration of the remaining ions so that they precipitate if their DRH/CRH is reached, e.g. in case of decreasing RH (and thus water activity). The prescribed neutralization order based on the Hofmeister series is not dependent on temperature, as it relies on a fixed order of the DRH/CRH values, while the DRH/CRH order automatically involves a T-dependency, either because a prescribed T-dependency is considered for the certain compounds (where available) of the DRH/CRH are deduced during runtime at a given temperature from the solute solubility, for which a simplified T-dependency is assumed according to the gas-solution analogy (Metzger and Lelieveld, 2007). A brief inter-comparison between these two neutralization orders will be presented in Section 2.3.

EQSAM4 has an option to either prescribe the T-dependency for the DRH of major compounds (consistent with other thermodynamic models including EQUISOLV II), by using the T-coefficients for the DRH from ISORROPIA2 (Fountoukis and Nenes, 2007) to account for different T-dependencies of different compounds. This option can be used for either precipitation order (prescribed or DRH/CRH dependent) and has been applied in this work. Alternatively, EQSAM4 allows to calculate (assume) a T-dependencies of DRH and CRH for single or mixed solutions based on parameterizations that depend on RH and an assumed T-dependent (effective) solubility of the chemical compound. The key equation underlying the DRH and CRH parameterization is also used to calculate (online) the mean binary activity coefficients and the single solute molality of the electrolyte pair in the solution at the ambient RH, from which the aerosol water content is derived. The mixed solution DRH/CRH is inferred from the same equations used to derive the DRH/CRH of single solutes by simply using the mean values of the required

thermodynamic properties, i.e. the compound's effective solubility and molar masses. Optionally, various MDRH values (as used in ISORROPIA2) can be prescribed for certain mixed solutions.

For mixed solutions the mean mixed activity coefficient of a (semi-)volatile electrolyte is parameterized using a mean binary activity coefficient parameterization with different exponents for certain cation-anion ratios (domains). These domain dependent exponents have been derived from various reference model calculations (details are given in Metzger et al., 2011b). The equilibrium aerosol water content can be either determined at equilibrium from the ZSR-method (as done in this study), or, optionally calculated from the same mixing rule as used for the mean DRH/CRH, which is based on a mixing rule that applyies mean values of the coefficients used to calculate the equilibrium aerosol water content of the underlying single solute solutions (Metzger et al., 2011b).

As mentioned above, the entire gas-liquid-solid equilibrium partitioning, including solid concentrations of each species, activity coefficients for (semi-)volatile compounds, all single electrolyte molalities of single or multiple charged ion-pairs, the liquid water content, DRH and CRH, are all calculated analytically in EQSAM4 online, by solving the equilibrium neutralization reactions for each species separately, all being merely based on the compound's effective solubility (see Metzger et al., 2011b for more details). The solute activity coefficients and water contents, and all other properties, are calculated just once for a given RH and T. EQSAM4 is positive-definite, mass-conserving, and charge-conserving. The compounds considered in EQSAM4 are listed in Metzger et al. (2011b). The partitioning of ions to relevant solutes (H_2SO_4, $(NH_4)_2SO_4$, NH_4HSO_4, $(NH_4)_3H(SO_4)_2$) can be inferred by solving the solid-liquid equilibrium reactions as a

function of temperature and relative humidity from the key-equations given in Metzger et al. (2011b). The main advantage of EQSAM4 is its open architecture makes it easy to incorporate new compounds and its numerical efficiency, while the shortcoming certainly is that the analytical parameterizations might not under all conditions (mixed solutions) be as accurate as more explicit thermodynamic reference models. However, EQSAM4 has various options to easily control its complexity/accuracy, which is another advantage.

Common to both thermodynamic models is that both consider the so-called hysteresis loop by which atmospheric aerosols take up water when solids deliquesce in case the RH increases above the DRH of individual solid compounds (i.e., following the lower bound of the hysteresis loop), while aerosol water evaporates until crystallization occurs at the CRH when the aerosol water decreases abruptly (i.e., following the upper bound of the hysteresis loop). In the latter case, an electrolyte is allowed to form solids which precipitate from the solution if the RH is below its deliquescence relative humidity (DRH), whereas the electrolyte solid is not allowed to form when the RH is above the electrolyte's DRH, even if the electrolyte is in a multi-component mixture. On the other hand, if the ambient RH is decreasing, water evaporates from the aerosol particles, which increases the solute concentration. At the DRH, the solution remains supersaturated and is not allowed to crystallize until the crystallization relative humidity (CRH) is reached. The aerosol particle is considered dry when the RH drops below the lowest CRH of the solutes present in the actual solution.

Since aerosol water depends on both the composition of the solution and the solute concentrations, an iterative procedure is usually required to solve the gas-liquid-solid aerosol partitioning, as is the case for EQUISOLV II. However, since the RH fixes the

water activity of atmospheric aerosols in equilibrium with the ambient air, the new solubility method introduced with EQSAM3 and now applied in EQSAM4 with some revisions is capable to calculate the water uptake of atmospheric aerosol particles analytically and sufficiently accurately. Note that the Kelvin effect, which can be neglected for particles larger than about 0.1 μm (Bassett and Seinfeld, 1984), is not considered in EQUISOLV II but could be in principle accounted for by EQSAM4; an evaluation is, however, beyond the scope of this work.

2.3 Comparison of Simulation Results

In order to compare these two models under similar conditions, some modifications were made. In EQUISOLV II we switched off the chemical reaction involved in the formation of solid $(NH_4)_3H(SO_4)_2$ (letovicite) to make the results consistent with those of EQSAM4 which did not include letovicite at the time this study was undertaken. As discussed in Section 2.2, the derived DRH in EQSAM4 depends only on the solubility of the solute given the temperature and ambient RH to determine which compounds precipitate through either the prescribed or DRH(T)-dependent precipitation order. In EQSAM4, the DRHs are consistent with the literature and those used by state-of-the-art equilibrium models (e.g., EQUISOLV II). The solubilities used to calculate the DRH in EQSAM4 are listed in Table 2.2 for those compounds, those values deviate from EQSAM3. The values for all EQSAM4 compounds are shown in Metzger et al. (2011b).

Table 2.2: List of solubility and corresponding DRH of major solid compounds in EQSAM4 at a temperature 298K that deviate from EQSAM3.

	Solubility (%)[a]	DRH (298K)[b]
$(NH_4)_2SO_4$	45.11 (43.31)	0.7960 (0.7980)
NH_4NO_3	68.05 (68.05)	0.6150 (0.6067)
NH_4Cl	27.30 (28.34)	0.7710 (0.7659)
$NaHSO_4$	66.18 (22.18)	0.5250 (0.9285)
$NaNO_3$	48.70 (47.70)	0.7390(0.7476)
NaCl	27.97 (26.47)	0.7550 (0.7540)
K_2SO_4	11.71 (10.71)	0.9770 (0.9827)
$KHSO_4$	38.60 (33.60)	0.8650 (0.8836)
KNO_3	28.39 (27.69)	0.9279 (0.9279)
$CaSO_4$	05.21 (0.205)	0.9940 (1.0000)
$Ca(NO_3)_2$	58.22 (59.02)	0.4910 (0.4806)
$CaCl_2$	48.84 (44.84)	0.2810 (0.3228)
$MgSO_4$	34.31 (26.31)	0.8630 (0.8950)
$Mg(NO_3)_2$	59.59 (41.59)	0.5440 (0.7161)
$MgCl_2$	37.90 (35.90)	0.3290 (0.3508)

[a]The number within the parenthesis refers to EQSAM3, while the number outside is the updated solubility used by EQSAM4 in this study.

[b]The DRH within the parenthesis is derived from the solubility of solutes, based on the Handbook of Chemistry and Physics and refers to EQSAM3, while the value outside the parentheses is the updated DRH used by EQSAM4 in this study.

Table 2.3 lists a set of 20 different initial conditions similar to the 20 cases in the thermodynamic model inter-comparison of Zhang *et al.* (2000), but with the addition of initial conditions for the crustal elements (K^+, Ca^{2+}, and Mg^{2+}). These chemical

compositions cover most of the expected range of thermodynamic equilibrium regimes under typical urban, rural and coastal atmospheric conditions (Zhang *et al.*, 2000). Ansari and Pandis (1999a) show that the inclusion of crustal species could improve the agreement of their model with measurements by up to 15% in locations where crustal elements are significant, and Jacobson (1999) found that the presence of the Ca^{2+} and Mg^{2+} significantly affected the prediction of nitrate and ammonium in polluted locations such as Los Angeles. Metzger *et al.* (2006) showed that the consideration of mineral cations is important to balance aerosol ammonium. Hence, it is essential to account for the impacts of crustal species on the prediction of particulate ammonium and nitrate in general. We conducted 10 simulations for each initial condition, by using 10 different RH varying from 10% to 95% at a temperature of 298.15 K. For these 20 initial conditions, the concentration of total sulfate is fixed at 20 μg m^{-3}. Because H_2SO_4 has a very low vapor pressure, its gas phase concentration is negligible, so that its concentration can be used as a reference for the other species. Thus, we define the initial chemical concentrations of the other compounds according to seven dimensionless ratios with respect to total sulfate: the molar ratio of total ammonium (i.e., $t_{NH_4} = n_{NH_4^+(p)} + n_{NH_3(g)}$) to total sulfate (referred to as $\frac{t_{NH_4}}{t_{SO_4}}$), the molar ratio of total nitrate (i.e., $t_{NO_3} = n_{NO_3^-(p)} + n_{HNO_3(g)}$) to total sulfate (referred to as $\frac{t_{NO_3}}{t_{SO_4}}$), the molar ratio of total sodium chloride to total sulfate (referred to as $\frac{t_{NaCl}}{t_{SO_4}}$), the molar ratio of total potassium to total sulfate (referred to as $\frac{t_K}{t_{SO_4}}$), the molar ratio of total calcium to total sulfate (referred

to as $\frac{t_{Ca}}{t_{SO_4}}$), the molar ratio of total magnesium to total sulfate (referred to as $\frac{t_{Mg}}{t_{SO_4}}$) and the molar ratio of total cation species to total sulfate (referred to as $\frac{t_{CAT}}{t_{SO_4}}$), where t_{CAT} is defined as:

$$t_{CAT} = n_{NH_4^+} + n_{Na^+} + n_{K^+} + 2n_{Ca^{2+}} + 2n_{Mg^{2+}}.$$

The dominant composition potentially present in the system is determined by the ratio $\frac{t_{CAT}}{t_{SO_4}}$. If $\frac{t_{CAT}}{t_{SO_4}} < 2$, all available cation species react with sulfate and the system contains excess sulfate, which we call the sulfate rich regime. If $\frac{t_{CAT}}{t_{SO_4}} = 2$, all available cation species are just sufficient to neutralize the sulfate present in the system, and this is called the sulfate neutral regime. If $\frac{t_{CAT}}{t_{SO_4}} > 2$, the available sulfate in the system is not enough to neutralize the cation species, and this is called the sulfate poor regime. For the 20 sets of conditions, conditions 1-5 are in the sulfate rich regime, conditions 6-10 are sulfate neutral, and conditions 11-20 are sulfate poor. Note that we also include some of the same cases in each of these three regimes that were included in the inter-comparison of Zhang *et al.* (2000), which allows us to make a direct comparison of the results simulated by EQSAM4 and EQUISOLV II with the results simulated by four other inorganic aerosol thermodynamic modules (MARS-A, SEQUILIB, SCAPE2 and AIM2) for the same initial conditions. Simulations are carried out under the assumption that aerosols lie on the deliquescence branch. A sensitivity test to explore differences when using efflorescence will be investigated in Section 2.4.

Table 2.3: List of 20 sets of conditions applied in the model simulations[a]

Sulfate condition	Case No.	$\frac{t_{NH_4}}{t_{SO_4}}$	$\frac{t_{NO_3}}{t_{SO_4}}$	$\frac{t_{NaCl}}{t_{SO_4}}$	$\frac{t_K}{t_{SO_4}}$	$\frac{t_{Ca}}{t_{SO_4}}$	$\frac{t_{Mg}}{t_{SO_4}}$
Sulfate Rich	1(2)	1.0	1.0	0	0	0	0
	2(8)	1.5	3.0	0	0	0	0
	3(10)	0.5	1.0	0.5	0	0	0
	4	0.5	1.0	0.5	0.04	0.02	0.01
	5	1.5	3.0	0	0.04	0.02	0.01
Sulfate Neutral	6(4)	2.0	1.0	0	0	0	0
	7(15)	1.5	0.33	0.5	0	0	0
	8(17)	1.5	3.0	0.5	0	0	0
	9	1.5	0.33	0.4	0.04	0.02	0.01
	10	1.5	3.0	0.4	0.04	0.02	0.01
Sulfate Poor	11(5)	4.0	1.0	0	0	0	0
	12(9)	4.0	3.0	0	0	0	0
	13(13)	2.0	1.0	0.5	0	0	0
	14(14)	4.0	1.0	0.5	0	0	0
	15(20)	4.0	1.0	2.0	0	0	0
	16	2.0	1.0	0.5	0.04	0.02	0.01
	17	4.0	1.0	0.5	0.04	0.02	0.01
	18	4.0	1.0	2.0	0.04	0.02	0.01
	19	4.0	1.0	0	0.04	0.02	0.01
	20	4.0	3.0	0	0.04	0.02	0.01

[a]The particulate sulfate concentration is fixed at 20 μg m^{-3} for all cases. The concentration of other aerosol components is listed as molar ratio with respect to the particulate sulfate concentration. Simulations under each set of initial compositions were conducted for 10, 20, 30, 40, 50, 60, 70, 80, 90 and 95% relative humidity at a temperature 298.15 K. The case numbers in the parenthesis refer to the cases in the study by Zhang *et al. (*2000).

Figure 2.1 shows scatter plots of the concentration of aerosol water, total particulate matter, nitrate, ammonium, chloride, and potential of hydrogen labeled as H_2O(aq), PM,

$[NO_3^-]_p$, $[NH_4^+]_p$, $[Cl^-]_p$, and pH predicted by EQSAM4 and EQUISOLV II under all 200 simulation conditions specified in Table 2.3. The solid black lines are the 1:2, 1:1 and 2:1 lines. The DRH-dependent neutralization order in EQSAM4 was used for this figure.

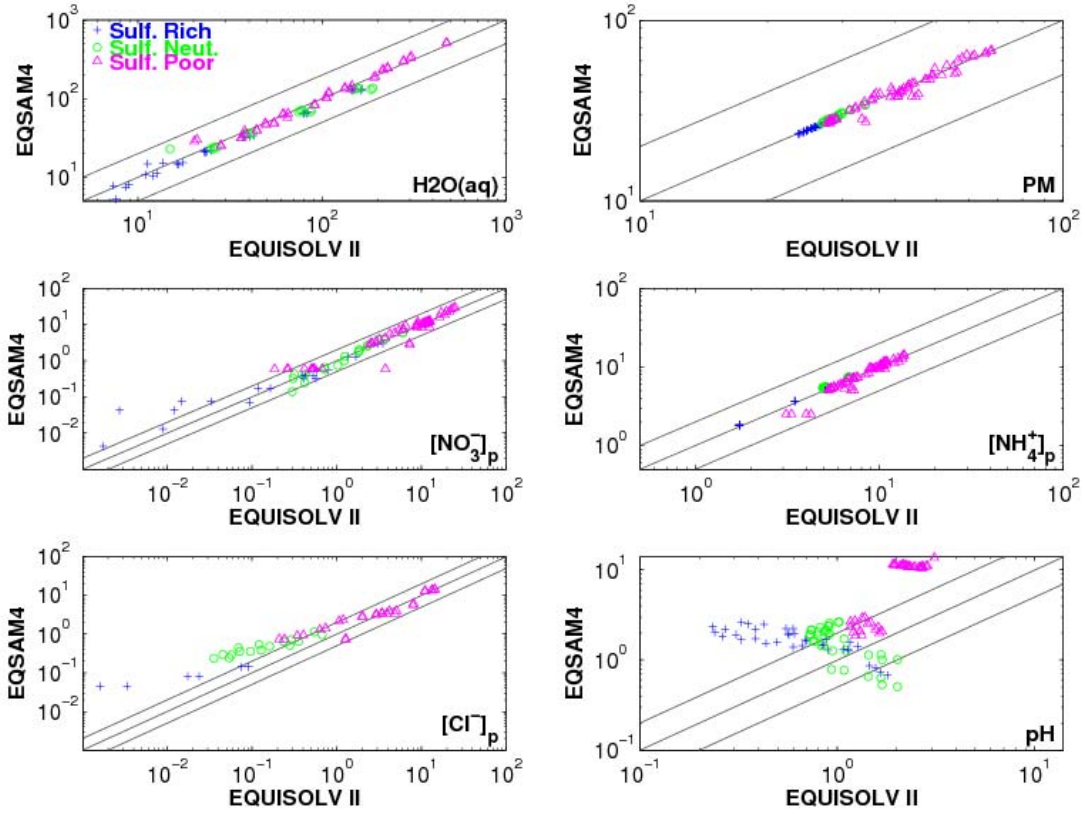

Figure 2.1: Scatter plots of aerosol water ($H_2O_{(aq)}$), total particulate matter (PM), particulate NO_3^- ($[NO_3^-]_p$), particulate NH_4^+ ($[NH_4^+]_p$), particulate Cl^- ($[Cl^-]_p$), and potential of hydrogen (pH) predicted by EQSAM4 and EQUISOLV II based on the 200 initial conditions specified in Table 2.3 at a temperature of 298.15K. The black diagonal lines are the 1:2, 1:1, 2:1 lines, respectively. The units are μg m^{-3}. The concentration is shown using a logarithmic scale.

2.3.1 Aerosol water

For all conditions, the aerosol water $H_2O(aq)$ predicted by EQSAM4 is close to that predicted by EQUISOLV II. For most cases, the difference for aerosol water is well within a factor of 2, and on average EQSAM4 and EQUISOLV II differ by 4% for all 200 conditions. Table 2.4 gives the relative difference and the linear regression slope along with its 95% confidence interval (CI) of aerosol water and total particulate matter between EQSAM4 and EQUISOLV II for the three sulfate regimes at 298.15 K under all RH conditions shown in Figure 2.1. "Rich" stands for the sulfate rich regime (i.e., cases 1-5); "Neutral" stands for the sulfate neutral regime (i.e., cases 6-10); "Poor" stands for the sulfate poor regime (i.e., cases 11-20); "All" stands for the conditions including all three sulfate regimes. Here we exclude values in our statistical table and the linear regression calculation, if the aerosol water predicted by both models is less than 5.0 μg m^{-3}. The relative difference is defined as $\frac{EQ4 - EQ2}{EQ2} \times 100\%$, where EQ4 and EQ2 stand for EQSAM4 and EQUISOLV II, respectively. Overall, the slope of regression line between the aerosol water predicted by EQUISOLV II and that predicted by EQSAM4 is 1.06 with a 95% CI of 0.03 for all 200 conditions shown in Table 2.3. For the sulfate rich regime, the slope is 0.83 with a 95% CI of 0.02 while it is 0.76 with a CI of 0.06 for the sulfate neutral regime and 1.10 with a CI of 0.02 for the sulfate poor regime. Figure 2.2 shows the the aerosol water predicted by EQSAM4 and EQUISOLV II for all 20 cases listed in Table 2.3. The prediction of aerosol water from EQSAM4 agrees well with that from EQUISOLV II. The largest discrepancy in the aerosol water between these two models is caused by either differences in the prediction of bi-sulfates (sulfate rich regime) or the liquid-solid partitioning involving volatile species (i.e., ammonium nitrate and

ammonium chloride), which affects the water uptake (mainly in the sulfate neutral regime) and will be discussed in more detail later.

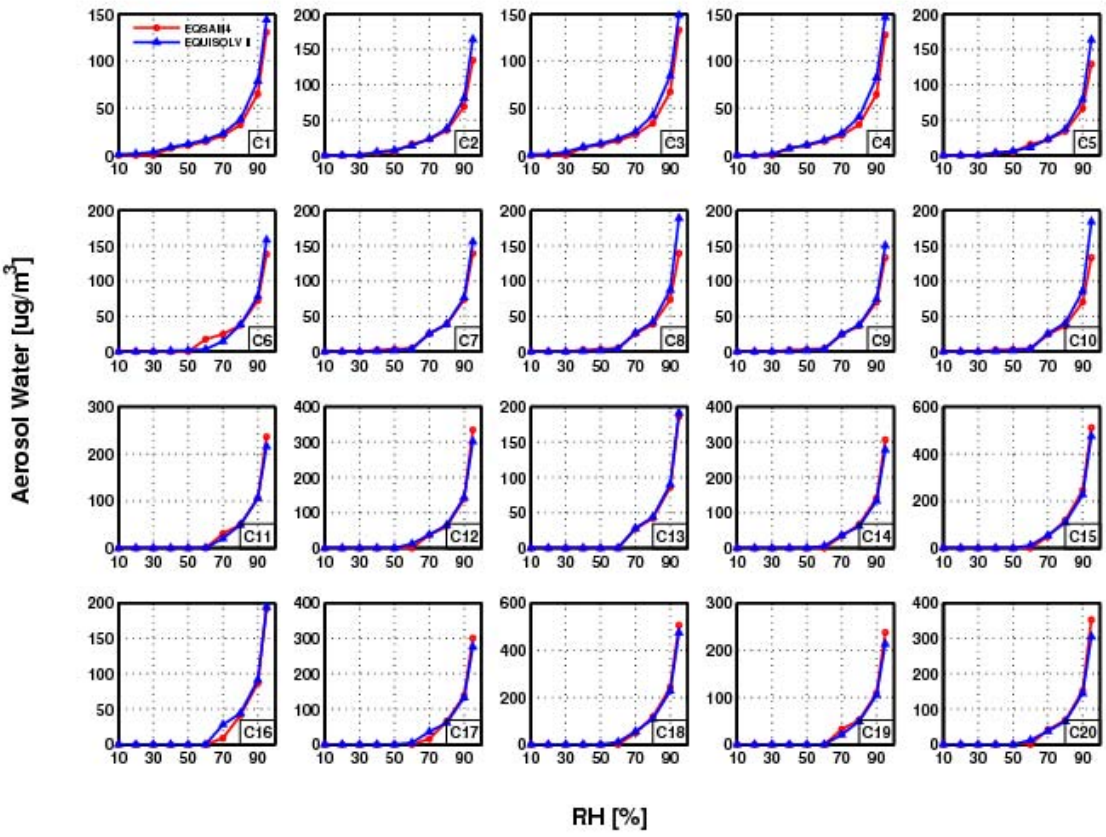

Figure 2.2: Aerosol water predicted by EQSAM4 and EQUISOLV II for all 20 cases listed in Table 2.3.

2.3.2 Total particulate matter

Figure 2.3 shows the total particulate matter (PM) predicted by EQSAM4 and EQUISOLV II for all 20 cases listed in Table 2.3. The prediction of PM from EQSAM4 agrees well with that from EQUISOLV II. Similar to the aerosol water the relatively largest discrepancy in the PM is caused by either differences in the prediction of bi-

sulfates (sulfate rich regime) or the liquid-solid partitioning involving volatile species (i.e., ammonium nitrate and ammonium chloride), which affects the PM mainly in the sulfate neutral and poor regime around the deliquescence of the mixed solutions. Nevertheless, as shown in Table 2.4, EQSAM4 predicts only 1% lower total particulate matter compared to EQUISOLV II for all 200 simulations shown in Table 2.3 when the DRH-dependent neutralization order was adopted. But the choice of the neutralization order does not significantly alter these results (see note at the end of this section). The slope of the linear regression line between the PM predicted by EQUISOLV II and that predicted by EQSAM4 is 1.01 with a 95% CI of 0.02 for all 200 conditions, which indicates reasonably good agreement between the two models with respect to the prediction of PM. In the sulfate rich regime, the EQSAM4 predicted PM is close to or a little less than EQUISOLV II by about 1% while it predicts lower PM by 0.08% in the sulfate neutral regime and by 1% in the sulfate poor regime. Table 2.5 shows the total particulate matter predicted by EQSAM4 and EQUISOLV II at 298.15 K and 30% RH for all 20 conditions and their relative difference. The total PM predicted by EQSAM4 is less than that of EQUISOLV II for almost all conditions, except for case 12. For the case 12,, i.e., the condition with high ammonium ($\frac{t_{NH_4}}{t_{SO_4}}$=4.0) and high nitrate ($\frac{t_{NO_3}}{t_{SO_4}}$=3.0), EQSAM4 predicts 8% higher total particulate than EQUISOLV II because more NH_4NO_3 is formed in EQSAM4, however, EQSAM4 is in this case more close to AIM2 which predicts an even higher amount of total particulate matter for same condition (denoted in bold and italics in Table 2.5).

Table 2.4: Relative difference as well as linear regression slope with the 95% confidence interval of total particulate matter (PM), aerosol water (AW) and pH between EQSAM4 and EQUISOLV II for the three sulfate regimes at 298.15 K under all RH conditions shown in Figure 2.1

Sulfate Regime[a]	AW		PM		pH	
	Rel. Diff. (%)	Reg. Slope	Rel. Diff. (%)	Reg. Slope	Rel. Diff. (%)	Reg. Slope
Rich	-10.16	0.83±0.02	-1.21	0.95±0.03	256.91	-0.97±0.22
Neutral	-5.68	0.76±0.06	-0.08	1.07±0.05	77.51	-1.17±0.43
Poor	1.96	1.10±0.02	-1.36	1.02±0.04	258.08	6.71±1.18
All	-3.92	1.06±0.03	-1.01	1.01±0.02	203.03	4.31±0.66

[a]"Rich" refers to the sulfate rich regime (i.e., cases 1-5); "Neutral" the sulfate neutral regime (i.e., cases 6-10); "Poor" the sulfate poor regime (i.e., cases 11-20); "All" refers to the conditions including all three sulfate regimes.

The normalized relative difference in Table 2.5 is defined the same as that in Table 2.4. The value in parentheses in the EQUISOLV II column in Table 2.5 is the model-average PM concentration presented in Zhang *et al.* (2000) and that by AIM2 (denoted in bold and italics), respectively. The value in parentheses in the EQSAM4 column and the relative difference column refer to the prediction using the prescribed neutralization order in EQSAM4. Notice that there is a slight difference with respect to the PM concentration predicted in EQUISOLV II in this study compared to that in Zhang *et al.* (2000) because we switched off the formation of letovicite in order to match the solid components predicted in EQSAM4. At RH 30%, the PM predicted by EQSAM4 is about 1% lower than that predicted by EQUISOLV II for all conditions when using the DRH-dependent neutralization order (which is used in general for all cases). For the sulfate rich and neutral regimes, EQSAM4 predicts total particulate matter that is slightly lower by about

1% than that predicted by EQUISOLV II while it predicts about 2% lower particulate matter in the sulfate poor regime.

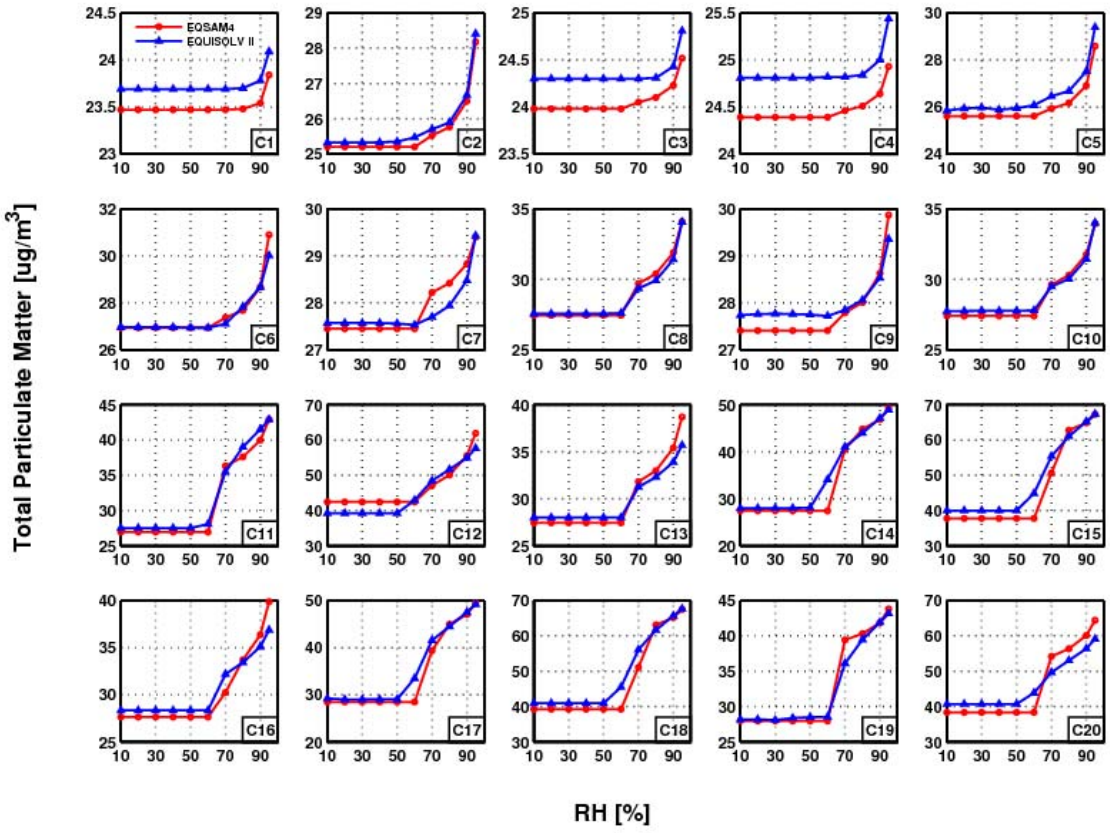

Figure 2.3: Total particulate matter predicted by EQSAM4 and EQUISOLV II for all 20 cases listed in Table 2.3.

When using the prescribed neutralization order, the total PM predicted by EQSAM4 is comparable, i.e., lower by about 1% compared to that in EQUISOLV II. The results using the prescribed neutralization order are thus similar to those using the DRH-dependent neutralization order in EQSAM4. In the following, we choose the DRH-dependent neutralization order hereafter for further evaluation as its advantage is that it automatically accounts for any temperature effects on the precipitation order.

Table 2.5: Total Particulate matter (PM) concentration predicted at 298.15 K and RH 30% under all conditions.

Case	PM concentrations (μg m^{-3})		Relative difference[c] (%)
	EQSAM4[a]	EQUISOLV II[b]	
1	23.47 (23.47)	23.69 (23.3, ***23.3***)	-0.93 (-0.93)
2	25.2 (25.2)	25.32 (25.1, ***25.1***)	-0.47 (-0.47)
3	23.98 (23.98)	24.3 (21.5, ***23.3***)	-1.32(-1.32)
4	24.46(24.39)	24.81	-1.31 (-1.69)
5	25.61(25.61)	25.97 (26.8, ***26.9***)	-1.39(-1.39)
6	26.94 (26.94)	26.96 (25.6, ***25.0***)	-0.07 (-0.07)
7	27.45 (27.45)	27.57 (24.9, ***25.0***)	-0.44 (-0.44)
8	27.45 (27.45)	27.57	-0.44 (-0.44)
9	27.41 (27.41)	27.77	-1.30 (-1.30)
10	27.41 (27.41)	27.77	-1.30 (-1.30)
11	26.95(26.95)	27.51 (26.9, ***NA***)	-2.04 (-2.04)
12	42.24 (42.41)	39.21 (40.5, ***47.3***)	7.73 (8.16)
13	27.45 (27.45)	28.01 (27.4, ***25.1***)	-2.00 (-2.00)
14	27.45 (27.45)	28.01 (30.5, ***NA***)	-2.00 (-2.00)
15	37.48 (37.76)	40.00 (40.6, ***NA***)	-6.30 (-5.60)
16	27.62 (27.62)	28.32	-2.47 (-2.47)
17	28.41 (28.45)	28.98	-1.97 (-1.83)
18	38.84 (39.19)	40.87	-4.97 (-4.11)
19	27.91 (27.94)	28.06	-0.53 (-0.43)
20	38.11 (38.30)	40.66	-6.27(-5.80)

[a]The value in parentheses in the column for EQSAM4 is the PM concentration using the prescribed neutralization order.

[b]The values in parentheses are those from the model-average PM concentration and AIM2 (bold and italic) from Zhang *et al.* (2000) for reference. AIM2 does not simulate alkaline systems (i.e., cases 11, 14 and 15).

[c]The relative difference is defined as the normalized difference in the PM concentration predicted by EQSAM4 and EQUISOLV II. The value in the parentheses is the difference corresponding to the prescribed neutralization order (specified by the Hofmeister series) while that outside the parentheses corresponds to the DRH-dependent neutralization order in EQSAM4.

2.3.3 Particulate nitrate

Overall the particulate nitrate concentrations predicted by both models agree well within a factor of 2. The main differences occur around the mixed solution deliquescence in the sulfate poor and rich conditions as shown in Figure 2.4, which complements Figure 2.1. Figure 2.4 shows the particulate nitrate predicted by EQSAM4 and EQUISOLV II for 20 cases shown in Table 2.3. For most cases in the sulfate poor regime (i.e., case 11-20), the particulate nitrate concentrations predicted by both models agree, except for some of the conditions at higher RH (i.e., case 12, 13, 16, 20) and around the deliquescence at RH 60% (i.e., case 14, 15, 17, 18). For the high ammonium ($\frac{t_{NH_4}}{t_{SO_4}}$=4.0) and high nitrate ($\frac{t_{NO_3}}{t_{SO_4}}$=3.0) concentrations without NaCl (i.e., cases 12 and 20) or the cases 13 and 16, the discrepancy at higher RH (RH > 70%) between these two models can be ascribed to the activity coefficient parameterization which yields a slightly higher activity coefficient of NH_4NO_3 used in EQSAM4 at lower molalities (i.e. higher relative humidities) as shown in Figure 2.5(a).

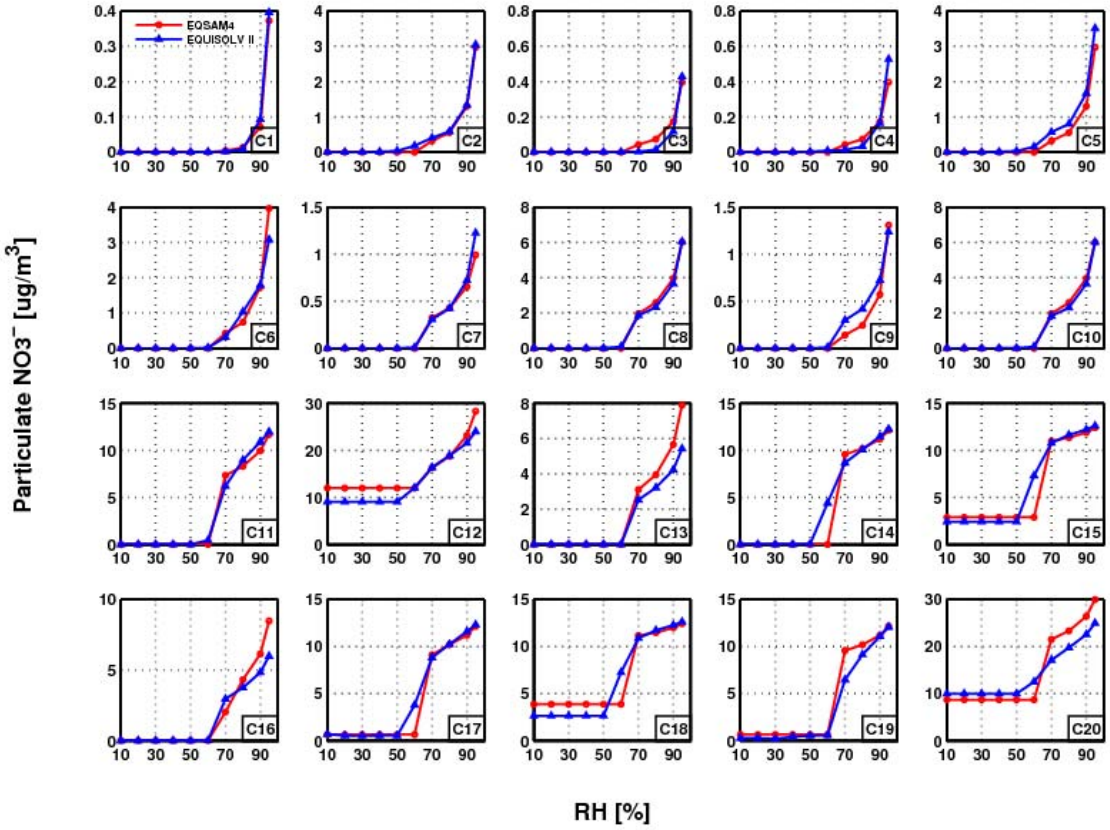

Figure 2.4: Particulate nitrate predicted by EQSAM4 and EQUISOLV II for all 20 cases listed in Table 2.3.

Despite these differences in the activity coefficient parameterization the difference in the particulate nitrate concentration between these two models is much smaller at conditions with high ammonium ($\frac{t_{NH_4}}{t_{SO_4}}$=4.0) with NaCl or mineral species (K, Ca and Mg) loadings at higher RH (RH > 70%), although a somewhat larger discrepancy occurs around RH 60%. Overall, both models consistently predict higher $NH_4NO_3(s)$ for case 15 than case 14 because the amount of particulate NO_3^- depends on the amount of sodium (Figure 2.4). The addition of sodium chloride drives the reaction $NaCl(s) + HNO_3(g) \Leftrightarrow NaNO_3(s) + HCl(g)$ to the right-hand side and the dissociation

of $NaNO_3$(s) produces the NO_3^- ion which can bind with NH_4^+ to form NH_4NO_3(s), resulting in the increase of nitrate present in the aerosol phase (case 15 vs case 14) and further enhances the amount of total particulate matter. A similar chemical mechanism holds for the formation of NH_4Cl(s) (i.e., case 15 vs. case 14 or case 18 vs. case 17). In EQUISOLV II (Jacobson, 2005), a solid electrolyte is allowed to form when the RH is less than its DRH and the product of its reactant ion concentration and mean solute activity coefficient exceeds its solubility product, i.e. the equilibrium coefficient, $K_{eq}(T)$. For example, in the reversible reaction $NH_4NO_3(s) \Leftrightarrow NH_4^+ + NO_3^-$, the precipitation of ammonium nitrate from the solution phase in EQUISOLV II may occur when

$$m_{NH_4^+} m_{NO_3^-} \gamma^2_{NH_4^+, NO_3^-} > K_{eq,i}(T)$$

where the subscript *i*, differentiates the equilibrium coefficient for this reaction. In EQSAM4 this only depends on the compound's DRH that is based on the (effective) solubility. In EQUISOLV II a solid may also form directly due to the heterogeneous reaction of gases on the surface of a particle, while in EQSAM4 the solid formation always depend on the DRH and the DRH-dependent neutralization reaction order. For example, in the reaction $NH_4NO_3(s) \Leftrightarrow NH_3(g) + HNO_3(g)$, a solid will form In EQUISOLV II when RH < RHD and

$$p_{NH_3(g)} p_{HNO_3(g)} > K_{eq,j}(T),$$

while in EQSAM4 the solid formation of NH_4NO_3(s) primarily depends on the DRH-dependent neutralization reaction order. However, EQSAM4 has an option to consider for the two (semi-)volatile species NH_4NO_3(s) and NH_4Cl(s), their equilibrium constant as an additional condition that must be fulfilled for the neutralization reaction. This option was used in this study. The values of K_e and the temperature coefficients used in

EQSAM4 are taken from ISORROPIA2 and are the same as used in EQUISOLV II (see Metzger et al., 2011b for details). Regardless what K_e values is used for NH_4NO_3(s), addition of Na^+ yields more $NaNO_3$(s), and as a consequence this "unused" amount of NH_4^+ is able to neutralize SO_4^{2-} rather than NO_3^-, which increases the alkalinity of the residual aerosol system. In turn, any excess of NH_3(g) can further neutralize NO_3^- or Cl^- to form NH_4NO_3 and NH_4Cl, resulting in higher concentrations of particulate nitrate as well as total PM. This behavior is shown by (a) case 15 with its higher sodium chloride loadings versus the case 14, or by (b) case 18 versus 17. On the other hand, when NaCl is absent, the addition of total nitrate to the system increases the vapor pressure of HNO_3(g) and shifts the reaction of $NH_4NO_3(s) \Leftrightarrow NH_3(g) + HNO_3(g)$ to the left-hand side which increases the formation of solid NH_4NO_3, leading to higher concentrations of particulate nitrate as well as total particulate matter – shown by case 12 vs. case 11, and case 20 vs. case 19.

Similar to EQUISOLV II, a solid electrolyte is allowed to form in EQSAM4 when the RH is less than its DRH, but before a solid electrolyte precipitates out of the solution the product of the reactant ion concentration must exceed the (temperature-dependent) solubility constant, for non-volatile compounds independent of the mean solute activity coefficient, in contrast to EQUISOLV II. Here, we found that in case the RH is lower than the DRH of nitrate salts, the amount of solid nitrate predicted by EQSAM4 is slightly larger than that from EQUISOLV II with low nitrate loadings (e.g., case 15 and 18). The amount of particulate nitrate in the solid phase at lower RH is determined by the minimum amount of total nitrate and the available cation species in EQSAM4 based on the NH_4NO_3 activity coefficient at RHD, whereas, in EQUISOLV II, the solid particulate

nitrate is calculated by solving the equilibrium reaction equations of the solid compounds individually. For the sulfate rich and neutral regimes, both models predict similar amounts of particulate nitrate except for some excursions of EQSAM4 from EQUISOLV II at very low nitrate concentrations.

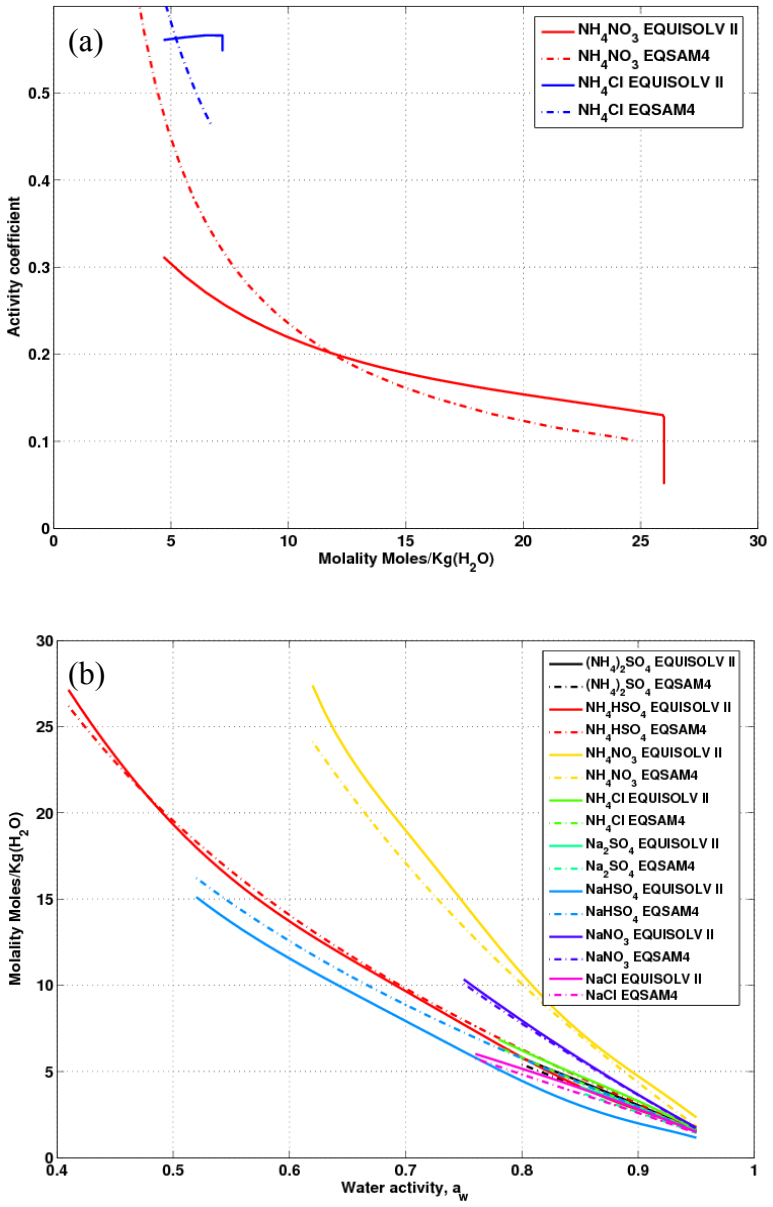

Figure 2.5: Mean binary activity coefficients of NH_4NO_3 and NH_4Cl as a function of molality (a) and molality for several electrolytes at a temperature 298.15 K as a function of water activity (b) (i.e. RH with a 0-1 scale).

2.3.4 Particulate ammonium

The particulate ammonium concentrations predicted by EQSAM4 and EQUISOLV II are in good agreement under most conditions, especially in the sulfate rich and neutral regimes ($\frac{t_{CAT}}{t_{SO_4}} < 2$ or $\frac{t_{CAT}}{t_{SO_4}} = 2$) in which the sulfate is in excess of the number of cations, or just sufficient for neutralization. For these two cases (sulfate rich and neutral), all the available ammonium is neutralized by sulfate and present in the aerosol phase. In sulfate poor conditions, the particulate ammonium in EQSAM4 deviates a bit more because of the differences discussed above for nitrate, but it is still well within a factor of 2 of that predicted by EQUISOLV II. Overall, EQSAM4 predicts similar or rather smaller amounts of particulate ammonium for the entire range of relative humidities compared to EQUISOLV II. The reason is that the activity coefficients of NH_4NO_3 and NH_4Cl in EQUISOLV II are slightly higher than those used in EQSAM4 at lower molality (i.e., higher RH) as mentioned before. At lower RH, the amount of particulate ammonium is determined in EQSAM4 by the total ammonium as well as the amount of anion species available for neutralization, where the nitrate concentration also depends on the activity coefficients of NH_4NO_3 at RHD. In accordance with EQUISOLV II, the temperature-dependent equilibrium constant (K_{eq}) for NH_4NO_3 and NH_4Cl is considered in EQSAM4. However, since the $K_{eq(NH4NO3)}$ and $K_{eq(NH4Cl)}$ have rather low (values in EQSAM4 are 57.46 $nmol^2$ and 108.6 $nmol^2$, respectively), switching K_{eq} on or off in EQSAM4 did not make a noticeable difference for any of our cases (not shown), since the input concentration used for all cases are in the μmol range and thus above the nmol concentration range where the K_{eq} becomes active.

2.3.5 Particulate chloride

The concentrations of particulate chloride predicted by EQAM4 are also in reasonable agreement with those predicted by EQUISOLV II in most sulfate poor conditions, where NH_4Cl becomes important. Under sulfate rich and neutral conditions EQSAM4 predicts slightly higher amounts of particulate chloride than does EQUISOLV II, as shown in Figure 2.1; especially for certain sulfate rich conditions. However, the total amount of particulate chloride is negligible (less than 1 $\mu g\ m^{-3}$) and limited to a partly enhanced HCl uptake in these two regimes, because of the abundance of free ammonium (since ammonium is entirely bound to sulfate for these two regimes). In contrast, under the sulfate poor conditions, the amount of particulate chloride that forms depends on NH_4Cl and the amount of NaCl or other crustal species (i.e., K^+, Ca^{2+}, Mg^{2+}) for the same reason as described above for nitrate. The presence of metal cations can neutralize sulfate and increase the alkalinity of the system, which allows any excess $NH_3(g)$ to be neutralized by Cl^- to form NH_4Cl, resulting in a higher concentration of particulate chloride. This is similar to the effects of sodium on the amount of the particulate nitrate and EQSAM4 agrees well with EQUISOLV II on the prediction of particulate chloride in this most complicated thermodynamic regime.

2.3.6 Potential of hydrogen

The potential of hydrogen (pH) is most difficult to predict and the most uncertain parameter in any model, since it is influenced by the entire gas-liquid-solid partitioning and especially by the liquid water and the uptake of gases in acid solutions. Thus, as a result the relatively largest discrepancies between the predictions of EQUISOLV II and EQSAM4 are found for the pH. According to Table 2.4, EQSAM4 predicts about a factor

2.6 higher pH of the solution system than EQUISOLV II does in the sulfate rich and poor regimes, while according to Figure 2.1 most cases are clustered around the center of the log-log pH plot. The largest deviations are found for the sulfate neutral regime, where EQSAM4 predicts about 77% higher pH than EQUISOLV II does. The reason is that EQSAM4 predicts for some alkaline cases a very high alkalinity with a pH larger than 9, while EQUISOLV II does not. This alkalinity predicted by EQSAM4 is results of the fact that the metal cations Na^+, K^+, Ca^{2+} and Mg^{2+} are prescribed in the input concentration as cations, while the acidic gases HCl, HNO_3 and H_2SO_4 are so prescribed as acids (not anions), so that the presence of metal cations, which leads to a preferred neutralization of these acids (compared to NH_3), results in a mass and charge conserving system automatically to a release of H^+ (from the acids) and thus yields an excess of H^+; hence the high alkalinity for the sulfate poor cases, where metal cations are present. Note that EQSAM4 behaves in these cases exactly as ISORROPIA II (not shown). Also note that this high alkalinity can be "suppressed" in EQSAM4 if it is assumed that metal cations are "neutralized", e.g. they are prescribed in the input concentration as e.g. NaOH (etc.). Then H^+ of the acids would combine with the OH^- from the metal cations to form H_2O, and hence a neutral solution. In EQUISOLV II, the equilibrium concentrations of H^+ and OH^- are determined by solving correspoinding equilibrium reactions in an iterative manner. A more detailed investigation on the prediction of the pH between two models is out of the scope of this study.

2.3.7 Dominant solid PM compounds

Figure 2.6 shows the concentrations of the dominant solid compounds (i.e., $(NH_4)_2SO_4$, NH_4HSO_4, NH_4NO_3, NH_4Cl, Na_2SO_4, $NaHSO_4$, $NaNO_3$ and NaCl) predicted

by EQSAM4 and EQUISOLV II at RH 30% and a temperature of 298.15 K. The "other(s)" category in the figure includes the remaining solid metal compounds in the system. In the sulfate rich regime (i.e., cases 1-5), the ammonium ion neutralizes sulfate ions to form NH_4HSO_4 in both models. This prediction is consistent with the fact that aqueous sulfate mainly dissociates to form one hydrogen ion and one bisulfate ion when sulfate is in excess. The prediction of dominant solid compounds in ISORROPIA II is similar in the sulfate rich regime (Foutoukis and Nenes, 2007). Seinfeld and Pandis (1998) also showed that the particles consist mainly of bisulfate in the sulfuric acid-ammonia-water system for an acidic atmosphere ($TNH_4/TSO_4 > 0.5$ and $TNH_4/TSO_4 < 1.5$). The preferred composition of the aerosol phase is only ammonium sulfate if there is sufficient ammonia to neutralize the available sulfuric acid in the system. Spann and Richardson (1985) observed that ammonium bisulfate is the preferred composition in mixed ammonium and sulfate particles if the molar ratio of $\frac{t_{NH_4}}{t_{SO_4}}$ is between 1.0 and 1.5. The addition of crustal species (i.e., K^+, Ca^{2+}, Mg^{2+}) allows Na^+ or NH_3 to neutralize the sulfate to form $NaHSO_4$(s), Na_2SO_4(s) and NH_4HSO_4(s). If crustal species are added to the system, which directly form a solid at 30% RH, the solid particulate matter increases slightly; as it is the case in going from case 3 to case 4 in both EQUISOLV II and EQSAM4 in Table 2.5. Notice that the predicted amount of NH_4HSO_4(s) and $NaHSO_4$(s) are associated with the relatively largest differences between EQSAM4 and EQUISOLV II w.r.t. to the 20 cases investigated. The reason is the above noted differences the bi-sulfate prediction, which, although not significant in the prediction of the total PM (dry and aqueous), obviously results in more noticeable differences for the solid PM due to associated differences in the liquid-solid partitioning of the bi-sulfate salts. In

EQUISOLV II, the liquid-solid partitioning of the salts are determined by solving corresponding equilibrium reactions for all conditions as mentioned before, i.e., partial NH_4^+ and Na^+, HSO_4^- are allowed to exist in liquid phase for case 3 or case 4. In contrast, only solid bi-sulfate salts are allowed to form in EQSAM4 for same situations. In EQSAM4, all the Na^+ is firstly neutralized by HSO_4^- and then so does NH_4^+. That's why more NH_4HSO_4(s) are formed for case 1, case 3 and case 4 in EQSAM4 than does EQUISOLV II but there is not significant different on the prediction of PM for these cases.

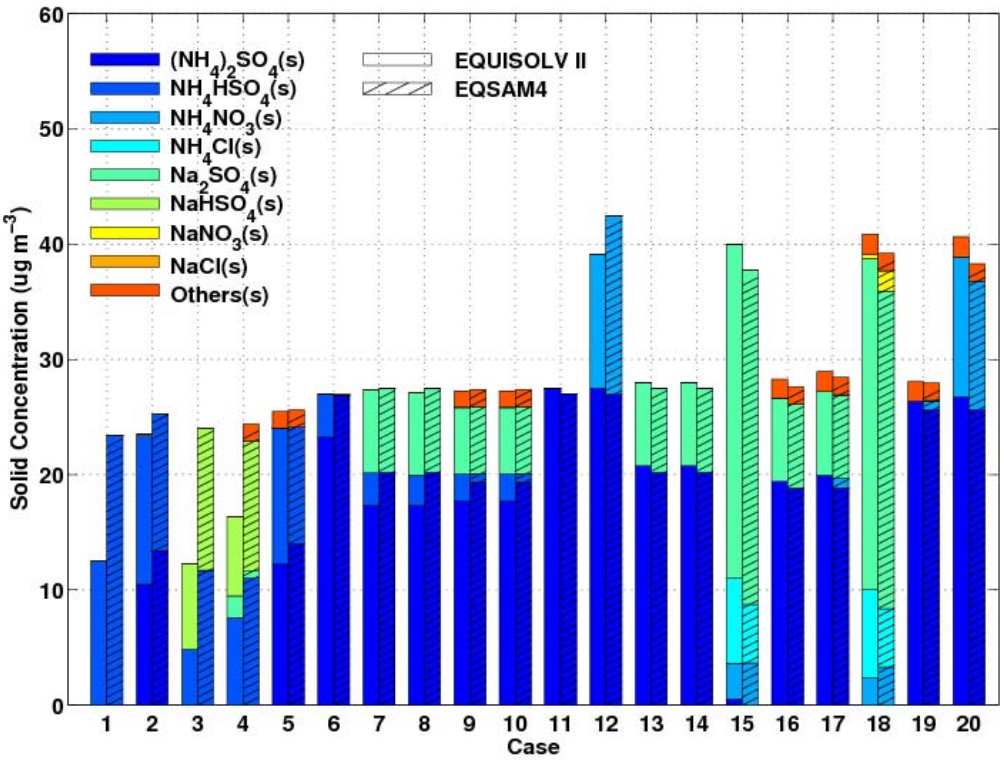

Figure 2.6: Concentrations of major solid compounds predicted by EQSAM4 and EQUISOLV II at an RH of 30% and a temperature of 298.15 K for the 20 cases listed in Table 2.3.

In the sulfate neutral regime (i.e., cases 6-10), the total solid particulate matter predicted by EQUISOLV II (which is dominated by sulfate salts mixed with some bisulfate salts) is very close to that in EQSAM4 in which a similar mixture of sulfate and bisulfate salts is predicted. In the sulfate poor regime, however, EQSAM4 predicts slightly less or more solid NH_4NO_3 but always slightly less solid NH_4Cl than that EQUISOLV II at an RH of 30%.

Under conditions with high ammonium and low nitrate (e.g., case 11) there is no solid NH_4NO_3 predicted by both models. By adding more total nitrate to the system, which increases the vapor pressure of $HNO_3(g)$, NH_4NO_3 begins to form in both models (i.e., case 12), but EQSAM4 predicts slightly more solid NH_4NO_3. For the other conditions EQSAM4 shows a similar behavior. Additionally, no solid NH_4Cl forms in both EQUISOLV II and EQSAM4 in case 17. Increasing the ratio $\frac{t_{NaCl}}{t_{SO_4}}$ from 0.5 to 2, allows more Na^+ to neutralize SO_4^{2-}, resulting in an increase in the availability of ammonium to bind with NO_3^- and Cl^- to form NH_4NO_3 and NH_4Cl in case 18.

Figure 2.5a shows the mean binary activity coefficients of NH_4NO_3 and NH_4Cl as a function of molality while Figure 2.5b shows the predicted molality of several electrolytes at a temperature 298.15 K as a function of water activity. There is some difference in the activity coefficients parameterizations as well as the EQSAM4 parameterization of the electrolyte molality slightly differs compared to the (observational) data used by EQUISOLV II, which is also responsible for the model discrepancies in the sulfate poor regime and the above noted differences between the predictions of the two dominant solid compounds (NH_4NO_3 and NH_4Cl) by EQSAM4 and EQUISOLV II.

2.3.8 Hygroscopic growth factor (HGF)

Figure 2.7 shows the relative difference in the growth factor between EQSAM4 and EQUISOLV II as a function of RH at a temperature of 298.15 K. The error bars indicate the range of change in the growth factor for all 20 cases. Here the growth factor is defined as the increase in the particle radius due to the uptake of water, mathematically expressed as

$$GF = (\rho / \rho_w \times w_{H_2O} / PM + 1)^{1/3},$$

where HGF is the growth factor, ρ is the density of the dry aerosol mass ρ_w is the density of liquid water, w_{H_2O} is the aerosol water predicted by the model, and PM is the dry aerosol mass. The growth factors predicted by EQSAM4 and EQUISOLV II are in good agreement, with relative difference of 3% on average for all 200 conditions. The largest standard deviation at 60% RH is due to a different prediction of the transition state for solid dissociation in the sulfate poor regime. When ammonium is in excess, ammonium sulfate and ammonium nitrate are the dominant solid compounds predicted in both models. EQUISOLV II predicts the multi-stage dissociation of multi-component mixtures by rigorously solving the solid equilibrium reactions at various RH. For example, Figure 2.5 in Jacobson *et al.* (1996) shows that ammonium sulfate and ammonium nitrate dissolve when the RH increases to about 50% and that the liquid water content of the solution increases with an increasing rate of dissolution of nitric acid and ammonia from the gas phase as the RH passes the DRH of the mixed solution (MDRH). This indicates that the transition of mixed salts composed of ammonium sulfate and ammonium nitrate from the solid phase to the aqueous phase in EQUISOLV II occurs at a RH of around 50%, which is less than the DRH of ammonium nitrate (DRH = 61.5%)

and ammonium sulfate (DRH = 79.6%). This agrees with the findings in this study for the mixture of ammonium sulfate and ammonium nitrate, e.g., case 12. In EQUISOLV II, the solid ammonium nitrate starts to dissolve in the solution system at an RH of around 50% in case 12. In contrast, for the same initial condition, the transition in EQSAM4 occurs at an RH of around 60% in the simulation, when RH passes the DRH of NH_4NO_3. This slightly affects the aerosol water content, which is hence predicted to be higher by EQUISOLV II in the mutual DRH transition regime (RH 50-60%) compared to EQSAM4. As a result, the HGF differs most in the mutual DRH transition regimes (RH 50-70%). Although this discrepancy on the phase transition exists, the water uptake predicted by these two models is overall very close as shown in Figure 2.2.

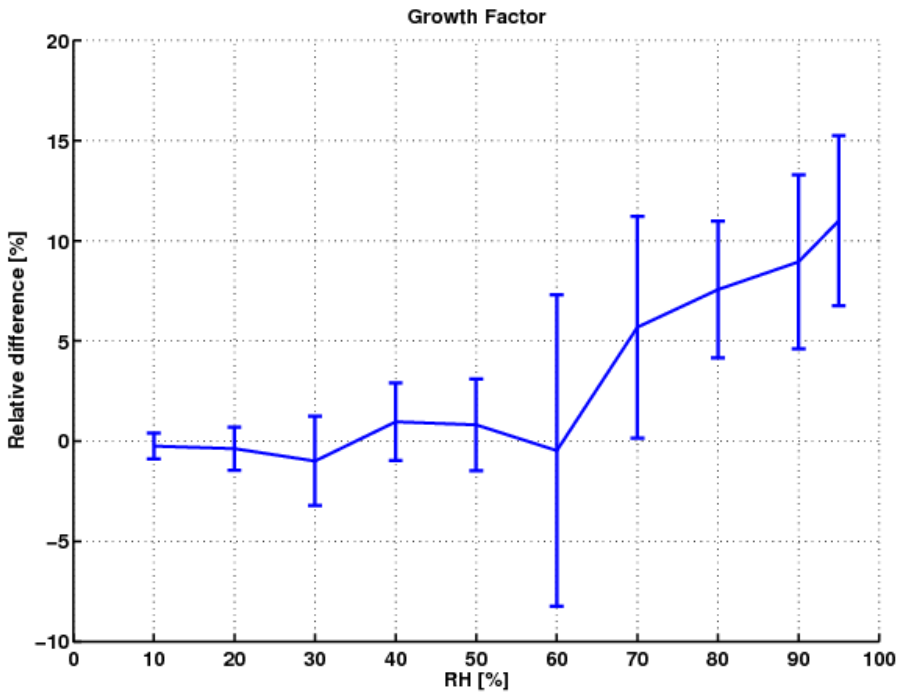

Figure 2.7: Relative difference in the growth factor between EQSAM4 and EQUISOLV II for all 200 conditions in Table 2.3 as a function of RH at a temperature 298.15 K. The error bars indicate the range of values for different cases.

2.4 Comparison with MINOS observations

The Mediterranean Intensive Oxidant Study (MINOS) was conducted in Crete, Greece, in the summer of 2001 from July 28th to August 21st and included a combination of ground-based measurements (i.e., gases, radiation, and meteorological parameters) observed at Finokalia in the north of Crete (35°N, 25°E) and two aircraft operated from Heraklion airport which performed measurements across the Mediterranean from the surface throughout the troposphere (Lelieveld *et al.*, 2002; Salisbury *et al.*, 2003). This region is characterized by high solar intensity, humid marine air and polluted air from Europe in the summer, so that one of the goals of MINOS was to investigate the role of chemistry and transport processes in the Mediterranean environment in contributing to the high level of air pollutants. The study also offered an opportunity to investigate the partitioning of volatile species (i.e., HNO_3, NH_3 and HCl) between the gas and the aerosol phase. In this section we focus on a comparison between EQSAM4 and EQUISOLV II using the MINOS observational data with respect to the gas and aerosol concentrations, which have been also used in Metzger et al. (2006) and Metzger and Lelieveld (2007).

Atmospheric HNO_3 and NH_3 were collected by a Cofer sampler with a flow rate 16 L min^{-1} and a sampling time 2-3 hours. The concentration of HNO_3(g) and NH_3(g) were determined by using ion chromatography with a detection limit for the mean sampling volume of 3 m^3 of 20 pmol mol^{-1} and a precision of about 15%. The bulk aerosol samples were collected by PTFE filters running simultaneously with the Cofer sampler. A total 226 aerosol samples were collected during the period of the campaign. The main anions and cations on the filters were analyzed by ion Chromatography, using a Dionex AS4A-

SC column with ASRS-I suppressor in auto-suppression mode of operation for the main anions (i.e., Cl^-, NO_3^-, SO_4^{2-}) while the main cations (i.e., NH_4^+, Na^+, K^+, Mg^{2+}, Ca^{2+}) were analyzed using a CS12-SC column with CSRS-I suppressor. The detection limits for both main anions and cations were around 5 ppb. More details can be found in Kouvarskis and Mihalopoulos (2002).

The measured concentrations of gases(g) and aerosols(p) used as input to the two thermodynamic models include total ammonium ($NH_{3(g)}$ and $NH_4^+{}_{(p)}$), total nitrate ($HNO_{3(g)}$ and $NO_3^-{}_{(p)}$), total sulfate ($H_2SO_{4(g)}$ and $SO_4^{2-}{}_{(p)}$), total chloride ($HCl_{(g)}$ and $Cl^-{}_{(p)}$), sodium ($Na^+{}_{(p)}$), potassium ($K^+{}_{(p)}$), calcium ($Ca^{2+}{}_{(p)}$), and magnesium ($Mg^{2+}{}_{(p)}$). The aerosol precursor gases and aerosol compounds were partitioned between the gas, liquid, or solid aerosol phase by assuming thermodynamic and chemical equilibrium.

The timescale for a particle to reach equilibrium depends on its size, which can range from seconds or minutes for small particles up to days for coarse particles at low relative humidity and low aerosol concentration conditions (Meng and Seinfeld, 1996). To avoid non-equilibrium effects, we only use the amount measured in the fine-mode particles ($D<1.2$ μm) and the gas phase, i.e. the total ammonium, total nitrate and total chloride, which were used as the input for both models. The measurement sampling time was 2-3 hours which is sufficiently long to achieve equilibrium for the fine mode aerosols.

Figs. 8a and c show the time series from July 29th to August 22nd of aerosol NH_4^+(p) and gaseous NH_3(g) partitioned by EQSAM4 and EQUISOLV II and the total ammonium tNH_4, aerosol NH_4^+(p) and gas NH_3(g) from observations, respectively; Figs. 8b and d show scatter plots between the model predicted NH_4^+(p) and the observed values for EQSAM4 and EQUISOLV II. The red line is a linear fit of the blue points. Figs. 8e, f, g,

and h show similar plots for aerosol NO_3^-(p). The regression line as well as the goodness of fit parameter (i.e., the square of correlation coefficient) between the model predictions and observations is included in Figure 2.8. Table 2.6 presents a summary of the comparison between the model predicted and observed concentrations of ammonium, nitrate and chloride in the gas and aerosol phase for EQSAM4 (referred to as EQ4) and EQUISOLV II (referred to as EQ2) as well as the model predicted concentrations of total particulate matter, solid particulate matter and aerosol associated water.

Generally, the predictions of EQSAM4 and EQUISOLV II are similar for particulate ammonium and gaseous ammonia. Both capture the hourly and diurnal variations of NH_4^+ seen in the observations, although with occasional excursions. Figure 2.8 shows that both EQSAM4 and EQUISOLV II underestimate particulate ammonium in general, since organic compounds that were measured are omitted here for modeling consistency, in contrast to the previous studies by Metzger *et al.* (2006). Still, as shown in Table 2.6, 57% and 68% of the predicted aerosol NH_4^+ concentrations are within a factor of 1.5 of the observations for EQSAM4 and EQUISOLV II, respectively, and up to 90% within a factor of 2. EQSAM4 underestimates aerosol NH_4^+ by 32% on average while EQUISOLV II predicts a somewhat smaller underestimation of about 25%. However, the comparison of EQSAM4 and EQUISOLV II with observations for aerosol NO_3^- is less favorable. In general, the prediction of particulate nitrate by EQSAM4 is closer to the observations than is EQUISOLV II for the same period of time as shown in the scatter plot. The mean aerosol NO_3^- in EQSAM4 is roughly by 0.01 μg m^{-3} higher than the observations, while EQUISOLV II predicts about 0.04 μg m^{-3} lower (the observed mean value is 0.09μg m^{-3}). Nevertheless, as further shown in Table 2.6, both models can

represent the concentration of gaseous nitric acid satisfactorily within a factor of 1.5 of the measurements for 98% of the time for both EQUISOLV II and EQSAM4. A similar conclusion holds for the partitioning of total chloride. Table 2.6 shows that 91% of the predictions of both EQUISOLV II and EQSAM4 are within a factor of 2 of the observations for gaseous hydrochloric acid. Notice that the observed concentrations of aerosol nitrate and chloride are very low (<0.1μg m^{-3}) compared to the amounts present in the gas phase. Thus, there is only a small impact of these compounds on the uptake of water. The prediction of the total particulate matter from the models is slightly lower than that of the observations mostly because the organic are excluded in this study. However, both models are able to reproduce the observed total particulate matter within a factor 2. The predictions on the total particulate matter by EQSAM4 are slightly better than that of EQUISOLV II, i.e., within a factor of 1.5 of observations for 69% and 61%, respectively. EQSAM4 predicts a lower fraction of solid particulate matter (41%) compared to that in EQUISOLV II (49%), which leads to higher aerosol associated water. Figure 2.9 shows the time series by EQSAM4 and EQUISOLV II for aerosol water (μg m^{-3}) during the MINOS campaign. The temperature and relative humidity during the campaign are also shown. The average difference in the prediction of liquid water content between EQSAM4 and EQUISOLV II is about 0.59 μg m^{-3} while the correlation coefficient of 0.99 indicates that the aerosol associated water content predicted by these two models is highly correlated, although some discrepancies of the prediction of the absolute water content occurs when the RH is moderately low, that is the RH is in the mutual DRH transition regime of mixed solutes, which is here around 30-60% because of the metal salts of Na^+, K^+, Ca^{2+} and Mg^{2+}.

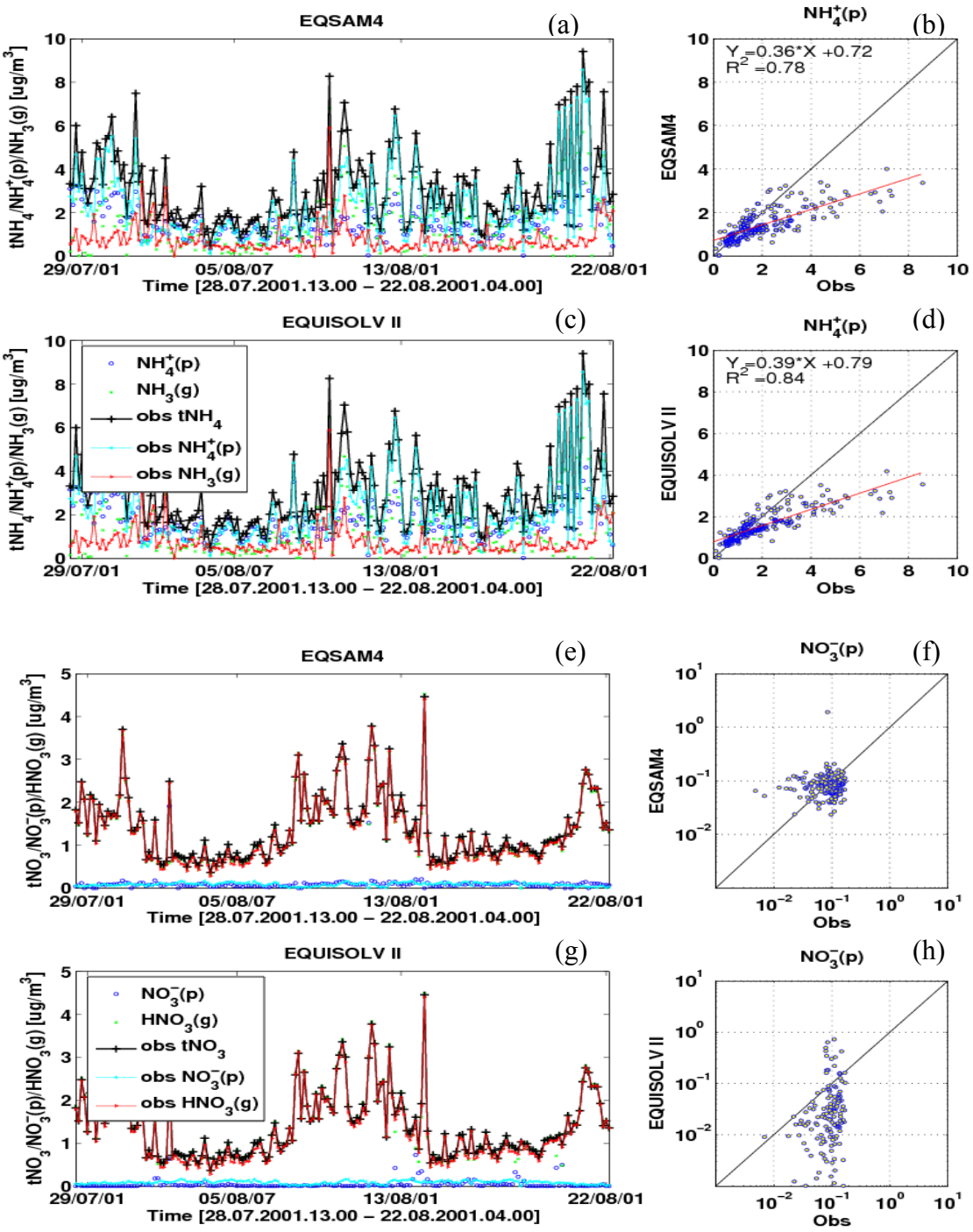

Figure 2.8: Time series by EQSAM4 and EQUISOLV II and observations for NH_4^+(p), NH_3(g), tNH_4, NO_3^-(p), HNO_3(g), tNO_3 during the MINOS campaign. The red lines in the panels at the right represent the linear fits to the data. The NO_3^-(p) within the range (10^{-3}-10^1 μg m^{-3}) in the panel (f) and (h) are plotted.

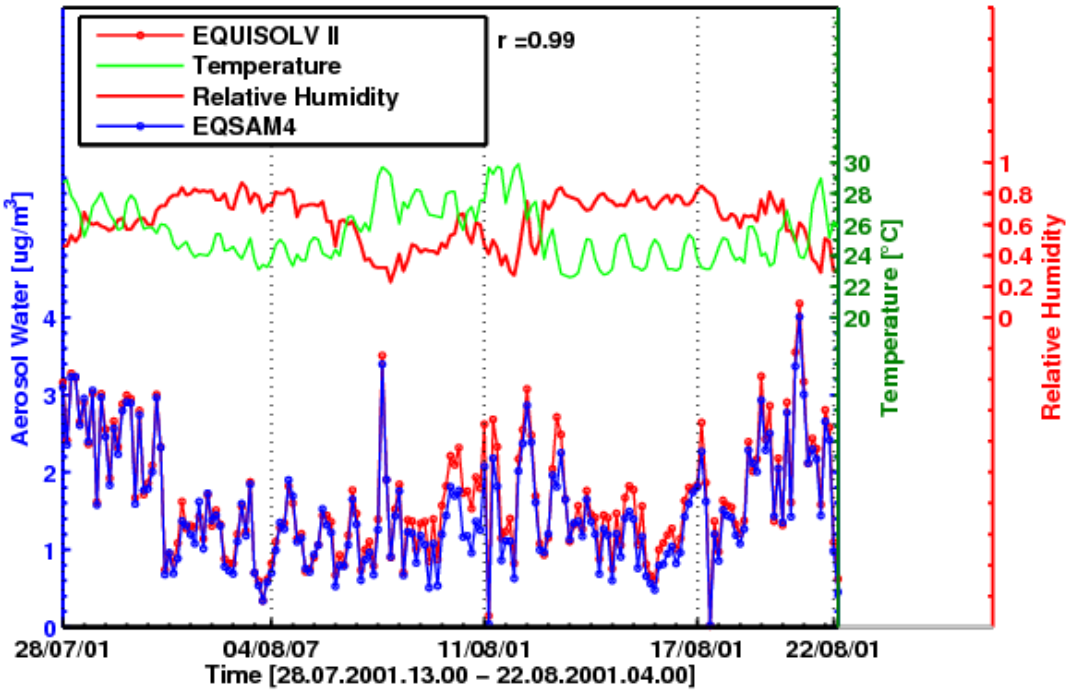

Figure 2.9: Time series by EQSAM4 and EQUISOLV II for aerosol water (μg m^{-3}) during the MINOS campaign. The temperature and relative humidity during the campaign are shown. The correlation coefficient (r) between EQSAM4 and EQUISOLV II on the prediction of aerosol water is shown at the top of figure.

Figure 2.10 shows the absolute difference between the predictions of the particulate nitrate concentrations from EQSAM4 and EQUISOLV II and the observations as the function of temperature, relative humidity, sulfate concentration, and the molar ratio of total ammonium to total sulfate. Both EQSAM4 and EQUISOLV II show large discrepancies with observations at low temperatures and high relative humidities. EQUISOLV II slightly underestimates particulate NO_3^- for almost all conditions but some overpredictions occur at lower temperatures, higher relative humidities, and sulfate poor regimes (molar ratio of $tNH_4/SO_4^{2-} > 2.0$). This agrees with findings discussed in Yu *et al.* (2005). Yu *et al.* (2005) found that ISORROPIA overpredicts particulate nitrate at the conditions of lower temperature, high RH and sulfate poor regimes in Atlanta while

underpredictions occur at high temperature, low RH and sulfate rich conditions (molar ratio of tNH_4/SO_4^{2-} <2.0). Moya *et al.* (2001) suggested that a dynamic instead of an equilibrium model may improve the agreement between the model predictions and observations for particulate nitrate under the conditions with high temperatures and low RH based on observations collected during the IMADA-AVER field study in Mexico City in 1997. Instead, EQSAM4 tends to slightly overestimate particulate nitrate, but overall the nitrate predictions are in better agreement with the observations, especially at low T or high RH.

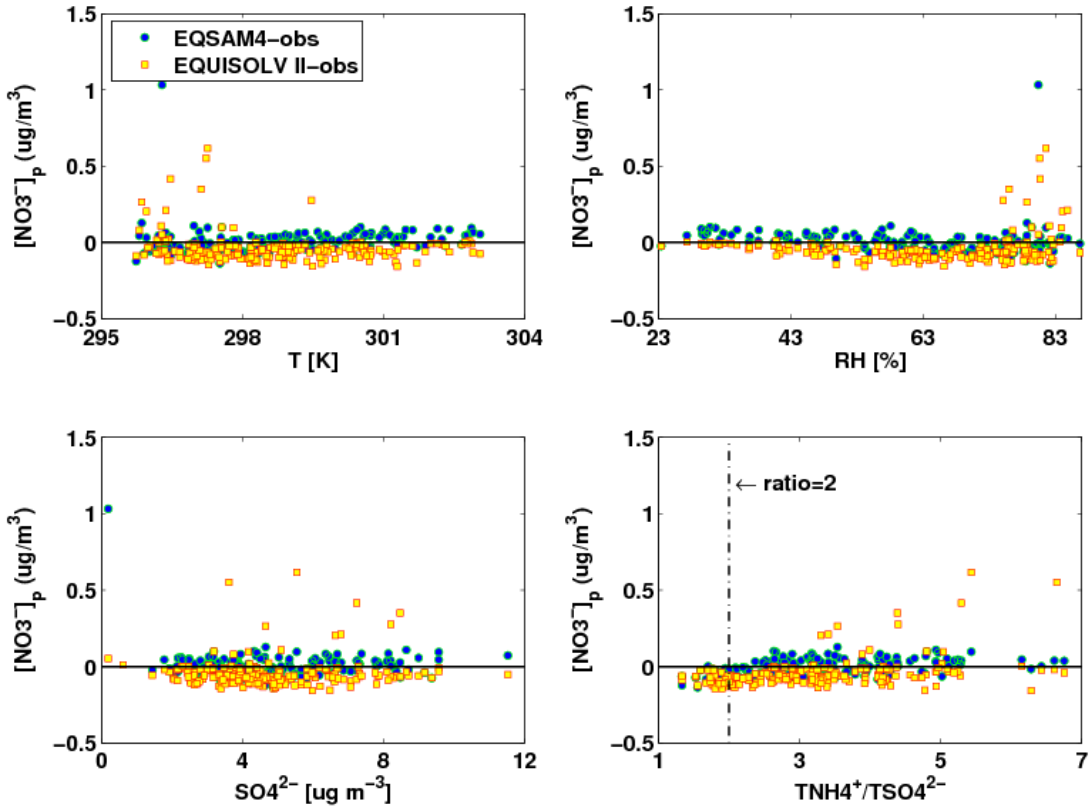

Figure 2.10: The difference between the modeled and observed concentrations of NO_3^- as a function of temperature, RH, SO_4^{2-} concentration, and the molar ratio of tNH_4 to SO_4^{2-} during the MINOS campaign.

Table 2.6: Comparison between modeled and observed concentrations of gas and particulate phase ammonium, nitrate and chloride by EQSAM4 (EQ4) and EQUISOLV II (EQ2) as well as the model predicted concentrations of total particulate matter, solid particulate matter and aerosol associated water.

Variable	Concentration[a] (μg m^{-3})			Bias[a] (μg m^{-3})		Percentage within a factor of 2 (%)[b]		Percentage within a factor of 1.5 (%)[b]	
	EQ4	EQ2	Obs.	EQ4	EQ2	EQ4	EQ2	EQ4	EQ2
NH_4^+(p)	1.51±0.75	1.65±0.75	2.20±1.62	-0.70±1.14	-0.56±1.07	81.42	89.62	56.28	67.76
NH_3(g)	1.43±1.25	1.30±1.19	0.77±0.69	0.66±1.08	0.53±1.01	48.63	55.19	33.33	36.61
NO_3^-(p)	0.10±0.19	0.04±0.10	0.09±0.04	0.01±0.20	-0.04±0.10	63.93	16.39	35.52	10.38
HNO_3(g)	1.31±0.75	1.38±0.78	1.33±0.78	-0.01±0.20	0.05±0.10	98.36	100.00	98.36	98.36
Cl^-(p)	0.02±0.02	0.10±0.12	0.06±0.07	-0.04±0.07	0.04±0.12	25.14	32.79	13.66	21.31
HCl(g)	2.46±1.45	2.46±1.45	2.42±1.47	0.04±0.08	0.03±0.12	91.26	91.26	91.26	91.26
PM	6.99±2.68	6.66±2.75	9.62±3.57	-2.63±1.74	-2.96±1.71	93.99	91.26	69.40	61.75
PM(s)	2.96±3.86	3.23±4.22	-	-	-	-	-	-	-
H_2O(aq)	4.66±3.90	4.07±4.01	-	-	-	-	-	-	-

[a]The values of the concentration and bias are given as the mean ± standard deviation and the bias is defined as the absolute difference between the model predictions and the observations. The observational data are from the MINOS campaign (Metzger *et al.* 2006).

[b]The percentages of the model predicted points that are within a factor of 1.5 or 2.0 of the observations. The total number of samples during the MINOS campaign was 183.

Figure 2.11 is similar to Figure 2.10 but shows particulate ammonium. The prediction of ammonium from these two models is rather similar. The prediction of particulate ammonium is not as sensitive to temperature and relative humidity as the prediction of particulate nitrate in both EQSAM4 and EQUISOLV II. Both models show small biases with respect to observations when the molar ratio of tNH_4 to tSO_4 is less than 2 (in the sulfate rich regime) but have a larger discrepancy with the observations at larger molar ratios of tNH_4 to tSO_4 or higher concentration of SO_4^{2-}.

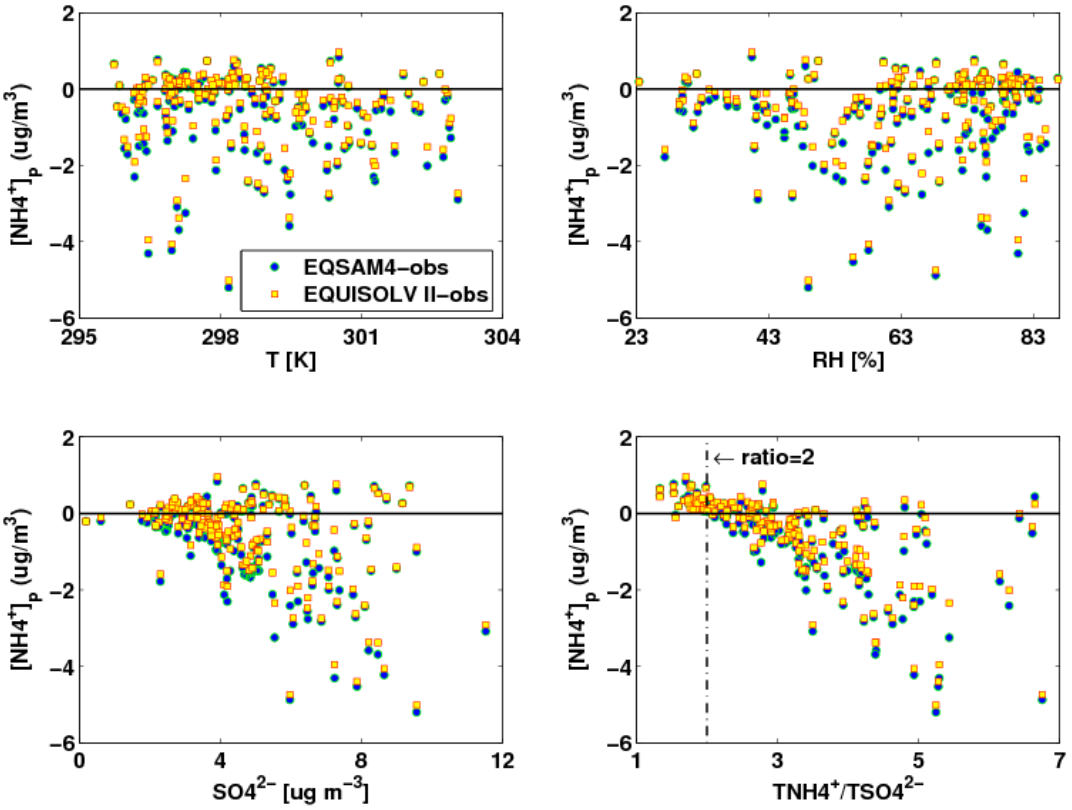

Figure 2.11: The difference between the modeled and observed concentrations of NH_4^+ as a function of temperature, RH, SO_4^{2-} concentration, and the molar ratio of tNH_4 to SO_4^{2-} during the MINOS campaign.

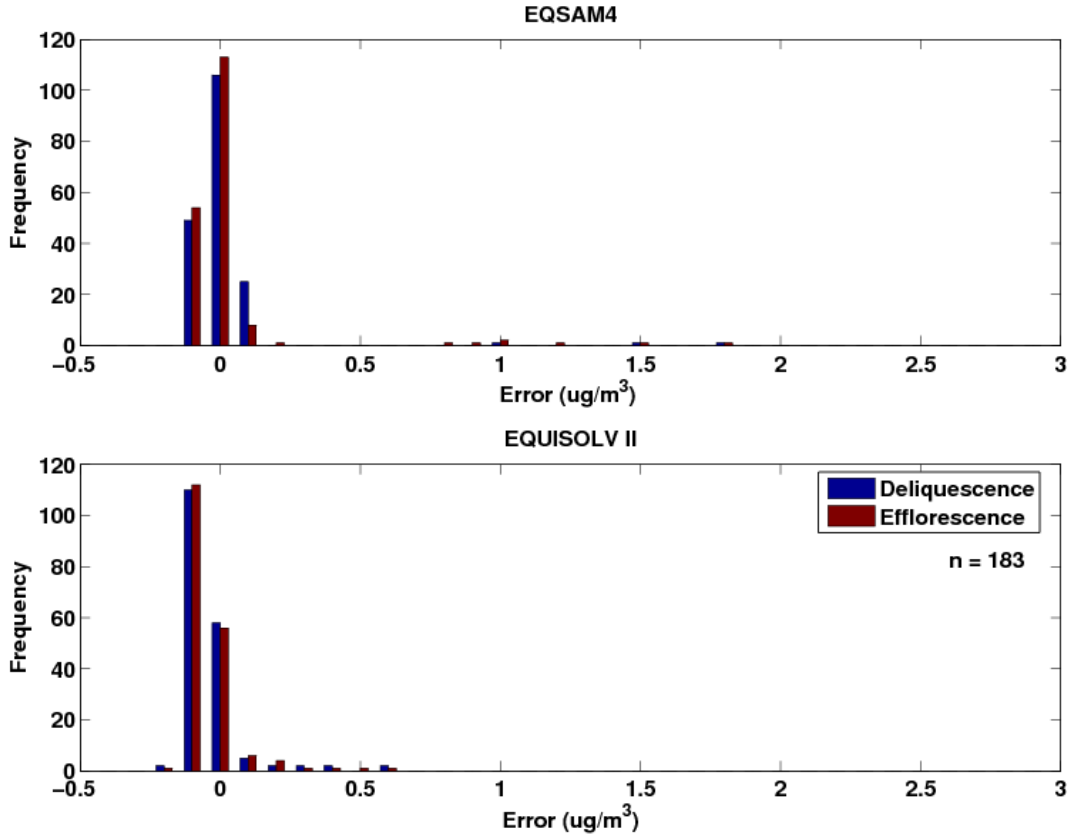

Figure 2.12: Error distributions of aerosol nitrate assuming different equilibrium states (deliquescence vs. efflorescence) of the particles during the MINOS campaign. Errors are calculated as the predicted minus the observed values of aerosol nitrate. The number of samples was 183.

Ansari and Pandis (2000) found that efflorescence branch (metastable regime) concentrations of aerosol nitrate are 11% larger than those of the deliquescence branch at low aerosol nitrate concentrations (< 8 μg m^{-3}). Here we additionally investigate the biases of the models in the metastable regimes. Figure 2.12 shows a histogram of the model bias in the prediction of aerosol nitrate assuming both the deliquescence and efflorescence branch. The absolute difference between EQSAM4 and the observations are shown for efflorescence branch to be similar to that of the deliquescence branch for the prediction of aerosol nitrate. The average model bias shifts from 0.01 μg m^{-3} for

deliquescence to 0.03 μg m^{-3} for efflorescence. In the EQUISOLV II, the model mean bias shifts from -0.04 μg m^{-3} for deliquescence to -0.05 μg m^{-3} for efflorescence. This indicates that the model mean bias is not significantly changed in EQUISOLV II and EQSAM4 during the MINOS campaign when a metastable regime is considered.

2.5 Discussion and conclusions

In this chapter, we conducted a comprehensive evaluation of two gas-aerosol equilibrium partitioning models EQSAM4 and EQUISOLV II under various RH and composition domains. EQSAM4 and EQUISOLV II predict a similar amount of aerosol water for most conditions, with a statistically significant linear regression slope of about 1.06. The agreement is slightly better in the sulfate poor regime where the relative difference on average is 2%, while the relative difference on average of the two models in the sulfate rich and neutral regimes is about 5-10%. Also the phase transition predicted by these two models is generally comparable for most conditions (Figure 2.2). Discrepancies occur under certain conditions, which can be explained by the different prediction of bi-salts (NH_4HSO_4, $NaHSO_4$, $KHSO_4$) and the different prediction of the phase transition in cases of mixed salt solutions, in particular mixtures of ammonium sulfate and ammonium nitrate.

In general, the PM concentration predicted by these two models is similar except under conditions with high ammonium and high nitrate. EQSAM4 predicts slightly lower total particulate matter (PM) by 1% compared to EQUISOLV II for all 200 simulation conditions with a statistically significant linear regression slope of 1.01 and 95% CI of 0.02. At a temperature of 298.15 K and a RH of 30%, the normalized absolute difference in the concentration of total PM predicted by the two models is about 1%. The largest

discrepancies occur in the sulfate poor regime where the two models differ by 1% on average with the largest difference as high as 8% in some specific cases. This leads to the associated differences in the predicted aerosol water. Also, the particulate nitrate concentration predicted by the two models agrees satisfactorily, except for the conditions around the DRH (60%). At higher RH, EQSAM4 predicts similar or for a few cases a somewhat more nitrate, because the EQSAM4 parameterizations results in a slightly larger activity coefficient for NH_4NO_3. At a RH regime between 50-60%, the relatively largest discrepancies occur due to differences in the prediction of the mixed phase transitions, which affects the associated water concentration. Similar to particulate nitrate, both models agree under most conditions for particulate ammonium, especially in the sulfate rich and neutral regimes. For most cases, the EQSAM4 predictions are comparable with the EQUISOLV II within a factor of 2. For particulate chloride, the largest difference in the prediction occurs in the sulfate rich and neutral regimes. The overall largest discrepancies between the predictions of both models are found for the pH, with noticeable large differences for the sulfate neutral regime. The reason is explained in Section 2.3.6 and has to do with an inconsistent treatment of the input concentration in case of metal cations, which can cause a high alkalinity due to an excess of H^+; which is released from the acids. But this effect can be "suppressed" if it is assumed that metal cations are "neutralized", e.g. they are prescribed in the input concentration as e.g. NaOH rather than Na^+ (KOH instead of K^+, etc.).

By comparing the dominant solid PM compounds predicted by the two models at an RH of 30%, we noticed that the degree to which the ammonium ion neutralizes the bisulfate ion to form ammonium bisulfate in EQUISOLV II in the sulfate rich regime is

mainly responsible for the difference between the two models in the sulfate rich and neutral regimes. The difference in the activity coefficients as well as the derived molality of major salts in EQSAM4 contributes slightly to the difference in the gas-liquid-solid partitioning in the sulfate poor regime. Notwithstanding, with all differences mentioned so far the relative difference of the mass growth factor between EQSAM4 and EQUISOLV II at various RH and at a temperature of 298.15 K is only about 3% on average over all cases. A slightly larger difference of around 8% occurs at a RH 80-90% because of differences in the water uptake and the total dry PM, while the largest standard deviation of the relative difference of these two models occurs around an RH of 60%, due to differences in the phase partitioning of mixed solutions involving the two (semi-)volatile compounds NH_4NO_3 and NH_4Cl.

A comparison was also conducted using observed atmospheric conditions. The nitrate and ammonium concentrations during the MINOS campaign were simulated for the summer of 2001 from July 28th to August 21st in Crete, Greece, a location characterized by high solar intensity and polluted air from Europe. Overall, both EQSAM4 and EQUSOLV II underestimate particulate ammonium compared to the observations by 32% and 25% on average as expected, since organic compounds that were measured are omitted here for modeling consistency, in contrast to the previous studies conducted by Metzger *et al.* (2006). The predictions of particulate nitrate by both models deviate significantly from the observations only for the dry period (see Metzger *et al.* 2006 for the characteristics of the three major MINOS periods), while EQSAM4 is able to capture the fine mode particulate nitrate for the two humid periods whereas EQUISOLV II fails to predict any particulate nitrate. This is related to the fact that the concentration of total

nitrate is very low and most of total nitrate was observed in the gas phase. Overall, both EQSAM4 and EQUISOLV II are able to reproduce the gaseous nitric acid to within a factor of 1.5 in 98% of the observations. However, because of the very low nitrate concentrations, the impact of these differences on the prediction of total particulate matter as well as aerosol water is minor. Both models are also able to reproduce the observed particulate matter to within a factor of 2 in more than 90% of the observations, and the predicted water associated with the aerosol in the two models is strongly correlated with a correlation coefficient 0.99.

Finally, a sensitivity test was carried out in order to evaluate the impacts of temperature, RH, sulfate concentration and ammonium-to-sulfate ratio on the prediction of nitrate. We found that EQUISOLV II over-predict particulate nitrate at lower temperatures and higher RH more than EQSAM4 does. This over-predict by EQUISOLV II mainly occurs in the sulfate poor regime, and our findings are consistent with the findings noted of Moya *et al.* (2001) and Yu *et al.* (2005).

Overall, our results show that the results of EQSAM4 and EQUISOLV II are comparable under most conditions. The investigation of using the efflorescence branch vs. the deliquescence branch showed that the mean bias in both EQSAM4 and EQUISOLV II is not significantly changed regardless of which branch of the hysteresis loop is chosen. The few discrepancies found can be mainly attributed to EQSAM4 model deficiencies with respect to the parameterization of mixed solutions for certain conditions. EQSAM4 will be further developed in this respect. Probably more important for global modeling needs is the underlying assumption of both models that equilibrium is achieved between gas and aerosol phase. At least for coarse aerosol modes (not

considered in this work) the equilibrium assumption will be a limiting factor for global scale applications, since non-equilibrium situations between the gas and aerosol phase might then become pre-dominant for particulate matter or growth factor predictions.

Overall, our comparisons show that the predicted results of EQSAM4 and EQUISOLV II are comparable under most conditions. However, debates on the validation of concepts of the EQSAM4 arise when we submitted the manuscript based on this part of work (Xu et al., 2009) to the Atmospheric Chemistry and Physics Discussion (ACPD). Two accompanying papers (Metzger et al., 2011a, b) were then submitted to clarify EQSAM4 as a parameterization module. In light of that, the EQUISOLV II is used for the rest of the dissertation.

CHAPTER III

BOX MODEL SIMULATIONS OF NITRATE AND AMMONIUM AEROSOLS

3.1 Introduction

In the last Chapter, we reported on a comparison of the prediction of the partitioning of semi-volatile species between their gas and aerosol phase along with water uptake from two inorganic modules in the fine mode with particle diameter less than 1.25 μm under the assumption of thermodynamic equilibrium. This study improves our understanding of the discrepancy between aerosol chemical composition as well as associated hygroscopic growth from different equilibrium modules. In the real atmosphere, the time to establish thermodynamic equilibrium between gas and aerosol phase varies substantially depending on particle sizes and ambient meteorological conditions (Seinfeld and Pandis, 1998). The instantaneous thermodynamic equilibrium assumption may be applicable in the fine aerosol mode with aerosol particle diameter less than 1 μm since small particles achieve equilibrium with the gas phase within a few minutes under typical atmospheric conditions (Wexler and Seinfeld, 1990; Dassios and

Pandis, 1999). In contrast, the time to establish equilibrium between semi-volatile gases and large aerosols particles is generally longer, especially under cold temperatures and low species concentrations, with a timescale of the order of several hours or even several days (Meng and Seinfeld, 1996; Seinfeld and Pandis, 1998). In other words, these coarse particles are not generally in equilibrium with their gas phase. The non-equilibrium phenomenon between gases and aerosols has been observed for coarse particles during the Southern California Air Quality Study (SCAQS) (John et al., 1989). Hence, an appropriate representation of the partitioning of semi-volatile species (e.g., HNO_3, HCl and NH_3) between their gas phase and particle phase for both fine and coarse aerosol mode is essential to accurately predict aerosol chemical compositions that have significant impacts on the uptake of water as mentioned in the last chapter and further aerosol wet size distribution, wet refractive index and optical properties, which determine their climate effects on the earth climate system.

In recent years, although a few global models (Adams et al., 1999; Jacobson, 2001; Metzger et al., 2002a, 2002b, 2007; Bauer et al;, 2007; Pye et al., 2009) have included aerosol thermodynamics in order to study the formation of semi-volatile inorganic aerosols, these studies assumed that a thermodynamic equilibrium (EQ) between the gas and aerosol phase was valid for both small and large aerosol particles, which is not physically accurate as discussed earlier. At this time, there are five global model studies (Liao et al., 2003; Liao et al., 2004; Rodriguez and Dabdub, 2004; Bauer et al., 2004; Myhre et al., 2006; Feng and Penner, 2007; Pringle et al., 2010) that considered aerosol thermodynamics for both fine-mode and coarse-mode with different degrees of complexity or simplification to account for the mass transport limitation to achieve

equilibrium between the gas and aerosol phase. For instance, Liao et al. (2003; 2004) assumed instantaneous equilibrium on non-dust particles, and applied the first-order loss rates, which are based on measurements in the laboratory, for the transport of gases to dust aerosols (hereafter referred as HYB); Rodriguez and Dabdub (2004) first calculated the gas and bulk-phase aerosol concentrations at thermodynamic equilibrium, and then distributed the total aerosol concentrations to different size ranges according to a weighting function; Bauer et al. (2004) considered the interaction between nitrate and dust aerosols using a first-order removal approximation based on update coefficients (hereafter referred as UPTAKE); Myhre et al. (2006) simply chose to separate sulfate aerosols into the "fine mode" and sea salt aerosols into the "coarse mode" and then let the smallest mode drive the gas phase to equilibrium with the sulfate aerosols before the coarse mode aerosols (i.e., sea salt) are allowed to "see" the new gas; Feng and Penner (2007) were the first to consider explicit kinetics for the formation of nitrate and ammonium in the coarse mode by incorporating a hybrid dynamic method (HDYN) (Capaldo et al., 2000) into the global chemistry transport model; Pringle et al. (2010) implemented a simple kinetic-limited equilibrium (KEQ) method that first calculates the amount of gases kinetically able to condense onto aerosols assuming the diffusion limited condensation following Vignati et al. (2004) and then a thermodynamic model is used to re-distribute the mass between gas and aerosol phase. Feng and Penner (2007) conducted sensitivity tests among four different treatments (i.e., EQ, UPTAKE, HYB and HDYN) of nitrate and ammonium in the global model. They founded: i) the method with a pure thermodynamic equilibrium assumption (i.e., EQ) underestimates the fine-mode nitrate aerosol burden by 25% and excessive nitrate are formed on the coarse mode; ii) both

HYB and UPTAKE predict higher nitrate aerosol burden than HDYN by 106% and 47%, respectively; iii) Both fine and coarse mode nitrate aerosols are overestimated by the UPTAKE method while the HYB method mainly predicts higher nitrate on the coarse aerosols. Their findings suggest that using the hybrid dynamic method to study the formation of semi-volatile inorganic aerosols in the global model is more accurate.

In the previous study (Feng and Penner, 2007), they assumed nitrate and ammonium was internally well mixed with other inorganic aerosols (e.g., sulfate, dust and sea salt) that were present in the same size bin, since the global chemistry model (i.e., IMPACT, Liu and Penner, 2002; Feng et al., 2004) used in their studies only predicts sulfate mass without considering sulfur dynamics as well as the interaction between sulfate and other aerosol components (e.g., organic matter, black carbon, dust and sea salt). The assumption of an internally mixed state among multi-component aerosols subject to various processes might be valid in regions far from their sources. However, it may distort the predicted chemical composition (Kleeman et al., 1997) as well as further impact on aerosol water content since aerosol particles near their sources are generally founded externally mixed. Due to the lack of information on the aerosol mixing state in each size bin given by the global aerosol model, the assumption that the particles in the same size bin have a uniform composition is made. Liu et al. (2005) implemented sulfur dynamics (Herzog et al., 2004) into the IMPACT model in which two modes (nuclei and accumulation mode) and two moments (aerosol number and mass concentration) of pure sulfate are predicted. In this study, they found that the inclusion of sulfur dynamics (e.g., nucleation, condensation, coagulation, cloud process, etc) improves the representation of sulfate number as well as size distribution when compared with observations. Their

results suggest that the interaction between semi-volatile species with other aerosol components needs to be taken into account if using this version of the global aerosol model as the framework to study nitrate and ammonium because the formation of nitrate and ammonium aerosols strongly depends upon the availability of pre-existing aerosols. In other words, assuming all pre-existing aerosols are completely internally mixed (hereafter denoted as IM) to calculate the formation of nitrate and ammonium is no longer appropriate under this circumstance. Following the implementation of sulfur dynamics described in Liu et al. (2005), a treatment which assumes that five pre-existing aerosol types (i.e., pure sulfate, fossil fuel and biomass burning aerosols, dust and sea salt) are externally mixed and aerosol composition is internally mixed within each aerosol type (hereafter denoted as EM) would be more consistent with the treatment of other processes in the global model.

This chapter examines the differences in the prediction of nitrate and ammonium using two treatments of aerosol mixing state for multi aerosol components (IM vs EM) as well as two methods (HDYN vs KEQ) that account for mass transfer between gas and aerosol phase. In the first section, the hybrid dynamic (HDYN) method (Feng and Penner, 2007) was applied in both fine and coarse aerosol particles. Two mixing states were examined: IM versus EM. The objective of this work is to gain some insight into the future implementation of external mixing treatment (or partially internally mixing state) with aerosol thermodynamic module in a global aerosol model. In the second section, the simple kinetic-limited equilibrium (KEQ) method proposed by Pringle et al. (2010) was compared to the hybrid dynamic method. The objective of this comparison is to understand discrepancies and similarities between these two methods. A description of

aerosol thermodynamic module and diffusion-limited mass transfer, the concepts of the hybrid dynamic method and the simply kinetic-limited equilibrium method as well as the introduction of the aerosol mixing state along with schematic illustrations of the implementation of the hybrid dynamic method accounting for both externally and internally mixture is detailed in Section 3.2. Section 3.3 discusses the results in this work followed by the discussion and conclusions in Section 3.4.

3.2 Methods

3.2.1 Aerosol thermodynamic module

In this Chapter, the thermodynamic equilibrium module EQUISOLV II was used, which partitions the total amount of nitric acid/nitrate (i.e., HNO_3+NO_3^-) and ammonia/ammonium (i.e., NH_3+NH_4^+) between the gas and aerosol. As described in the last chapter, EQUISOLV II provides the ability to compute size-resolved equilibrium composition of an internally mixed aerosol particle composed of sulfate, nitrate, chloride, carbonate, ammonium, sodium, potassium, magnesium, calcium and water. In such cases, diffusion-limited mass transfer between gas and particle phase is ignored. In addition, it can be used to solve internal aerosol equilibrium to provide saturation vapor pressure terms for diffusion-limited mass transfer equations between the gas and multiple size bins of aerosol phases (Jacobson, 1999). In EQUISOLV II, the aerosol phase is divided into discrete population bins, assuming the same composition of aerosol particles in each bin. The driving forces for condensation of semi-volatile species in each discrete size section are considered depending on chemical compositions of well-mixed aerosols at each size bin. The model used in this chapter treats aerosol particles in 4 size bins (0.05-0.63 μm,

0.63-1.26 μm, 1.26-2.5 μm and 2.5-10 μm). 10 sub bins are used for the 1st and 4th bin with particle radii ranging from 0.05 to 0.63 μm and from 2.5 to 10 μm, respectively, while 4 sub bins are used for the 2nd and 3rd size bin with radii ranging from 0.63 to 2.5 μm. This resolution of aerosol size representation allows sufficient accuracy for the partitioning of HNO_3 and NH_3 between gas and aerosol phase (Feng, 2005).

The uptake of water by an aerosol solution was treated following its deliquescence growth at a specific relative humidity. As discussed in the last chapter, in general, atmospheric aerosols take up water when solids deliquescence in case the relative humidity increases above the deliquescence relative humidity (DRH) of individual solid compounds (i.e., following the lower branch of the hysteresis loop), while aerosol water evaporates until crystallization occurs at the crystallization relative humidity (CRH) when the ambient relative humidity decreases (i.e., following the upper branch of the hysteresis loop). For example, the hysteresis phenomenon with different deliquescence and crystallization points is illustrated in Figure 3.1 for $(NH_4)_2SO_4$. Therefore, the water uptake of an aerosol particle following either the deliquescence or efflorescence particle growth is determined not only by the ambient relative humidity but also the history of the ambient relative humidity. Without sufficient knowledge of the latter, we assumed the particle does not grow until its DRH was reached in our study. Note that Ansari and Pandis (2000) found that the aerosol concentrations following the crystallization branch are 11% larger than those of the deliquescence branch at low aerosol nitrate concentrations (< 8 μg m^{-3}). The total aerosol direct forcing by assuming particle growth following the efflorescence branch is expected to exert more negative forcing due to higher aerosol water content.

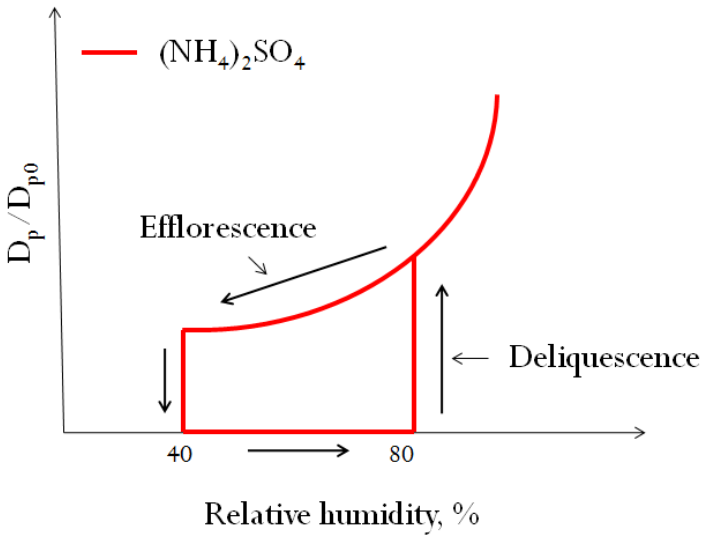

Figure 3.1: Diagram of size growth factor of $(NH_4)_2SO_4$ particles as a function of relative humidity. D_{p0} is the diameter of the particle at 0% RH.

3.2.2 Diffusion-limited mass transfer

As discussed earlier, the gas-to-particle diffusion may not be instantaneous for large aerosol particles, the rate of mass transfer between gas and aerosol phase need to be taken into account, dependent on the particle size relative to the mean free path of gas molecules in the air. Three regimes for modeling particle transport process are typically defined according to the key dimensionless parameter, Knudsen number (i.e., $Kn = \frac{\lambda}{R}$, where λ and R are the mean free path of the gas molecule in air and particle radius, respectively): 1) Continuum regime as $Kn << 1$, where the particle size is relatively large and equations associated with continuum mechanics can be applied; 2) Kinetic regime as $Kn >> 1$, where the particle exists in more or less rarefied medium since the particle size is rather small and its transport properties can be obtained from the kinetic theory of gases; 3) Transition regime as $Kn \approx 1$ (i.e., $\lambda \approx R$), lying in the intermediate state

between former two regimes and thus the single solution based on either the continuum transport equation (i.e., Maxwell's equation) or the kinetic theory of gases are no longer valid. The particle transport properties result from the combination of the two former regimes. In general, the concentration distributions of the diffusing species in the transition regime are rigorously governed by the Boltzmann equation,

$$\frac{d^2C}{dr^2} + \frac{2dC}{rdr} = 0, \tag{3.1}$$

where C is the concentration of diffusing species at any radial position r and time t. Unfortunately, a general solution to the Boltzmann equation valid over an entire range of Knudsen numbers for arbitrary masses of the diffusing species does not exist. Consequently, in order to avoid solving the Boltzmann equation directly, an approach based on so-called flux matching is typically used, which assumes that the simple kinetic theory of gases can be applied to the regime $R \le r \le \lambda + R$, and that the continuum theory applies for the region $r \ge \lambda + R$, where r is any radial position. Following the approach of Fucks and Sutugin (1971), the solution of the Boltzmann equation is given by

$$J_{i,j} = k_{i,j}\left[C_{g,i} - C^{eq}_{g,i,j}\eta_j\right], \tag{3.2}$$

where $C_{g,i}$ (mole m^{-3}) is the ambient concentration of gas specie i; $C^{eq}_{g,i,j}$ (mole m^{-3}) is the equilibrium gas-phase concentration of species i with the particle-phase in bin j; η_j is the Kelvin effect correction of size bin j; $J_{i,j}$ (mole m^{-3} s^{-1}) represents the total flow of the species i diffusing into the particles in size bin j at unit time; $k_{i,j}$ (s^{-1}) is the first order mass transfer coefficient for species i in bin j, which is estimated as

$$k_{i,j} = 4\pi D_{g,i} R_j N_j f(Kn_{i,j}, \alpha_i), \tag{3.3}$$

where $D_{g,i}$ ($cm^2\ s^{-1}$) is the gas diffusivity of the specie *i*; R_j is the radius of the particles in the size bin *j*, N_j (cm^{-3}) is the number concentration of particles at bin *j*; $f(Kn_{i,j},\alpha_i)$ is the correction factor in the transition regime (Fuchs and Sutugin, 1971) to non-continuum effects and imperfect accommodation as a function of the Knudsen number $Kn_{i,j} = \lambda_i / R_j$ (where λ_i is the mean free path of gas species *i*) of gas species *i* in bin *j*:

$$f(Kn_{i,j},\alpha_i) = \frac{0.75\alpha_i(1+Kn_{i,j})}{Kn_{i,j}^2 + Kn_{i,j} + 0.283Kn_{i,j}\alpha_i + 0.75\alpha_i}. \quad (3.4)$$

Note that the above correction factor also accounts for the interfacial mass transport limitation characterized by the mass accommodation coefficient α_i of species *i*, which represents the sticking probability of a vapor molecule encounters the surface of a particle. We used 0.193, 0.092, and 0.1 for the mass accommodation coefficients of HNO_3, NH_3 and N_2O_5 on aerosols in this study same as Feng and Penner (2007). If we denote J_c and J_k as the total flow toward the particle in the continuum and kinetic regime, respectively, the ratio of $J_{i,j}$ relative to J_c and J_k is given by

$$\frac{J_{i,j}}{J_c} = \frac{0.75\alpha_i(1+Kn_{i,j})}{Kn_{i,j}^2 + Kn_{i,j} + 0.283Kn_{i,j}\alpha_i + 0.75\alpha_i}, \quad (3.5)$$

$$\frac{J_{i,j}}{J_k} = \frac{Kn_{i,j}(1+Kn_{i,j})}{Kn_{i,j}^2 + Kn_{i,j} + 0.283Kn_{i,j}\alpha_i + 0.75\alpha_i}. \quad (3.6)$$

Note here that for $Kn \to 0$, $J_{i,j}/J_c \to 1$, the solution of diffusion-limited transfer is close to that in the continuum theory; on the other hand, for $Kn \to \infty$, $J_{i,j}/J_k \to 1$, as expected, the flow diffusing into particles is close to that in the kinetic regime .

The mean free path λ_i of gas species *i* in air is defined as the average distance traveled by the gas molecule *i* before it encounters another molecule *i* or air molecule. Following

the approach of Fuchs and Sutugin (1971), the mean free path λ_i can be related to the gas diffusivity,

$$\lambda_i = \frac{3D_{g,i}}{\bar{c}_i}, \tag{3.7}$$

where $D_{g,i}$ is the diffusivity of gas species *i* in the air and $\bar{c}_i$ is the mean speed of gas molecules *i*. The diffusivity can be either measured directly or calculated theoretically from the Chapman-Enskog theory for binary diffusivity (Reid et al., 1977, p554). The diffusivity of gas species *i* in the air is dependent on the temperature, pressure, molecule properties of gas species *i* and air. The mean speed of gas molecules is given (Moore, 1962, p238) by,

$$\bar{c}_i = \left(\frac{8RT}{\pi M_i}\right)^{1/2}, \tag{3.8}$$

where M_i is the molecular weight of gas species *i*, R is the universe constant (8.314 J mol^{-1} K^{-1}), and T is the temperature. Table 3.1 gives molecular velocities, diffusivity and mean free path of HNO_3, NH_3 and N_2O_5 at the temperature 298 K and the pressure 1000 hPa. Note that these three gas species are major species considered in the diffusion-limited mass transfer in this study. The mean free path of HNO_3, NH_3 and N_2O_5 approximates 0.14 μm, 0.12 μm and 0.15 μm, which is comparable to the size of majority aerosol particles. Since the mean free path of gas species is dependent on the temperature and pressure, it varies with height above the Earth's surface due to corresponding temperature and pressures changes. For example, in the upper troposphere where the temperature is 258 K and the pressure is 300 hPa, the calculated mean free path of HNO_3, NH_3 and N_2O_5 increases due to low temperature and pressure, equaling to 0.40 μm, 0.33 μm and 0.42 μm, respectively, which is still within the order of the size range of most

aerosol particles. Hence, the choice of particle transport equation in the transit regime is appropriate for most aerosol particles suspending in the standard atmosphere.

Table 3.1: Molecular velocities, diffusivity and mean free path of HNO_3, NH_3 and N_2O_5 at the surface (temperature: 298K; pressure: 1000 hPa) and at the upper troposphere (temperature: 258 K; pressure: 300 hPa).

Gas	M (g mol^{-1})	$\bar{c}$ (m s^{-1})[a]	D_g (cm^2 s^{-1})[a]	λ (μm) [a]
HNO_3	63	316(294)	0.15(0.40)	0.14(0.40)
NH_3	17	609(566)	0.24(0.63)	0.12(0.33)
N_2O_5	108	242(225)	0.12(0.31)	0.15(0.42)

[a]The values in the parenthesis are for the upper troposphere (temperature: 258 K; pressure: 300 hPa).

3.2.3 Hybrid dynamic method

To emulate the mass transfer process between gas and aerosol phase, a fully dynamic mass transfer consideration applied to each aerosol size bin is most accurate named as dynamic method (Meng and Seinfeld, 1996; Meng et al., 1998; Jacobson et al., 1996; Jacobson, 1997a, b; Sun and Wexler, 1998a, b; Pilinis et al., 2000). This approach is mathematically represented by a set of nonlinear ordinary differential equations (ODE):

$$\frac{dC_{g,i}}{dt} = -\sum_{j=1}^{N_B} k_{i,j}\left(C_{g,i} - C_{g,i,j}^{eq}\eta_j\right), \tag{3.9}$$

$$\frac{dC_{a,i,j}}{dt} = k_{i,j}\left(C_{g,i} - C_{g,i,j}^{eq}\eta_i\right), \tag{3.10}$$

$$k_{i,j} = 4\pi D_{g,i} R_j N_j f(Kn_{i,j}, \alpha_i), \tag{3.11}$$

$$f(Kn_{i,j}, \alpha_i) = \frac{0.75\alpha_i(1+Kn_{i,j})}{Kn_{i,j}^2 + Kn_{i,j} + 0.283Kn_{i,j}\alpha_i + 0.75\alpha_i}, \tag{3.12}$$

where $C_{g,i}$ is the ambient concentration (mole m^{-3} of air) of gas specie i; $C_{g,i,j}^{eq}$ is the equilibrium gas-phase concentration (mole m^{-3} of air) of species i with the particle-phase

in bin *j*; η_j is the Kelvin effect correction in size bin *j*; $C_{a,i,j}$ is the particle-phase concentration (mole m^{-3} of air) of species *i* in bin *j*. The denotation of the mass transfer coefficient $k_{i,j}$ and the correction factor in the transition regime (Fuchs and Sutugin, 1971) to the Maxwellian flux $f(Kn_{i,j},\alpha_i)$ is same as that for Eqn. (3.3) and Eqn. (3.4). The equilibrium gas-phase concentration $C_{g,i,j}^{eq}$ is calculated based on the specific aerosol composition in bin *j* (*j*=1,2,3,…,N_B where N_B is the number of size bins) using a thermodynamic equilibrium model, determined at the beginning of a time step. Moreover, the term $\left(C_{g,j}-C_{g,i,j}^{eq}\eta_j\right)$ can be regarded as the "driving force" for mass transfer of species *i* to or from bin *j*, respectively. In order to obtain a stable numerical solution, finer time steps are needed to solve the above nonlinear differential equations, which increase the computational cost and limit applications of the dynamic method in large-scale or global models.

In light of above limitation embedded in the dynamic method, Feng and Penner (2007) used a hybrid dynamic approach (HDYN) to account for the heterogeneous uptake of nitrate and ammonium by aerosol mixtures simulated in the Umich/IMPACT model. This method followed a similar approach by Capaldo et al. (2000), who applied this hybrid dynamic method to an air quality model. Capaldo et al. (2000) showed that the hybrid dynamic method not only maintains most of the predictive capability of the full dynamic method but also is 50 times more computationally efficient. The basic idea of the hybrid method is that the instantaneous thermodynamic equilibrium is assumed for fine-mode aerosol particles with diameter less than a threshold diameter D_{thr}, while a dynamic method is used for aerosol particles larger than D_{thr}. In the work of Feng and

Penner (2007) and this study, the thermodynamic equilibrium model (Jacobson et al., 1999) is applied for the size range with aerosol diameter less than 1.25 μm (i.e., bin 1, hereafter referred to as the fine mode) while the dynamic method solving mass transfer equations is applied for the size range with aerosol diameter larger than 1.25 μm (i.e., other 3 size bins, hereafter referred to as the coarse mode). This selection of the threshold diameter $D_{thr} = 1.25 \mu m$ is close to the $D_{thr} = 1.0 \mu m$ used in the study of Capaldo et al. (2000). This is because that the particles with diameter less than 1 μm generally have equilibrium timescales of the order of a few minutes under typical atmospheric conditions (Wexler and Seinfeld, 1990; Dassios and Pandis, 1999) while equilibrium on aerosol particles with larger sizes is established slowly with a timescale of the order of several hours or up to several days (Meng and Seinfeld, 1996; Seinfeld and Pandis, 1998).

Specifically, for the size bin 2, bin 3 and bin 4 with particle diameter ranging from 1.25 μm to 20 μm in the aerosol model, the mass transfer equations (3.9)-(3.12) are applied to calculate the gas-phase and aerosol-phase concentrations for each size bin. The gas-phase equilibrium concentration $C_{g,i,j}^{eq}$ can be related to the aerosol-phase concentration $C_{a,i,j}$ by an effective Henry's law constant $H_{i,j}^{*}$, which relies on the chemical composition of particles as well as the ambient temperature,

$$C_{a,i,j} = H_{i,j}^{*} C_{g,i,j}^{eq} . \tag{3.13}$$

For example, for the gaseous HNO_3 dissolving in solution in size bin j (i.e., i = NO_3^- or HNO_3) through the reaction $HNO_3 \Leftrightarrow NO_3^- + H^+$,

$$C_{a,NO_3^-,j} = H_{NO_3^-,j}^{*} C_{g,HNO_3,j}^{eq} = \frac{H_{HNO_3} K_{eq,HNO_3}}{C_{a,H^+,j}} C_{g,HNO_3,j}^{eq} , \tag{3.14}$$

where H_{HNO_3} is the Henry's law constant for gaseous HNO_3; $C_{a,H^+,j}$ is the aqueous-phase concentration of H^+; K_{eq,HNO_3} is the equilibrium constant ($mol^2\ kg^{-2}\ atm^{-1}$). Plugging the Eqn. (3.13) into the Eqn. (3.9) and Eqn. (3.10) applied for bin 2, 3 and 4 in our study,

$$\frac{dC_{g,i}}{dt} = -\sum_{j=2}^{N_B} k_{i,j}\left(C_{g,i} - \frac{C_{a,i,j}}{H^*_{i,j}}\eta_j\right), \tag{3.15}$$

$$\frac{dC_{a,i,j}}{dt} = k_{i,j}\left(C_{g,i} - \frac{C_{a,i,j}}{H^*_{i,j}}\eta_i\right), \tag{3.16}$$

Given the effective Henry's constant $H^*_{i,j}$, Eqn. 3.15 and 3.16 can be solved implicitly for the two unknowns (i.e., $C_{g,j}$ and $C_{a,i,j}$) for each bin *j*. Since $H^*_{i,j}$ is a function of the composition of particles indicated in the Eqn. (3.14), it varies as the semi-volatile species diffuses into the particle-phase, which in turn affects the equilibrium gas-phase concentration of species *i* over the surface of particles in size bin *j* (i.e., $C^{eq}_{g,i,j}$). Therefore, the value of $H^*_{i,j}$ is updated at each newly-established equilibrium state where the diffused gaseous species equilibrate with their particle-phase.

According to equations (3.15) and (3.16), the mass transfer process between gas and particulate phase at each size bin depends on the particle size. If we assume that all particles across an entire size range are in equilibrium with the ambient gas at an initial state, with additional gaseous species, a greater amount is favorable to diffuse into the particles with smaller sizes in a very small time step while a smaller amount diffuses into the particles with larger. That is, the equilibrium concentration at the surface of smaller particles changes significantly while that over the surface of larger particles may remain approximately same owing to their larger sizes. To avoid excessive calculations of

equilibrium concentrations over the surface of particles, we choose to update the $C_{g,i,j}^{eq}$ and $H_{i,j}^{*}$ for the largest size bin (i.e., bin 4) in our model once during each operator time step (i.e., 1 hour) (Feng, 2005). For the smaller size bin 2 and 3, their chemical composition and gas-phase equilibrium concentrations of semi-volatile species over the surface of particles are updated at an adjustable internal time interval δt within each model (operator) time step. This internal time interval δt is determined by the characteristic time for achieving thermodynamic equilibrium between gas and aerosol phase with the shortest timescale governing the equilibration process. According to the equations (3.10), the characteristic times required for the semi-volatile species i in the size bin j to reach equilibrium is defined as

$$\tau_{i,j} = \frac{C_{a,i,j}}{\left|\frac{dC_{a,i,j}}{dt}\right|} = \frac{C_{a,i,j}}{\left|k_{i,j}(C_{g,i} - C_{g,i,j}^{eq})\right|}. \tag{3.17}$$

If a semi-volatile species is transferred to the solid aerosol phase, the system will achieve thermodynamic equilibrium when the bulk gas-phase concentration becomes equal to the equilibrium gas-phase concentration over the surface of the solid aerosol phase. Here for the solid particles, the equilibrium gas-phase concentration over the particle surface $C_{g,i,j}^{eq}$ is only dependent on temperature and not on the particle composition. Note that, if $C_{g,i} = C_{g,i,j}^{eq}$, the flux between gas and aerosol phase is zero, and the aerosol is in equilibrium with the surrounding gas phase. The characteristic time for the semi-volatile species transferred to the solid aerosol $\tau_{s,i,j}$ is approximated by

$$\tau_{s,i,j} = \frac{1}{\left|k_{i,j}\right|} = \frac{1}{4\pi D_{g,i} R_j N_j f(Kn_{i,j}, \alpha_i)}. \tag{3.18}$$

Note that the mass transfer coefficient $k_{i,j}$ for gas-phase has unit of s^{-1}. One can express this time scale in terms of aerosol mass concentration $m_{i,j} = \frac{4}{3}\pi R_j^3 \rho_i N_j$ as

$$\tau_{s,i,j} = \frac{\rho_j R_j^2}{3 D_{g,i} m_{i,j} f(Kn_{i,j}, \alpha_i)}, \tag{3.19}$$

where ρ_j is the aerosol density in the size bin *j*. Equation (3.19) suggests that the equilibrium timescale increases for larger aerosol (i.e., larger R_j) and cleaner atmospheric conditions (i.e., lower aerosol mass concentration $m_{i,j}$). In other words, semi-volatile species in the smaller size bins under polluted atmospheric conditions have much shorter characteristic times and establish equilibrium faster. The timescale does not depend on the chemical composition as well as thermodynamic properties of aerosol particles, as it is solely related to the diffusion of gas-phase molecules to the particle surface.

If considering the diffusion of a semi-volatile species to aqueous aerosol particles, the equilibrium gas-phase concentration over the particle surface $C_{g,i,j}^{eq}$ changes during the condensation of the semi-volatile species and the reduction of gas-phase concentration. The time scale $\tau_{s,i,j}$ accounting for the process of the diffusion of semi-volatile species to the solid aerosol particles remains applicable, an additional timescale $\tau_{a,i,j}$ are given (Seinfeld and Pandis, 1998) below to characterize the change of $C_{g,i,j}^{eq}$.

$$\tau_{a,i,j} = \frac{m_w}{K_{eq,i}} \tau_{s,i,j}, \tag{3.20}$$

where m_w is the mass concentration of aerosol water in kg m^{-3}; $K_{eq,i}$ is an equilibrium constant of species *i*. Equation (3.20) suggests that the timescale of $\tau_{a,i,j}$ increases with increasing aerosol water content. The higher the aerosol water concentration, the slower

the change of the aqueous-phase concentration of species *i* in size bin *j* resulting from the condensation of a given amount of same species *i* in the gas phase, and thus the slower the corresponding adjustment of the equilibrium gas-phase concentration $C_{g,i,j}^{eq}$ over the particle surface to the ambient gas-phase concentration $C_{g,i,j}$. This timescale also depends on the thermodynamic properties of semi-volatile species *i* via the equilibrium constant $K_{eq,i}$. The more soluble a species is, the lower its $K_{eq,i}$ and the longer the timescale.

In summary, two timescales governing the diffusive transport between the gas and aerosol phases eventually approaching to the equilibrium are one timescale $\tau_{s,i,j}$ characterizing the approach due to changes in the gas-phase concentration field and the other one $\tau_{a,i,j}$ due to changes in the aqueous-phase concentrations if there is aerosol water content present in the aerosol particles. For solid particles, the partial pressures (equilibrium gas-phase concentration) at the particle surface do not change, $\tau_{a,i,j}$ approaches to infinite, the establishment of equilibrium between gas and aerosol phase is mainly governed by $\tau_{s,i,j}$; for aqueous aerosols, both timescales are applied as the system reaches equilibrium through both ways, with the shorter timescale governing the equilibration process (Wexler and Seinfeld, 1991).

In our model, the internal time interval δt at the beginning of each model time step is assumed to be $0.1(\tau_{s,i,j})_{\text{minimum}}$, where *i* and *j* are the indicies for the species *i* and size bin *j*, respectively. Note dust and sea salt aerosols are regarded as solids at the beginning of each model time step. The fraction of 0.1 is chosen to ensure that the amount of the

diffused species during the time δt is not going to cause any significant changes in the surface equilibrium concentration $C_{g,i,j}^{eq}$.

Figure 3.2 illustrates the implementation of the hybrid dynamic method for semi-volatile species HNO_3, NH_3 and N_2O_5. First, the bulk gas-phase concentration $C_{g,i}$ and aerosol phase concentration $C_{a,i,1}$ are calculated assuming the instantaneous equilibrium for bin 1. The equilibrium concentrations of semi-volatile species over the aerosol size bins 2, 3 and 4 ($C_{g,i,2}^{eq}$, $C_{g,i,3}^{eq}$, and $C_{g,i,4}^{eq}$) are calculated simultaneously by solving internal aerosol equilibrium. Secondly, once the internal time interval δt is chosen to be equal to $0.1(\ \tau_{i,j}\ )_{\text{minimum}}$, the gas-phase concentration $C_{g,i}$ updated from the equilibrium calculation in size bin 1 as well as the equilibrium concentrations of semi-volatile species ($C_{g,i,2}^{eq}$, $C_{g,i,3}^{eq}$, and $C_{g,i,4}^{eq}$) calculated in size bins 2, 3 and 4 are used to solve diffusion-limited mass transfer equations during the internal time interval δt in size bin 2, 3, and 4. As discussed earlier, before proceeding to repeat solving mass transfer equations in the new time interval, the equilibrium concentrations of semi-volatile species ($C_{g,i,2}^{eq}$ and $C_{g,i,3}^{eq}$) in size bins 2 and 3 are updated. Then the next internal time interval δt is doubled from its previous value. The integration of the diffusion-limited mass transfer equations continues until the model (operator) time step ΔT is reached. Finally, the gaseous semi-volatile species are calculated, according to both the instantaneous equilibrium between the gas phase and aerosol particles in the fine mode (i.e., bin 1) and the diffusion-limited mass transfer process between the gas phase and aerosol particles in the coarse mode (i.e., bin 2, 3, and 4).

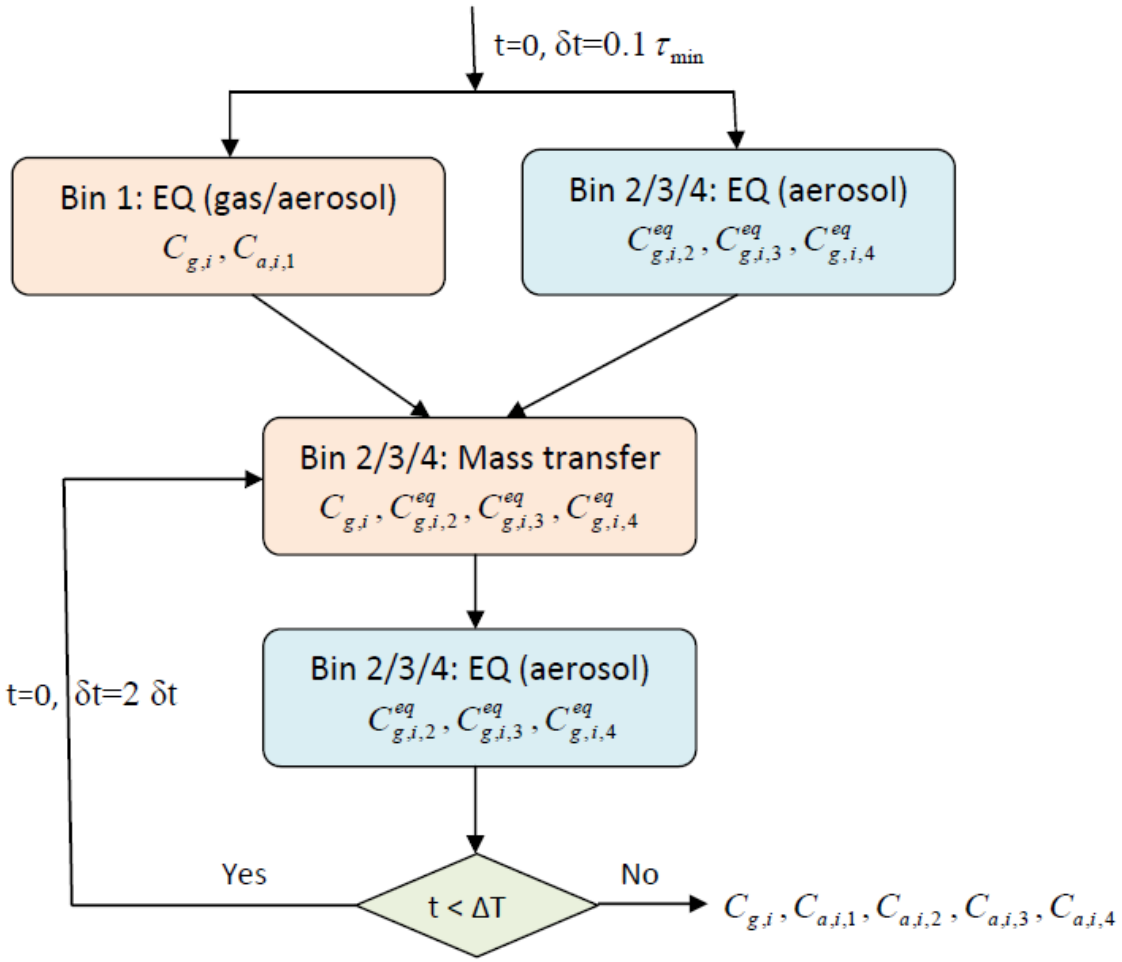

Figure 3.2: A schematic illustration of the implementation of the hybrid dynamic method into the aerosol thermodynamics module assuming all pre-existing aerosols are internally mixed. ΔT and δt are the model (operator) time step (i.e., ΔT = 3600 s) and the internal time interval in solving mass transfer equations, respectively. $C_{g,i}$, $C_{a,i,j}$, $C^{eq}_{g,i,j}$ are the concentration of bulk gas-phase, aqueous-phase and the equilibrium concentration over the particle surface, respectively. *i* and *j* are index for aerosol species (*i* = HNO_3, NH_3 and N_2O_5) and aerosol size bins (*j* = 1, 2, 3, and 4).

3.2.4 Simple kinetic-limited equilibrium method

In contrast to the hybrid dynamic method explicitly accounting for diffusion-limited mass transfer on coarse aerosol particles for non-equilibrium conditions, a simple kinetic limited equilibrium method (KEQ) was proposed by Pringle et al. (2010) to simulate the

process of gas/aerosol partitioning in the global aerosol model of GMXe. Two stages are taken into account in this method. First, the amount of gas phase species *kinetically able* to condense onto aerosol is calculated assuming the diffusion limited condensation following the work of Vignati et al. (2004) within one time step. Second, a thermodynamic model is then used to re-distribute the mass between gas and aerosol phase. Note that the second step of this KEQ method is actually same as the pure equilibrium method.

Vignati et al. (2004) applied the kinetic limitation to treat the condensation of H_2SO_4 gas in the model of M7 that classifies aerosols with seven modes,

$$\frac{dC_{SO_{4g}^{2-}}}{dt} = -\sum_{i=1}^{7} N_i k_i C_{SO_{4g}^{2-}}, \tag{3.21}$$

where N_i is the particle number (molecule cm^{-3}) in mode i; $C_{SO_{4g}^{2-}}$ is concentration of gaseous H_2SO_4 ($\mu g\ m^{-3}$); k_i is condensation coefficient (cm^3 $molecule^{-1}$ s^{-1}) for mode i. The condensation coefficient k_i for mode i is determined from Fuchs (1959) using the average radius of mode i:

$$k_i = \frac{4\pi D \bar{r}_{gi}}{\frac{4D}{s\nu\bar{r}_{gi}} + \frac{\bar{r}_{gi}}{\bar{r}_{gi} + \Delta}}, \tag{3.22}$$

where $\bar{r}_{gi}$ is the geometric mean radius (cm) of mode i; D, ν and s are the diffusion coefficient (cm^2 s^{-1}), mean thermal velocity (cm s^{-1}) and an accommodation coefficient, respectively. Note that Δ refers to a distance from the surface of the drop in Fuchs (1959). One can assume that Δ equals the mean distance from the surface of the drop at which the condensation molecules suffer their first collision with other molecules (i.e., Δ equals the mean free path length of vapor molecules, λ) when the radius of drop is much smaller

than the mean free path of gas (i.e., $\bar{r}_{gi} << \lambda$). Pringle et al. (2010) extended this treatment of H_2SO_4 gas to semi-volatile species, such as HNO_3, HCl and NH_3. Once the total amount of gas species that could kinetically be able to condense onto each aerosol mode is calculated, a thermodynamic model is then used to re-distribute the mass between gas and aerosol phase. For semi-volatile species, only a fraction of the gas that is kinetically able to condense on the surface of aerosol particles will go to the aerosol phase. Therefore, this gas fraction determined by the kinetic theory is a key parameter in this method. Note that the KEQ method is reduced to the pure equilibrium (EQ) method if this gas fraction is close to 1.

In this work, we implement this method in our size-segregated box model to examine discrepancies or similarities among three methods (i.e., the pure equilibrium method (EQ), the simple kinetic-limited equilibrium method (KEQ) and the hybrid dynamic method (HDYN)) assuming all pre-existing aerosols are completely internally mixed within each size bin. Similar as described in the hybrid dynamic method, four size sections are used to represent the size distribution across diameter ranges of 0.1~20 μm. For instance, for gaseous HNO_3, the concentration of HNO_3 in the gas phase *kinetically able* to condense onto the particle for all four size bins is solved following Eqn. (3.21) at first,

$$\frac{dC_{HNO_3}}{dt} = -\sum_{i=1}^{4} N_i k_i C_{HNO_3} \ . \tag{3.23}$$

According to Pringle et al. (2010), the diffusion coefficient D in the Eqn. (3.22) is approximated by

$$D = 0.073 \frac{1000}{P} \left(\frac{T}{298.15} \right)^{\frac{3}{2}}. \quad (3.24)$$

Note that this diffusion coefficient is actually for sulfuric acid gas which has a magnitude of about 0.073 $cm^2\ s^{-1}$ at 1000 hPa and 298.15 K. According to the GMXe code, Pringle et al. (2010) applied this sulfuric acid gas diffusion coefficient for all semi-volatile species (e.g., HNO_3, NH_3 and HCl). In contrast, the true diffusion coefficient of HNO_3 and NH_3 gas is 0.15 $cm^2\ s^{-1}$ and 0.24 $cm^2\ s^{-1}$ with higher values in the upper troposphere as shown in Table 3.1. A sensitivity test was conducted (not shown here) and the kinetic limited gas fraction is not very sensitive to the value of gas diffusion coefficient.

The mean velocity of gas molecules *v* is calculated following the Eqn. (3.8). The mean free path length of gaseous HNO_3 molecules are estimated from

$$\lambda_{HNO_3-air} = \frac{8D}{\pi v_{HNO_3}}. \quad (3.25)$$

The distance from the particle to where the kinetic regime applies is calculated by

$$\Delta = \frac{\left(\bar{r}_i + \lambda_{HNO_e-air}\right)^3 - \left(\bar{r}_i^2 + \lambda_{HNO_e-air}^2\right)^{3/2}}{3\bar{r}_i \lambda_{HNO_e-air}} - \bar{r}_i, \quad (3.26)$$

where $\bar{r}_i$ is the mean radius of size bin *i*. Note that the distance Δ is the order of the mean free path λ and the simple kinetic theory of gases applies within the regime from the particle surface up to the distance Δ. Substituting Eqn. (3.24) and Eqn. (3.26) into Eqn. (3.22), the condensation coefficient (k_i) of gaseous HNO_3 in each size bin can be calculated. Then the kinetic limited gas fraction ($f_{i,j}$) and mass ($m_{i,j}$) of gaseous species *j* which condenses onto aerosol particles in size bin *i* are calculated by

$$f_{i,j} = \min\left(\frac{\Delta t \sum_{i=1}^{4} N_i k_i}{C_{g,j}}, f_{g,j,\max} \right) \tag{3.27}$$

$$m_{i,j} = f_{i,j} C_{g,j}, \tag{3.28}$$

where $f_{g,j,\max}$ is the maximum mass fraction of gaseous species j that is allowed to condense on aerosol particles and Δt is one operator time step (i.e., 1 hour). Here $f_{g,j,\max}$ is set to be 0.95 in this current simulation which is the same choice made by Pringle et al. (2010). Figure 3.3 shows the kinetic limited gas fraction $f_{i,j}$ of HNO_3 gas as a function of the radius of aerosols (i.e., $\bar{r}_{gi}$) from equations (3.21-3.27). Obviously, a gas fraction constrained by the simple kinetic theory (i.e. less than the maximum value) only occurs for very small particles with radii less than 0.0036 μm. For any aerosol larger than this size, the gas fraction able to condense onto the aerosol particle is not actually constrained by the kinetic theory in the KEQ method. Therefore, the KEQ method is reduced to the pure equilibrium method for most aerosol sizes.

According to Eqn. (3.21) or Eqn. (3.23), $N_i k_i$ has the unit of s^{-1}. The characteristic time required for the semi-volatile species j to establish a steady state around a particle can be derived as

$$\tau_{g,j} = \frac{C_{g,j}}{\left| \frac{dC_{g,j}}{dt} \right|} = \frac{1}{\left| \sum_{i=1}^{4} N_i k_i \right|}. \tag{3.29}$$

Clearly, this characteristic time is mainly governed by the condensation coefficient of the smallest size bin since the condensation coefficient k_i is positively proportional to the mean radius of size bin i, i.e., the smaller the mean radius, the smaller the condensation

coefficient and consequently the faster to reach equilibrium. That is, this condensation rate favors the diffusion onto the surface of smaller particles rather than larger ones.

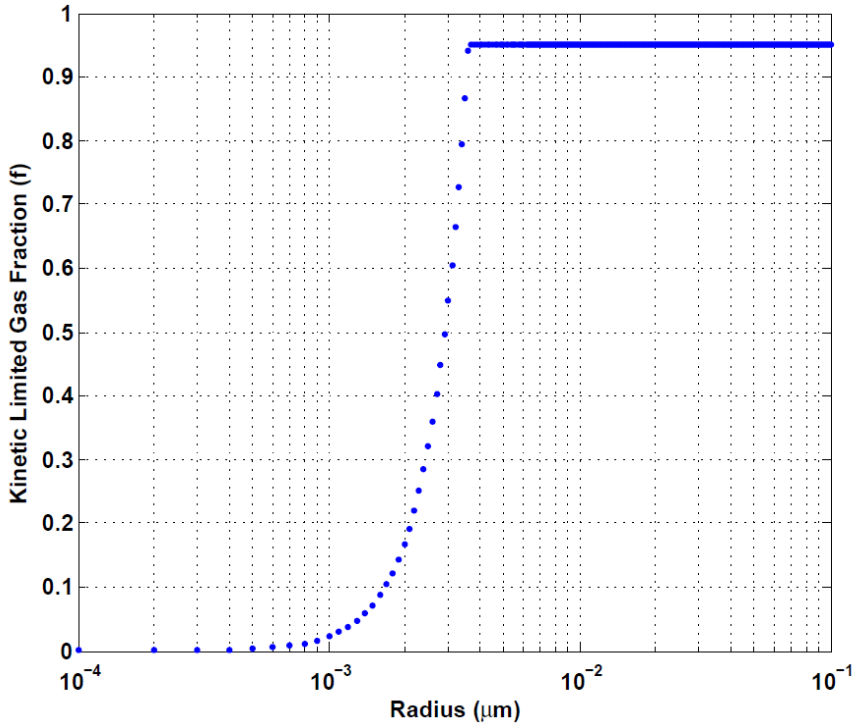

Figure 3.3: The kinetic limited gas fraction as a function of aerosol radius for HNO_3 gas.

Compared to the hybrid dynamic method, the advantage of this simple kinetic limited equilibrium method is its simplicity and computation expense. However, this method may be problematic. First, comparing Eqn. (3.21) with Eqn. (3.9), Eqn. (3.21) suits for gaseous species such as H_2SO_4 because the equilibrium surface concentration term presented in the more general expression of Eqn. (3.9) for gaseous H_2SO_4 is eliminated (i.e., $C^{eq}_{g,i,H_2SO_4} = 0$) due to its low volatility. Note that the exclusion of the equilibrium surface concentration is valid for gas species with low volatility, such as H_2SO_4. Such an assumption, however, is not applicable for extremely soluble and volatile species, like

HNO_3. The gas-phase HNO_3 concentration could be reduced by several orders of magnitude as it is partitioned in the aerosol phase to form either solid or liquid nitrate. Furthermore, its partial pressure over the particle surface is strongly determined by the chemical compositions within aerosol particle during this complex diffusion-condensation-dissociation-evaporation process. Hence, the equilibrium gas phase concentration $C_{g,i,j}^{eq}$ of semi-volatile species (e.g., HNO_3, NH_3 and HCl) could not be assumed as a constant just like gaseous H_2SO_4. Second, a one operator time step (i.e., approximately 1 hour) used to solve the Eqn. (3.21) at the first stage is too crude in the current setup (Pringle et al., 2010) so that the kinetic limited diffusion process is actually not resolved within such a long time since the typical timescale for the equilibrium between the gas and aerosol phase varies from seconds to several days as the particle radius increase from a few nanometers to several micrometers. Third, the diffusion coefficient of H_2SO_4 gas applied for all semi-volatile species leads to a bias in the estimate of the amount of gas kinetically able to condense onto particles. Most importantly, as we shown in Figure 3.3, the amount of gas "kinetically" able to condense on the aerosol particles described in the first step of the KEQ method is not actually limited by the simple kinetic theory for most fine and coarse mode particles because the radius of aerosol particles generally has the order of the mean free path of HNO_3 gas, about 0.15 μm in the surface, (i.e., R~λ or the Knudsen number is close to 1) that typically lies in the transition regime as we discussed in the Section 3.2.2.

3.2.5 Aerosol mixing state

Atmospheric aerosol particles involve a complex interaction of physical and chemical process in the air, whose mass concentration is governed by following equation:

$$\frac{\partial C_i}{\partial t} = \left(\frac{\partial C_i}{\partial t}\right)^{emiss} + \left(\frac{\partial C_i}{\partial t}\right)^{nucl} + \left(\frac{\partial C_i}{\partial t}\right)^{cond./evap.} + \left(\frac{\partial C_i}{\partial t}\right)^{therm} + \left(\frac{\partial C_i}{\partial t}\right)^{coag.-in} - \left(\frac{\partial C_i}{\partial t}\right)^{coag.-out} - \left(\frac{\partial C_i}{\partial t}\right)^{depos.} \quad (3.30)$$

where C_i is the mass concentration of species i and t is the time. In order to solve each process, operator splitting is generally employed in numerical models. As long as the model time step is enough small (i.e., less than characteristic timescales of individual processes), errors introduced by solving process operators in sequence could be controlled. In numerical models, aerosol particles with different chemical composition are commonly assumed externally mixed (see Figure 3.4 (left)), where particles with the same size could have different chemical compositions. This assumption is based on the fact that particles are likely to originate from different sources. However, particles far from their sources are often founded partially or completely internally mixed (see Figure 3.4 (right)), where particles with the same size have uniform chemical composition. In the real atmosphere, aerosol particles exist in a variety of complicated mixing states (e.g., Andreae et al., 1986; Levin et al., 1996; Murphy et al., 1998; Pósfai et al., 1999; Silva et al., 2001; Guazzotti et al., 2001; Okada and Hizenberger, 2001; Naoe and Okada, 2001). Multiple distributions and interactions among them need to be taken into account to some extent.

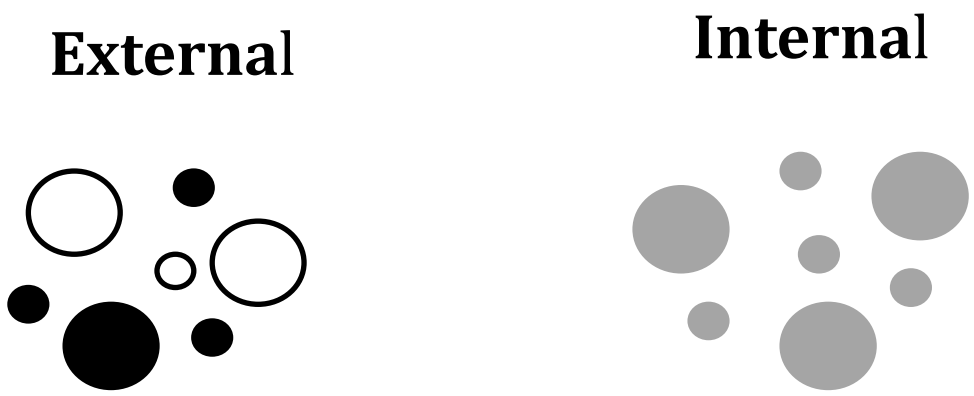

Figure 3.4: Two aerosol mixing state: external mixing (left) and internal mixing (right).

In a previous study of global simulation of nitrate and ammonium aerosols (Feng and Penner, 2007, hereafter as FP07), one aerosol size distribution has been considered for nitrate and ammonium aerosols. As described in FP07, the size distribution of nitrate and ammonium aerosols was determined by the dominant aerosol type in each size section. The size distribution of nitrate and ammonium aerosol in the radius range of 0.05-0.63 μm (bin 1) was treated as the same as sulfate (Chuang et al., 1997), while that in the radius range from 0.03 to 2.5 μm (bin 2 and bin 3) was treated the same as sea salt (Quinn et al., 1998), and that in the range of 2.5-10 μm (bin 4) was treated the same as mineral dust (de Reis et al., 2000). Internal mixing assumption was generally considered for particles in the same size bin having uniform chemical composition that is the average over the size range in each size bin, but the average chemical composition of each bin may vary from one bin to another. This assumption is held for particles far from their sources since aerosol particles are often found as partially or completely internally mixed with multiple components including sulfate, sea salt, nitrate and dust components (Zhang et al., 2003). However, particles near their sources are generally externally mixed. Thus, the representation of only one size distribution treated in an entire domain of model (i.e.,

all components are considered internally mixed at source regions) can distort predicted chemical compositions (Kleeman et al., 1997). On the other hand, when multiple size distributions without interactions among them are treated, all aerosol components are treated as externally mixed, which is also unrealistic far away from source regions; when multiple size distributions with interaction among them are treated, some aerosol types can be treated as externally mixed whereas others can be treated as partially or completely internally mixed. The radiative effects of externally and internally mixed particles may differ. For example, the modeled global direct radiative forcing of black carbon (BC) by treating BC as an internally mixed core surrounded by a soluble shell is about a factor of two higher than the value calculated when BC was treated as externally mixed (Jacobson, 2001).

Table 3.2: Distribution and constituents and size bins applied for each distribution considered.

Distribution	Symbol	Constitutes other than NH_4^+, NO_3^- and H_2O	Size bin(s) applied
Sulfate	SU	SO_4^{2-}	Bin 1 (D<1.25 μm)
FF OM/BC	FF	SO_4^{2-}	Bin 1 (D<1.25 μm)
BB OM/BC	BB	SO_4^{2-}	Bin 1 (D<1.25 μm)
Dust	DU	Ca^{2+},Na^+,K^+,Mg^{2+}, SO_4^{2-}	Bin 1, 2, 3, 4
Sea salt	SS	Na^+, Cl^-, SO_4^{2-}	Bin 1, 2, 3, 4

In this study, in order to be consistent with the aerosol treatment in other processes in the global model (i.e., sulfate related aerosol dynamics), nitric acid and ammonia are allowed to interact with other pre-existing particles, such as pure sulfate, carbonaceous particles, sea salt and dust. Hence, five aerosol types are considered according to the origins of aerosol sources shown in Table 3.2. Internally mixed multiple aerosol components are assumed within each distribution while externally mixed aerosol

components are assumed among distributions. Given the distribution, chemical compositions can be resolved using a thermodynamic model (Jacobson, 1999) shown in Table 3.3. Note that only interaction of semi-volatile species with coated sulfate is considered for the distribution FF and BB since little is known about the reaction of organic aerosols with semi-volatile species. For the illustration purpose, we only consider three size distribution (i.e., SU, DU, and SS) listed in Table 3.2 present in following sections.

Table 3.3: List of chemical compositions resolved in each distribution of Table 3.2.

Phase	Compositions
Gas	HNO_3, NH_3, HCl, CO_2
Liquid	H_2O(a), H_2SO_4(a), H^+, NH_4^+,Na^+,Mg^{2+}, Ca^{2+}, K^+, HSO_4^-, SO_4^{2-}, NO_3^-, Cl^-, HCO_3^-, CO_3^{2-}, OH^-
Solid	$(NH_4)_2SO_4$(s), NH_4HSO_4(s), $(NH_4)_3H(SO_4)_2$(s), NH_4NO_3(s), NH_4Cl(s), $(NH_4)_2CO_3$(s), Na_2SO_4(s), $NaHSO_4$(s), $NaNO_3$(s), NaCl(s), Na_2CO_3(s), K_2SO_4(s), $KHSO_4$(s), KNO_3(s), KCl(s), K_2CO_3(s), $CaSO_4$(s), $Ca(NO_3)_2$(s), $CaCl_2$(s), $CaCO_3$(s), $MgSO_4$(s), $Mg(NO_3)_2$(s), $MgCl_2$(s), $MgCO_3$(s)

Following the hybrid dynamical approach proposed by FP07, for given size distribution, the thermodynamic equilibrium model (Jacobson, 1999) is applied to aerosol in size bin 1 (D<1.25 μm) while the gas and aerosol concentration are determined by dynamically solving the mass transfer equations for particles in other 3 size bins (D>1.25 μm). Figure 3.5 depicts a schematic illustration of the implementation of the hybrid dynamic method for aerosol thermodynamics for external mixed three size distribution: SU, DU and SS. Note that the distribution of SU is only applied for the size section with diameter less than 1.25 μm as described in Table 3.2. Quinn and bates (2005) reported results for size-segregated chemical composition for six large aerosol campaigns taken

place over ocean and coastal regions in different areas of the world. They found that almost all of the mass of non-seasalt sulfate was in the fine mode and that in the supermicron (coarse mode) very small amount of non-seasalt sulfate were present. Their results give confidence to our assumption of a fine sulfate mode as a reasonable treatment. The size distributions of DU and SS are applied for full size range with the diameter varying from 0.1 μm to 20 μm. According to the flow chart shown in Figure 3.5, first, equilibrium was solved in the size bin 1 for each size distribution in a sequential manner and then the diffusion-limited mass transfer in the size bin 2-4 was solved for each size distribution. The sequential order that is used will be revisited in Section 3.3.

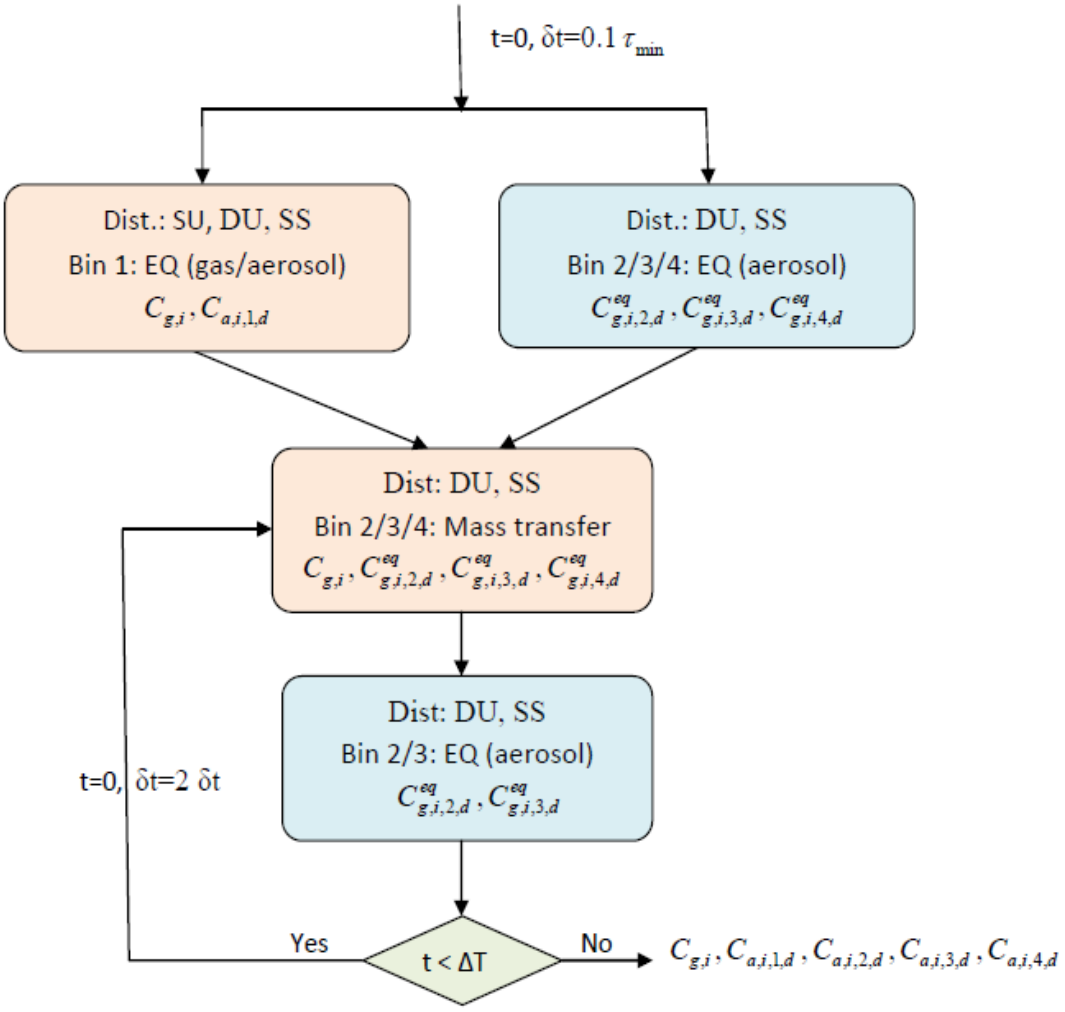

Figure 3.5: A schematic illustration of the implementation of the hybrid dynamic method in the aerosol thermodynamics module for externally mixed three size distributions. ΔT and δt are the model (operator) time step (i.e., ΔT = 3600 s) and the internal time interval in solving mass transfer equations, respectively. $C_{g,i}, C_{a,i,j}, C^{eq}_{g,i,j}$ are the concentration of bulk gas-phase, aqueous-phase and the equilibrium concentration over the particle surface, respectively. i and j are index for aerosol species (i = HNO_3, NH_3 and N_2O_5) and aerosol size bins (j = 1, 2, 3, and 4) given size distribution (d = SU, DU, SS).

3.3 Results

3.3.1 Nitrate treatment using EM and IM

In this section, the comparison of nitrate treatment using the original internally mixing (IM) state versus the external mixing (EM) state is conducted. The purpose is to investigate the difference by accounting for the interaction between semi-volatile species and pre-existing aerosols, such as pure sulfate, fossil fuel and biomass burning aerosols, dust and sea salt. In this box model simulation, three test cases are carried out (Table 3.4). One is a typical continental polluted aerosol concentration, 10 μg m^{-3} sulfate with 50 μg m^{-3} dust aerosols representing an influence from dust events. The second one represents a typical marine aerosol background at coastal sites composed of 10 μg m^{-3} sulfate with 5 μg m^{-3} sea salt aerosols where continental pollutants such as sulfate have heavy influence due to transport. The third test case accounts for more comprehensive situations having the same amount of sulfate (10 μg m^{-3}) with varying amounts of dust and sea salt aerosols. The range of sea salt (0.01~50 μg m^{-3}) and dust aerosol (0.1~100 μg m^{-3}) concentrations was determined according to annual averaged concentration from the global model (Wang et al., 2009). For all three cases, 3.53 μg m^{-3} ammonia (with a molar ratio of 2:1 over sulfate aerosol) and 3.214 μg m^{-3} gaseous nitric acid (with a molar ratio of 0.5:1 over sulfate aerosols) were used for the diffusion into the aerosol phase. The amount of sulfate, dust and sea salt aerosols is distributed into aerosol size bins based on their global annual average distributions in the surface layer predicted by our transport model IMPACT: 94.897%, 1.473%, 3.63% of sulfate aerosol mass were assigned on pure sulfate, dust and sea salt in size bin 1, respectively; and 7%, 27%, 58% and 8% of mineral dust aerosol mass were assigned to size bins 1-4, respectively; and 29%, 29%,

30% and 12% of sea salt aerosol were assigned to the aerosol size bins 1-4, respectively. Note that 99.6% and 0.4% of sulfate aerosol mass are distributed into size bin 1 and 2 in the IM treatment. A typical surface atmosphere temperature of 298 K and relative humidity of 85% were used in the box model simulations.

Table 3.4: Initial aerosol and gas concentrations (μg m^{-3}).

Species	Continental	Marine	Mix
H_2SO_4[a]	10	10	10
NH_3	3.53	3.53	3.53
HNO_3	3.214	3.214	3.214
Dust[b]	50	0	0.1~100
Sea salt[c]	0	5	0.01~50

[a]For the consideration of externally mixed distribution, total sulfate is assumed to be present in 94.897%, 1.473%, 3.63% on pure sulfate, dust and sea salt, respectively.

[b]Total dust is assumed to be present in 7%, 27%, 58% and 8% in size bins 1-4, respectively.

[c]Total sea salt is assumed to be present in 29%, 29%, 30% and 12% in size bins 1-4, respectively.

Figure 3.6 shows a time evolution of the gaseous and size-segregated aerosol concentrations for nitrate and ammonium during the process of achieving the thermodynamic equilibrium assumed for internal mixing (IM) and external mixing (EM) simulated with the hybrid dynamic method for the continental case. The discrepancy between two implementations (EM versus IM) is negligible for the predicted NH_3, NH_4^+ as well as gaseous HNO_3 concentrations. Both solutions approach equilibrium in a similar manner given a sufficient long time. However, large difference occurred in the

prediction of NO_3^- concentration, especially in size bin 1 for all the time of 12 hours. The differences between two treatments are quite small for bin 2 and bin 3, less than a few percent.

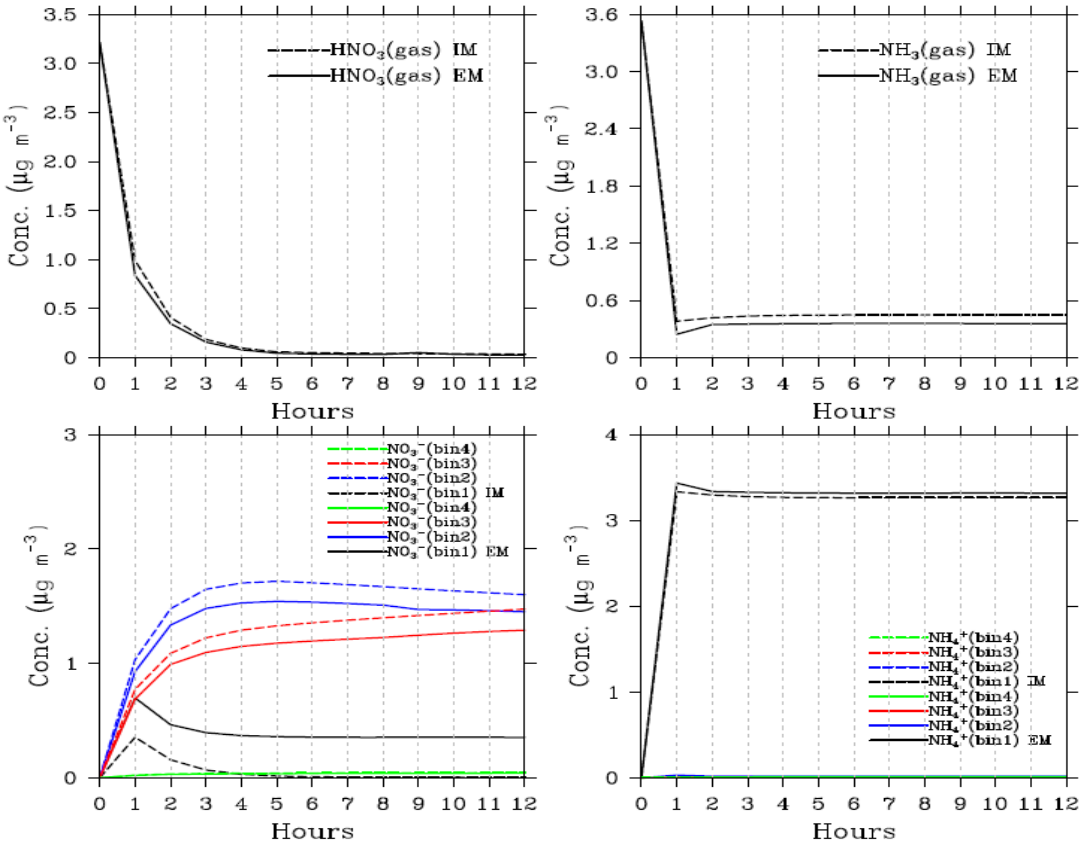

Figure 3.6: The simulated gaseous and size-segregated aerosol concentrations for nitrate and ammonium using the hybrid dynamic method (HDYN) by treating aerosols internally mixed (IM) and externally mixed (EM) in each size bin, varying as a function of time during the establishment of the thermodynamic equilibrium for the continental case.

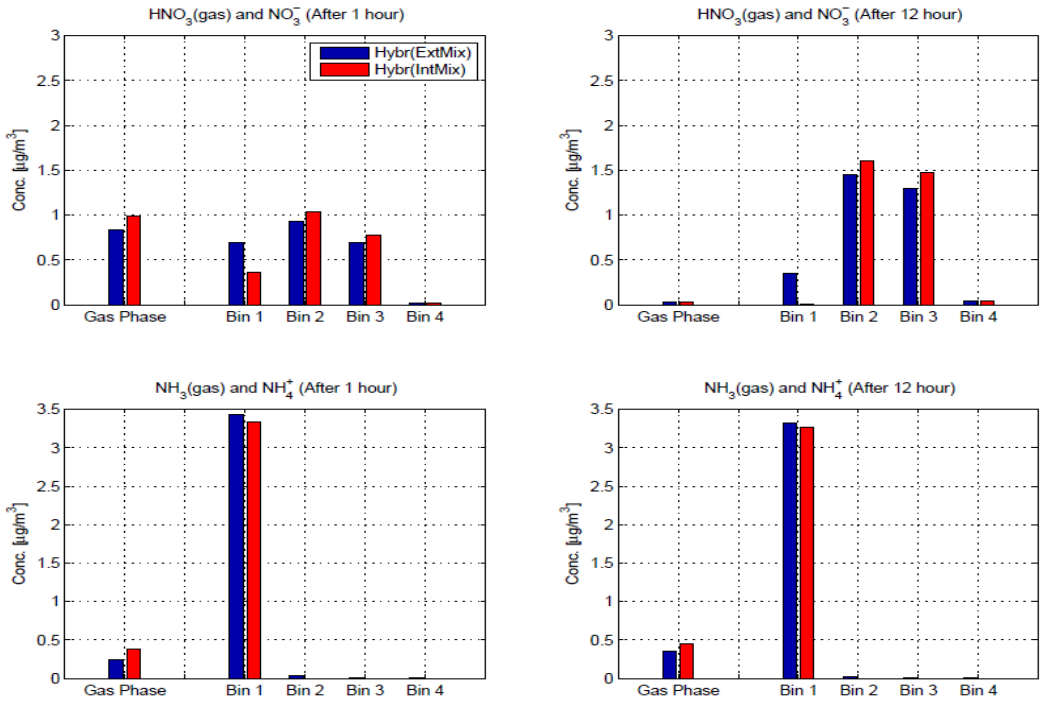

Figure 3.7: Comparison of the box-model simulated gaseous and size-segregated aerosol concentrations of nitrate and ammonium using the hybrid dynamic method (HDYN) by treating aerosols internally mixed (IntMix) and externally mixed (ExtMix) in each size bin after 1 hour (left) and after 12 hours (right) of diffusion for the continental case.

Figure 3.7 gives a snapshot of the box-model simulated gaseous and size-segregated aerosol concentration for nitrate and ammonium by each of the IM and EM treatment after 1 hour and 12 hours of diffusion for the continental case. After 1 hour, the prediction of total nitrate and total ammonium present in gas phase and aerosol phase are quite similar to each other, with a slight lower amount of gaseous HNO_3 and NH_3 and consequent higher amount of NO_3^- and NH_4^+ predicted by the EM treatment. The size distribution of NO_3^- across 4 size bins differs between these two treatments of mixture. The IM treatment favors the condensation of HNO_3 on larger particles through the diffusion limited mass transport while the EM treatment predicts higher NO_3^- in the fine

mode. The internal mixing state with aerosols composed of sulfate, dust and sea salt in the fine mode prevents the formation of HNO_3 on the surface of dust and sea salt particles if sulfate in is excess. This is because sulfate anion (i.e., SO_4^{2-}) prefers to be combined with cations provided by dust aerosol (e.g., Ca^{2+}, Na^+, K^+, Mg^{2+}) before it starts to be associated with NH_3. Once the metal cations are associated with SO_4^{2-} to form corresponding sulfate salts, sulfate starts reacting with NH_3 to form $(NH_4)_2SO_4/NH_4HSO_4/(NH_4)_3H(SO_4)_2$ dependent upon the molar ratio of ammonium to sulfate. If NH_3 is in excess, gaseous HNO_3 is able to react with it to form NH_4NO_3 over the surface of pre-existing particles. Hence, the IM treatment prevents NO_3^- associated with metal cations, which results in that NH_4NO_3 is major nitrate salt in the IM treatment. In contrast, the EM treatment provides more particle surface and allows directly heterogeneous reaction between HNO_3 and metal cations from mineral dust, which leads to the formation of metal nitrates. Thus, in the EM treatment, NO_3^- is not only able to be reacted with NH_4^+ but also be associated with Ca^{2+}, Na^+, K^+, Mg^{2+} in either aqueous or solid phase. The difference in the chemical composition of nitrate salts can also contribute to the difference in the nitrate distribution between these two treatments after 12 hours diffusion. Given a sufficient long time, nitric acid depletes for both treatment. In other words, both treatments predicted nearly complete partitioning of total nitrate into the aerosol phase. The IM treatment predicts a different equilibrium state of species concentrations from that by the EM treatment. One reason is that the formation of solids during the diffusion process is irreversible; in other words, once the solids form in the small particles due to a faster diffusion rate of gases into them, they can not be transported to large particles through the gas phase. On the other hand, as mentioned

earlier, the direct heterogeneous reaction between HNO_3 and metal cations (e.g., K^+) maintains anion NO_3^- in the aqueous or solid phase to neutralize K^+. Therefore, in the IM treatment, all particulate nitrates in size bin 1 are completely transported to larger particles because of the unstable nature of NH_4NO_3 while the partial nitrate associated with metal cations in either aqueous or solid phase in the EM treatment is still present in the size bin 1. This results in higher NO_3^- concentration in the smallest size bin predicted by the EM treatment. Both treatments predict similar amount of NH_4^+ because the partitioning of ammonium between the gas and aerosol phase is mainly determined by the thermodynamic equilibrium on sulfate aerosols.

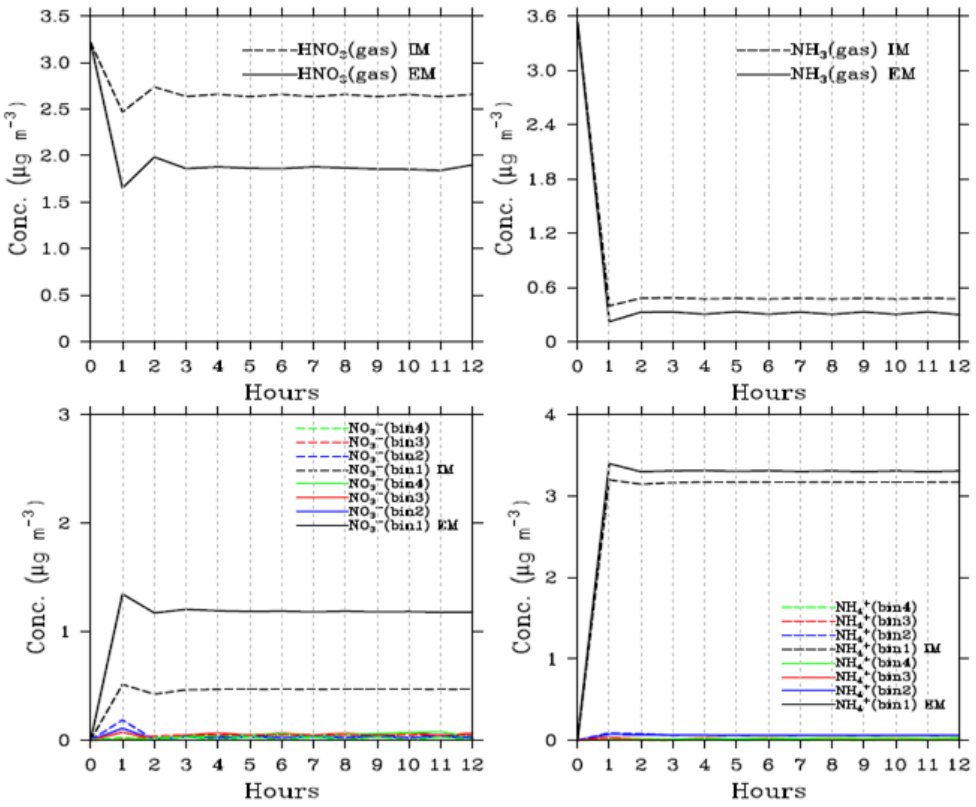

Figure 3.8: As for Figure 3.6, but for the marine case.

Figure 3.8 shows a time history of the gaseous and size-segregated aerosol concentrations for nitrate and ammonium during the process of achieving the thermodynamic equilibrium assumed for internal mixing (IM) and external mixing (EM) simulated with the hybrid dynamic method for the marine case. Similar to the continental case, both solutions approach equilibrium in a similar manner and there is negligible difference in the prediction of NH_3 and NH_4^+ concentrations. Because sea salt particles are generally smaller than mineral dust aerosols, the uptake of nitrate and ammonium by sea salt aerosols from both treatments reach equilibrium faster than the uptake by mineral dust aerosols shown in Figure 3.6. Large difference occurred in the prediction of gaseous HNO_3 and NO_3^- concentration in size bin 1 for all the time of 12 hours. Figure 3.9 gives snapshots of the box-model simulated gaseous and size-segregated aerosol concentration for nitrate and ammonium by each of IM and EM treatments after 1 hour and 12 hours of diffusion for the marine case. There is no significant difference between the snapshots of species concentrations after 1 hour and that after 12 hour diffusion for both IM and EM treatments in this test case. The size distribution of NO_3^- across 4 size bins is similar to each other for these two treatments of mixture with the peak occurred in the fine mode aerosol (i.e., bin 1). The EM treatment predicts lower gaseous HNO_3 and consequently higher NO_3^- in the size bin 1 than does the IM treatment. Specifically, the EM treatment predicts 0.3462 $\mu g\ m^{-3}$ NO_3^- in the distribution of sulfate aerosol and 0.997 $\mu g\ m^{-3}$ NO_3^- associated with sea salt aerosol while the IM treatment predicts 0.514 $\mu g\ m^{-3}$ NO_3^- associated with NH_4^+ and Na^+ in the internal mixture of sulfate and sea salt aerosol. This discrepancy is ascribed to the effect of sulfate on sea salt aerosols similar to that was discussed above in the continental case for the effect of sulfate on dust particles.

Moreover, the presence of sulfate in the IM treatment inhibits the direct heterogeneous reaction of gaseous HNO_3 with Na^+ tied to sea salt, resulting in lower NO_3^- concentration in the size bin 1 by about a factor of two in this test case compared with that in the EM treatment.

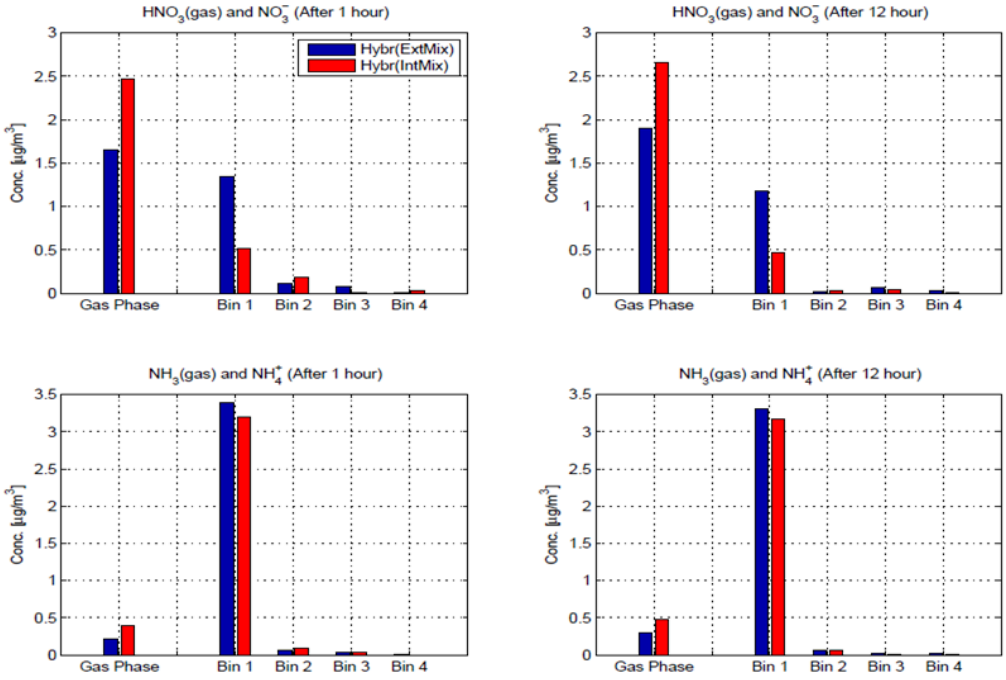

Figure 3.9: As for Figure 3.7, but for the marine case listed in Table 3.4.

The third case examined the sequential order involved with each size distribution. Figure 3.10 gives the aerosol nitrate in the size bin 1 after 1 hour diffusion using the sequential order of SU1-DU2-SS3 (i.e., sequentially solving equilibrium and mass transfer equations in an order of the distribution SU, DU and SS) and of SU1-SS2-DU3 (i.e., sequentially solving equilibrium and mass transfer equations in an order of the distribution SU, SS and DU) in the EM treatment as well as the absolute and relative difference between two orders used. The difference is trivial as the dust concentration is less than about 40 µg m^{-3} across an entire range of sea salt concentration while the

relative difference is about 10% as sea salt and dust aerosol concentration is around 10 μg m^{-3} and 100 μg m^{-3}, respectively. This maximum relative difference of 10%, however, corresponds to very tiny value of absolute difference of about 0.25 μg m^{-3}. Although these concentrations of bias are small, an alternative order in a switch manner of these two sequential orders dependent upon the time step is used for the implementation of the EM treatment in the global model discussed in the next chapter. That is, the sequential order of SU1-DU2-SS3 is used in the odd time step and then that of SU1-SS2-DU3 is adopted in the even time step and so on and so forth. This adoption of this alternative sequential order, to some extent, helps eliminating the bias present here.

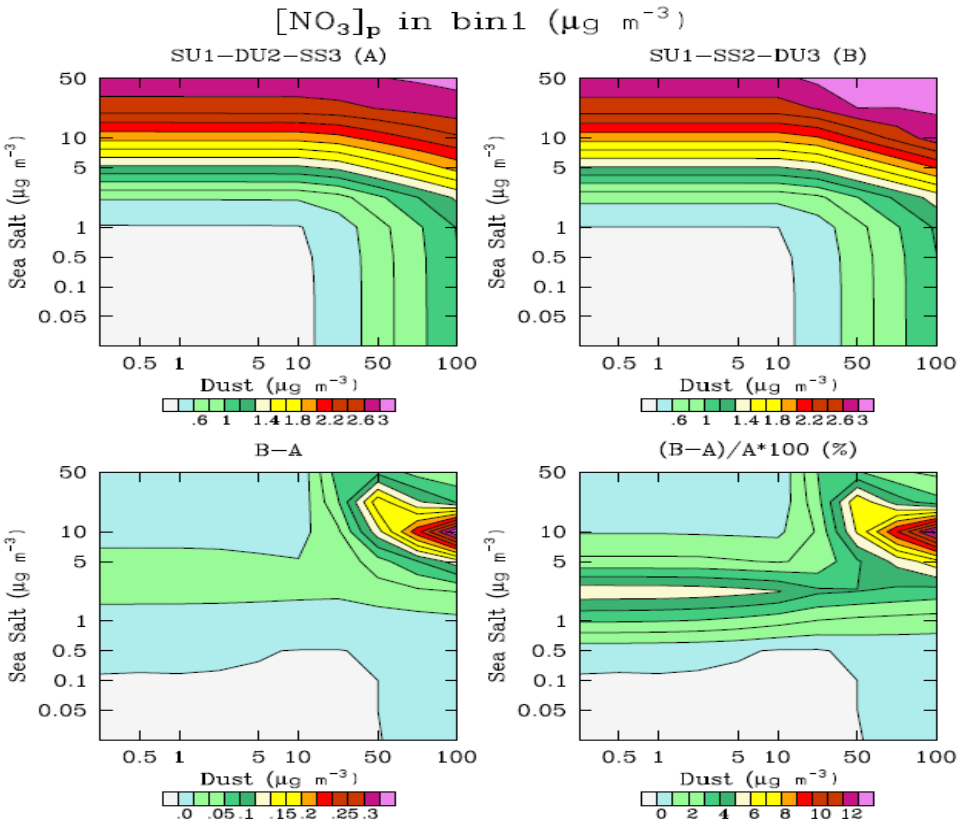

Figure 3.10: The simulated aerosol concentration of nitrate in the first size bin using the loop order of SU1-DU2-SS3 (top left panel) and of SU1-SS2-DU3 (top right panel) for the mix case shown in Table 3.4, respectively, varying with aerosol concentrations of sea salt and dust. The bottom two panels give the absolute difference as well as relative difference of top two panels.

3.3.2 Nitrate treatment using KEQ and HDYN

In this section, the comparison of nitrate treatment using the kinetic limited equilibrium method (KEQ) and hybrid dynamic method (HDYN) was conducted. Two cases including continental and marine background aerosols shown in Table 3.4 are present here. A typical surface atmosphere temperature of 298 K and relative humidity of 85% was used.

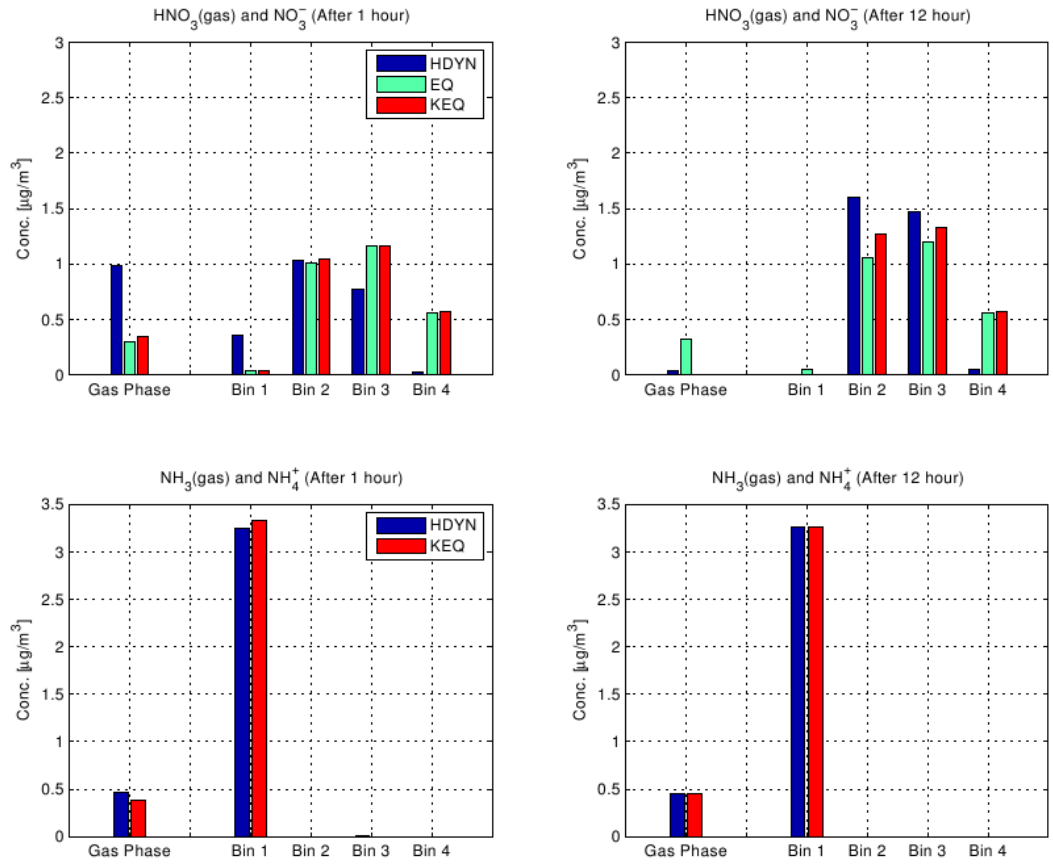

Figure 3.11: Comparison of the box-model simulated gaseous and size-segregated aerosol concentrations of nitrate and ammonium using the hybrid dynamic method (HDYN) and the kinetic limited equilibrium (KEQ) method by treating aerosols internally mixed (IM) in each size bin after 1 hour (left) and after 12 hours (right) of diffusion for the continental case.

Figure 3.11 shows snapshots of the box-model simulated gaseous and size-segregated aerosol concentration for nitrate and ammonium by each of HYDN and KEQ treatments after 1 hour and 12 hours of diffusion for the continental case. The simulated size-resolved concentration of nitrate using the pure equilibrium (EQ) method is also included here for the comparison. The discrepancy in simulated results with two implementations (HDYN versus KEQ) is negligible for the predicted NH_3 and NH_4^+ concentration after 1 hour and 12-hour simulations while that is quite different on the prediction of gaseous HNO_3 and NO_3^- concentrations. In general, the KEQ method, similar to the EQ method, predicts lower gaseous HNO_3 and consequently higher amount of aerosol NO_3^- concentrations. As shown in the Section 3.2.4, the amount of nitric acid gas "kinetically" able to condense on aerosol particles described in the first step of the KEQ method is not actually limited by the simple kinetic theory for any aerosol particle with size larger than 0.0036 μm. Hence, the fraction of gaseous species *j* allowed to condense onto aerosol particles is mainly determined by the assumed maximum mass fraction of gaseous species *j*, $f_{g,j,\max}$. Since the arbitrary $f_{g,j,\max}$ of 95% is assumed in the KEQ method, it indicates that 95% mass of gaseous species participate in the equilibrium calculations at each time step at the second stage described in Section 3.2.4. Moreover, the KEQ method implicitly assumes that the surface equilibrium concentration of gaseous species is 0 on all particle surfaces, which favors the diffusion to small particle. Figure 3.12 gives the calculated distance from particle up to where the kinetic regime applies (Δ), Knudsen number (Kn) as well as fraction (frac) kinetically allowed to condense onto aerosol particles of gaseous HNO_3 and NH_3 for each size bin. Obviously, the kinetic limited gaseous mass fraction allowed to condense onto surface of aerosol particles is related to

Knudsen number. The higher the Knudsen number, the larger the fraction is. Since the Knudsen number in the smallest size bin (i.e., bin 1) is way larger than those in larger size bins (i.e., bin 2~4), gaseous species predominantly diffuse onto the smallest size bin. In addition, the kinetic limited diffusion process at the first stage of the KEQ method is only conducted once within one operator time step (i.e., 1 hour). In contrast, HDYN couples size-resolved chemical adjustments in the aerosol phase and the diffusion limited mass transport at a shorter internal time step, which results in better predictions for NO_3^- size distribution.

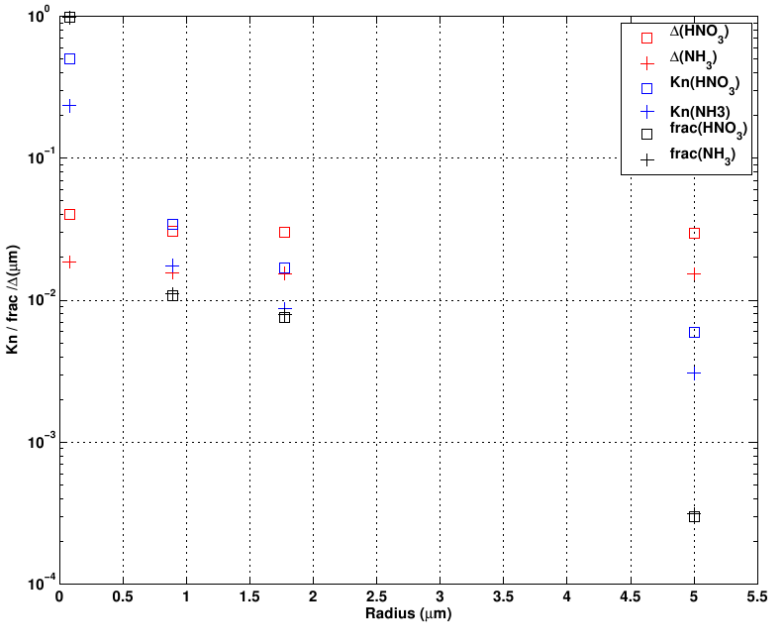

Figure 3.12: The calculated distance from the particle to where the kinetic regime applies (Δ), Knudsen number (Kn) as well as fraction (frac) kinetically allowed to condense onto aerosol particles for gaseous HNO_3 and NH_3 for each size bin.

After a 12-hour simulation, both HDYN and KEQ predict nearly complete partitioning of total nitrate into aerosol phase. HDYN obtains a different size distribution of aerosol

NO_3^- after 12 hours than it does after 1 hour, i.e., the mass from gas phase as well as the smallest size bin tends to be transferred to the larger size bins. Similar to the EQ method, the KEQ method maintains the same size distribution as that after a 1 hour simulation due to its equilibrium assumption.

Figure 3.13 shows snapshots of the box-model simulated gaseous and size-segregated aerosol concentration for nitrate and ammonium by each of HDYN and KEQ treatments after 1 hour and 12-hour diffusion for the marine case where sulfate and sea salt aerosol are considered. Same as in Figure 3.11, the simulated size-resolved concentration of nitrate using the pure equilibrium (EQ) method is also included. The model predictions in both HDYN and KEQ methods after 1 hour are similar to those predicted after 12 hour simulations. In general, the KEQ method predicts higher amount of nitrate appearing in the aerosol phase than does the HDYN method, but it predicts lower amount of nitrate formed on small particles and consequently higher aerosol nitrate formed on the surface of larger particles because of the shift of nitrate aerosols to coarse aerosol particles during the establishment of equilibrium. Moreover, for this specific case, both gas and aerosol concentration of nitrate predicted by the KEQ method under the background of marine aerosols tends to be very close to that predicted by the EQ method for the simulation either after 1 hour or after 12 hour. That is because the KEQ method described in Section 3.2.4 does not actually constrain the amount of mass transported to particles in different size bins in the model.

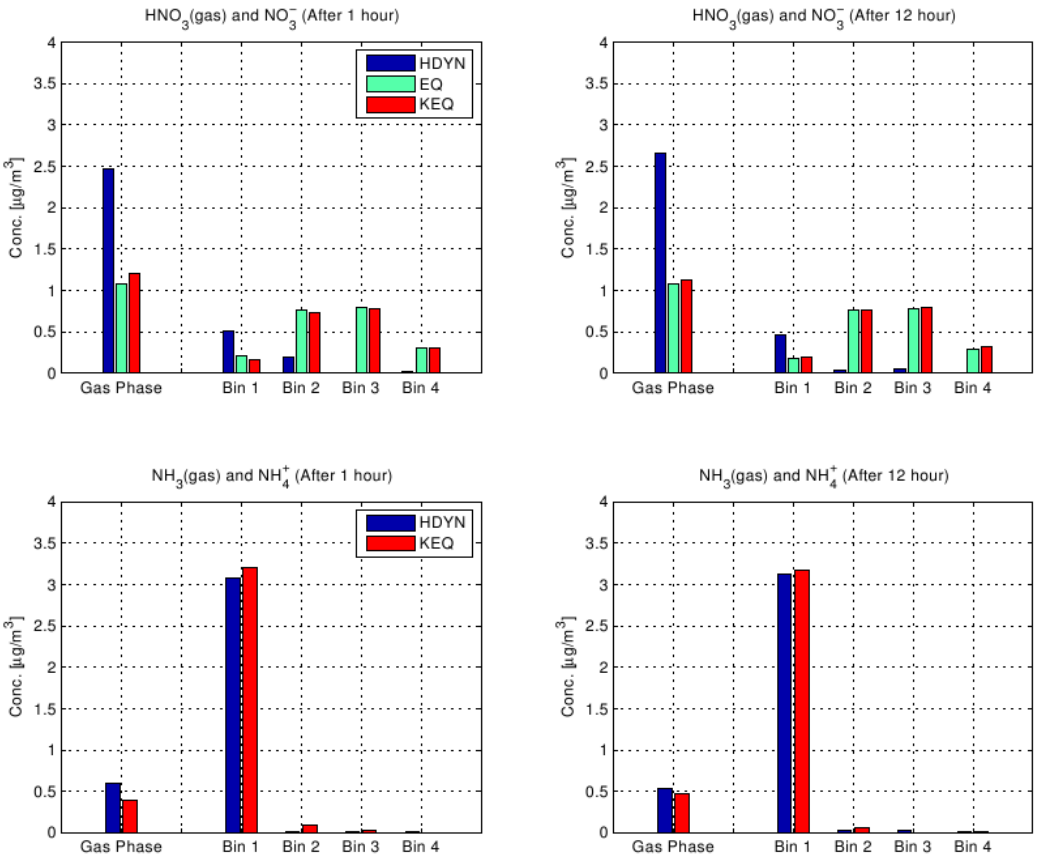

Figure 3.13: As for Figure 3.11, but for the marine case listed in Table 3.4.

3.4 Discussion and conclusions

The simulation of the partitioning of semi-volatile inorganic aerosols (e.g., nitrate and ammonium) between their gas and aerosol phase is one of the most challenging tasks in the global or regional chemical transport model. This chapter presents a box modeling study of the heterogeneous formation of nitrate and ammonium aerosols considering two mixing states assumed either completely internally mixed (IM) or externally mixed (EM) with partially internal mixture for pre-existing aerosol particles using a thermodynamic model EQUISOLV II and the hybrid dynamic method (HDYN) in order to gain some insights for the future implementation in the global chemistry transport model. Two

treatments for mass transfer between gas and aerosol phase (i.e., a simple kinetic-limited equilibrium method versus the hybrid dynamic method) are also compared.

Firstly, the model assuming all pre-existing aerosols are completely internally mixed at each size bin (Feng and Penner, 2007) is compared against one in which the pre-existing aerosols (e.g., pure sulfate, fossil fuel aerosols, biomass burning aerosols, dust and sea salts) are assumed externally mixed with partial internal mixture (e.g. sulfate) for three different aerosol backgrounds: continental, marine as well as comprehensive mixed condition with varying dust and sea salt concentrations. For the continental case in which sulfate and dust are assumed to be the predominant pre-existing aerosols, the difference in two implementations is negligible for the predicted NH_3, NH_4^+ as well as gaseous HNO_3 concentrations. Large difference occurred in the prediction of NO_3^- concentration. The IM treatment favors the condensation of gaseous HNO_3 on larger particles through the diffusion limited mass transfer while the EM treatment predicts higher NO_3^- in the smaller size of aerosols because the additional aerosol surface provided by dust aerosols allows the heterogeneous reaction between HNO_3 and cations (e.g., Ca^{2+}, Na^+, K^+ and Mg^{2+}) tied to dust and forms more metal nitrate salts. This difference also results in the different size distribution predicted by these two mixing states. Similar discrepancy in the prediction of nitrate and ammonium is also found in the marine case. The EM treatment predicts lower gaseous HNO_3 and consequently higher NO_3^- in the size bin 1 than does the IM treatment. This results from the additional aerosol surface provided by sea salt aerosols, allowing the predominant cation (i.e., Na^+) from sea salt preferentially uptake gaseous HNO_3 heterogeneously over NH_4^+. For the mixed case, two sequential orders (i.e., first for sulfate, then dust and sea salt versus first for sulfate, then sea salt and dust)

among three aerosol types have been examined and the maximum 10% relative difference is calculated for wide range of dust (i.e., 0.1~100 μg m^{-3}) and sea salt (0.01~50 μg m^{-3}) concentrations. The alternant order between these two sequential orders with respect to the time interval (e.g., 1 hour) is proposed for the purpose of eliminating this bias in the global model.

The appropriate treatment of nitrate and ammonium, especially on the coarse mode, is important to determine total amount as well as size distribution of nitrate and ammonium present in the aerosol phase. In the second section of this chapter, one simple kinetic limited equilibrium (KEQ) method (Pringle et al., 2010) that is more computationally efficient is examined against the hybrid dynamic (HDYN) method that is theoretically more accurate. The idea behind the KEQ method is to calculate the amount of volatile species kinetically able to condense onto aerosol particles at the first stage and then re-distribution this amount of gas between the gas and aerosol phase using a thermodynamic equilibrium model. As discussed in the Section 3.2.4, the most important aspect of the KEQ method following the treatment of Pringle et al. (2010) is that it does not explicitly constrain the mass fraction of volatile species 'kinetically' able to condense onto aerosol particles for any aerosol with particle radius larger than 0.0036 μm during the first stage of the computation. Therefore, for aerosol particles with a radius range from 0.05 to 10 μm as considered in this study, the KEQ method is actually reduced to the pure equilibrium method.

For the continental case, little difference on the predicted NH_3 and NH_4^+ was found between these two approaches while the KEQ method predicts lower gaseous HNO_3 and higher NO_3^- concentrations after 1 hour simulation. For the marine case, the KEQ

predicts higher amount of nitrate occurring in the aerosol phase than does the HDYN method but it predicts lower nitrate formed on small particles and consequently higher amount of nitrate formed on the surface of particles with larger sizes, which results in the large discrepancy in the representation of aerosol nitrate size distribution between these two methods. There is striking similarities between the KEQ method and the pure equilibrium method for both continental and marine cases. This is confirmed in Figure 3.11 and 3.13 in which the KEQ method predicts similar amount of nitrate in both gas and aerosol phase as the pure equilibrium method. Thus, any future implementation of this simple kinetic-limited equilibrium method into the global model needs to be cautious.

In summary, the combination of the hybrid dynamic (HDYN) method and the treatment assuming all the pre-existing aerosols are externally mixed (EM) with partial internally mixed sulfate is physically and theoretically more accurate to study the formation of nitrate and ammonium aerosols, which is planned to be implemented in the global chemical transport model.

CHAPTER IV

GLOBAL SIMULATIONS OF NITRATE AND AMMONIUM AEROSOLS AND THEIR RADIATIVE EFFECTS

4.1 Introduction

Aerosols, especially of an anthropogenic origin, play an important role in changing the Earth's climate. Substantial progress has been made towards understanding how aerosols, such as sulfate, carbonaceous particles, mineral dust and sea salt, impact on atmospheric chemistry as well as the Earth's climate (Penner et al., 2001; Textor et al., 2006; Forster et al., 2007). However, little has been done to quantify the direct and indirect effects of aerosol nitrate and ammonium in spite of the fact that nitrate and ammonium aerosols have been identified as significant anthropogenic sources of aerosols (Intergovernmental Panel on Climate Change (IPCC), 1994). In fact, ammonium nitrate aerosols are found to play a significant role in contributing total aerosol mass, especially in Europe (van Doland et al., 1997) and in polluted continental areas (Adams et al., 1999). A limited number of global models have been used to predict nitrate and ammonium aerosol concentrations (Adams et al., 1999; Metzger et al., 2002b; Liao et al., 2003; Rodriguez

and Dabdub, 2004; Bauer et al., 2007; Feng and Penner, 2007; Pringle et al., 2010) as well as their global radiative effects (van Doland et al., 1997; Adams et al., 2001; Jacobson, 2001a; Liao et al., 2004; Liao et al., 2005; Bauer et al., 2007). Most global aerosol models included in the AeroCom exercise exclude ammonium and nitrate aerosols when the direct aerosol radiative forcing is evaluated (Schulz et al., 2006; Textor et al., 2006; Kinne et al., 2006). Major nitrate salts (e.g., ammonium nitrate, sodium nitrate) have lower deliquescence relative humidity (DRH) than their corresponding sulfate salts (e.g. ammonium sulfate, sodium sulfate). Nitrate aerosols are highly hygroscopic and can affect aerosol optical properties and further radiative forcing by changing the amount of aerosol water as well as wet refractive indexes. The Fourth Assessment Report (i.e. AR4) from IPCC (Forster et al., 2007) gives the best estimates of the direct radiative forcing for nitrate to be -0.10±0.10 W m^{-2} at the top of atmosphere (TOA) for the first time. Note that the relatively small number of studies is not sufficient to accurately characterize the magnitude and the uncertainties of radiative forcing associated with aerosol nitrate (Forster et al., 2007). Studies (Adams et al., 2001; Liao et al., 2006; Liao and Seinfeld, 2005) using global models have also suggested that the decreased radiative forcing of sulfate aerosols due to their reduced emissions could be partially offset by increases in the radiative forcing of nitrate aerosols. Furthermore, a number of studies (Kulmala et al., 1993, 1998; Goodman et al., 2000) show that the condensation of nitric acid on aerosol particles contributes soluble material to the particle surface and hence enhance water uptake and growth of aerosol particles, leading to increased aerosol activation to cloud. Therefore, the full consideration of aerosol

composition including ammonium and nitrate is essential to proper estimation of both the aerosol direct and indirect forcing.

The formation of nitrate aerosols strongly depends on the availability of its precursor gases and on the ambient conditions. Nitrate aerosols form if sulfate aerosols are irreversibly neutralized and atmospheric ammonia is in excess. Nitrate is predominantly present in the submicron mode at continental sites (Ten Brink et al., 1997; Heintzenberg et al., 1998; Putaud et al., 2003) in the form of ammonium nitrate (NH_4NO_3) which is commonly unstable at typical temperatures and relative humidities in the troposphere. Aerosols in this size-range scatter ultraviolet-visible light most efficiently, which indicates that nitrate could exert a significant radiative forcing regionally. Nitrate aerosols have been found to be at least as important as sulfate in some regions of Europe (ten Brink et al., 1996; Schaap et al., 2004) and some highly industrialized regions (Malm et al., 2004). Nitrate has been observed to be internally mixed with sulfate, ammonium, elemental and organic carbon in the western Europe (Dall'Osto et al., 2009) and in the Amazon basin (Trebs et al., 2005). In nature, aerosol nitrate is not only associated with ammonium in the accumulation mode. Coarse mode aerosol nitrate can be produced by adsorption of nitric acid on sea salt particles (Savoie and Prospero, 1982) and basic soil particles (Wolff, 1984). Lefer and Talbot (2001) found that 86% of nitrate mass was associated with water-soluble super-micron soil-derived Ca^{2+} in an acid environment. Other mental species like Mg^{2+}, Na^{+}, and K^{+} can also be associated with nitrate.

Aerosol nitrate is formed through heterogeneous reactions of nitrogen radicals such as gaseous NO_3, N_2O_5 and HNO_3 dissolved into wet aerosol (Ehhalt and Drummond, 1982; Parrish et al., 1986; Li et al., 1993). Ammonium helps to retain nitrate in the aerosol

phase by neutralizing the aerosol acidity during heterogeneous formation processes (Adams et al., 1999). Liao and Seinfeld (2005) demonstrate that the heterogeneous chemistry reactions on particles increase the radiative forcing due to nitrate and account for 25% of its radiative forcing.

One must consider the partitioning of nitrate and ammonium between their gas and aerosol phases in order to determine the radiative effect of nitrate and ammonium aerosols. In the past two decades, many thermodynamic equilibrium models have been developed for this purpose. Instantaneous thermodynamic equilibrium may be assumed for the fine mode aerosols (particle diameter less than 1 μm) since small particles achieve equilibrium with the gas phase within a few minutes (Wexler and Seinfeld, 1990; Dassios and Pandis, 1999). On the other hand, assuming thermodynamic equilibrium between the gas and aerosol phase is not likely to be valid for coarse particles, such as sea salt and mineral dust because it may take up to a week to reach equilibrium and that is longer than the lifetime of these particles. Meng and Seinfeld (1996) and Seinfeld and Pandis (1998) showed that equilibrium between the gas and aerosol phase is only slowly established at low temperatures and low aerosol concentrations, with a timescale of the order of several hours or even several days. This is longer than the time step typically used in chemical transport models (e.g., about 1 hour). Gas phase concentrations and coarse aerosol particles were observed to be in non-equilibrium in the South Coast Air Quality Study (SQAQS) (John et al., 1989).

Three common approaches have been widely used in current air quality models to treat nitrate and ammonium in aerosols. The first approach is so-called “equilibrium method” (Pilinis et al., 1987; Russell et al., 1988; Binkowski and Shankar, 1995; Lurmann et al.,

1997), which assumes instantaneous chemical equilibrium between the gas and aerosol phase (hereafter referred to as EQ). This method neglects both the time necessary for the mass transfer between the gas and aerosol phase to occur and differences in the chemical driving forces of the specific aerosol size "bins" (Capaldo et al., 2000). The major advantages of this equilibrium method are its speed, simplicity and stability. However, it has been shown that equilibrium cannot be established over the atmospheric relevant timescales of minutes to a few hours under certain conditions (e.g., low temperatures and low aerosol concentrations or coarse particles) as mentioned above (Wexler and Seinfeld, 1990; Meng and Seinfeld, 1996). To address this problem, a more accurate representation of the partitioning of semi-volatile species called the "dynamic method" (hereafter referred to as DYN) has been developed (Meng and Seinfeld, 1996; Meng et al., 1998; Jacobson et al., 1996; Jacobson et al., 1997a, b; Sun and Wexler, 1998a, b; Pilinis et al., 2000). In this approach, a fully dynamic mass transfer calculation is applied to each aerosol size bin. Although the dynamic method is probably most accurate, its use in large-scale air quality models as well as global chemical transport models has been limited due to its high computation cost. To combine the computational efficiency of the equilibrium method with the accuracy of the dynamic method, the hybrid dynamic method (hereafter referred to as HDYN) was proposed by Capaldo et al. (2000). In the hybrid dynamic method, the equilibrium method is employed to determine the composition of aerosol particles with diameters less than a threshold diameter (around 1 μm) while the dynamic method developed by Pilinis et al. (2000) is used to calculate the mass transfer-limited concentrations in larger particles. In the global chemical transport model, the first method (i.e., equilibrium method) has commonly been adopted to predict the concentrations of

nitrate and ammonium aerosols (Adams et al., 1999; Rodriguez and Dabdub, 2004; Myhre et al., 2006; Bauer et al. 2007; Pye et al., 2009) and their radiative effects (Adams et al., 1999; Jacobson, 2001a; Bauer et al., 2007). In addition to the equilibrium method, another three approaches have been used in global chemical transport models. One approach is a first-order removal approximation based on uptake coefficients (hereafter referred to as UPTAKE). This method was adopted by Bauer et al. (2004) to account for the interaction of nitrate with dust aerosols. Liao et al. (2003, 2004) combined this UPTAKE method to treat sulfate and dust aerosols with the EQ method on either sulfate aerosols (Liao et al., 2003) or sulfate and sea salt aerosols (Liao et al., 2004) forming a simple hybrid method (hereafter referred to as HYB). The third approached used in the global model is the more accurate hybrid dynamic method proposed by Feng and Penner (2007, hereafter referred to as FP07) following the methods outline in Capaldo et al. (2000). FP07 presented the differences in the predicted nitrate and ammonium aerosols using methods in the available literatures. They found that the thermodynamic equilibrium assumption underestimates the fine-mode nitrate aerosol burden by 25%. Moreover, they also found that the nitrate and ammonium treatment using the UPTAKE method overestimates both fine and coarse mode nitrate aerosols while the HYB method mainly overestimates the coarse mode nitrate. The UPTAKE and HYB methods are found to predict 106% and 47% higher nitrate aerosol burden than the HDYN method, respectively.

In this study, we updated the FP07 global simulation of nitrate and ammonium aerosols based on the HDYN method but also accounting for the dynamics of sulfate aerosol and its interaction with non-sulfate aerosol components (Herzog et al., 2004; Liu

et al., 2005; Wang et al., 2009). FP07 only simulated aerosol mass concentrations and did not account for the formation of pure sulfate aerosols and sulfate coated on other aerosol types. Since aerosol nitrate is allowed to form when sulfate is fully neutralized and free ammonia exists, an accurate representation of sulfate is key to determining the amount of aerosol nitrate that can form. The treatment of nitrate aerosols in this work follows the hybrid dynamic approach used by FP07 (Capaldo et al., 2000; Feng and Penner, 2007). Nitrate and ammonium aerosols with diameters less than a threshold diameter (i.e., $D < 1.25$ μm) are calculated using a gas-aerosol thermodynamic equilibrium model (Jacobson, 1999) while the gas-to-particle mass transfer to coarse aerosols (i.e., $D > 1.25$ μm) is dynamically determined following the dynamic method (Pilinis et al. (2000) described in Chapter III (3.2.3). In this study, nitrate aerosols are allowed to interact with five types of pre-existing aerosols (i.e., pure sulfate, carbonaceous aerosols from fossil fuel combustion, carbonaceous aerosols from biomass burning, mineral dust and sea salt). These five aerosol types are assumed to be externally mixed while an internal mixture with sulfate coated on each aerosol type is assumed. Here we consider chemical reactions among sulfate, nitrate, ammonium, dust and sea salt for inorganic aerosols and ignore the formation of organic nitrates. The omission of organic nitrates may result in overprediction of NO_x in the source regions and underprediction of HNO_3 in the remote troposphere, since organic nitrates usually form in source regions of NO_x and they are able to transport NO_x to the remote troposphere (Singh et al., 1998, 2000; Schultz et al., 1999). In other words, we only take into account the chemical interaction of gaseous nitric acid and ammonia with sulfate coated on the surface of organic matter and black carbon in this work.

A three-dimensional global aerosol and chemistry transport model used in this study is described in the Section 4.2. Section 4.3 presents the present-day global distribution of predicted sulfate, nitric acid and nitrate, ammonia and ammonium and aerosol water. The zonal averaged mixing ratios of these species are also shown. Section 4.4 analyzes the global budgets of gaseous nitric acid and nitrate as well as ammonia and ammonium. The calculated aerosol optical properties are presented in Section 4.5, which is followed by estimates of direct and indirect radiative forcing of nitrate and ammonium as well as their anthropogenic contribution in Section 4.6. The summary and conclusions are presented in Section 4.7.

4.2 Model description

4.2.1 Global aerosol and chemistry transport model

The version of the IMPACT global aerosol and chemistry model (Rotman et al., 2004; Penner et al., 1998; Liu et al., 2005; Wang et al., 2009), which is able to simulate the microphysics of sulfate aerosol and its interaction with non-sulfate aerosols (Herzog et al., 2004; Liu et al., 2005), was used as the framework in this study. The transport model is driven by assimilated meteorological fields from the NASA Goddard Data Assimilation Office (DAO) general circulation model (GCM) for the year 1997 with a 6-hour time interval in this study. The DAO meteorological fields were interpolated to a 1-hour time interval for tracer advection time step in IMPACT. The spatial resolution of the model is 2 ° latitude by 2.5° longitude in the horizontal with 26 vertical layers ranging from the surface to 2.5 hPa. The model uses the flux form semi-Lagrangian (FFSL) advection scheme (Lin and Rood, 1996) while vertical diffusion is based on an implicit scheme

described in Walton et al. (1988) using vertical diffusion coefficients provided by the DAO meteorological fields.

Table 4.1 Size distribution parameters for non-sulfate aerosols.

Aerosol	N_i[a]	r_i, μm	σ_i
Fossil fuel OM/BC	0.428571	0.005	1.5
	0.571428	0.08	1.7
	1.e-6	2.5	1.65
Biomass OM/BC and natural OM	0.9987	0.0774	1.402
	1.306e-3	0.3360	1.383
	2.830e-3	0.9577	1.425
Sea salt	0.965	0.035	1.92
	0.035	0.41	1.70
Dust	0.854240	0.05	1.65
	0.145687	0.27	2.67
	7.3e-5	4.0	2.40

[a]N_i is normalized fraction by total number concentration in a given size range and is dimensionless.

In the present study, the aerosol model simulated the dynamics of sulfate aerosol (i.e., nucleation, condensation and coagulation) and its interaction with non-sulfate aerosols (i.e., carbonaceous aerosols (organic matter (OM) and black carbon (BC)), dust and sea salt) using a modal representation of sulfate aerosol microphysics with two modes (Herzog et al., 2004; Liu et al., 2005). Sulfate aerosol dynamics is based on the method of modes and moments. Here each mode treats two moments (mass and number) of pure sulfate aerosol, which includes a nucleation/Aitken mode (r < 0.05 μm) and an accumulation mode (r > 0.05 μm). Non-sulfate aerosols are assumed to follow prescribed background size distributions (Table 4.1, Liu et al., 2005; Wang et al., 2009). Carbonaceous aerosols (OM and BC) are represented by a single submicron size bin with

a superposition of three lognormal distributions separately assumed for biomass burning, natural and fossil fuel particles based on their source origins. Sea salt and mineral dust aerosols are represented in four bins with radii varying from 0.05-0.63 μm, 0.63-1.26 μm, 1.26-2.5 μm, and 2.5-10 μm accounting for their mass size distribution, thermodynamics as well as the cloud condensation nuclei activation spectrum under typical super-saturations. The size distribution within each size bin follows a predefined distribution with a superposition of three lognormal distributions for dust and two lognormal distributions for sea salt (Liu et al., 2005).

The concentration of sulfuric acid gas (H_2SO_4(gas)) produced from the gas phase oxidation of DMS and SO_2 is allowed to nucleate to form new sulfate particles in the nucleation mode or to condense onto pre-existing sulfate and non-sulfate aerosol particles. Sulfate aerosol particles are also allowed to coagulate with each other or with other non-sulfate particles. Binary homogeneous nucleation of H_2SO_4 (gas) following Vehkamäki et al. (2002) is used to determine the nucleation of sulfate aerosols since the Vehkamäki et al. (2002) scheme was thought to have the best performance for simulating the aerosol number concentration in the upper troposphere (Liu et al., 2005). In addition, 2% of anthropogenic sulfur emissions are assumed to be primary emitted aerosols with a specified size distribution to mimic the effects of sub-grid scale processes leading to aerosol nucleation. The hydrophilic and hydrophobic properties and corresponding scavenging efficiency of non-sulfate aerosols are determined by the amount of sulfate coating that is produced through coagulation and condensation. Condensation growth is kinetically limited by the diffusion of sulfuric acid gas to the particle surface. Coagulation is allowed to occur between particles of the same mode (termed as

intramodal coagulation) and between particles of different modes (termed as intermodal coagulation). The aqueous production of sulfate is equally distributed among the hygroscopic aerosol particles that are larger than 0.05 μm in radius.

Dry deposition rates for gaseous species are calculated based on the work of Jacob and Wofsy (1990), Wesely (1989) and Walcek et al. (1996), using a module developed at Harvard University. Dry deposition of aerosol particles uses a resistance-in-series parameterization following Zhang et al. (2001). Gravitational settling is also taken into account for aerosol species. Wet deposition is calculated by using the wet scavenging model described in Mari et al. (2001) and Liu et al. (2001). Two types of scavenging are included: 1) scavenging in wet convective updrafts, and 2) first-order rainout and washout in precipitating columns. For scavenging that occurs in convective updrafts, the fraction of tracer scavenged depends on the rate constant for conversion of cloud condensate to precipitation including both liquid and ice (assumed to be 0.005 s^{-1}) as well as the fraction of tracer present in the condensate f_i (i.e., the scavenging efficiency). The fraction of highly soluble gaseous species such as HNO_3(g) and H_2SO_4(g) in the cloud condensate phase is assumed to be 100% while scavenging efficiencies of less soluble gaseous species are calculated based on their Henry's law coefficients. Scavenging efficiencies of aerosol species are either prescribed to be constant for pure sulfate aerosol and sea salt with $f_i = 1$ or calculated for BC/OM and mineral dust particles dependent on the amount of sulfate, ammonium and nitrate associated with them ($0 < f_i < 1$).

In the present model to account for the interaction between nitrate and other pre-existing aerosols with different types, we have set the scavenging efficiencies as follows.

As described in Liu et al. (2005), wet scavenging efficiencies for the accumulation mode sulfate and sea salt are assumed to be 1.0 while the nuclei mode sulfate aerosols are only allowed to be scavenged by its Brownian coagulation with cloud droplets. The scavenging efficiency is calculated from the Brownian coagulation coefficient (Seinfeld and Pandis, 1998), and an estimated cloud droplet number together with assumed cloud life time of 4 hours. The estimated cloud droplet number is calculated from the sum of accumulation mode pure-sulfate aerosols and the non-sulfate aerosols accounting for the hygroscopicity which depends on the surface sulfate, ammonium and nitrate coatings. For example, as a result of aging within the atmosphere, BC, OM and mineral dust particles may change from hydrophobic (with $f_i = 0$ when they are freshly emitted) to hydrophilic (with $f_i = 1$ when they are effectively coated with soluble sulfate, ammonium and nitrates). Here we calculate the fraction area coverage of a single non-sulfate-ammonium-nitrate particle surface by internally mixed sulfate, ammonium and nitrate molecules (e.g., for carbonaceous aerosols) as

$$f_{BC+OM}^{so4+no3+nh4} = \frac{r_{avg}^2 N_{avg}}{4(r_{BC+OM} + r_{avg})^2}, \qquad (4.1)$$

where r_{BC+OM} is the mass-weighted average radius for carbonaceous particles; r_{avg} is the average radius of internally mixed sulfate, ammonium and nitrate molecules; and N_{avg} is the total number of molecules of internally mixed sulfate, ammonium and nitrate on the particle surface. We assume here that when $f_{BC+OM}^{so4+no3+nh4} = 10$ (layers), the particle becomes hygroscopic. This ten-layer coating criterion for hygroscopicity is in accordance with laboratory measurements for soot particles by Wyslouzil et al. (1994) and Lammel and Novakov (1995). Since we are not aware of surface coating experiments for mineral

dust, we used this ten-layer coating treatment for mineral dust particles as well. The scavenging efficiency is linearly interpolated between 0 and 1.0 for $0 < f_{BC+OM}^{so4+no3+nh4} < 10$ and for $0 < f_{dust}^{so4+no3+nh4} < 10$.

4.2.2 Nitrogen chemistry

The simple nitrogen chemistry treatment developed by Feng and Penner (2007) is adopted in the current work. This treatment calculates the gas phase precursors of nitrate (i.e., HNO_3 and N_2O_5) online and allows five gaseous tracers (i.e., NO, NO_2, NO_3, N_2O_5 and HNO_3) to be transported. The scheme treats nitrogen chemistry in the troposphere and stratosphere differently.

In the troposphere, day and night schemes are considered separately. In the daytime, the conversion of NO_x ($NO+NO_2$) to HNO_3 is simulated by the reaction of hydroxyl radical (OH) with NO_2, following Kraus et al. (1996),

$$NO_2 + OH + M \rightarrow HNO_3 + M \,, \tag{4.2}$$

where M is the N_2 and O_2 molecules in the atmosphere. HNO_3 is converted back to NO_x through the reaction with OH and its photolysis,

$$HNO_3 + OH \rightarrow NO_2 + OH \,, \tag{4.3}$$

$$HNO_3 + h\nu \rightarrow NO_3 + H_2O \,, \tag{4.4}$$

The nitrate radical, NO_3, from the reaction (4.4) is assumed to instantaneously photolyze to NO_2. Note that the nitrate radical (NO_3) is an important constituent in tropospheric chemistry, especially at night with mixing ratios ranging up to 300 parts per trillion (ppt) in the boundary layer (Seinfeld and Pandis, 1998). At night, the production of HNO_3 is mainly through the conversion of NO_x by following reactions,

$$NO_2 + O_3 \rightarrow NO_3 + O_2, \quad (4.5)$$

$$NO_2 + NO_3 \overset{M}{\leftrightarrow} N_2O_5, \quad (4.6)$$

$$N_2O_5 + H_2O(s) \rightarrow 2HNO_3. \quad (4.7)$$

The heterogeneous hydrolysis of N_2O_5 (i.e., reaction 4.7) mainly occurs over the surface of aerosol particles or water droplets at night since one of the precursors of N_2O_5 (i.e., NO_3) is rapidly photolyzed to NO_2 in the daytime. This reaction provides an alternative pathway to produce HNO_3 gas.

In the stratosphere, the scheme is much simpler than that in the troposphere. Basically, NO_x is converted to HNO_3 everywhere above the tropopause with a constant e-folding time of 13 days at night and HNO_3 is converted back to NO_2 through its photolysis in the daytime (Feng and Penner, 2007). Note that the major role of this scheme is to provide an appropriate input of NO_x and HNO_3 at the tropopause with the proper partitioning between NO_x and NO_y (NO_x+HNO_3) from the stratosphere.

The three dimensional concentration fields of OH and O_3 used in the reactions (4.2) and (4.5) are fixed as monthly averages, taken from a 1-year simulation of the chemical transport model GRANTOUR using the climate model CCM1 meteorological fields (Penner et al., 1994). The diurnal cycle of OH and HO_2 is approximated by scaling monthly average fields with the cosine of the solar zenith angle.

4.2.3 Treatment of nitrate and ammonium

The heterogeneous uptake of nitrate and ammonium by aerosol mixtures is simulated in the University of Michigan version of the IMPACT model using a hybrid dynamic approach (HDYN) (Feng and Penner (2007). This approach follows that developed by

Capaldo et al. (2000) who applied it to an air quality model. The EQUISOLV II thermodynamic equilibrium model (Jacobson et al., 1999) is applied for aerosol diameters less than 1.25 μm (i.e., bin 1, hereafter referred to as the fine mode) while a dynamic method that solves mass transfer equations for particles with aerosol diameters larger than 1.25 μm (i.e., other 3 size bins, hereafter referred to as the coarse mode) is applied. This is because particles with diameters less than 1 μm are generally able to reach equilibrium within a few minutes under typical atmospheric conditions (Wexler and Seinfeld, 1990; Dassios and Pandis, 1999) while aerosol particles with larger sizes reach equilibrium with a timescale of the order of several hours or up to several days (Meng and Seinfeld, 1996; Seinfeld and Pandis, 1998). The equilibrium assumption is well justified for fine mode aerosols in our global aerosol transport model since a transport time step of one hour is used. An operator-splitting method is used to simulate the heterogeneous interaction of nitrate and ammonium with other pre-existing aerosols during the model time step.

Table 4.2: Constitute composition simulated for each aerosol type.

Constitute composition	Size bin(s) applied
Pure sulfate with NO_3^-, NH_4^+ and H_2O(aq)	Bin 1 (D<1.25 μm)
FF OM/BC coated with SO_4^{2-}, NO_3^-, NH_4^+ and H_2O(aq)	Bin 1 (D<1.25 μm)
BB OM/BC coated with SO_4^{2-}, NO_3^-, NH_4^+ and H_2O(aq)	Bin 1 (D<1.25 μm)
Dust coated with SO_4^{2-}, NO_3^-, NH_4^+ and H_2O(aq)	Bin 1, 2, 3, 4
Sea salt coated with SO_4^{2-}, NO_3^-, NH_4^+ and H_2O(aq)	Bin 1, 2, 3, 4

The concentrations of nitrate and ammonium in the coarse model are determined by solving mass transfer equations given in Eqn. (3.9)-(3.12) in Chapter III. Note the

accommodation coefficients of 0.193, 0.092 and 0.1 are used for HNO_3, NH_3 and N_2O_5 on aerosols in this study (Feng and Penner, 2007).

Although aerosol particles are often found as partially or completely internally mixed with multiple components including sulfate, sea salt, nitrate and dust components (Zhang et al., 2003), particles near their sources are generally externally mixed. If all components are considered internally mixed in a model as they are at the emission source, such a representation can distort the predicted chemical compositions (Kleeman et al., 1997). Also, the radiative effects of externally and internally mixed particles may differ. In this study, in order to be consistent with the aerosol treatment of other processes in the global model, nitric acid and ammonia are allowed to interact with the other pre-existing particles, i.e., pure sulfate, sulfate-coated carbonaceous particles, sea salt and dust. Hence, the 11 aerosol populations listed in Table 4.2 are considered. Internally mixed multiple aerosol components are assumed within each population while externally mixed aerosol components are assumed among populations. Following the hybrid dynamical method used by Feng and Penner (2007), a thermodynamic equilibrium model (Jacobson, 1999) is applied for five types of aerosols consecutively (i.e., pure sulfate, carbonaceous aerosols from fossil fuel, carbonaceous aerosols from biomass burning, dust and sea salt) in the size bin 1 while gas and aerosol concentrations are determined by solving the mass transfer equations for particles (e.g. dust and sea salt) in the other 3 size bins ($D>1.25$ μm). Nitric acid is allowed to react with ammonia and other aerosol particles after sulfate is neutralized by ammonia. This is in accordance with the treatment in the study (Myhre et al., 2006) who modeled the interaction of nitrate, ammonium, sulfate and sea salt. The thermodynamic model is applied to pure sulfate, carbonaceous aerosol from fossil fuel

and biomass burning first and then to dust and sea salt. As shown in the last chapter, the reaction order that we used to apply the thermodynamic model to dust and sea salt may differ less than 10% for high concentrations of both dust and sea salt. In order to eliminate the difference induced by this assumed sequence of reactions with dust and sea salt populations, we choose to solve the equilibrium model as well as mass transfer equations by switching the order of reactions (i.e., by solving the reactions with dust first at odd time steps and with sea salt first at even time steps) in this work.

4.2.4 Emission Scenarios

To calculate the anthropogenic forcing by nitrate and ammonium aerosols, simulations for preindustrial (PI, roughly corresponding to the year 1850) and present-day (PD, for the year 2000) emissions were carried out. Table 4.3 summarizes the emissions for PD and PI conditions.

Ammonia emissions for the present-day were taken from the global inventory of Bouwman et al. (1997). The total ammonia source specified in this inventory is estimated to be 53.6 Tg N per year and Table 4.3 lists the contributions of each source type to the total emission. Among nine sources, domestic animals contribute the largest fraction, 34%, followed by synthetic fertilizers, oceans, biomass burning, soils under natural vegetation, wild animals and other sources. The total emissions estimate from the inventory used in our work is higher than that used in the study of Dentener and Crutzen (1994) with was 45 Tg N per year, lower than that estimated by Schlesinger and Hartley (1992) (75 Tg N per year) and almost the same as the 54 Tg N per year estimated by Warneck (1988). Although some sources, for instance, those from crops, fertilizers and animal waste should vary seasonally depending on the crop production cycle and

temperature, their monthly variations are not available in the current ammonia inventory. Therefore, in the absence of more detailed information, only the annual average emission fluxes from all sources were used. The ammonia emissions for the pre-industrial conditions include the emission sources from oceans, soils under vegetation and wild animals. We assume that all other sources have anthropogenic origins and were near zero in the year 1850. The total ammonia emission in PI condition is estimated to be 10.7 Tg N per year.

The estimated PD global annual NO_x emission follows the study of Rotman et al. (2004) with the 21.5 Tg N per year from industrial activities and fossil fuel combustion out of the total emission 38.9 Tg N per year, followed by biomass burning, soil processes, lightning and aircraft emissions. The total NO_x emission for the PI condition, the representative of 1890 emission, is estimated to be 11.7 Tg N per year in which biomass burning and lightning contribute most. Regarding to each individual source, the emissions from industrial activities, fossil fuel combustion as well as soil process are taken from the study of van Aardenne et al. (2001) while that from biomass burning and lightning are based on the work (Ito et al., 2007; Ito et al., 2008).

The IMPACT model uses the anthropogenic sulfur emission from the draft IPCC-specified 2000 scenario (Nakicenovic et al., 2000) including emission of SO_2 and SO_4^{2-} from fossil fuel combustion and industrial activities, SO_2 emission from biomass burning and aircraft. We assume that 2% of fossil fuel sulfur emissions occur as primary sulfate aerosol to account for fast conversion of SO_2 to SO_4^{2-} in combustion plumes (Liu et al., 2005). In addition, 85% of the sulfate mass is assumed to be emitted in the accumulation mode with a geometric mean radius of 0.07 μm and standard deviation of 2.0 while 15%

of the mass is distributed in the nucleation/Aitken mode with a geometric mean radius of 0.01 μm and standard deviation of 1.6, in accordance with measurements by Whitby et al. (1978) and Cantrell and Whitby (1978). The total SO_2 emission that is of anthropogenic origin is estimated to be 68.9 Tg S per year. Volcanic SO_2 emissions with a total 4.8 Tg S yr^{-1} are taken from the work by Andres and Kasgnoc (1998), which includes sporadic and continuously emitting volcanoes averaged over a 25-year time period. Marine DMS fluxes with a total of 26.1 Tg S yr^{-1} were estimated using the average of the low and high values from Kettle and Andreae (2000). The total emission of SO_2 in the PI scenario is estimated to be 40.9 Tg S per year, less than half that in the PD scenario.

Natural OM fluxes with a total of 14.5 Tg yr^{-1} for both PD and PI conditions were derived assuming that 9% of the terpene emissions from Guenther et al. (1995) are rapidly converted to OM (Penner et al., 2001). Emissions of fossil fuel and biofuel carbonaceous aerosol were taken from the inventories developed from the inventories of Penner et al. (1993) and Liousse et al. (1996) for a calendar year representative of the mid-1980s. Fossil fuel and biofuel carbonaceous aerosol are assumed to be emitted into the surface layer. The open biomass burning sources for the year 2000 are taken from the study of Zhang et al. (2005), who used an inverse model to adjust their a priori emissions to determine a best fit to the aerosol index (AI) measured by the EP TOMS satellite. The open biomass burning aerosols are emitted uniformly into the boundary layer. The total fossil fuel and biomass burning emission for carbonaceous aerosols are 37.3 Tg yr^{-1} (30.6 Tg OM and 6.7 Tg BC) and 68.4 Tg yr^{-1} (62.0 Tg OM and 6.4 Tg BC), respectively. In contrast, the total fossil fuel and biomass burning emissions for carbonaceous aerosols in the PI scenario are estimated to be 5.9 Tg yr^{-1} (5.1 Tg OM and 0.8 Tg BC) and 19.5 Tg

yr^{-1} (17.8 Tg OM and 1.7 Tg BC), which is nearly one third of total OM and one fifth of BC from the present-day.

Sea salt emissions in the model are provided according to Gong et al. (1997) offline. An interpolation following the algorithm of Monahan et al. (1986) was made in order to distribute the total mass flux into 4 size bins (0.05-0.63 μm, 0.63-1.26 μm, 1.26-2.5 μm, and 2.5-10 μm). The total sea salt emissions used in this study are 3768 Tg yr^{-1}. Sea salt particles are injected into the lowest model layers. The dust emission fluxes at each 6 hour intervals were provided by Ginoux et al. (2001) which is based on the 10 meter wind speed and soil wetness. The dust emissions fluxes are represented by the same 4 size bins as the sea salt aerosols and are described in detail in Liu et al. (2005). Similar to biomass burning aerosols, mineral dust emissions are uniformly injected in the boundary layer.

Table 4.3: Global annual emission for preindustrial and present-day scenarios.

Species	Scenario	
	Preindustrial	Present-Day
NH_3, Tg N yr^{-1}		
Domesticated animals	-	21.6
Synthetic fertilizers	-	9.0
Oceans	8.2	8.2
Biomass burning	-	5.9
Crops	-	3.6
Humans	-	2.6
Soils under natural vegetation	2.4	2.4
Wild animals	0.1	0.1
Others	-	0.3
Total[a]	10.7	53.6
NO_x, Tg N yr^{-1}		
Industrial activities/Fossil fuel	1.0[c]	21.5
Biomass burning	4.8[d]	6.4
Soil processes	2.9[c]	5.5
Lightning	3.0[e]	5.0
Aircraft	-	0.5
Total	11.7	38.9[b]
SO_2, Tg S yr^{-1}		
Anthropogenic emission	1.5	68.9
Volcanic emission	4.8	4.8
Biomass burning	-	-
DMS oxidation	34.6	34.6
Total	40.9	108.3
DMS, Tg S yr^{-1}		
Oceanic source	26.1	26.1
OM, Tg yr^{-1}		
Fossil fuel emission	5.1	30.6
Biomass burning emission	17.8	62.0
Photochemistry from terpenes	14.5	14.5
Total	37.4	107.1
BC, Tg yr^{-1}		
Fossil fuel emission	0.8	6.7
Biomass burning emission	1.7	6.4
Total	2.5	13.1

[a]Bouwman et al., 1997
[b]From Rotman et al., 2004
[c]From van Aardenne et al., 2001
[d]From Ito et al., 2007
[e]From Ito et al., 2008

4.3 Present-day global Aerosol Concentration Fields

4.3.1 Sulfate

Global results for the sulfur model used in this work have been already presented and compared with observations in Liu et al. (2005). Therefore the simulated sulfate results presented here are only presented in order to understand the behavior of the other aerosol components. Figure 4.1 gives the predicted averaged mixing ratios (pptv) of pure sulfate and coated sulfate in the surface (i.e., the first model level) for the PD scenario based on the average of the simulation results for January and July. The highest pure sulfate concentrations are mainly located in the industrialized areas of Europe, North America, and eastern Asia where they typically exceed 1 ppbv (1 $\mu g\ m^{-3}\ SO_4^{2-}$ = 258 pptv SO_4^{2-} at 298 K and 1000 mb). The coated sulfates are highest near source regions of the corresponding pre-existing aerosols. For example, the sulfate coated on fossil fuel/biofuel OM/BC aerosols generally exceeds 300 pptv in eastern Asia and Europe while that coated on open biomass burning aerosols is highest in South Asia, South Africa and the southern United States with the maximum value ranging from 100 pptv to 300 pptv. The highest sulfate mixing ratio on the surface of dust aerosols ranges from 30 to 300 pptv, occurring over the Sahara desert. The sulfate mixing ratios on sea salt are comparably lower than the three other coated aerosol types, less than 100 pptv. The total sulfate mixing ratio is highest, exceeding 1 ppbv, over east and south Asia, Europe and the North America. The sulfate mixing ratio in remote continental areas ranges from 100 pptv to 1 ppbv while that in marine areas generally ranges from 30 pptv to 300 pptv. The lowest sulfate mixing ratios, less than 100 pptv, occur over Greenland as well as over Antarctica and the remote oceans in the southern tropics.

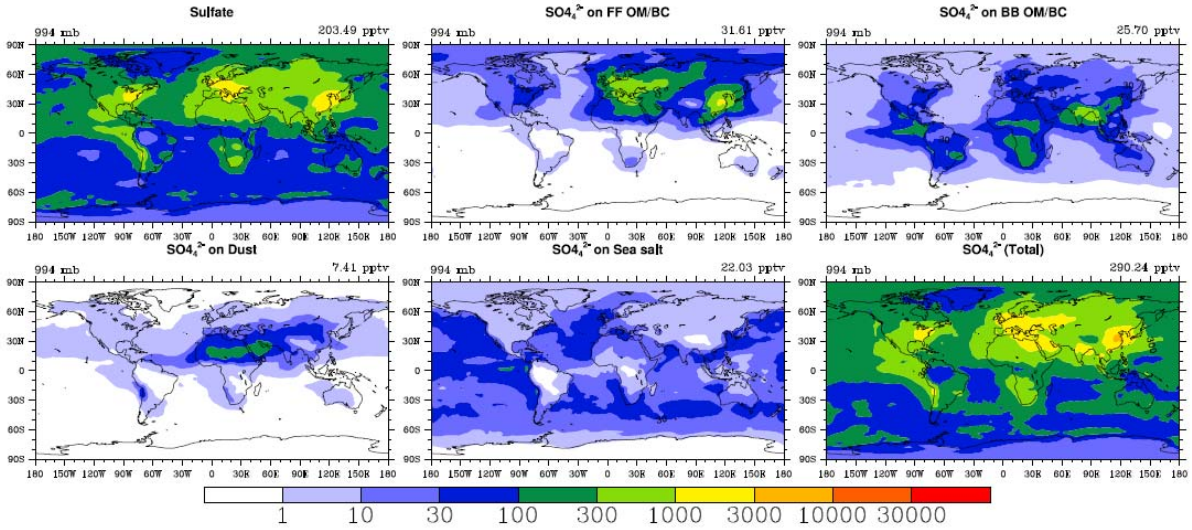

Figure 4.1: Predicted mixing ratios (pptv) of pure sulfate and coated sulfate in the surface layer averaged for January and July. The pressure level of the surface layer together with the average mixing ratio for that layer is indicated above each panel.

4.3.2 Nitric acid and nitrate

The predicted gas-phase HNO_3 in the surface for the average of January and July is given in Figure 4.2 (left panel). During daytime, nitric acid is produced by the reaction of NO_2 with OH while the alternative production pathway through the hydrolysis of N_2O_5 on aerosol surfaces is predominant at night. Gas-phase HNO_3 is removed by its photolysis, the reaction with OH, the conversion to aerosol nitrate, as well as wet and dry deposition. In general, the HNO_3 mixing ratios in the Northern Hemisphere are higher in January than in July because the loss of HNO_3 by the photolysis and its reaction with OH is comparably smaller in winter (not shown here) due to weaker sunlight. The winter-summer contrast also applies to its accompanying aerosol component, aerosol nitrate. The predicted HNO_3 mixing ratios, generally exceeding 1 ppb, are highest in the

industrialized areas of Europe, central and eastern Asia, North America as well as over the open biomass burning regions in the tropics.

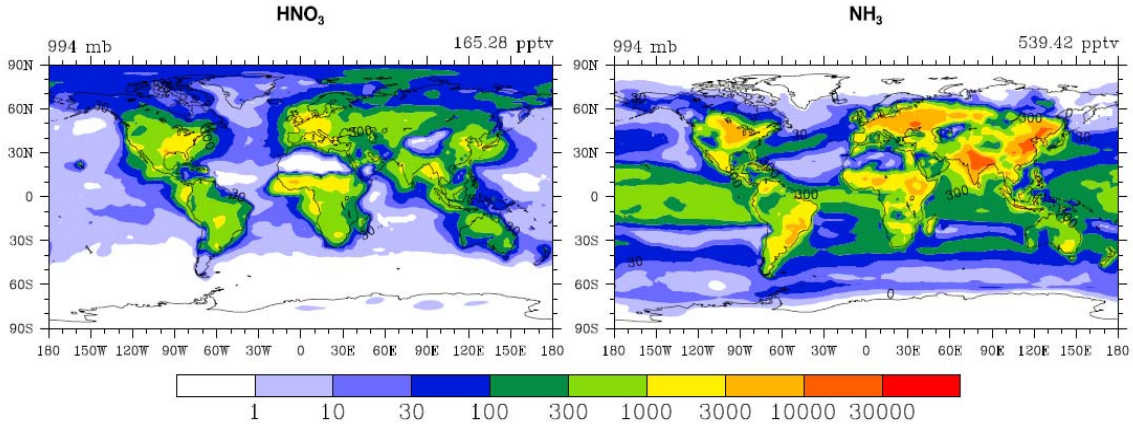

Figure 4.2: Predicted mixing ratios (pptv) of gaseous HNO_3 (left) and NH_3 (right) in the surface layer averaged for January and July. The pressure level of the surface layer together with the average mixing ratio for that layer is indicated above each panel.

The predicted mixing ratios (pptv) of nitrate aerosols formed on five types of pre-existing aerosols and total nitrate aerosols in the surface based on the average of January and July are shown in Figure 4.3. Note that 1 μg m^{-3} NO_3^- = 400 pptv NO_3 at 298 K and 1000 mb. The nitrate mixing ratios condensed on pure sulfate generally exceed 1 ppbv over eastern United States, Europe, India, and eastern Asia. The reaction of nitrate with fossil fuel/biofuel OM/BC maximizes in eastern Asia with an average value of about 100 pptv to 300 pptv while that associated with biomass burning aerosols is highest over the three source regions of biomass burning (i.e., South Asia, South Africa, and South America). The location of the peak in the aerosol nitrate predicted on dust and sea salt aerosols occurs over the Sahara desert for dust and over coastal regions close to the continents for sea salt. Note that the comparably lower mixing ratio of aerosol nitrate near the coast of Australia than those coast regions in the Northern Hemisphere

corresponds to lower sources of HNO_3 and severely limited gas-phase NH_3 (see Figure 4.9). Generally speaking, the locations of the peaks in the aerosol nitrate mixing ratio are consistent with those from previous studies (Feng and Penner, 2007; Liao et al., 2003; Adams et al., 1999, hereafter referred as A99). In these regions, nitrate aerosols occur mainly in the form of neutralized ammonium nitrate, in the amount determined by thermodynamic equilibrium. Since ammonia preferentially reacts with sulfate, the presence of sulfate aerosols reduces nitrate formation. Most continental areas in the Northern Hemisphere have nitrate mixing ratio exceeding 300 pptv. In the Southern Hemisphere, a value as this large only occurs in highly localized areas such as part of South America, South Africa and Australia. Marine mixing ratios of nitrate aerosols are generally in the range of 1-100 pptv except in coastal regions.

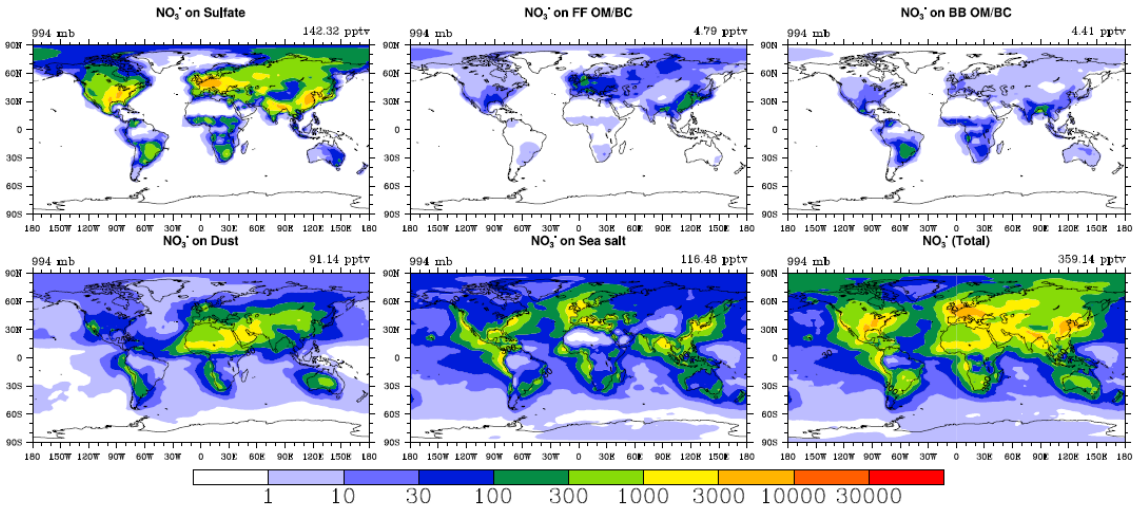

Figure 4.3: Predicted mixing ratios (pptv) of nitrate associated with each aerosol type and for total nitrate in aerosols (bottom right) in the surface layer averaged for January and July. The pressure level of the surface layer together with the average mixing ratio for that layer is indicated above each panel.

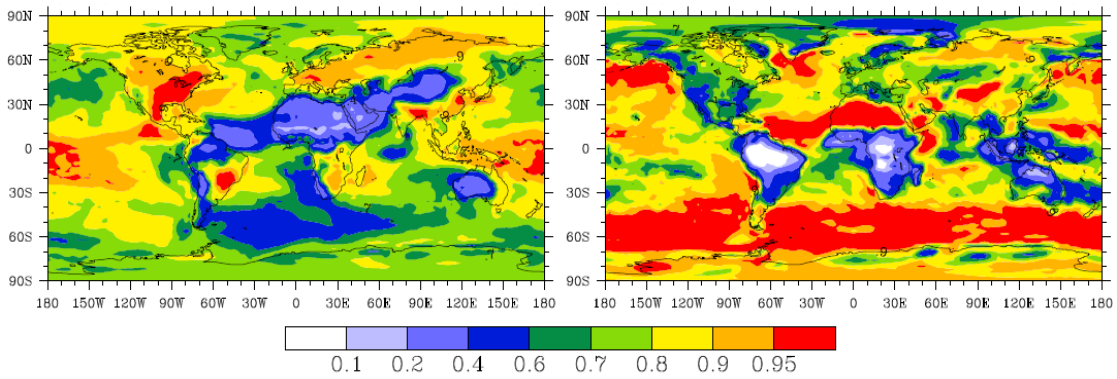

Figure 4.4: Fraction of the fine mode nitrate to total aerosol nitrate (left): [NO_3^- (D < 1.25 μm)]/[NO_3^- (D < 1.25 μm) + NO_3^- (D > 1.25 μm)] and fraction of total nitrate (gas HNO_3 + aerosol NO_3^-) predicted to occur as aerosol NO_3^- (right) in the surface layer (i.e., 994 mb) averaged for January and July.

Figure 4.4 (left panel) shows the fraction of nitrate in fine-mode aerosols at the surface averaged for January and July. The regions with a high fraction of fine-mode nitrate are consistent with those that have peak in the total aerosol nitrate (e.g., the eastern United States, Europe and the eastern Asia) while less than 10% of the nitrate aerosol is associated with fine particles in regions close to deserts (e.g., the Sahara, Asian and Australian deserts). The fine-mode fraction of nitrate is also dominant in the tropical Pacific due to high free ammonia available over that region. Figure 4.5 (bottom) shows the gas ratio defined by Ansari and Pandis (1998) near the surface for the average for January and July. The gas ratio is defined as the free ammonia $\left([NH_3]+[NH_4^+]-2\times[SO_4^{2-}]\right)$ divided by the total nitrate $\left([HNO_3]+[NO_3^-]\right)$ expressed in molar concentration units. The gas ratio is useful for indicating which reactant, ammonia or nitric acid, limits the formation of ammonium nitrate. If the gas ratio is greater than 1, it indicates that nitric acid is limiting. A gas ratio with the value between 0 and 1 indicates that ammonia is limiting even though some ammonia is available for reaction with nitric

acid. If the gas ratio is less than 0, it indicates that that ammonia is significantly limited. For the last case, no free ammonia is available at all and therefore the formation of ammonium nitrate is impossible because all ammonia will preferentially react with sulfate. On an annual average basis, free ammonia exists in most populated areas of the globe. The high gas ratio is also found in Brazil, Patagonia, India as well as the southern Atlantic and Indian oceans. The high gas ratio over oceans is expected in accordance with the ocean sources of ammonia and the absence of HNO_3 sources. The concentration of ammonium nitrate is expected to increase significantly if there is an increase in HNO_3 concentrations over these regions. On the other hand, ammonia is limited in remote continental and marine areas. Note that the gas ratio decreases with altitude because the concentration of ammonia decreases with altitude more rapidly than that of sulfate shown in Figure 4.6. The abundance of ammonia is also shown in Figure 4.5 (top panel). The molar ratio of total ammonium to total sulfate is generally larger than 2 over continents and less than 2 over oceans, indicating that excessive ammonia over continents could react with nitrate and ammonia is limiting in most ocean areas. Figure 4.4 (right panel) shows the fraction of total nitrate (gas-phase HNO_3 + aerosol NO_3^-) predicted to occur as nitrate aerosol (NO_3^-) in the surface averaged for January and July. A high percentage of aerosol nitrate to total nitrate occurs in regions where aerosol nitrate formed on mineral dust and sea salt. In regions with high concentrations of dust or sea salt aerosol, more than 90% of the total nitrate is present in the aerosol phase. The percentage of aerosol nitrate approaches to 100% over southern oceans, North Pacific, Asian deserts, the Sahara desert as well as its extended region over the North Atlantic, where the formation of nitrate is mainly limited by the availability of gas-phase HNO_3.

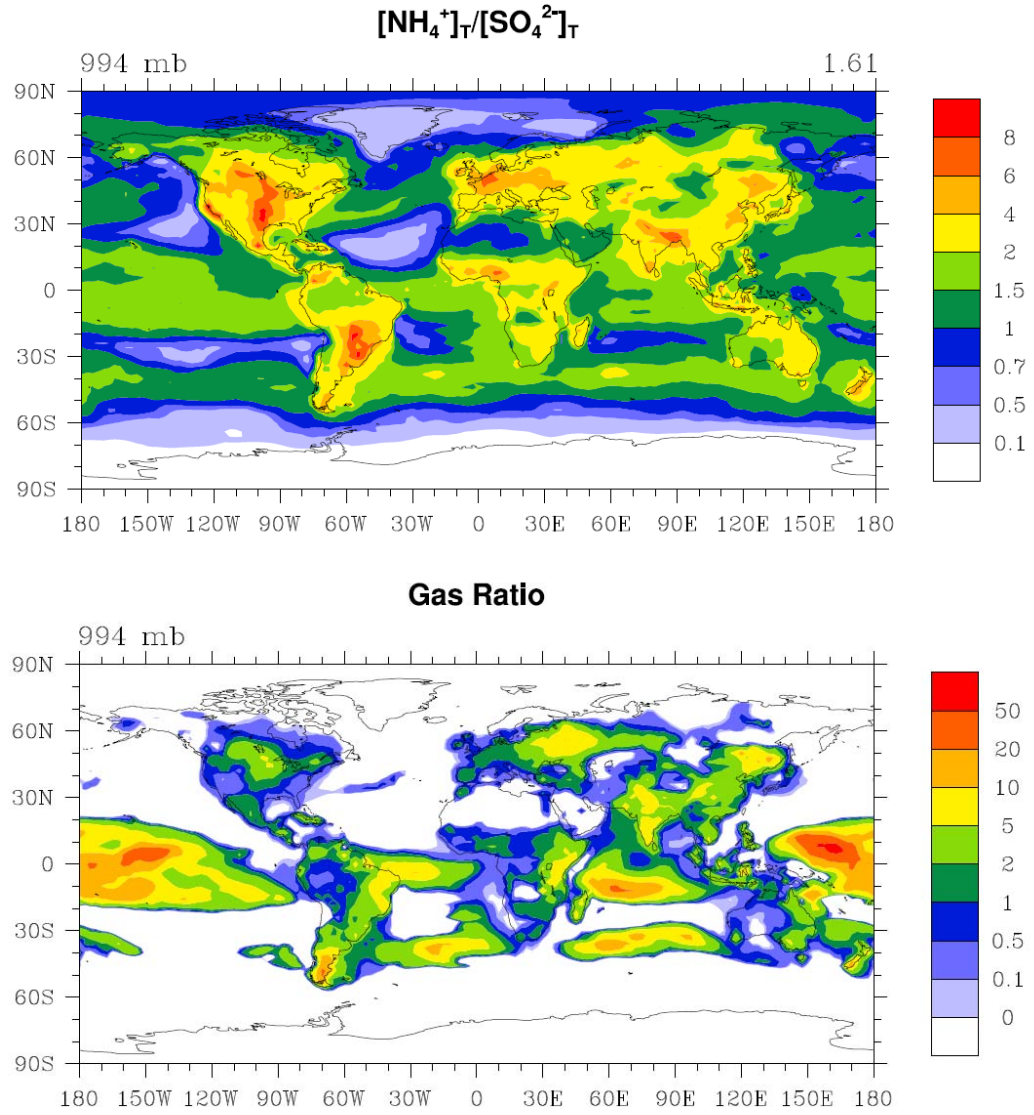

Figure 4.5: Molar ratio of total ammonium to total sulfate (top) and gas ratio (bottom) in the the surface layer averaged for January and July. See text for the definition of the gas ratio.

4.3.3 Ammonia and ammonium

The average mixing ratio of gas phase ammonia for January and July at the surface are shown in Figure 4.2. The highest surface mixing ratios, in excess of 3 ppbv with some peaks more than 10 ppbv (1μg m^{-3} = 1457 pptv NH_3 at 298K and 1000 mb), are found in

China, India, Europe, eastern United States, Brazil and South Africa. Continental mixing ratios exceed 300 pptv everywhere except the Arctic, Sahara, and southwestern Australia. Marine mixing ratios of gas phase ammonia are highest near the equator and over the Southern ocean as a result of high ammonia emissions in that part of the ocean; otherwise, they are less than 100 pptv. Ammonia mixing ratios are negligibly small (less than 1 pptv) over most of Antarctica. Ammonia surface mixing ratios are mainly determined by both the emission of ammonia and its uptake by sulfate and nitrate.

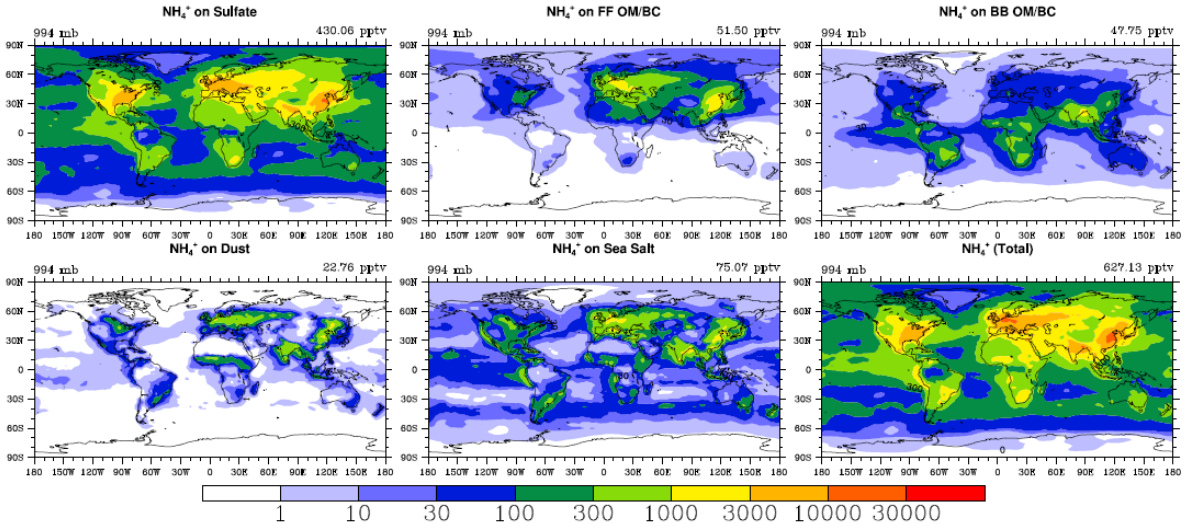

Figure 4.6: Predicted mixing ratios (pptv) of ammonium associated with each aerosol type and for the total ammonium aerosols (bottom right) in the surface layer averaged for January and July. The pressure level of the surface layer together with the average mixing ratio for that layer is indicated at each panel.

The average mixing ratios of ammonium aerosols on each type of aerosols and total aerosols at surface are shown in Figure 4.6 averaged for January and July. In general, ammonium is preferentially associated with sulfate and therefore the peaks in the ammonium mixing ratios are closely tied with those of sulfate. As expected, ammonium on pure sulfate is largest among all aerosol types. The highest total ammonium mixing

ratios exceed 3 ppbv and are found in industrialized regions, such as eastern Asia, Europe and the eastern United States (1 μg m^{-3} = 1377 pptv NH_4^+ at 298K and 1000 mb). Continental mixing ratios exceed 300 pptv almost everywhere while marine mixing ratios of ammonium are in the range of 100-300 pptv except for remote oceans. Generally speaking, the alkaline compounds (i.e., Ca^{2+}, Na^+, K^+, Mg^{2+}) in dust and the cation Na^+ tied to sea salt make it difficult for ammonia to partition into dust and sea salt particles. The anion (e.g., Cl^-) in sea salt may be associated with ammonium when both sulfate and nitrate are poor. A very small amount of aerosol ammonium is formed in the regions with abundant dust and sea salt. However, if there are high mixing ratios of free gas phase ammonia (i.e., with a gas ratio larger than 1) (e.g., the polluted regions of eastern Asia, Europe, North America) and biomass burning regions in South America and central Africa, aqueous ammonium (i.e., NH_3(aq)) can form on these large particles. The ammonium concentration predicted here are similar to that of Adams et al. (1999) and Feng and Penner (2007), including locations and magnitudes of the peak ammonium levels in China, Europe, North America, South Africa and the pattern of oceanic ammonium concentrations. Ammonium formed in the fine mode aerosol dominates while only about 10% is formed on coarse particles on a global average basis as shown in Figure 4.7 (left panel). Over 50% of the total ammonia partitions into the aerosol phase in continental polluted regions with values approaching to 100% at high latitudes as shown in Figure 4.7 (right panel).

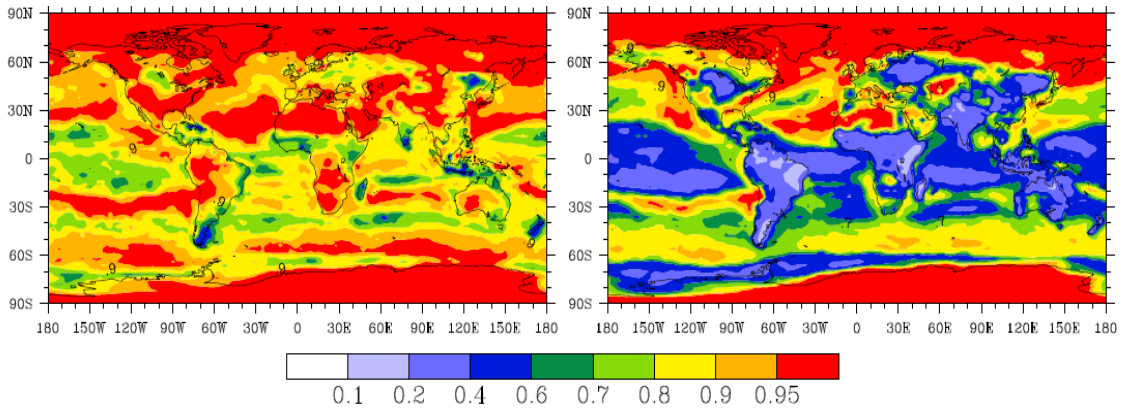

Figure 4.7: Fraction of the fine mode ammonium to total aerosol ammonium (left): [NH_4^+ ($D < 1.25$ μm)]/[NH_4^+ ($D < 1.25$ μm) + NH_4^+ ($D > 1.25$ μm)] and fraction of total ammonia (gas NH_3 + aerosol NH_4^+) predicted to occur as aerosol NH_4^+ (right) in the surface layer (994 mb) averaged for January and July.

4.3.4 Aerosol water

The average mixing ratios of aerosol water at the surface are shown in Figure 4.8. Over continents, aerosol water mixing ratios are usually highest in industrialized regions, exceeding 30 ppbv, due to high hygroscopic aerosol concentrations of sulfate, ammonium and nitrate formed in these areas. Comparably lower aerosol water mixing ratios, less than 1 ppbv, are predicted in the Sahara and Australian deserts, and northern South America where sulfate or nitrate concentrations are low. Marine aerosol water mixing ratios are as high as 10 ppbv over the areas with abundant sea salt concentrations such as the Southern Pacific Ocean, North Pacific and Atlantic.

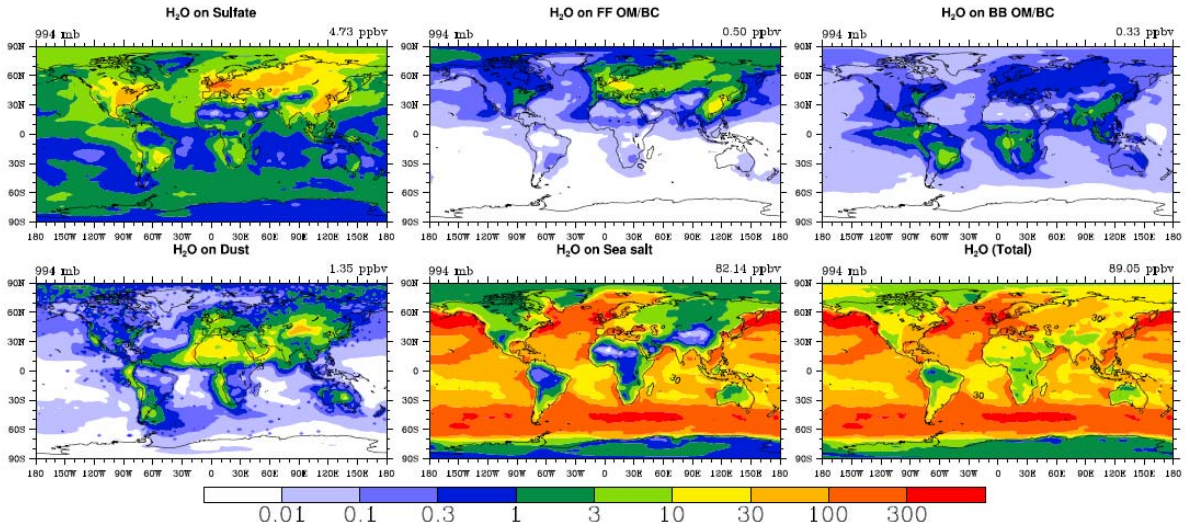

Figure 4.8: Predicted mixing ratios (pptv) of aerosol water associated with each aerosol type and for the total aerosol water (bottom right) in the surface layer averaged for January and July. The pressure level of the surface layer together with the average mixing ratio for that layer is indicated above each panel.

4.3.5 Zonal average mixing ratios

Nitrate aerosol mixing ratio decreases rapidly as altitude increases. This decrease is accompanied by higher gas phase nitric acid concentrations as shown in Figure 4.9. The mixing ratio of gas-phase HNO_3 decreases less dramatically than aerosol nitrate. Notice that both aerosol nitrate and HNO_3 gas start increasing in the upper troposphere. The increase of HNO_3 gas is more uniform in the upper troposphere than that of aerosol nitrate. There is a peak in the aerosol nitrate in the upper troposphere over both Antarctica and the Arctic. The peak over the Arctic is due to maximum predicted in January while that over Antarctica is due to a maximum in July. The formation of these peaks is due to the cold temperatures present in winter over both polar regions, which drives the partitioning of gas phase HNO_3 into the aerosol phase. The amount of aerosol nitrate

formed in the upper troposphere over Antarctica winter seems greater than that over the Arctic. That is because the temperature in winter over Antarctica is much colder than that over the Arctic in winter, which promotes the conversion of gas-phase HNO_3 to the aerosol phase.

Ammonium mixing ratios do not decline with altitude as rapidly as aerosol nitrate; the average mixing ratio in the middle troposphere (i.e., around 400 mb) decreases to about 10-75 pptv. Gas phase ammonia has a steeper vertical gradient than ammonium. This is because there are no additional sources of ammonia in the free troposphere and all ammonia emission is at the surface, whereas ammonium is more easily produced in the upper troposphere due to the decrease in temperature with altitude. Above 600 hPa, ammonia is completely converted to ammonium aerosol.

Sulfate aerosols have maximum concentrations in regions with high sulfur emissions in the latitude band between 30°N and 60°N. Compared with ammonium and nitrate aerosols, sulfate aerosols have another maximum concentration with moderate magnitude in the Southern Hemisphere which mainly comes from the oxidation of DMS. Sulfate decreases with altitude less rapidly than that of ammonium and nitrate aerosols. Aerosol water mixing ratios decline with the altitude even more quickly than sulfate, nitrate and ammonium aerosols. The average aerosol water mixing ratios in the middle troposphere (i.e., at around 400 hPa) is only about 1% of the surface value.

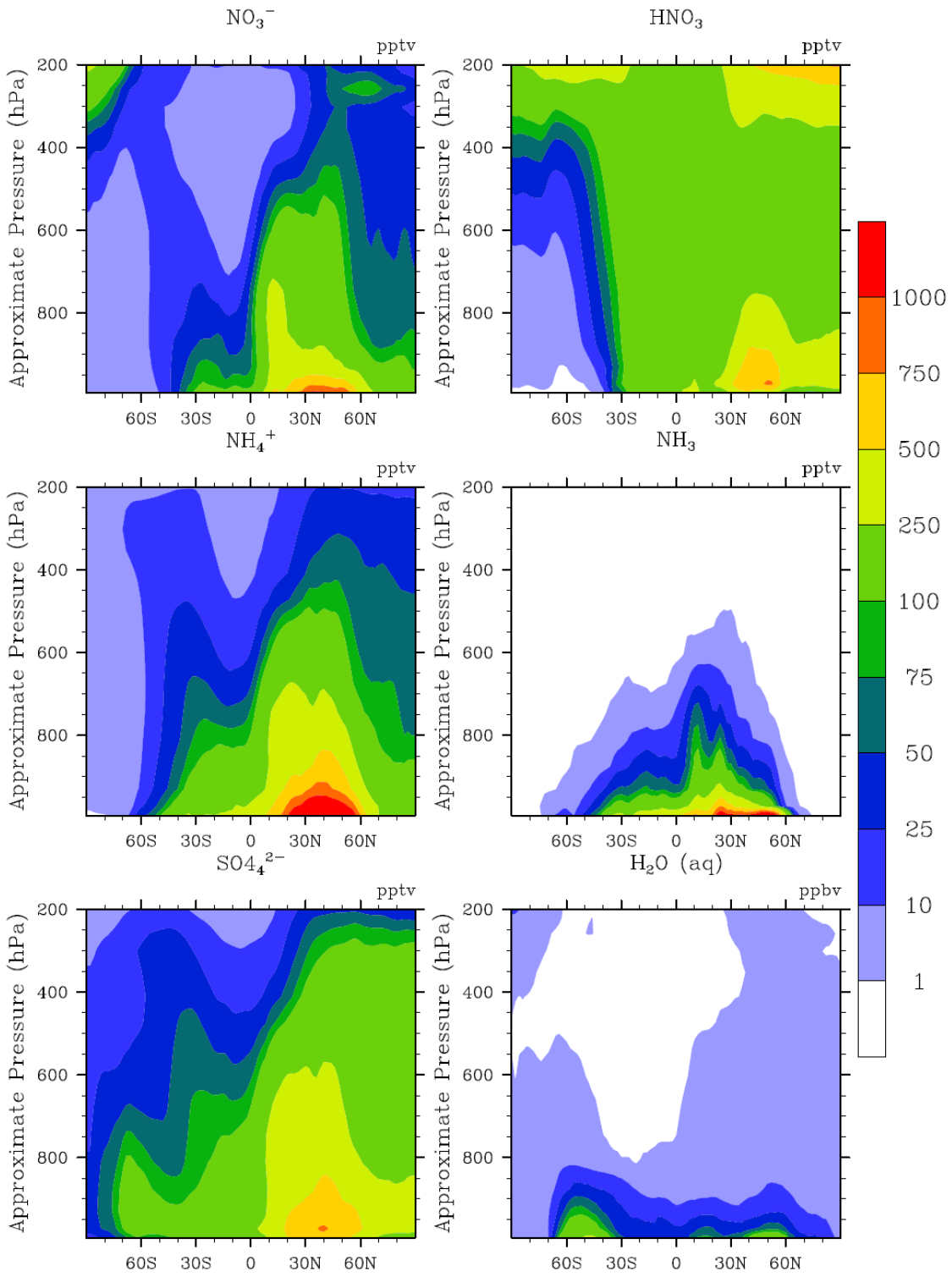

Figure 4.9: Zonal mean mixing ratio of NO_3^-, HNO_3, NH_4^+, NH_3, SO_4^{2-} and H_2O(aq) averaged for January and July. Above each panel, the unit is indicated.

4.4 Global budgets

The global and annual average budgets for gas-phase nitric acid and particulate nitrate in the troposphere (i.e., the model level below 200 hPa) and their net mass conversion rate to/from their gaseous precursors are shown in Figure 4.10. Note that all the annual budget components such as the burden and deposition mass fluxes were estimated based on the simulated results for January and July which we take to represent the "annual" budget in this study. Additionally, the budgets of nitrate and ammonium for both PD and PI scenarios are summarized in Table 4.4 and 4.5.

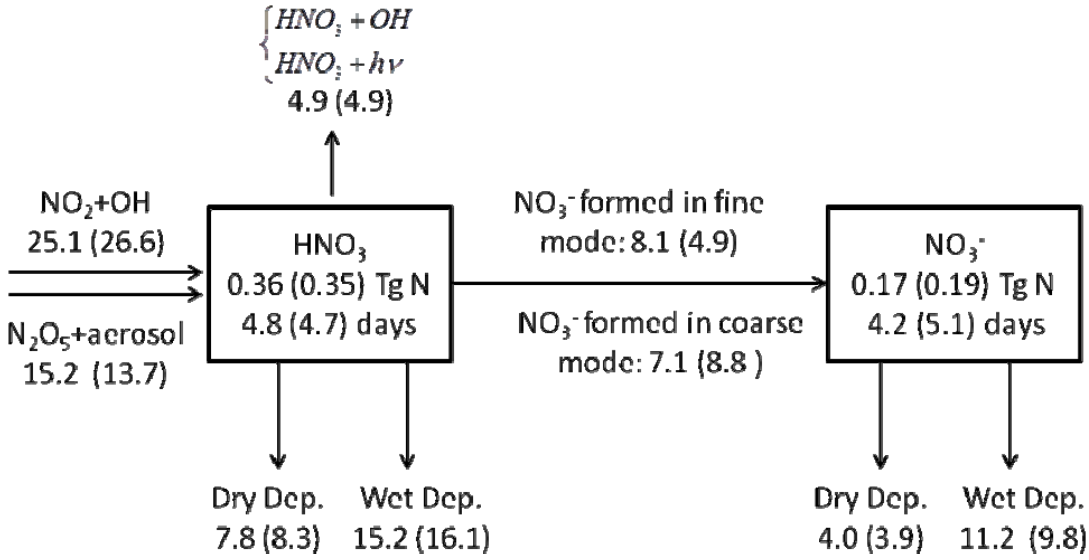

Figure 4.10: Schematic diagram of the global and annual budgets of nitric acid and nitrate aerosol calculated in this work. Burden and lifetime of HNO_3 gas and aerosol NO_3^- are shown in the boxes. Arrows indicate emission, deposition fluxes and net conversion rates in Tg N per year. The values in parentheses refer to the results simulated using the framework of Feng and Penner (2007) that assumes the internal mixing state of pre-exisiting aerosols.

The total chemical production of gaseous HNO_3 is 40.3 Tg N per year with 25.1 Tg N per year from reaction of NO_2 with OH and 15.2 Tg N per year through the

heterogeneous conversion of N_2O_5 on aerosols, respectively. 37% of the gaseous HNO_3 removal is due to the formation of particulate nitrate including 8.1 Tg N per year in the fine-mode and 7.1 Tg N per year in the coarse-mode while 12% of the gas-phase HNO_3 loss (i.e., 4.9 Tg N per year) is through the photolysis of HNO_3 and its reaction with OH. About one third of the gas-phase nitric acid is removed from the atmosphere through wet deposition. The gaseous HNO_3 tropospheric burden is calculated to be 0.36 Tg N with a lifetime of 4.8 days. In contrast, the estimated lifetime of nitrate aerosol is about 4.2 days, shorter than the predicted tropospheric HNO_3 lifetime, indicating that gas-phase nitric acid can be transported farther than aerosol nitrate. The predicted nitrate lifetime is comparable to the 5.0 days by FP07 and the 4.93 days given by Liao et al. (2004) (hereafter referred as L04), but much smaller than that of Rodriguez and Dabdub (2004) (hereafter referred as RD04). Our predicted nitrate burden of 0.17 Tg N in this work, which is close to the 0.16 Tg N given by FP07 and the 0.18 Tg N given by L04, slightly greater than the 0.13 Tg N given by Pringle et al. (2010), but much smaller than the 0.35 Tg N from Pye et al. (2009), the 0.417 from RD04 and the 0.52 Tg N from Bauer et al., (2007) (hereafter referred as B07). The discrepancy between this work and RD04 may be explained by the fact that the RD04 significantly overestimated nitrate formation through the gas-to-particle conversion by assuming thermodynamic equilibrium while that between this work and L04 along with B07 is due to an overestimated nitrate formation being present on the coarse particles in L04 and B07. The comparison of the prediction of nitrate and ammonium between the hybrid dynamic method used in this work and those used by RD04, L04 and B07 is discussed in details in FP07. Figure 4.10 also encloses the global budgets and mass fluxes of nitrate calculated by assuming that all aerosols are

internally mixed within each size bin following the same treatment as that assumed in FP07. The discrepancy between this work and that produced using the FP07 treatment for the prediction of the total nitrate burden is very small but there is a major difference in the fraction of aerosol nitrate that is present in the fine and coarse modes. 53% of the nitrate is in fine-mode in this work in contrast to the 36% using the treatment of FP07. This is mainly due to the fact that FP07 assumed that all aerosol components were internally mixed within each size bin. In addition, the dry and wet scavenging strategies used by FP07 differed from that used here. Note that FP07 assumed that the dry deposition of nitrate and ammonium in the size section of 0.01-0.65 μm (bin1) was treated the same as that of sulfate, while that in the size range from 0.63 to 2.5 μm (bin 2 and bin3) was treated the same as that of sea salt, and that in the range of 2.5~10 μm (bin 4) was treated the same as that of dust aerosol. Additionally, the wet scavenging efficiency for nitrate and ammonium aerosol was set to 1.0, the same as that for sulfate aerosol. In order to understand the difference in removal processes and lifetimes between these two treatments, we define the removal rate coefficient (k) following Textor et al. (2006).

$$-\frac{dm}{dt} = \tau^{-1} m = km, \tag{4.8}$$

where m is the aerosol mass and t is the time. The removal rate coefficient k is the inverse of the lifetime τ. It is the sum of the individual removal rate coefficients. In this study, removal processes from dry (k_{dry}) and wet (k_{wet}) deposition are taken into account, i.e.,

$$k = k_{dry} + k_{wet}. \tag{4.9}$$

Comparison of the removal rate coefficients allows us to isolate differences in the simulated individual removal pathways between various models for a given aerosol type

(Textor et al., 2006). As shown in Figure 4.10, the total removal rate calculated from the treatment assuming that all aerosols are internally mixed is 0.20 per day with 71% through wet deposition while the calculation in this work is estimated to be 0.24 per day with 74% though wet deposition. Table 4.6 gives the burden and removal coefficient for nitrate aerosol for each size bin predicted in this work and that using the internal mixture assumption. We see that the total nitrate burden is very close between these two treatments. Clearly, this work predicts 0.01 Tg N higher fine mode nitrate burden but 0.02 Tg N lower nitrate in the coarse mode than does the treatment of FP07. The removal coefficients predicted in this work are generally higher than that in the treatment of FP07. As a result, although we predicted 60% higher fine mode aerosol nitrate as a result of the gas-to-aerosol conversion on the additional aerosol surfaces provided by dust and sea salt aerosols, the different treatments of depositions eventually results in only a 6% enhancement in the fine mode. For the coarse mode, the treatment of FP07 predicted a 20% higher coarse mode nitrate aerosol through gas-to-aerosol conversion, which causes a 25% higher burden in the coarse mode than that predicted by this work.

Figure 4.11 shows the global annual average ammonia budget in the troposphere (i.e., for the model layers below 200 hPa). Nearly half of the total ammonia emissions (i.e., 53.6 Tg N per year) are partitioned into the aerosol phase. As a result, the deposition flux of gas phase ammonia is almost the same as that of particulate ammonium. 64% of the gas-phase ammonia is removed from the atmosphere through dry deposition while 72% of ammonium is removed by wet deposition. This is in accordance with the percentage of deposition values reported in FP07 and A99. The lifetime of ammonium aerosols, 3.0 days, is much longer than that of gas phase ammonia, 0.37 day. As a result of the longer

lifetime of NH_4^+ than that for NH_3, there is nearly four times as much particulate ammonium as gas phase ammonia on annual average basis. The calculated burden of particulate ammonium is 0.24 Tg N while that of gas phase ammonia is 0.06 Tg N. The NH_4^+ lifetime is shorter than that calculated by FP07, 4.1 days. On the other hand, the FP07 ammonia lifetime, 0.57 days, is longer than predicted here because the burden of ammonia predicted by this work is 25% less than that in FP07 even though the same ammonia emissions are used. In FP07, there was less gas-phase NH_3 conversions to NH_4^+ because they assumed that all aerosol components are internally mixed as discussed earlier, compared to this work in which gas phase ammonia is allowed to interact with pure sulfate, sulfate coated on fossil fuel and biomass burning aerosols, along with dust and sea salt. This treatment of externally mixed pre-existing aerosols provides a larger total amount of particle surfaces than does that in the treatment of FP07. The ammonium production in this work is 23% and 75% higher in the fine and coarse modes than those by the treatment of FP07. However, the burden of aerosol ammonium predicted in this work is slightly smaller than that using the treatment of FP07. As for nitrate, this is because the removal rate coefficient from the treatment of FP07 is smaller than that in this work, which eventually causes a lower ammonium burden even though we have a higher production of aerosol ammonium.

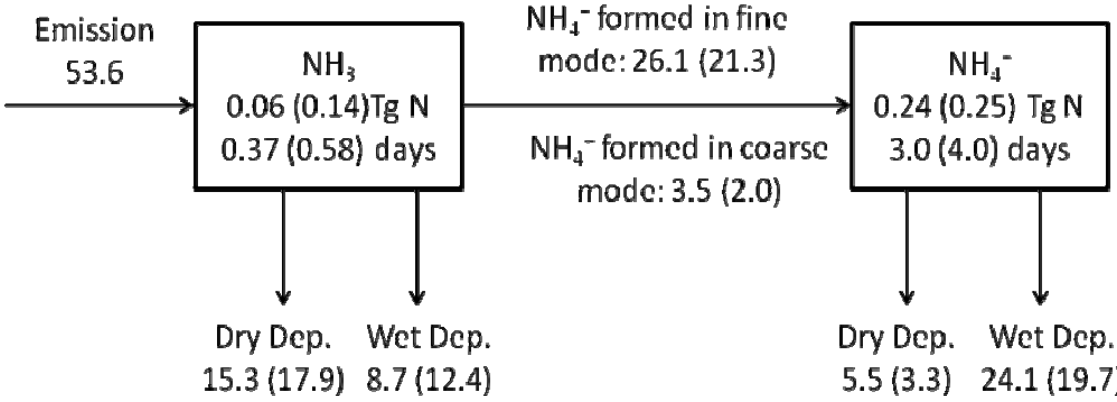

Figure 4.11: Schematic diagram of the global and annual budgets of ammonia and ammonium calculated in this work. Burden and lifetime of gas NH_3 and aerosol NH_4^+ are shown in the boxes. Arrows indicate emission, deposition fluxes and net conversion rates in Tg N per year. The values in parentheses refer to the simulated results based on the framework of Feng and Penner (2007) assumes the internal mixing state of pre-exisiting aerosols.

Tables 4.4 and 4.5 summarize the global budgets of gas phase nitric acid and nitrate as well as gas phase ammonia and ammonium for the PD and PI scenarios calculated by the hybrid dynamic method assuming five externally mixed pre-existing aerosol types (internal mixing is assumed within each aerosol type). The simulated results using the treatment of FP07 are also included (i.e., the values in parenthesis) here for the PD scenario. Here we chose a characteristic height of 5 km following Textor et al. (2006) and discuss the mass fraction above this height as an indicator of the vertical dispersivity. Stronger vertical dispersivity corresponds to slower removal rate coefficients in the models. Wet scavenging becomes increasingly less significant when aerosols reach altitudes where the clouds show decreased precipitation efficiency (Textor et al., 2006). We also calculate the mass fractions in polar regions which serves as an indicator for the horizontal dispersivity (i.e., for meridional long-range transport because polar regions are far from the aerosol sources). In general, long-range transport is most significant for

small particles, which have longer lifetimes. The removal rate coefficients defined in Eqn. (4.8) are also reported.

The total tropospheric burden of nitric acid for the PD scenario is 0.36 Tg N, which is slightly higher than that simulated by the treatment of FP07, 0.35 Tg N. The slightly higher burden (and longer lifetime) stems from two aspects. One is due to the larger loss to aerosol nitrate, with 35% HNO_3 converted to aerosol nitrate in this work in contrast to 32% in the treatment of FP07. In addition, the smaller removal rate coefficient from wet scavenging in this work contributes to this difference as well. The rate coefficient for wet removal of nitric acid is about 0.18 per day so that wet removal process contributes 66% of the total removal. As shown in Table 4.4, about 83% of the nitric acid burden is above 5 km compared to 80% from the treatment of FP07, which is consistent with the lower wet removal rate coefficient in this work. The mass fraction of gaseous nitric acid at the poles is 2%, close to that for sulfate aerosol (Wang et al., 2009). The model predicts that 27% of the total nitrate mass is associated with pure sulfate with the remaining nitrate mass associated with sulfate-coated non-sulfate aerosols (2% on carbonaceous aerosols, 56% on dust and 15% on sea salt). The mass fraction of fine-mode nitrate aerosols is predicted to be 54% compared with 42% predicted by the treatment of FP07. The differences in the fine nitrate mass fraction originate from the different mixing states treated in these two simulations as discussed earlier. About 28% of the total nitrate mass is above 5 km, which is smaller than the 42% predicted by the treatment of FP07, due to the higher wet removal rate coefficient of aerosol nitrate in this work. The total nitrate burden predicted is 0.17 Tg N, slightly lower than the 0.19 Tg N predicted in the treatment of FP07.

The total burden of gas phase ammonia for the PD scenario is 0.06 Tg N, which is 30% lower than that simulated by the treatment of FP07 (0.085 Tg N). The lower burden (and shorter lifetime) of ammonia compared to that using the treatment of FP07 can be explained by following two aspects. First, there is a large loss to aerosol ammonium, with 55% NH_3 converted to aerosol ammonium in this work compared to 43% in the treatment of FP07. Second, there is a larger removal rate coefficient from both dry and wet processes in this model. The rate coefficient for wet and dry removal process of ammonia is about 1.32 per day, in which 64% is from dry removal processes. As shown in Table 4.5, only 0.22% of the ammonia burden is above 5 km in this work, significantly lower than that from the treatment of FP07 (1.5%). The mass fraction of gaseous ammonia at the poles is negligible. The model predicts 75.5% of the total ammonium mass is associated with pure sulfate with the remaining ammonium mass coated on non-sulfate aerosols (22% on carbonaceous aerosols, 1% on dust and 2.5% on sea salt). The mass fraction of fine-mode aerosols predicted by this model and the treatment of FP07 is very close to each other, 98% versus 96%, respectively, because of the close tie between ammonium aerosol and sulfate. About 11% of the total ammonium mass is above 5 km in this work, which is half of that from the treatment of FP07, resulting from higher removal rate coefficient of aerosol ammonium from both dry and wet process predicted in this work. The total ammonium burden is 0.24 Tg N, slightly lower than 0.25 Tg N predicted in the treatment of FP07.

For the PI scenario, the total burden of nitric acid and aerosol nitrate is 0.15 Tg N and 0.08 Tg N, respectively, which are nearly half as large as the values for the PD scenario. The lower removal rate coefficients for nitric acid and aerosol nitrate for the PI scenario

lead to comparably longer lifetimes than those in the PD scenario. The total burden of ammonia and ammonium is 0.01 Tg N and 0.03 Tg N, respectively. The predicted lifetimes for both ammonia and ammonium are shorter than those in the PD scenario, mainly due to the higher removal rate coefficients from both dry and wet removal processes.

Table 4.4: Global annual budgets of HNO_3(g) and nitrate (NO_3^-) for present-day and preindustrial scenarios.

	Scenario	
	Present-Day	Preindustrial
HNO_3(g)		
Sources (Tg N yr^{-1})	43.12 (43.36)	14.53
NO_2+OH	25.12 (26.61)	11.07
N_2O_5 + aerosol	18.00 (16.75)	3.46
Loss (Tg N yr^{-1})	43.12 (43.36)	14.53
HNO_3+OH and HNO_3+hν	4.87 (4.86)	3.29
Loss to nitrate	15.21 (13.70)	4.62
Dry deposition	7.81 (8.25)	2.37
Wet deposition	15.23 (16.10)	4.25
Burden (Tg N)[a]	0.36 (0.35)	0.15
Above 5km (%)	83.36 (80.30)	91.52
In polar (%)[b]	1.89 (1.96)	2.05
Lifetime	4.84 (4.73)	5.22
Removal rate (day^{-1})	0.18 (0.19)	0.12
Wet	0.12 (0.13)	0.08
Dry	0.06 (0.06)	0.04
Wet (%)	66.11 (66.10)	64.20
NO_3^-		
Sources (Tg N yr^{-1})	15.21 (13.70)	4.62
Gas-to-aerosol (D < 1.25 μm)	8.12 (4.91)	2.52
Gas-to-aerosol (D> 1.25 μm)	7.09 (8.79)	2.10
Loss (Tg N yr^{-1})	14.99 (13.60)	4.55
Dry deposition	3.96 (3.94)	0.77
Wet deposition	11.13 (9.66)	3.78
Burden (Tg N)	0.17 (0.19)	0.08
On pure sulfate (%)	26.59	24.34
On carbonaceous aerosols (%)	1.90	2.24
On dust bins 1-4 (%)	11.99, 14.97, 26.55, 3.11	23.00,14.69, 21.99 1.25
On sea salt bins 1-4 (%)	13.16, 0.99, 0.66, 0.08	11.53, 0.54, 0.37 0.04
Fine-mode (D < 1.25 μm)	53.63 (42.11)	61.12
Coarse-mode (D> 1.25 μm)	46.37 (57.89)	38.88
Above 5km (%)	27.90 (41.65)	40.50
In polar (%)	1.45 (2.13)	2.38
Lifetime	4.20 (5.11)	6.28
Removal rate (day^{-1})	0.24 (0.20)	0.16
Wet	0.18 (0.14)	0.13
Dry	0.06 (0.06)	0.03
Wet (%)	74.23 (71.00)	80.13

[a]The tropospheric HNO_3 burden was calculated by the summation of HNO_3 concentrations over the model levels below 200 hPa in this work.
[b]South of 80°S and north of 80°S.

Table 4.5: Global Annual budgets of NH_3(g) and ammonium (NH_4^+) for present-day and preindustrial scenarios.

	Scenario	
	Present-Day	Preindustrial
NH_3(g)		
Emission (Tg N yr^{-1})	53.60 (53.60)	10.71
Loss (Tg N yr^{-1})	53.60 (53.60)	10.71
Loss to ammonium	29.59 (23.26)	5.73
Dry deposition	15.32 (17.95)	2.89
Wet deposition	8.69 (12.39)	2.19
Burden (Tg N)	0.06 (0.085)	0.01
Above 5km (%)	0.22 (1.48)	0.43
In polar (%)	0.006 (0.03)	0.05
Lifetime	0.37 (0.58)	0.34
Removal rate (day^{-1})	1.32 (0.98)	1.72
Wet	0.48 (0.40)	0.74
Dry	0.84 (0.58)	0.98
Wet (%)	36.36 (40.80)	43.10
NH_4^+		
Sources (Tg N yr^{-1})	29.59 (23.26)	5.73
Gas-to-aerosol (D < 1.25 μm)	26.08 (21.30)	4.96
Gas-to-aerosol (D> 1.25 μm)	3.51 (1.96)	0.77
Loss (Tg N yr^{-1})	29.59 (23.04)	5.73
Dry deposition	5.49 (3.34)	0.86
Wet deposition	24.10 (19.71)	4.87
Burden (Tg N)	0.24 (0.25)	0.03
On pure sulfate (%)	74.59	81.53
On carbonaceous aerosols (%)	22.03	13.36
On dust bins 1-4 (%)	0.03, 0.67, 0.16, 0.03	0.01, 0.18, 0.05, 0.07
On sea salt bins 1-4 (%)	0.88, 1.03, 0.52, 0.08	1.23, 2.31, 1.07, 0.17
Fine-mode (D < 1.25 μm)	97.53 (96.03)	0.03
Coarse-mode (D> 1.25 μm)	2.47 (3.97)	0.00
Above 5km (%)	10.71 (20.95)	10.77
In polar (%)	0.60 (0.95)	0.63
Lifetime	3.00 (3.99)	2.08
Removal rate (day^{-1})	0.33 (0.25)	0.48
Wet	0.27 (0.21)	0.41
Dry	0.06 (0.04)	0.07
Wet (%)	81.64 (85.52)	84.39

Table 4.6: The calculated nitrate burden, total, wet and dry removal rate coefficient (k, k_{wet} and k_{dry}) as well as the percentage of wet removal rate coefficient for each size bin and all bins. The size range is indicated in the first row.

	bin 1 (0.05 ~ 0.63 μm)	bin 2 (0.63 ~ 1.25 μm)	bin 3 (1.25 ~ 2.5 μm)	bin 4 (2.5 ~ 10 μm)	All (0.05 ~ 10 μm)
Burden	0.093 (0.084)	0.028 (0.032)	0.047 (0.064)	0.006 (0.011)	0.172 (0.190)
k	0.237 (0.161)	0.187 (0.181)	0.193 (0.192)	0.893 (0.517)	0.238 (0.196)
k_{wet}	0.200 (0.126)	0.159 (0.159)	0.145 (0.144)	0.146 (0.153)	0.177 (0.139)
k_{dry}	0.037 (0.036)	0.028 (0.022)	0.049 (0.048)	0.747 (0.364)	0.061 (0.0057)
Wet (%)	84.484 (77.97)	84.999 (87.98)	74.747 (74.918)	16.396 (29.564)	74.232 (70.995)

4.5 Aerosol optical properties

Here, we use an off-line radiative transfer model to compute the aerosol optical properties and the resulting radiative forcing (Wang and Penner, 2009). Consistent to the global chemical transport model, we assume that five types of aerosol populations (i.e., pure sulfate, carbonaceous aerosols from fossil fuel, carbonaceous aerosols from biomass burning, dust and sea salt) are externally mixed with all aerosol constitutes internally mixed within each aerosol type. The refractive indices of sulfate ($1.53\text{-}10^{-7}$i at 550nm), dust (1.53-0.0014i at 550nm) and sea salt ($1.38\text{-}5.8\times10^{-7}$i at 550nm) are the same as those used in Liu et al. (2007). The refractive index of fossil fuel soot (1.85-0.71i at 550 nm) is taken from Bond et al. (2006) while that of biomass burning soot (1.75-0.46i at 550 nm) is used by Zhang et al. (2005). The refractive index of organic matter is assumed same as ammonium sulfate at 550 nm. We use a refractive index for some of the organic matter that is similar to that for biomass burning OM (1.53-0.03i at 550 nm) in order to account for the absorption characteristics of the humic-like substance (HULIS) (Kirchstetter et al., 2004). We assumed that 50% of organic matter originating from fossil fuel combustion is HULIS. Refractive indices of sulfate are used for ammonium. The refractive index of nitrate at 550 nm is assumed to be the same as sulfate. Refractive indices of nitrate at 19 wavelengths used for radiative forcing calculation in the offline CAM3 radiative transfer model are taken from the Global Aerosol Climatology Project database (http://gacp.giss.nasa.gov/data_sets). The refractive indices of each internal mixture are calculated by volume-weighting the refractive indices of each individual aerosol species including its associated water. The size distribution of pure sulfate is calculated according to the predicted mass and number at each grid cell from the global aerosol model while

the other four types of aerosols use the prescribed size distribution given in Table 4.1. We assumed that two ammonium cations are first associated with one sulfate anion to form ammonium sulfate before they are allowed to be associated with nitrate to form ammonium nitrate. This assumption is valid over most continental areas since the gas ratio is generally higher than 1 over continents indicating that free ammonia exists but the HNO_3 limits the formation of ammonium nitrate. For pure sulfate, nitrate is allocated to each sulfate size bin in the accumulation mode according to the surface area fraction of that size bin to the total surface areas. For the other four aerosol types, sulfate, ammonium and nitrate are distributed into each size bin proportional to the surface area of that type given the specified size distribution (see Table 4.1). We use the Köhler theory together with the soluble fraction present on each type of aerosols to predict the amount of water on each aerosol type. The hygroscopicity of nitrate is assumed to be 0.67 taken from Petters and Kreidenweis (2007), higher than ammonium sulfate of 0.51. The hygroscopicity of other aerosols is 1.16, 0.14, 0.14, and 5e-7 for sea salt, organic matter, dust and black carbon, respectively. Note that sea salt is most hygroscopic among all aerosols. The hygroscopicity of the internal mixture within each aerosol type is calculated by volume-weighting hygroscopicity of each individual aerosol species.

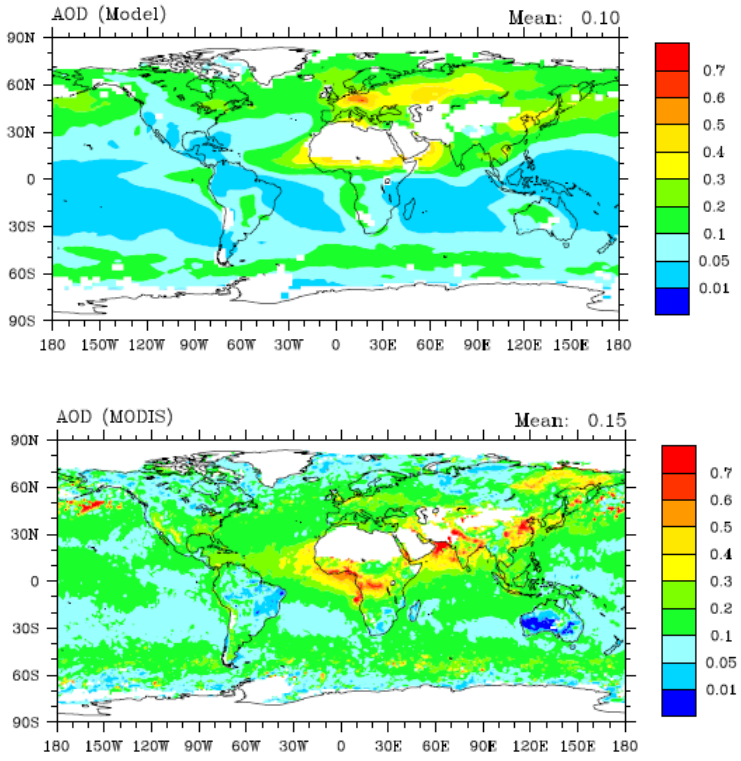

Figure 4.12: Global annual mean distribution of modeled aerosol optical depth (AOD) and observed AOD from MODIS satellite for the year 2001 at 550 nm.

Predicted aerosol optical depth (AOD) averaged for January and July is compared with the averaged AOD for January and July derived from the MODIS satellite data for the year 2001 in Figure 4.12. The highest AODs are found over Europe, eastern Asia and over the Sahara desert and range from 0.4 to 0.6. The highest AODs in Eastern North America are around 0.1. In general, the modeled AOD is lower than the observed AOD. The modeled AOD over the ocean may be lower than that observed if sea salt emissions are too low. Alternatively, the low AOD may be due to the fact that we used meteorology fields for the year of 1997 while the observations were for the year of 2001. Over continents, the modeled AOD captures general spatial pattern of AOD although the magnitude is still smaller than the observations, especially over central Africa and

Siberia. Low values in these regions may be due to lower biomass burning emissions in the model than those for 2001. The model predicted AOD is too high over Europe, which may be due to different sulfur and NO_x emissions than those for the year of the observations. Modeled optical depths in the Arabian Sea (0.1-0.4) and Indian Ocean (0.1-0.2) are within the range of values observed during the Indian Ocean Experiment (INDOEX) by Jayaraman et al. (1998) (i.e., 0.2-0.4 and about 0.1, respectively).

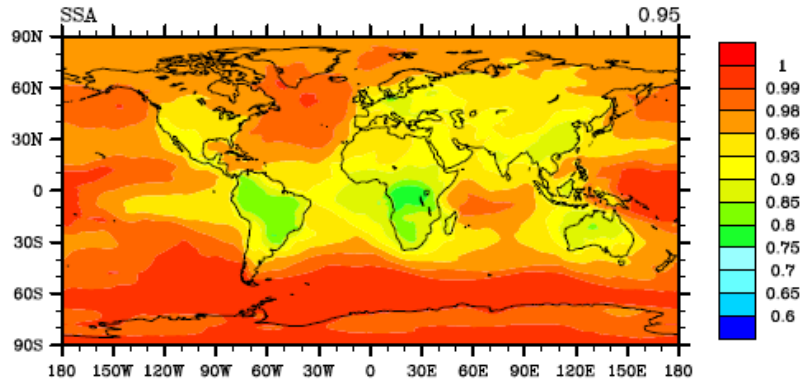

Figure 4.13: Global annual mean distribution of modeled aerosol single-scattering albedo at 550 nm.

Figure 4.13 shows the simulated mean global distribution of single scattering albedo (SSA) at 550 nm for all aerosol types for the PD simulation. The SSA over the North America generally ranges from 0.9 to 0.96. The simulated SSA ranges from 0.9 to 0.96 over Eastern Europe and 0.85-0.9 in Western Europe. The SSA over regions with biomass burning aerosols and mineral dust are generally lower than 0.9 and 0.93, respectively. Table 4.8 shows a comparison of modeled aerosol single-scattering albedos with annual average observations at several locations reported by Heintzenberg et al. (1997). Note that the modeled single-scattering albedo calculated here is based on the average of

January and July. The results are in general agreement with the observations is within 7% for all sites, which is less than the error of the measurements (Heintzenberg et al., 1997).

Table 4.7: Comparison of model predicted single scattering albedo at 550 nm with annual average measurements[a].

Location	Predicted	Observed
Arctic	0.96	0.96
Amundsen scott (90 °S)	0.99	0.965
Barrow (71.2 °N, 156.3 °W)	0.95	0.948
Ny Alesund (79 °N, 12 °E)	0.98	0.96
Mesa Verde (37.1 °N, 108.3 °W)	0.98	0.91
Abastumani (43.4 °N, 42.5 °E)	0.89	0.89
Anderson Mesa (35.12 °N, 111.38 °W)	0.99	0.94

[a]Heinzenberg et al. (1997)

4.6 Radiative forcing of nitrate and ammonium

Direct and indirect radiative forcings of nitrate and ammonium aerosols were calculated for the simulation for both preindustrial (PI) and present-day (PD) scenarios. Note that the same meteorology field is used for both PI and PD simulations. The cloud fields are held constant for the simulations with and without nitrate and ammonium to assess the direct forcing of nitrate and ammonium. For the indirect forcing, the cloud droplet number concentrations change, but the cloud liquid water path and cloud fraction do not. The direct and indirect effect of nitrate and ammonium aerosols is also computed. This is defined as the difference in the net radiative flux with and without both nitrate and ammonium aerosols for both the PD and the PI scenarios. As in IPCC, the anthropogenic forcing of nitrate and ammonium aerosols is defined as the difference in the net radiative

flux due to the change in anthropogenic emissions of nitrate and ammonium precursors. Note that the global annual mean forcing is assessed based on the average of the simulated results for January and July.

4.6.1 Direct forcing of nitrate and ammonium

Figure 4.14 shows the annual mean distribution of the simulated radiative effect of nitrate and ammonium at the top of atmosphere (TOA) and at the surface for full-sky and clear-sky conditions for the PD simulation. For clear-sky conditions, the inclusion of nitrate and ammonium contributes to a strong cooling over continents but warming over the oceans at the surface. The warming effect over ocean is expected since nitrate and ammonium lowers the ability of sea salt aerosols to take up water, which then decreases the scattering characteristics of sea salt aerosols shown in Figure 4.15 (left panel). Figure 4.15 (left panel) shows global annual mean distribution of the difference in column-integrated aerosol optical depth at 550 nm between the simulations with and without ammonium and nitrate aerosols for the PD simulation. The decrease of aerosol optical depth at 550 nm including nitrate and ammonium is found over the Southern Oceans and part of North Pacific Ocean. With the presence of clouds, both cooling over land and warming over the southern oceans at the surface and TOA are decrease. Figure 4.16 gives the annual mean distribution of the simulated radiative forcing of nitrate and ammonium for the PI simulation. The spatial pattern of cooling and warming is similar to that for the PD simulation. The magnitude of cooling is smaller due to smaller mixing ratios of nitrate and ammonium while the warming effect over oceans over the ocean is similar but slightly higher. Although the same emission of ammonia from the ocean (Table 4.3) and sea salt emission are used for both PD and PI simulations, less nitrate predicted in the PI

simulation that are considered to be more hygroscopic than ammonium and sulfate leads to comparably more reduction of scattering characteristics of sea salt over the oceans shown in Figure 4.15 (right panel). Table 4.8 shows the comparison of direct forcing and anthropogenic forcing of nitrate and ammonium estimated in this work with other studies available in literatures. The direct forcing of nitrate and ammonium at TOA in the present-day in this work is estimated to be -0.12 W m^{-2}, within the range of -0.07 W m^{-2} estimated by Jacobson et al. (2001) to -0.30 W m^{-2} by Adams et al. (2001), close to -0.11 W m^{-2} from Bauer et al. (2007) and -0.14 W m^{-2} from Liao et al. (2004). The highest direct forcing of nitrate suggested by Adams et al. (2001) stems from the equilibrium assumption they made which overestimates the formation of nitrate, especially over small particles that are more optically efficient (Feng and Penner, 2007). The direct forcing of nitrate and ammonium at surface estimated in this work, -0.17 W m^{-2}, is comparable to that by Liao et al. (2004) since both studies predict similar nitrate burden, 0.17 Tg N by this work versus 0.183 Tg N by Liao et al. (2004),.

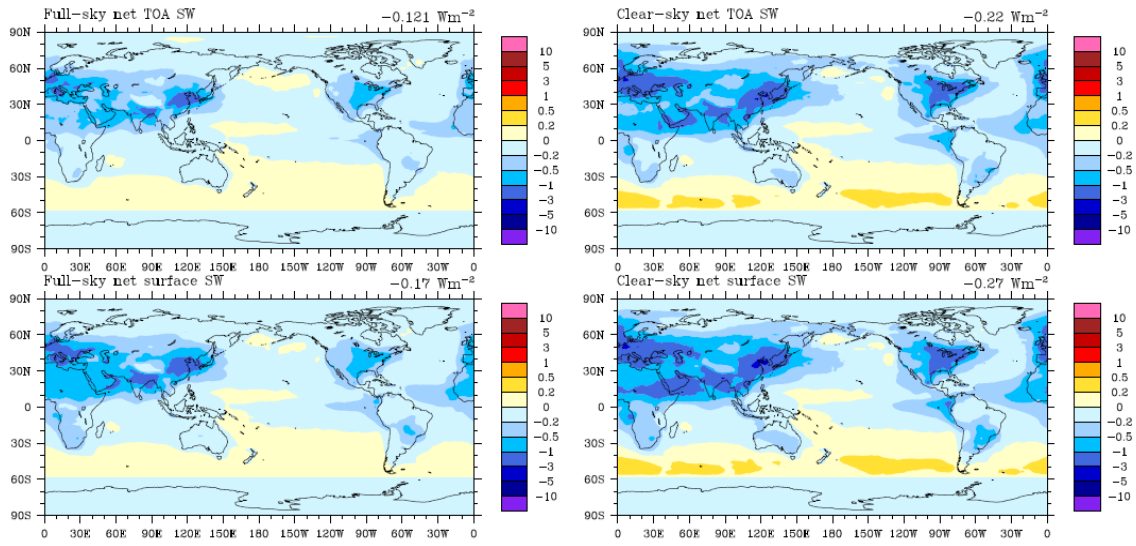

Figure 4.14: Annual mean distribution of the simulated radiative effects of nitrate and ammonium at the top of atmosphere (TOA) and at the surface for full-sky and clear-sky conditions for the PD simulation.

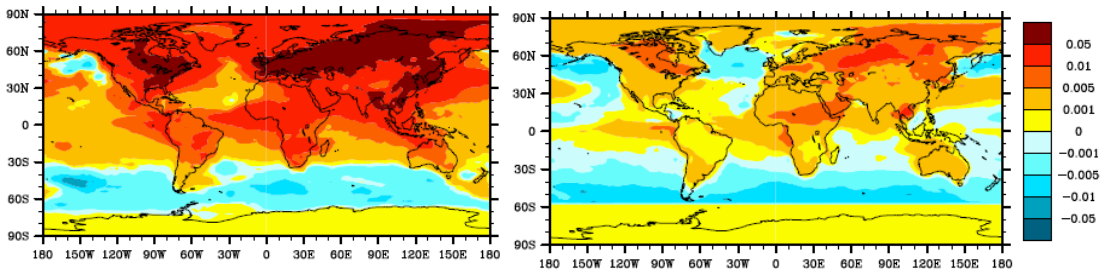

Figure 4.15: Global annual mean distribution of the difference in column-integrated aerosol optical depth at 550 nm between the simulations with and without ammonium and nitrate aerosols for the PD (left) and PI (right) scenario.

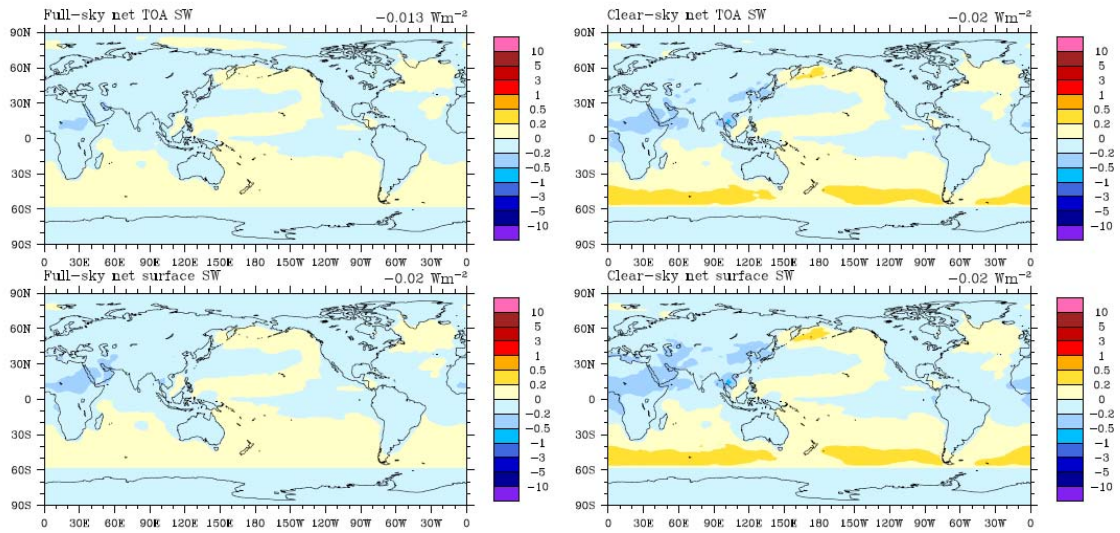

Figure 4.16: Annual mean distribution of the simulated radiative effects of nitrate and ammonium at the top of atmosphere (TOA) and at the surface for full-sky and clear-sky conditions for the PI simulation.

Figure 4.17 shows anthropogenic forcing of nitrate and ammonium (i.e., the difference between the fluxes shown in Figure 4.14 and 4.16). For clear-sky conditions, the nitrate and ammonium forcing is estimated to be -0.21 W m^{-2} and -0.25 W m^{-2} at the TOA and the surface, respectively. There is a cooling of up to -3 W m^{-2} over Eastern Asia, North America and Europe, which is consistent with the areas where nitrate and ammonium aerosols are highest. When clouds are present, surface and TOA nitrate and ammonium forcing is decreased to -0.15 W m^{-2} while and -0.11 W m^{-2}. The anthropogenic nitrate and ammonium direct forcing at the surface is -0.15 W m^{-2}, which is comparable to the -0.15 W m^{-2} estimated by Liao et al. (2005). Note that this work predicts smaller nitrate burden for both PD and PI simulation compared with those values reported in Liao et al. (2005) but the change of the nitrate burden from the PI scenario to the PD scenario (i.e., roughly increase by a factor of 2) is close between these two studies, which results in similar anthropogenic forcing of nitrate and ammonium.

Table 4.8: Comparison of direct radiative effect and anthropogenic forcing (W m^{-2}) of nitrate and ammonium with other studies.

ADE	Direct effect (PD)		Direct effect (PI)		Anthropogenic forcing	
	TOA	Surface	TOA	Surface	TOA	Surface
This work	-0.12	-0.17	-0.01	-0.02	-0.11	-0.15
B07[a]	-0.11		-0.05		-0.06	
L04[b]	-0.14	-0.17				
L05[c]	-0.22	-0.21	-0.06	-0.06	-0.16	-0.15
J01[d]	-0.07	-0.07				
A01[e]	-0.30		-0.11		-0.19	

[a]Bauer et al., 2007
[b]Liao et al., 2004
[c]Liao et al., 2005
[d]Jacobson et al., 2001
[e]Adams et al., 2001

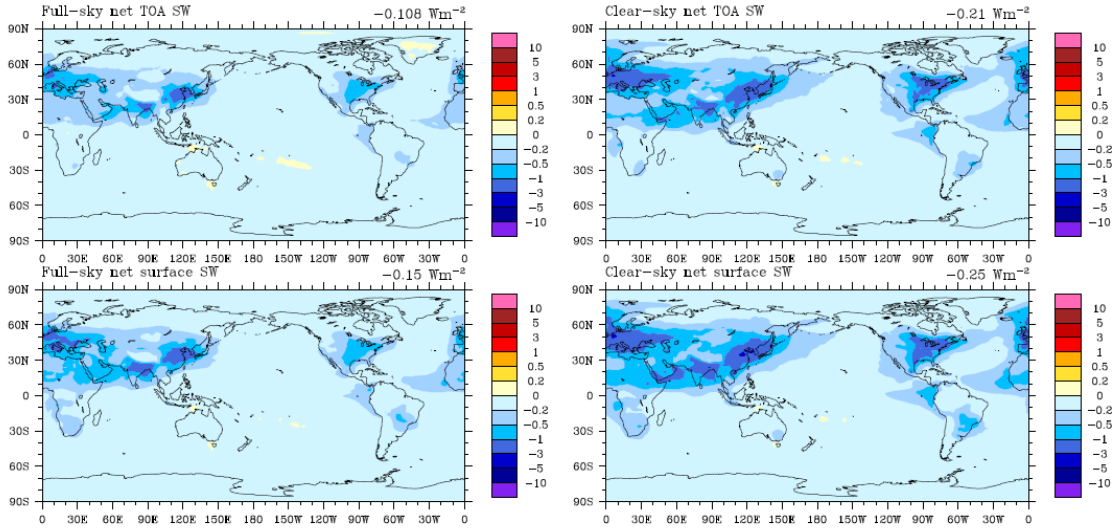

Figure 4.17: Annual mean anthropogenic forcing of nitrate and ammonium from the PI to PD scenario.

Above results are based on monthly averaged aerosol fields. Table 4.9 presents the calculated nitrate and ammonium direct effects for the PD and PI simulation and anthropogenic forcing (PD-PI) at the top of atmosphere (TOA) and at surface (SFC) using monthly average (M), daily average (D) and hourly average (H) aerosol fields. The results indicate that the frequency with which the aerosol fields are updated changes the global average direct effect of nitrate and ammonium by less than 5%.

Table 4.9: The calculated nitrate and ammonium direct effects (W m^{-2}) for the PD and PI simulation and the anthropogenic forcing (W m^{-2}) (PD-PI) at the top of atmosphere (TOA) and at surface (SFC) using monthly average (M), daily average (D) and hourly average (H) aerosol fields.

Case			M	D	H
PD	Full-sky	SFC	-0.17	-0.17	-0.17
		TOA	-0.12	-0.12	-0.13
	Clear-sky	SFC	-0.27	-0.27	-0.27
		TOA	-0.22	-0.23	-0.23
PI	Full-sky	SFC	-0.02	-0.02	-0.03
		TOA	-0.01	-0.02	-0.02
	Clear-sky	SFC	-0.02	-0.02	-0.04
		TOA	-0.02	-0.03	-0.03
PD-PI	Full-sky	SFC	-0.15	-0.14	-0.14
		TOA	-0.11	-0.11	-0.11
	Clear-sky	SFC	-0.25	-0.24	-0.24
		TOA	-0.21	-0.20	-0.20

4.6.2 Indirect forcing of nitrate and ammonium

In this section, we investigate the aerosol indirect effect of nitrate and ammonium and its accompanying gaseous HNO_3 in the atmosphere. This work is based on the substitution method proposed in a previous study (Chen, 2006). Chen (2006) investigated different distribution methods of nitrate in the gas phase and aerosol phase to calculate the cloud droplet number concentrations for different representative sites on the earth. In keeping with the results of Kulmala et al. (1993), he found that both nitrate in the aqueous phase and HNO_3 in gas phase can have an effect on aerosol activation. Kulmala et al. (1993) showed that in the presence of HNO_3 gas, the supersaturation needed to activate a nitrate-containing particle is suppressed. As a result, smaller particles can be activated more easily at high concentrations of HNO_3. Since the droplet number is mainly determined by the fine-mode aerosol number, Chen (2006) proposed to re-distribute the gas-phase HNO_3 to the fine-mode aerosol phase and to use this together with the parameterization scheme (Abdul-Razzak and Ghan, 2002) to approximate the effect of gaseous HNO_3 on cloud droplet number concentrations in global model studies. In this work, we implemented this treatment together with the parameterization of cloud droplet number developed by Abdul-Razzak and Ghan (2002) and the off-line calculation of forcing developed by Wang and Penner (2009). Thus, we account for the influence of both gaseous HNO_3 and aerosol nitrate and ammonium on the estimation of cloud droplet number concentration. In order to calculate these effects, first, we calculated the cloud droplet number from the five individual aerosol types ($N_{d,j}$, j is aerosol type and j=1,…,5) and total cloud droplet number (i.e., $N_d = \sum_{j=1}^{5} N_{d,j}$) without considering the effect of

nitric acid gas. Note that we consider the influence of aqueous phase nitrate and ammonium on the cloud droplet activation in this step. Then, we distribute the mass of nitric acid gas to each aerosol type in the fine mode (i.e., size bin 1) according to the fraction of cloud droplets formed on this aerosol type (i.e., $f_j = N_{d,j}/N_d$). Last, we updated the cloud droplet number with this new nitrate aerosol distribution.

Generally speaking, HNO_3 gas and aerosol nitrate/ammonium have two counteracting effects on modifying the estimation of cloud droplet number concentrations. First, the addition of aerosol nitrate and ammonium increases the size and the solute concentration in the aerosol particles, which affects both the Kelvin effect and Raoult effect in the Köhler curve. Basically, the increase in size lowers the surface tension, decreases the critical supersaturation (S_c) and hence affects the Kelvin term. Note that the Kelvin effect is negligible for very small sizes of particles. On the other hand, the addition of soluble molecules in the aqueous phase increases the hygroscopicity, which also leads to a decrease in the critical supersaturation due to Raoult effect (or "solute effect"). This solute effect is closely tied with the soluble fraction in pre-existing aerosols. If the pre-existing aerosol is soluble, the effect of aerosol-phase ammonium and nitrate and gas-phase nitric acid may not be of great importance. If the pre-existing aerosol is mainly non-soluble, the addition of soluble aerosol and gas species can increase the uptake of water, thereby causing an increase in the number of cloud droplets. Second, the effect of nitrate on cloud droplets is also related to the total mass of nitrate and HNO_3 gas. An increase in the total mass of the aerosol particle population due to the presence of nitrate and ammonium aerosols and HNO_3 gas tends to decrease the ambient maximum supersaturation (S_{max}). In this case, nitrate lowers the saturation water vapor associated

with aerosol particles, leading to decrease the size of particles that activate. Based on the theory of activation, each aerosol particle with $S_c < S_{max}$ is activated to become a cloud droplet and will grow spontaneously if the ambient supersaturation remains at or above the respective critical value. Hence, the number of droplets depends on the competition between the increasing effect of the lower critical supersaturations and the decreasing effect of the lower ambient maximum supersaturation within the parcel. In addition, the number of cloud droplets that form is related to how the soluble gases are distributed among the particles with different sizes. If small particles collect comparably more gases than larger particles, this favors the enhancement of aerosol activation while the number of cloud drops may decrease if larger particles take up gases more easily.

Table 4.10: Descriptions of experiments for the radiative calculations of the first aerosol indirect forcing.

Case	Description
NN (M, D, H[a])	The base line calculation including sulfate, carbonaceous aerosols from both fossil fuel and biomass burning, dust and sea salt.
PN (M, D, H)	The base line calculation (NN) with additional particulate NO_3^- and NH_4^+.
TN (M, D, H)	The baseline calculation (NN) with additional particulate NO_3^- and NH_4^+ and gaseous HNO_3.

[a]M, D and H represent the simulations based on monthly, daily and hourly aerosol concentration fields.

Table 4.10 outlines the experiment designs for the radiative calculations of the first aerosol indirect forcing. We ran two radiative forcing simulations for three cases listed in Table 4.10: one with the PD aerosol concentrations and one with the PI aerosol concentrations. The difference in radiative flux between TN and PN (i.e., TN-PN) is the

net HNO_3 gas effect while the difference between TN and NN is the total nitrate (NO_3^- + HNO_3 gas) and ammonium effect. The results simulated with monthly aerosol concentration fields are discussed below. The difference caused by the frequency of aerosol fields will be present in the last part of this section.

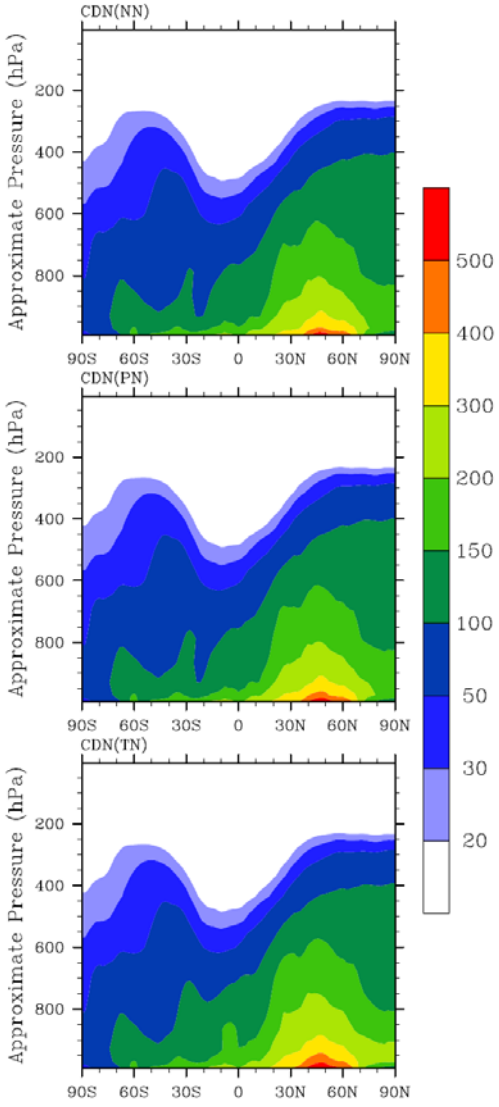

Figure 4.18: Present day zonal annual-average cloud droplet number (CDN) concentration for three cases.

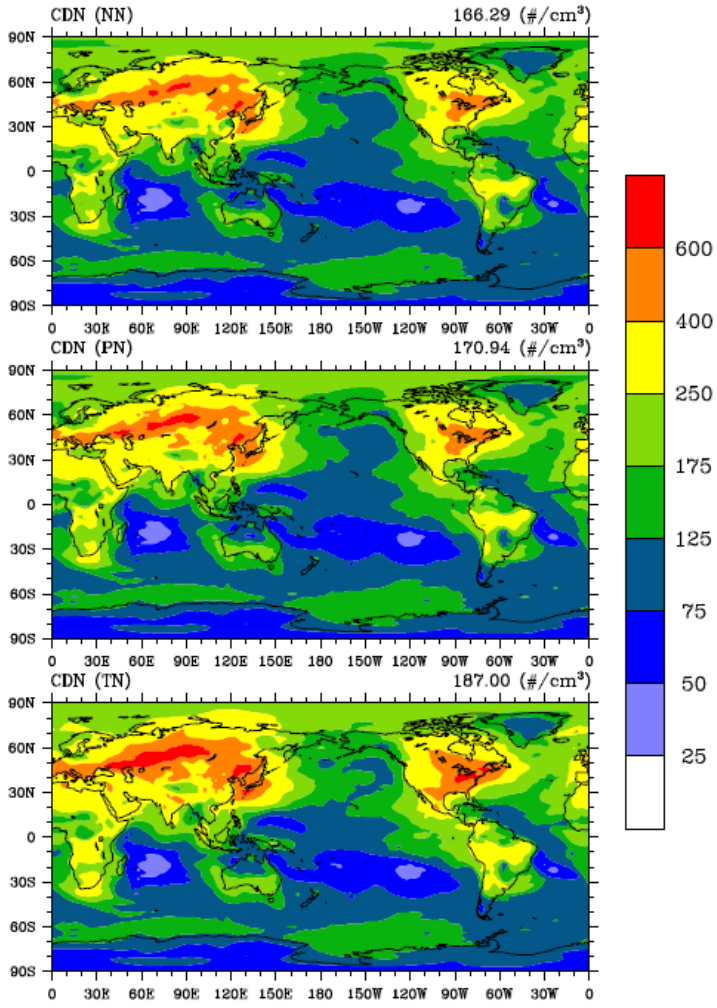

Figure 4.19: Present day annual average cloud top droplet number (CDN) concentration for three cases.

Figures 4.18 and 4.19 shows the present day zonal annual-average cloud droplet number concentration and present day annual average cloud top droplet number concentration based on monthly averaged aerosol field, respectively. As expected, the influence of nitrate and ammonium aerosols on the cloud droplet activation mainly occurs over the Northern Hemisphere near the surface since the major aerosol nitrate and ammonium occurs in the Northern Hemisphere and they decrease with altitude rapidly. There is some modification of cloud droplets between 0~30°S in the Southern

Hemisphere with the addition of nitric acid gas (i.e., the TN case) due to higher gas phase HNO_3 mixing ratios over these areas. In addition, the peak between 20°N and 60°N tends to expand upwards. The addition of nitrate and ammonium aerosols increases the cloud droplet number concentration by about 3% on a global average basis. With the further addition of nitric acid gas, the increase in cloud droplets is more than 10%. The local enhancement is even larger. Figure 4.20 shows the absolute difference of present day annual average cloud droplet number concentration activated for each aerosol type (i.e., sulfate, carbonaceous aerosols from fossil fuel, carbonaceous aerosols from biomass burning, dust and sea salt) and total cloud droplet number near 930 mb (the third model level) between the case PN and NN. It should be noted that we used 930 mb represents the boundary layer here. In general, the addition of aerosol nitrate and ammonium increases the number of total cloud droplets almost everywhere except some areas over oceans. The activated pure sulfate is inhibited with additional nitrate and ammonium except for sulfate concentration peak regions shown in Figure 4.20. The reduction of activated pure sulfate results from the increase in the activation of carbonaceous aerosols and dust due to the significant enhancement of their capability to uptake water by more soluble coatings of nitrate and ammonium besides sulfate. Ghan et al. (1998) found that the competition exists between sulfate and sea salt for typical marine cloud conditions. They found that the additional sea salt increases the total number of activated cloud drops for low sulfate concentration while the number of activated droplets decreases significantly with additional sea salt for high sulfate concentrations. They explained that the presence of large cloud condensation nuclei (CCN) with larger surface area will enhance condensation, reduce the maximum supersaturation and hence prevent the

activation of enough of smaller CCN, eventually resulting in the decrease of total number of activated drops. This example demonstrates a non-linear dynamic effect existing in the simple two-component aerosol systems (i.e., the effect of increasing the availability of aerosol populations does not necessarily causes an increase in cloud droplet concentration), indicating the dynamic competition in the multi-component aerosol systems could be even more complex. The activation of each aerosol particle highly depends on the presence of other CCNs because of limited water vapor given an updraft. Figure 4.21 shows similar figure for the difference between the case TN and the case NN. Note the only difference between the case TN and the case PN is the addition of HNO_3 gas on the case PN. The additional HNO_3 gas further enhances the activation of sulfate and carbonaceous aerosols but it does not change the activation of dust and sea salt so much. This is probably because dust and sea salt particles with nitrate and ammonium coatings are large enough to be activated and thereby the HNO_3 gas effect is not pronounced on these two types of aerosols. We also see some decrease of cloud drops over some areas in remote oceans with the addition of HNO_3 gas and nitrate and ammonium, which might be due to the competition effect between sulfate and sea salt (Ghan et al., 1998). Overall, the addition of nitrate aerosols increases the number of cloud droplets in Eastern Asia while the further addition of nitric acid increases the cloud droplets even more over eastern Asia, Europe, eastern United Sates, South America, and South Africa. The added mass of soluble gases facilitates the activation of smaller particles by causing a lower critical super-saturation and a higher hygroscopicity.

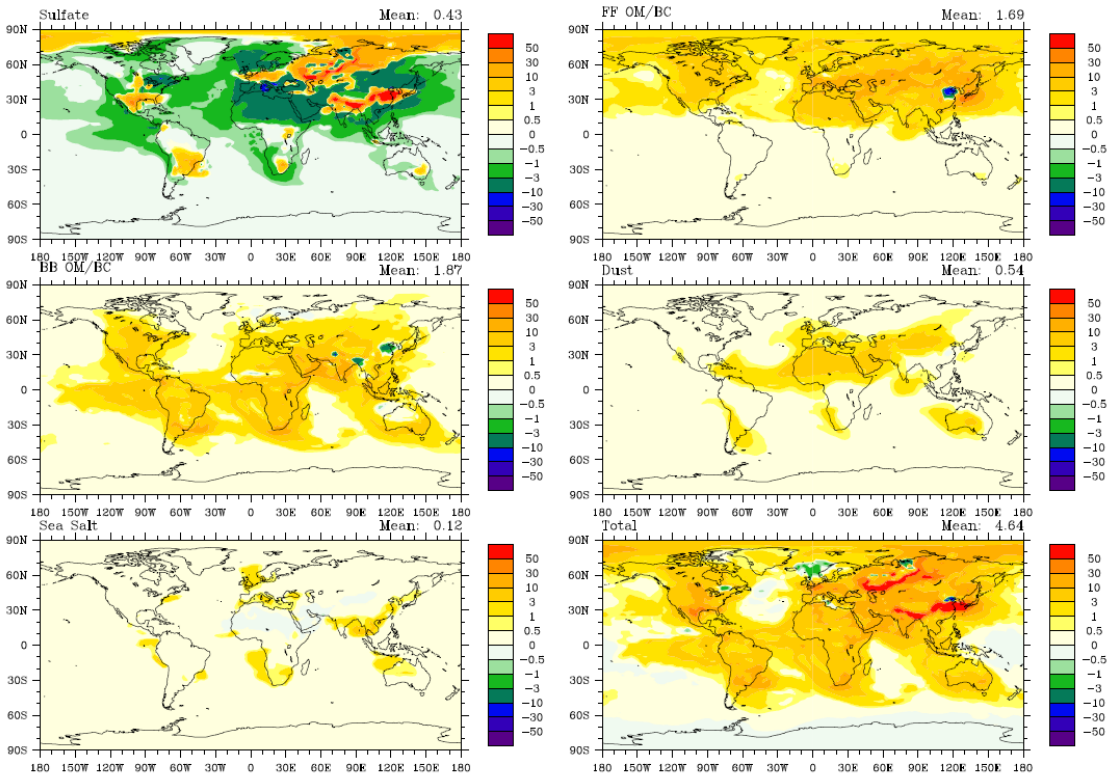

Figure 4.20: The absolute difference of present day annual average cloud droplet number concentration activated from each aerosol type and the total cloud droplet number near 930 mb (the third model level) between the case PN and NN.

Figure 4.22 shows the percentage change in zonal annual-average cloud droplet number for the case PN and the case TN compared with the baseline case NN near 930 mb. We see two peaks in change of cloud droplets near 25°S and 30°N as comparing both the case TN and PN with the case NN, which corresponds to an increase of activation of biomass burning aerosols and that of sulfate and carbonaceous and sulfate aerosols. We also notice that there is less than 1% decrease near tropics and 40°S due to a decrease of activated sulfate aerosol over these regions.

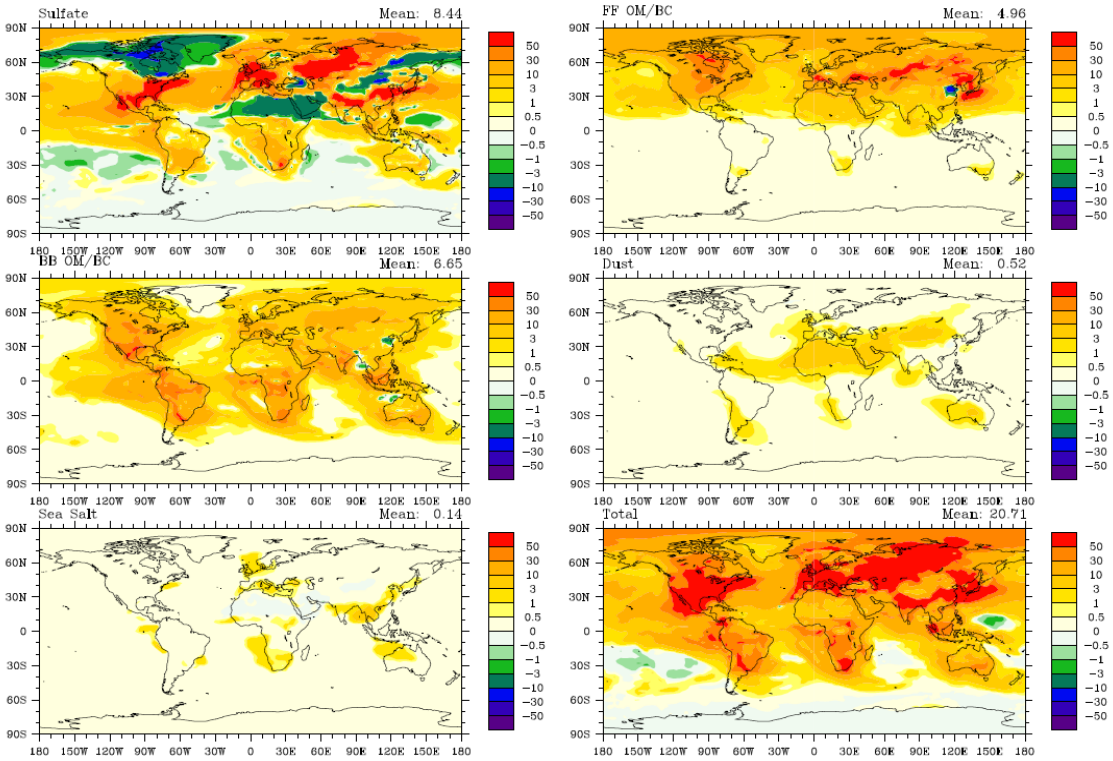

Figure 4.21: The absolute difference of present day annual average cloud droplet number concentration activated from each aerosol type and the total cloud droplet number near 930 mb (the third model level) between the case TN and NN.

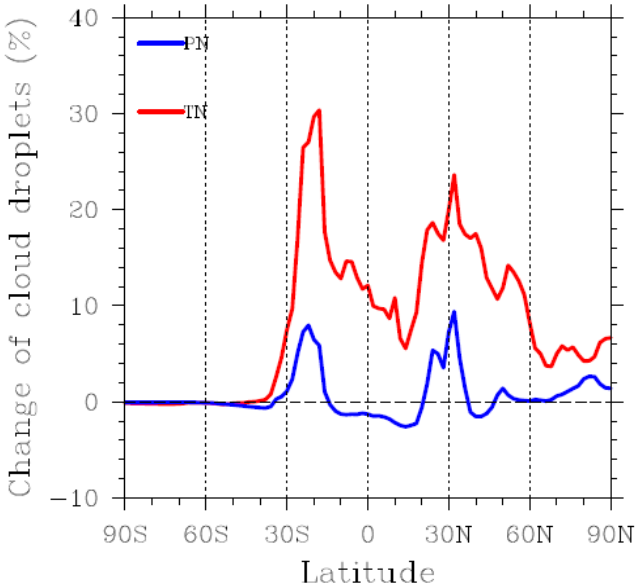

Figure 4.22: The percentage change in zonal annual-average cloud droplet number for the case PN and the case TN compared with the baseline case NN near 930 mb (the third model level).

Figure 4.23 shows the spatial distribution of change in droplet effect radius and the first aerosol indirect forcing for the TN case. The first aerosol indirect forcing in this case is -1.54 W m^{-2}. The spatial distribution of the first indirect forcing is not only determined by the change in the cloud top effective radius but also by the cloud forcing. The maximum in the first aerosol indirect forcing occurs in the storm track region over the north Pacific. This is consistent with the pattern shown in Wang and Penner (2009). This peak is mainly caused by both strong decrease in the cloud effective radius and a large cloud forcing over this region. Another peak of the first indirect forcing appears over the Tibet area, which is in accordance with the decrease of cloud effective radius varying from the PI to PD scenario due to anthropogenic aerosols shown in Figure 4.23 (left panel). Figure 4.24 shows the first aerosol indirect effect of nitrate and ammonium for the PD (top), PI (middle) simulation and the first anthropogenic aerosol indirect forcing of nitrate and ammonium (bottom) at the TOA. The first aerosol indirect effect of total nitrate and ammonium for the PD and PI simulations is estimated to be -0.24 W m^{-2} and -0.14 W m^{-2}, which results in an anthropogenic indirect forcing of -0.1 W m^{-2}, equivalent to a 7% enhancement compared to the case without nitrate and ammonium. The local effects of total nitrate and ammonium for the PD simulation is even larger, up to -1.5 ~ -2 W m^{-2} over Europe, eastern Asia, eastern United States and the coastal area close to central Africa.

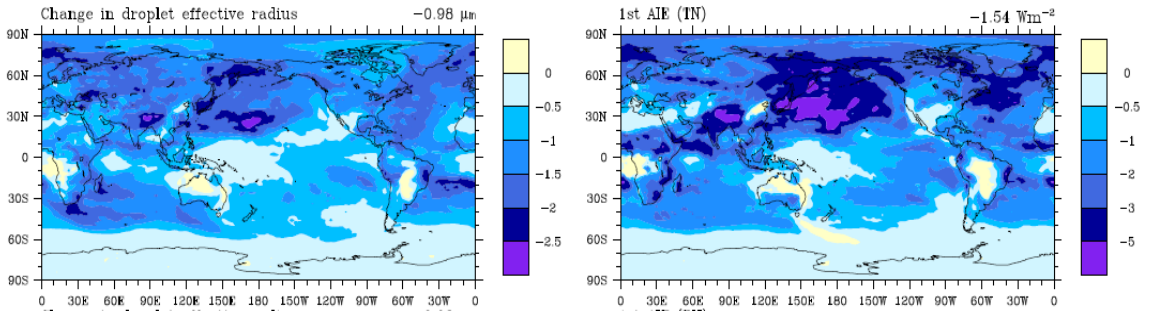

Figure 4.23: The spatial distribution of change in droplet effect radius (left) and the first aerosol indirect forcing (right) for the TN case.

Table 4.11 gives a summary of global annual-average cloud droplet number concentration at the cloud top in the PD and PI (i.e., values in parentheses) simulations, cloud top effective radius, cloud optical thickness, and the absolute change and relative percentage change (i.e., values in parentheses) in cloud top droplet number concentration, cloud top effective radius and cloud optical thickness from anthropogenic emissions, and the 1st AIE for all three cases at the top of atmosphere and at the surface (i.e., values in the parentheses) for all three cases listed in Table 4.10. In general, the cloud top droplet number and cloud optical thickness increase from the NN case to the TN case for both the PD and PI scenarios while the cloud top effective radius decreases. Varying from the PI era to the PD, the cloud top droplet number for the NN, PN and TN cases increases about 62%, 66% and 72%, respectively. However, the relative changes in cloud top effective radius and cloud optical depth are smaller, only about 8-9%. The addition of total nitrate and ammonium contributes to the increase of cloud top droplet number by 10% (comparing the NN case and the TN case in the 5th column) while it only decreases the cloud top effective radius by 0.06 μm (comparing the NN case and the TN case in the 6th column), equivalent to a 0.6% in the relative change. This indicates that the effect of total

nitrate and ammonium on the cloud top effective radius is not as significant as that due to the increase in cloud droplet number. This is consistent with the findings reported by Xue and Fiengold (2004). This is because the cloud droplet effective radius is related to both cloud droplet number and the relative spectral dispersion. As shown in Xue and Feingold (2004), if one assumes constant liquid water content, the change in the effective radius (r_e) and cloud optical thickness (τ) due to the change of cloud droplet number (N_d) and shape parameter of the droplet spectrum (k) can be expressed as

$$\frac{r_e}{r_{e0}} = \left(\frac{k}{k_0}\right)^{-1/3} \left(\frac{N_d}{N_{d0}}\right)^{-1/3}, \tag{4.10}$$

$$\frac{\tau}{\tau_0} = \left(\frac{k}{k_0}\right)^{1/3} \left(\frac{N_d}{N_{d0}}\right)^{1/3}, \tag{4.11}$$

where 0 stands for the case without nitrate. For the condensation process, an increase in N_d is accompanied with an increase in the width of the droplet spectrum ($k/k_0 < 1$) such that the absolute change in r_e is determined by these two counteracting effects simultaneously. They also show that an increase of τ with a range of 0 ~ 14% is accompanied by an increase of 0 ~ 70% in N_d when 1 ppb HNO_3 is present, compared to increases of 0 ~ 110% in N_d and 0 ~20% in τ when HNO_3 increases five-fold (i.e., HNO_3 = 5 ppb). In our work, an increase of 10% of the cloud droplet number at cloud top from the NN case to the TN case is accompanied with an increase of cloud optical thickness by 0.42%. Hence, the broadening effect apparently counters the effect of an increase in the cloud droplet number due to the presence of HNO_3 on the cloud droplet effective radius and cloud optical thickness so that changes in cloud optical properties are not as large as changes in cloud droplet number. As mentioned above, the first aerosol indirect forcing is closely tied to the change in cloud top effective radius. The change in cloud top effective

radius by 0.98 μm from the PI to PD simulation for the case TN causes the forcing about -1.54 W m^{-2}, the net indirect forcing due to the presence of anthropogenic total nitrate and ammonium is expected to be around -0.09 W m^{-2} (i.e., ~ -1.54 W m^{-2} × (0.06 μm/0.98μm)) resulting from the change in cloud top effective radius of 0.06 μm. This qualitative analysis is consistent with our findings shown in Figure 4.24 on a global average basis. Given in Table 4.12, the first aerosol indirect forcing of anthropogenic nitrate and ammonium is -0.1 W m^{-2} and -0.08 W m^{-2} at TOA and at surface, respectively. Figure 4.25 shows the first aerosol indirect forcing of anthropogenic nitrate and ammonium over 5 regions for three cases. Anthropogenic nitrate and ammonium aerosols have higher influence on clouds in the northern hemisphere than in the southern hemisphere and higher effects over the land than over the ocean. The total aerosol first indirect forcing is mainly determined by the nitric acid gas effect, which is -0.09 W m^{-2} on a global average basis. This is the estimate of the nitric acid gas effect in literatures for the first time.

Table 4.11: Global annual-average cloud droplet number concentration at the cloud top in the PD (PI) simulation, cloud top effective radius in the PD (PI) simulation, cloud optical thickness in the PD (PI) simulation[a], absolute (percentage[b]) change in cloud top droplet number concentration, cloud top effective radius and cloud optical thickness from anthropogenic emission, and 1st AIE for all three cases and the difference of the case NN and TN at the top of atmosphere (at surface).

Case	N_d (#/cm^3)	R_e (μm)	τ_c	Change in N_d (#/cm^3)	Change in R_e (μm)	Change in τ_c	1st AIE (W m^{-2})[c]
NN	121.17 (74.60)	10.36 (11.28)	30.49 (27.84)	46.57 (62.43%)	-0.92 (-8.17%)	2.66 (9.55%)	-1.44 (-1.16)
PN	124.95 (75.25)	10.33 (11.26)	30.57 (27.87)	49.70 (66.05%)	-0.93 (-8.26%)	2.70 (9.69%)	-1.45 (-1.17)
TN	134.98 (78.28)	10.22 (11.19)	30.83 (28.01)	56.70 (72.4%)	-0.98 (-8.76%)	2.82 (10.07%)	-1.54 (-1.24)
net[d]							-0.10(-0.08)

[a]The values outside and inside the parenthesis in column 2-4 represent the results from the PD and PI scenario.
[b]The percentage values inside the parenthesis in column 5-7 is calculated as the difference from the PI to the PD divided by the values in the PI scenario.
[c]The values outside and inside the parenthesis represent the forcing at top of atmosphere and at surface.
[d]"net" represents the first aerosol indirect forcing of anthropogenic HNO_3 and nitrate and ammonium aerosol.

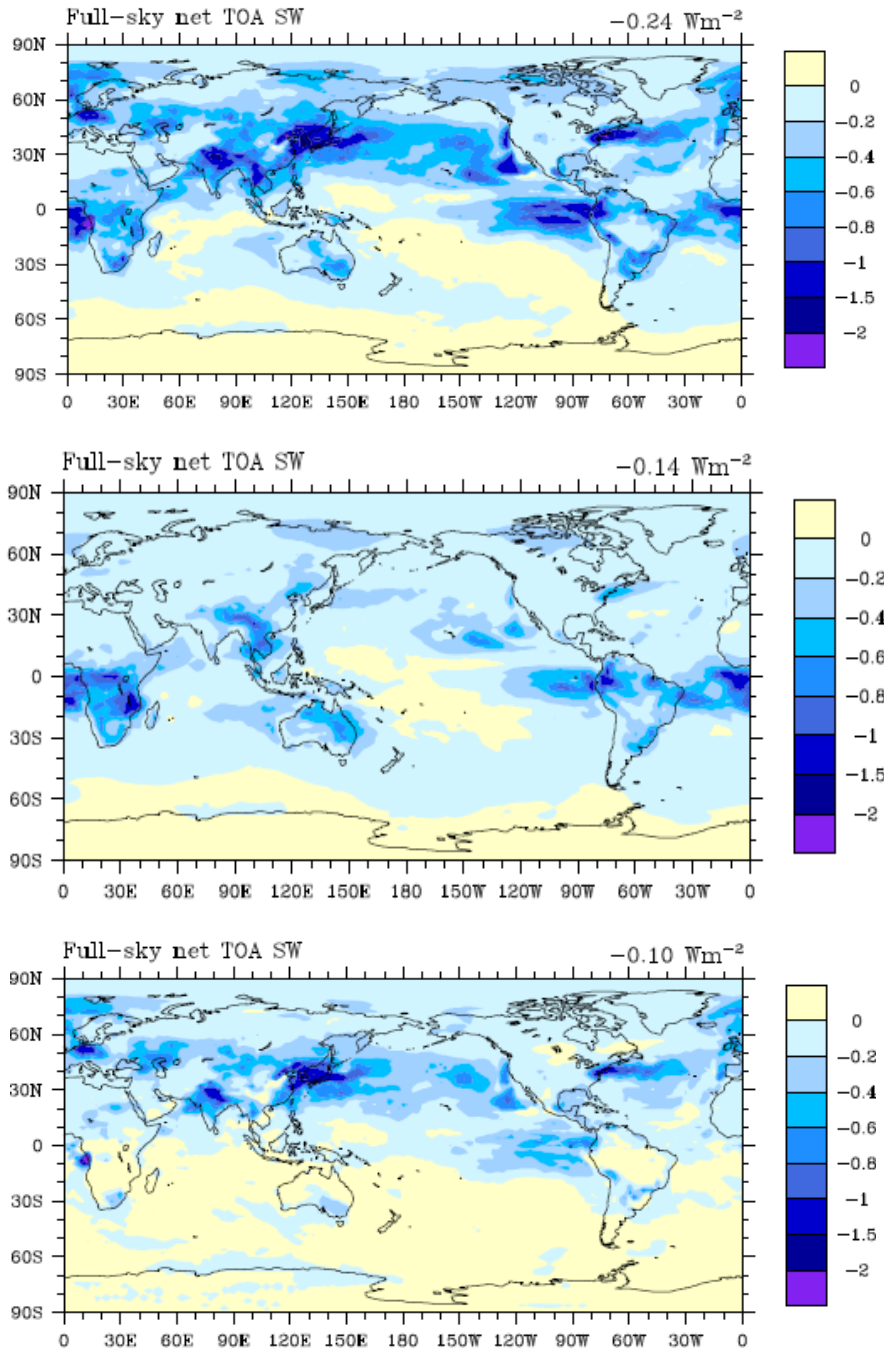

Figure 4.24: The first aerosol indirect effect of nitrate and ammonium aerosols for the PD (top), PI (middle) simulation and the first anthropogenic aerosol indirect forcing of nitrate and ammonium (bottom) at the TOA. The mean forcing value is indicated in each panel.

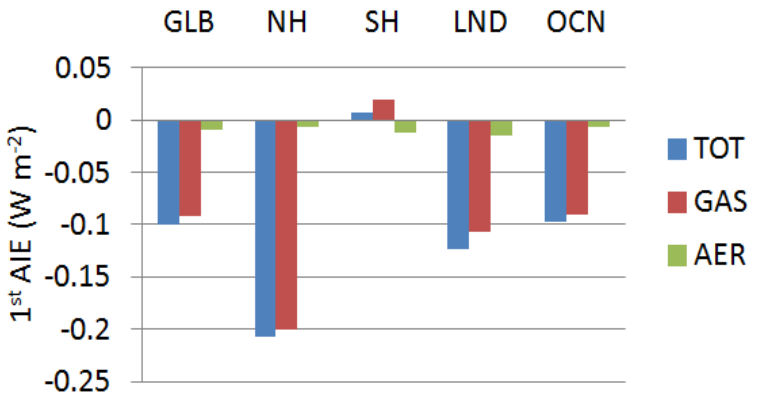

Figure 4.25: The first aerosol indirect forcing at the top of atmosphere over five regions for three cases (AER: PN-NN; GAS: TN-PN; TOT: TN-NN). GLB, NH, SH, LND and OCN stand for the global average, average over the northern and southern hemisphere, average over the land and ocean, respectively.

Figure 4.26 shows the first aerosol indirect forcing calculated for three cases listed in Table 4.10 using monthly, daily and hourly average aerosol fields. It suggests that there is systematic bias by using different frequency of aerosol fields. The estimates based on monthly average aerosol fields for all three cases are generally larger than those estimated from hourly aerosol fields. The change in the global average of the first aerosol indirect forcing using a different frequency to update aerosol fields is within 10%.

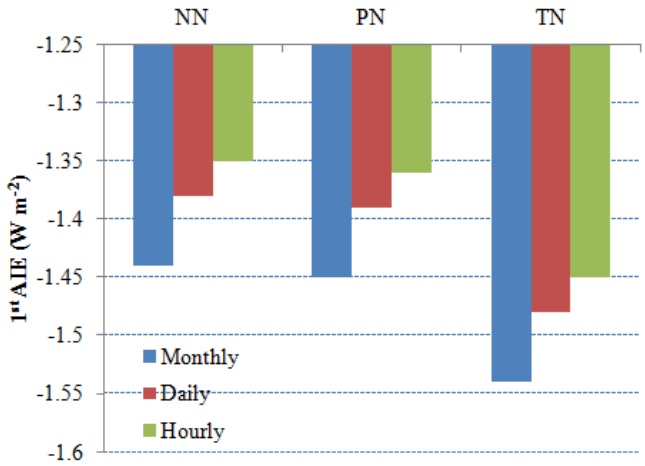

Figure 4.26: The first aerosol indirect forcing calculated for the three cases listed in Table 4.10 calculated using monthly average, daily average and hourly average aerosol concentration fields.

4.7 Summary and discussion

This chapter presents a global modeling study that simulates the heterogeneous formation of nitrate and ammonium by updating the previous model frame work of Feng and Penner (2007). The University of Michigan version of the IMPACT aerosol model which includes sulfur dynamics (Liu et al., 2005) is used as the transport framework to generate the chemical- and size- resolved aerosol global distribution. Here we account for the interaction between nitric acid and ammonia with all five types of pre-existing aerosols (i.e., sulfate, carbonaceous aerosols from fossil fuel combustion, carbonaceous aerosols from biomass burning, dust and sea salt) which differs from the study by Feng and Penner (2007) who assumed that all aerosol components internally mixed in each size bin. Two global simulations with the present day emissions were conducted: one in which we assumed that five pre-existing aerosols are externally mixed (EM) and one in which we assumed that all pre-existing aerosol are internally mixed (IM). The main focus of this study was to examine the difference in the prediction of aerosol ammonium and nitrate using these two treatments with respect to the mixing state of pre-existing aerosols. A second goal was to explore the aerosol direct and indirect radiative forcing induced by HNO_3 gas as well as aerosol ammonium and nitrate. For this purpose, two global simulations with present day (PD) and preindustrial (PI) emissions considering the EM mixing state were conducted. An offline- radiation transfer model was then used to assess both the direct and indirect forcing of HNO_3, nitrate and ammonium using the PD and PI concentration fields.

The model developed here predicts a similar spatial distribution for total nitrate and ammonium as did the pioneer studies (Feng and Penner, 2007; Liao et al., 2003; Adams et al., 1999) for the PD scenario. In most industrialized regions such as in the eastern United States, Europe and China, nitrate aerosol mainly exceeds 1 ppbv, existing in the form of ammonium nitrate in an amount determined by a thermodynamic equilibrium model in the sub-micron aerosols. The formation of ammonium nitrate is limited by the amount of available ammonia, which preferentially reacts with sulfate. Nitrate aerosols formed in these regions are typically present in the fine-mode while less than 10% of nitrate aerosols are associated with fine particles in the regions close to deserts (e.g., Sahara, Asian and Australian deserts). The nitrate formed on dust and sea salt aerosols is highest over the Sahara desert for dust and over coastal regions close to continents for sea salt. Nitrate over continents generally exceeds 300 pptv while the marine mixing ratio of nitrate is in the range of 1-100 pptv except near the coastal regions. In regions with high dust and sea salt aerosols, more than 90% of the total nitrate is present in the aerosol phase, indicating that the formation of nitrate in these regions is limited by the availability of gas-phase HNO_3. The predicted mixing ratios of ammonium are mainly determined by both ammonia emissions and its uptake by sulfate and nitrate. The highest ammonium mixing ratios are found in industrialized and agricultural regions, such as eastern Asia, Europe and the eastern United States and are closely tied with sulfate aerosol. Ammonia is allowed to react with nitrate only if sulfate concentrations are low enough and free ammonia is in excess. As expected, continental ammonium mixing ratios exceed 300 pptv almost everywhere while marine mixing ratios of ammonium range from 100 to 300 pptv.

The predicted NO_3^- lifetime in this work is 4.2 days, lower than that predicted in the simulation following the IM treatment, which was 5.1 day. The shorter lifetime results from larger sources (or sinks). By explicitly accounting for the interaction between nitric acid and all five aerosol types, the total chemical production of aerosol nitrate are increased by about 11% compared with the IM treatment because mineral dust and sea salt provide additional particle surfaces which allows a larger uptake of nitrate. Hence, this work predicts 60% higher fine mode aerosol nitrate through the gas-to-aerosol conversion. Due to different deposition strategies employed in these two treatments, the removal of nitrate in the IM treatment is less efficient than that in the EM treatment in this work. The higher removal rates in the EM treatment results in a lower burden, even though the higher gas-to-particle conversion rate is higher than that in the IM treatment. The nitrate burden in the fine mode is only enhanced by 6% in contrast to the 60% increase in the nitrate production in the fine mode. The difference in the removal rate between these two treatments also causes a lower burden and shorter lifetime of aerosol ammonium compared with the IM treatment.

For the PI scenario, the predicted total burden of nitric acid and nitrate is nearly half as large as that for the PD scenario. The lower removal rate coefficients of aerosol nitrate and nitric acid in the PI scenario result in comparably longer lifetimes than those in the PD scenario. The burden of ammonia and ammonium in the PI scenario is reduced by a factor of six and eight compared with the PD scenario, respectively, resulting from the reduction in the emissions of ammonia by a factor five in the PI scenario. The shorter lifetimes of ammonia and ammonium results from the higher removal rate coefficients from both dry and wet removal processes.

The predicted aerosol optical depth in the present day captures the general spatial pattern of MODIS-observed AOD (e.g. peaks in eastern Asia and the Sahara) but with smaller magnitude. The modeled AOD is underestimated, especially over Siberia and the central Africa biomass burning region, which may reflect intra-annual variations of biomass burning emissions used in this work versus the observations that were for 2001. The modeled single scattering albedo at 550 nm is in general agreement with observations within 7%.

Nitrate and ammonium are found to exhibit two counteracting effects with respect to the direct effect of the pre-existing aerosols in this work. The inclusion of ammonium and nitrate can boost the scattering efficiency of scattering aerosols such as sulfate and biomass burning organic matter since nitrate and ammonium is generally more hygroscopic than sulfate and organic matter and this increases their size and hence their cooling effect. Additionally, nitrate and ammonium contributes to a warming effect when they are internally mixed with sea salt, by lowering ability of sea salt aerosols to take up water due to its lower hygroscopicity than that of sea salt. The direct effect of nitrate and ammonium at TOA in the present-day in this work is estimated to be -0.12 W m^{-2}, within the range of -0.07 W m^{-2} estimated by Jacobson et al. (2001) to -0.30 W m^{-2} by Adams et al. (2001), close to -0.11 W m^{-2} from Bauer et al. (2007) and -0.14 W m^{-2} from Liao et al. (2004). Smaller forcing is estimated for the PI scenario due to smaller burden of ammonium and nitrate. The anthropogenic forcing of nitrate and ammonium is estimated to be -0.21 W m^{-2} and -0.25 W m^{-2} at TOA and at surface for the clear-sky condition while it is -0.11 W m^{-2} and -0.15 W m^{-2} at TOA and surface for the cloudy-sky condition. There is a strong cooling of up to -3 W m^{-2} over Easter Asia, North America and Europe,

which is consistent with the areas where nitrate and ammonium aerosols are highest. The anthropogenic nitrate and ammonium direct forcing at the surface of -0.15 W m^{-2} calculated here is comparable to the -0.15 W m^{-2} estimated by Liao et al. (2005). The simulated results using monthly, daily and hourly average aerosol fields indicate that the frequency of the update of aerosol fields does not change the direct effect of nitrate and ammonium by a large amount, since all treatments are within 5%.

The indirect effect induced by total nitrate (gas and particle phase) and ammonium was also examined in this work based on the parameterization proposed by Chen (2006) who found that both aqueous phase nitrate and gas phase nitric acid have effect on cloud activation. During the cloud formation in a parcel model, most of the gas phase nitric acid can be redistributed to the aerosol phase in the fine mode. In this work, we first calculated the cloud droplet number without accounting for the effect of gas phase nitric acid and then we distributed the nitric acid to each aerosol type in the fine mode according to their relative activation fraction calculated in the first step. Finally, an updated cloud droplet number was calculated with this new aerosol distribution. The total nitrate effect on the cloud droplet number concentration was found to have two counteracting effects. On one hand, the addition of nitrate (and ammonium) and nitric acid boosts the number of cloud droplets by lowering the critical supersaturation and increasing the hygroscopicity of smaller particles. This increasing effect is dominant over continents. On the other hand, the addition of total nitrate and ammonium also decreases cloud drop number if more HNO_3 is distributed to the larger particles. This decreasing effect is found to dominate over remote oceans, consistent with the dynamic competition phenomena between sea salt and sulfate reported by Ghan et al. (1998). As expected, the cloud droplet number

increases with the addition of nitrate and ammonium on a global basis. However, the magnitude of the cloud optical properties change is not as large as that of droplet number because the addition of total nitrate and ammonium contributes to the broadening of the cloud droplet spectrum when it increases the cloud droplet number. Hence, the relative change in cloud droplet effective radius and cloud optical depth is smaller than the relative change in cloud droplet number. This is consistent with the findings in Xue and Feingold (2004). In summary, the first aerosol indirect effect of total nitrate and ammonium for the PD and PI simulation is estimated to be -0.24 W m^{-2} and -0.14 W m^{-2} at TOA, leading to the first aerosol indirect forcing of -0.1 W m^{-2} at TOA induced by anthropogenic HNO_3 gas, nitrate and ammonium. Anthropogenic nitrate and ammonium aerosols have higher influence on clouds in the northern hemisphere than in the southern hemisphere and higher effects over the land than over the ocean. The anthropogenic first indirect forcing of total nitrate and ammonium is mainly determined by the nitric acid gas effect, which is -0.09 W m^{-2} on a global basis. This is the first estimate of the nitric acid gas effect in literatures. The change of the first aerosol indirect forcing caused by using a different frequency of the update of aerosol fields is less than 10%.

CHAPTER V

COMPARISON OF SATELLITE-BASED AND MODELED AEROSOL INDIRECT FORCING

5.1 Introduction

Atmospheric aerosols play an important role in the climate system. Aerosols can impact the earth's radiation balance directly through reflecting and absorbing incoming solar radiation back to space and indirectly through changing cloud microphysical properties by acting as cloud condensation nuclei or ice nuclei. Increased aerosol concentration may lead to an increase in the cloud droplet number concentration at constant cloud liquid water path, resulting in smaller cloud droplet effective radii and larger cloud albedo (Twomey, 1974). This process is referred to as the "first aerosol indirect effect" or "cloud albedo effect". The reduction of cloud effective radii may further enhance the cloud lifetime and liquid water content by lowering the collision/coalescence rate (Albrecht, 1989). This process is referred to as the "second aerosol indirect effect" or "cloud lifetime effect". These aerosol effects enhance the planetary albedo, thus contributing a negative climate forcing and cooling the earth

climate system. Radiative forcing is defined by IPCC as the net change in radiative flux at the tropopause after stratospheric equilibrium is reached (Ramaswamy et al., 2001). The cloud lifetime effect is consequently classified as a feedback by IPCC Fourth Assessment Report (AR4) (IPCC, 2007) as opposed to the "radiative forcing" of the albedo effect, since the hydrological cycle is altered by prolonging cloud lifetime through suppressing drizzle (i.e., feedbacks occur). Hence, the aerosol indirect effect is referred to as the first aerosol indirect effect (AIE) hereafter in this work.

The first aerosol indirect effects due to anthropogenic aerosols are observed in numerous field studies, for example, observations of ship tracks perturbing marine stratus cloud decks off the coast of California (Ferek et al., 1998), over the Atlantic Ocean (Brenguier et al., 2000; Schwartz et al., 2002), at the Pt. Reyes station on the coast of the California where marine stratocumulus are the predominant cloud type (McComiskey et al., 2009), over continental areas (Kauman et al., 1997; Feingold et al., 2003; Penner et al., 2004), and over the entire globe (Bréon et al., 2002; Brenguier et al., 2003). The interactions between natural and anthropogenic aerosol particles and clouds are complex and nonlinear (Ramaswamy et al., 2001). The existence of the first aerosol indirect effect is not in question, but the quantification of this effect is highly uncertain as it varies under various environmental and meteorological conditions in addition to different observational approaches.

The aerosol indirect effect is recognized as one of the largest uncertainties in our understanding of climate change since its magnitude can be comparable to warming effects due to greenhouse gases. Although there have been a large number of studies on the development of understanding aerosol indirect effects on the global climate system

over the past decade, uncertainties in the estimation of the indirect aerosol forcing are still large. The IPCC Third Assessment (AR3) concludes that the global modeled mean Twomey effect of anthropogenic aerosol particles is about 0 to -2 W m^{-2} (Ramaswamy et al., 2001) but did not assign a best estimate of the radiative forcing. Lohmann and Feichter (2005) summarized that the cloud albedo effect and the cloud lifetime effect according to available model-based estimates are within the range of -1.9 to -0.5 W m^{-2} and -1.4 to -0.3 W m^{-2}, respectively. The IPCC AR4 narrows down the uncertainty in the cloud albedo effect and presents a best estimate of -0.7 W m^{-2} as the median with a 5% to 95% confidence interval range of -0.3 to -1.8 W m^{-2}. They further increased the level of scientific understanding from *very low* in the IPCC AR3 to *low* at present (Forster et al., 2007).

Estimation of the aerosol indirect effect is typically made using free-running global models (Boucher and Lohmann, 1995; Kiehl et al., 2000; Lohmann et al., 2000; Ghan et al., 2001; Iversen et al., 2002; Menon et al., 2002; Kristjánsson, 2002; Chuang et al., 2002; Chen and Penner, 2005; Penner et al., 2006; Wang and Penner, 2009), using global models constrained by satellite observations (Lohmann and Lesins, 2002; Quaas et al., 2005; Quaas et al., 2006), and directly derived from satellite observations (Kaufman et al., 1997; Nakajima et al., 2001; Sekiguchi et al., 2003; Quaas et al., 2008; Quaas et al., 2009). The magnitudes as well as uncertainties in the quantification of the cloud albedo effect are approach dependent as indicated in the wide spread in the estimation of aerosol indirect forcing in IPCC AR4.

For the model-based estimates, the aerosol indirect effect is usually assessed by prognostic variables such as cloud droplet number, aerosol mass and number

concentration as well as updraft velocity to represent the aerosol-cloud interaction by use of a parameterization based on the classical theory of aerosol activation. The uncertainties stem from many aspects. For example, global models have weaknesses in representing the interaction between ambient aerosol particle concentrations and resulting cloud droplet size distribution, the convection-cloud interaction, along with simulating updraft velocities, etc. Chen and Penner (2005) examined the spatially-resolved uncertainty in estimates of the first indirect aerosol forcing and found that the aerosol burden calculated by chemical transport models and the cloud fraction are the most important sources of uncertainty. Variation in the aerosol mass concentration from the minimum values obtained from IPCC model inter-comparison to the maximum values (Table 5.2 and 5.3 in Penner et al., 2001) causes the change of the aerosol indirect forcing by a factor of 2 from -0.94 W m^{-2} to -2.16 W $^{-2}$ in the global mean. Note that the IPCC aerosol inter-comparison project is to estimate the uncertainty associated with aerosols mass concentration provided by a fixed set of aerosol precursor emissions and aerosol concentrations are closely tied with their emission in the models used in the IPCC inter-comparison. Chen and Penner (2005) also explored the impact of different cloud nucleation schemes on the aerosol indirect effect and found that changing from the Abdul-Razzak and Ghan (2002) to the Nenes and Seinfeld (2003) parameterization results no significant change of the aerosol indirect effects while changing to the Chuang et al. (1997) parameterization results in more negative radiative forcing in the absolute value. Chen and Penner (2005) further investigated the uncertainty of the aerosol first indirect effect due to the inclusion of the dispersion effect and found that the radiative effect is generally less negative than the base case, which is consistent with the study of

Rotstayn and Liu (2003) who found a 12 to 35% decrease in the aerosol indirect effect when the size dispersion effect was included for the sulfate aerosols. This range might be even larger if the particle nucleation is included. Wang and Penner (2009) found that the forcing from various treatments of aerosol nucleation ranges from -1.22 to -2.03 W m^{-2}. Hoose et al. (2009) confirmed this uncertainty due to the particle nucleation mechanism and found that the short-wave cloud forcing can vary from -1.88 to -0.62 W m^{-2} if the lower bound of cloud droplet number is increased from 0 to 40 cm^{-3}.

On the other hand, for the satellite-based estimates, the aerosol indirect effect is quantified by incorporating empirical statistical relationships between proxy of column aerosol loadings (e.g., aerosol optical depth, aerosol index, etc) and proxy of column cloud properties (e.g., cloud droplet number concentration, cloud effective radius, cloud fraction, liquid water path, etc) derived from satellite observations. Various assumptions made during the retrieval of satellites, such as the assumption that aerosol and cloud properties are coincident or aerosol optical depth can be linked to the aerosol concentration below the cloud, may introduce uncertainties. Differences in perspective as well as mismatched sampling in space and time will result in variability and error in the characterization of aerosol-cloud interactions (McComiskey et al., 2009). Moreover, as shown in the study of Grandey and Stier (2010), the spatial scale choices used for the satellite-based estimation of aerosol indirect effects are of great importance. For region sizes larger than 4°x4°, significant error of calculations of slopes of $\ln(N_d)$ versus ln(AOD) or ln(AI) can be introduced. Several research groups tend to use satellites to estimate aerosol indirect forcing. For instance, Nakajima et al. (2001) presented an estimate of the global averaged aerosol indirect effect of -1.3 W m^{-2} ranging from -0.7 to

-1.7 W m^{-2} over the ocean derived from the advanced Very High Resolution Radiometer (AVHRR) remote sensing data. Lohmann and Lesins (2002) used the aerosol index (i.e., aerosol optical depth times Angström exponent) and cloud droplet radius from the POLarization and Directionality of the Earth's Reflectances (POLDER) satellite to constrain the modeled susceptibility of clouds to aerosols, which yields a global aerosol indirect effect of -0.85 W m^{-2}. This reduced the pure modeled estimation by 40%. Sekiguchi et al. (2003) presented that the aerosol indirect effect estimated from the AVHRR satellite is -0.64 ± 0.16 W m^{-2} and that from the POLDER satellite is -0.37 ± 0.09 W m^{-2}. In light of discrepancies among satellite observations of the aerosol indirect effect, Rosenfeld and Feingold (2003) pointed out that limitations of the POLDER satellite retrieval could explain this discrepancy. They also suggested that caution should be exercised when using the POLDER-retrieved aerosol indirect effect on clouds since it's blind to deeper clouds with stronger updrafts, which is of great importance in determining the aerosol indirect effect according to in-situ measurements (Feingold et al., 2003), surface-based remote sensing (Ramanathan et al., 2001) and modeling (Chen and Penner, 2005). Quaas and Boucher (2005) constrained the Laboratoire de Météorologie Dynamique-Zoom (LMDZ) general circulation model (GCM) by using the POLDER and the Moderate Resolution Imaging Spectroradiometer (MODIS) satellites, which results in 50% reduction of the simulated AIE from their baseline simulation. Quaas et al. (2006) also attempted to estimate the AIE simulated from ECHAM4 and LMDZ climate models by constraining the modeled statistical relationship between cloud droplet number concentration and fine-mode aerosol optical depth to the one inferred from the MODIS satellite. The results show the agreement with their previous study (Quaas and Boucher,

2005), i.e., the weakening of the AIE consistently occurs for both models with the amount of the reduction 37% in LMDZ and 81% in ECHAM4. Quaas et al. (2008) attempted to estimate aerosol indirect forcing based on the exclusive information of the Earth radiation budget instrument (CERES) and MODIS satellites, in which the estimated value of aerosol cloud albedo effect -0.2 ± 0.1 W m^{-2} was reported.

In general, the pure satellite-based estimates or the GCM-estimated aerosol indirect radiative forcings constrained by satellites are consistently lower than those based on deterministic calculations of aerosol effects on cloud microphysical or optical properties in global models. Instrument artifacts as discussed by Rosenfeld and Feingold (2003) may be attributable to one of the reasons explaining this underestimation. On the other hand, it may also be ascribed to the fact that the satellite-based methods (i.e., the use of empirical statistical relationships between proxy of column aerosol loadings and proxy of column cloud properties based on the present-day values) do not practically account for the evolution of aerosol loadings and resulting cloud properties from the pre-industrial to present-day. The satellite-based method heavily depends on a key factor, i.e., the empirical statistical relationship, which is a measure of relative changes of cloud properties due to relative changes of aerosol amount at a given spatial scale. According to the IPCC AR4 (IPCC, 2007), the radiative forcing of the aerosol indirect effect can be interpreted as the difference in flux that occurs as a result of changes in cloud properties for present day (PD) and pre-industrial (PI) aerosol concentrations. As opposed to model-based estimates, satellite-based estimates of aerosol indirect effect are made basically by adopting spatial changes of cloud properties with spatial changes of aerosol amount during the PD conditions instead of temporal variations of aerosol and cloud fields in

going from the PI to PD condition. The question prompts out: is the magnitude of the spatial variation of cloud properties with spatial changes of aerosol amount during the PD conditions equivalent to that in temporal variations of aerosol and cloud fields in going from the PI to PD condition?

In the present study, we follow the satellite-based method described in Quaas et al. (2008) and address that satellites may underestimate the aerosol indirect effect. Section 5.2 describes our methods (including the coupled model, calculations of cloud droplet number as well as aerosol first indirect forcing, calculation of aerosol optical properties). In section 5.3, a description of empirical measures of the aerosol-cloud interaction used for estimates of aerosol indirect effects with observations are presented along with the calculation of two types of statistical slopes based on either only PD values or PD and PI values of aerosol and cloud properties. Section 5.4 presents global aerosol mass budgets in present day (PD) and pre-industrial (PI) simulations. Section 5.5 presents results of PD and PI simulations including statistical relationship between cloud droplet number concentration (CDNC) and aerosol optical depth (AOD) or aerosol index (AI), CDNC, cloud effective radius, AOD and AI for PD and PI simulations, and aerosol indirect forcing. The sensitivity of cloud condensation nuclei (CCN) activation varying with aerosol loadings is also explored in Section 5.5. Finally, Section 5.6 presents discussions and summarizes conclusions.

5.2 Methods

5.2.1 The coupled IMPACT/CAM model

The model used here has two components as described in details in Wang et al. (2009): the NCAR CAM3 atmospheric circulation model (Collins et al., 2006a), and the LLNL/Umich IMPACT aerosol model (Liu et al., 2005). The atmospheric general circulation model (GCM) component (NCAR CAM3) is a part of the Community Climate System Model (CCSM3) (Collins et al., 2006b). Boville et al. (2006) and Collins et al. (2006a) document the physical parameterizations used in the GCM and its performance in detail.

Table 5.1: Size distribution parameters for non-sulfate aerosols.

Aerosol Component	N_i[a]	r_i, μm	σ_i
Fossil fuel OM/BC	0.428571	0.005	1.5
	0.571428	0.08	1.7
	1.e-6	2.5	1.65
Biomass OM/BC and natural OM	0.9987	0.0774	1.402
	1.306e-3	0.3360	1.383
	2.830e-3	0.9577	1.425
Sea salt	0.965	0.035	1.92
	0.035	0.41	1.70
Dust	0.854240	0.05	1.65
	0.145687	0.27	2.67
	7.3e-5	4.0	2.40

[a]N_i is normalized fraction by total number concentration in a given size range and is dimensionless.

The aerosol model component (IMPACT) simulates the dynamics of sulfate aerosol and its interaction (i.e., nucleation, condensation and coagulation) with non-sulfate aerosols (i.e., carbonaceous aerosol (organic matter (OM) and black carbon (BC)), dust

and sea salt) (Herzog et al., 2004; Liu et al., 2005). Three modes of the mass and number of pure sulfate aerosol are predicted, which includes a nucleation mode (r < 0.005 μm), an Aitken mode (0.005 μm <= r < 0.05μm) and an accumulation mode (r > 0.05 μm). Non-sulfate aerosols are assumed to follow prescribed background size distributions given in Table 5.1 (Table 1, Wang et al., 2009; Liu et al., 2005). Carbonaceous aerosols (OM and BC) are represented by one single submicron size bin with a superposition of three lognormal distributions separately assumed for biomass burning, natural and fossil fuel particles based on their source origins. Sea salt and mineral dust aerosols are represented in four bins with radii varying from 0.05-0.63 μm, 0.63-1.26 μm, 1.26-2.5 μm, and 2.5-10 μm accounting for their mass size distribution, thermodynamics as well as the CCN activation spectrum under typical supersaturations. The size distribution within each size bin follows a predefined distribution with a superposition of three lognormal distributions on dust and of two lognormal distributions on sea salt. The concentration of sulfuric acid gas (H_2SO_4(g)) produced from the gas phase oxidation of DMS and SO_2 is allowed to nucleate to form new sulfate particles in the nucleation mode or to condense onto preexisting sulfate and non-sulfate aerosol particles. Sulfate aerosol particles are also allowed to coagulate with other particles. The empirical boundary layer nucleation scheme (Kulmala et al., 2006; Sihto et al., 2006; Ripinen et al., 2007) together with the binary homogeneous nucleation of sulfate particles for the free troposphere are used to determine the nucleation of sulfate aerosols (Wang et al., 2009). In addition, 2% of anthropogenic sulfur emissions are assumed to be primary emitted aerosols with a specified size distribution to mimic the effects of sub-grid scale processes leading to aerosol nucleation since Wang and Penner (2009) found that including primary emitted

sulfate particles significantly increases both anthropogenic fraction of cloud condensation nuclei concentrations as well as the first aerosol indirect effect. The hydrophilic and hydrophobic properties and corresponding scavenging efficiency of non-sulfate aerosols are determined by the amount of sulfate coating that is produced through coagulation and condensation. The aqueous production of sulfate is equally distributed among the hygroscopic aerosol particles that are larger than 0.05 μm in radius.

We used 26 vertical levels and a horizontal resolution of 2 × 2.5 degrees for both the CAM3 and IMPACT models in this study. The time step for CAM3 was 30 minutes, and the time step for advection in IMPACT was 1 hour.

5.2.2 Calculation of cloud droplet number concentration and the first aerosol indirect forcing

The calculation of cloud droplet number concentration (CDNC) and the estimation of the first aerosol indirect forcing follow the procedure described in Wang and Penner (2009). Figure 5.1 (Figure 1, Wang and Penner, 2009) shows processes included in the estimation of the first aerosol indirect effect (AIE).

Firstly, the cloud droplet number concentrations are calculated based on the Köhler theory following the parameterization of Abdul-Razzak and Ghan (2000; 2002) using present day (PD) and pre-industrial (PI) aerosol fields obtained from the coupled CAM-IMPACT model. This parameterization combines the treatment of multiple aerosol types and a sectional representation of size to deal with arbitrary aerosol mixing states and arbitrary aerosol size distributions. Five types of aerosols are assumed to be externally mixed: pure sulfate, fossil fuel OM/BC with sulfate coatings, biomass burning OM/BC with sulfate coatings, sea salt (4 bins) with coated sulfate and dust (4 bins) with coated

sulfate. The sulfate coatings on the non-sulfate aerosol components are treated as internally mixture. The hygroscopic parameter for each type of aerosol is calculated by the volume weighted average of the parameters for each aerosol component following the choices of Ghan et al. (2001) listed in the Table 5.2. The size distribution of pure sulfate aerosols is predicted from the coupled model while those of non-sulfate aerosols are prescribed as in Table 5.1. A lower limit of the cloud droplet number concentration of 20 cm^{-3} is set to represent the minimum cloud droplet number concentration in the background atmosphere since sea salt concentrations predicted in our model might be underestimated (Wang and Penner, 2009). Note that the use of this minimum number concentration brings uncertainties to the estimation of AIE (Wang and Penner, 2009; Hoose et al., 2009). The updraft velocity used in the cloud droplet number parameterization is based on Morrison et al. (2005) with some adjustments discussed in Wang and Penner (2009).

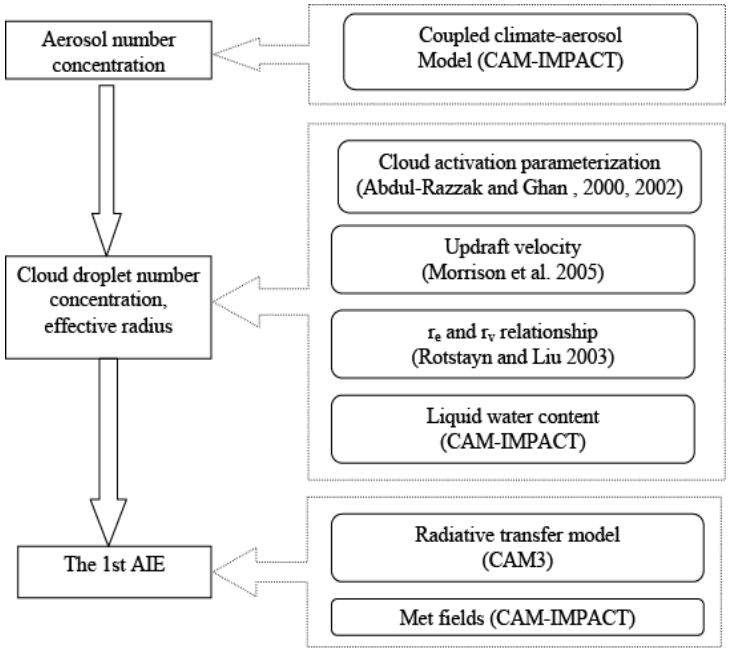

Figure 5.1: Diagram showing the processes included in the estimation of the first aerosol indirect effect (Wang and Penner, 2009).

Table 5.2:.Hygroscopicity, density and refractive index for each aerosol component.

Aerosol Component	Hygroscopicity[a]	Density (g/cm^3)	Refractive index[b]
Sulfate	0.51	1.7	1.53-1.e-7i
BC	5.0e-7	1.5	1.80-0.5i
OM	0.13	1.2	1.53-1.e-7i
Sea Salt	1.16	2.2	1.381-5.8e-7i
Dust	0.14	2.6	1.53-1.4e-3i

[a]The hygroscopicity parameter depends on the number of dissolved ions per molecule, the osmotic coefficient, the soluble mass fraction, the component density, and the molecular weight, as defined by Equation 3 in Abdul-Razzak and Ghan (2000). Values are taken from Ghan et al. (2001).
[b]Refractive index at the wavelength 550 nm.

The effective radius of nucleated droplet populations, related to the volume mean radius of the cloud droplets calculated from the cloud droplet number concentration and the liquid water content, are parameterized following Rostayn and Liu (2003) accounting for the dispersion effect. The liquid water path as well as the cloud fraction in the PD

condition taken from the coupled model is used when calculating radiative fluxes for both PD and PI conditions in order to calculate the first AIE defined by IPCC (i.e., the effects of perturbed aerosols on corresponding changes of cloud properties at the constant liquid water path).

Cloud droplet number concentration and effective radius were used to calculate the cloud optical depth and further the first aerosol indirect forcing in an offline radiative transfer model described in Wang and Penner (2009). The meteorological fields are taken from the coupled CAM3/IMPACT model with a four-hourly frequency. The time step in the radiative transfer model is one hour. The concentrations of trace gases, such as CO_2 and O_3, are same as those in the NCAR CAM3 model. The impacts of aerosols on all liquid water clouds including both large scale and convective clouds are considered in this study.

5.2.3 Calculation of aerosol optical properties

Aerosol optical depth (AOD) was calculated using a three dimensional lookup table that included optical properties from a Mie scattering calculation, i.e., real and imaginary refractive indices and the size parameter ($x=2\pi r/\lambda$, where r and λ are the aerosol radius and wavelength, respectively), so that arbitrary internal mixtures and sizes of aerosols could be included. The optical depth at 495 nm and 670 nm were used to compute Ångström exponent (AE) as follows,

$$AE = -\log(\tau_{a(\lambda_2)} / \tau_{a(\lambda_1)}) / \log(\lambda_2 / \lambda_1), \quad (5.1)$$

where τ_a is aerosol optical depth, $\lambda_1 = 495$ nm and $\lambda_2 = 670$ nm. The Ångström exponent varies inversely with particle size. The smaller the particle, the greater the corresponding Ångström exponent.

Five categories of aerosols are externally treated in the calculation of aerosol optical depth in accordance with the treatment in the parameterization of cloud droplet number concentrations as described in Section 5.2.2:

1) pure sulfate (2 modes: nucleation/Aitken and accumulation mode)
2) fossil fuel and bio-fuel OM/BC with their sulfate coatings
3) open biomass burning OM/BC with their sulfate coatings
4) dust (bin 1-4) with their sulfate coatings
5) sea salt (bin 1-4) with their sulfate coatings

The values for the hygroscopicity of organic matter and sulfates which determines the particle growth under different relative humidity conditions is same as used in the calculation of cloud droplets shown in Table 5.2. The wet size of aerosols is calculated accounting for soluble fraction for each type aerosol following the Köhler theory. For dust and sea salt aerosols, optical properties are calculated separately for the 4 size bins in the model (0.05-0.63 μm, 0.63-1.25 μm, 1.25-2.5 μm and 2.5-10 μm). The refractive index for each aerosol component used for the calculation of aerosol optical properties at the wavelength 550 nm is listed in Table 5.2 following Liu et al. (2007).

5.3 Empirical measures of aerosol-cloud interactions

5.3.1 Aerosol-cloud interaction relationships based on the theory

As the aerosol first indirect effect represents the response of the increase of cloud droplet number concentrations with increased aerosols at constant cloud liquid water path, the representation of this interaction in the observational world requires observed changes of cloud optical or microphysical properties due to observed changes of

associated aerosol loadings. According to Towmey (1977), as cloud condensation nuclei concentrations (N_{CCN}, defined as the subset of total aerosol population that can account for the formation of clouds), cloud droplet number concentrations (N_d) increase. At the fixed cloud liquid water, an increase in N_d results in a smaller cloud droplet effective radii (r_e), causing a higher cloud optical depth (τ_d), and thereby a higher albedo or reflectance. Observed proxies of aerosol amount usually include aerosol optical depth (τ_a), aerosol index (AI), aerosol mass (m_a or sometimes m_{SO4}) and number (N_a) concentrations while τ_d, r_e and N_d are used for corresponding proxies of clouds.

Kaufman and Fraser (1997, referred as to KF97 thereafter) used a matrix of $\Delta r_e / \Delta \tau_a$ as a measure of the aerosol indirect effect to study the effect of smoke particles on clouds using satellite data over the Amazon Basin and Cerrado. Following KP97, Feingold et al. (2001) introduced a measure of aerosol-cloud interaction as follows.

For a homogeneous or adiabatically stratified cloud with cloud droplet number concentration N_d and cloud drop effective radius r_e, the cloud optical depth τ_d can be expressed as:

$$\tau_d = \frac{3Q_{ext}W}{4r_e}, \tag{5.2}$$

where W is cloud liquid water path, Q_{ext} is extinction efficiency, which is about 2 for the wavelength much shorter than r_e. At the constant cloud liquid water path (LWP), according to Twomey (1977),

$$\tau_d \propto N_d^{1/3} \tag{5.3}$$

$$N_d \propto N_a^{a1} \tag{5.4}$$

If assuming

$$\tau_a \propto N_a \ , \tag{5.5}$$

combining Eqn. (5.2)-(5.5) yields

$$r_e \propto \tau_a^{-a1/3} . \tag{5.6}$$

Hence, the aerosol-cloud interaction (ACI) relationships can be expressed as

$$ACI = \left.\frac{\partial \ln \tau_d}{\partial \ln \alpha}\right|_{LWP} = -\left.\frac{\partial \ln r_e}{\partial \ln \alpha}\right|_{LWP} = \frac{1}{3}\frac{d \ln N_d}{d \ln \alpha} = \frac{a1}{3} . \tag{5.7}$$

Note that the ACI relationship is a microphysical response of clouds to changes of aerosol amount adjacent to clouds that is not equivalent to the radiative forcing of AIE (Feingold et al., 2001).

Based on Twomey (1977), it can be shown that ACI ranges from 0 to 0.33 since a1 is less than 1. a1 can reach maximum values only if all aerosol particles are activated to cloud droplets. A characteristic value of a1 is 0.7 (e.g., Pruppacher and Klett, 1997; Chalson et al., 1987) or 0.8 proposed by Twomey (1974), which yields ACI equal to 0.23 and 0.27, respectively. Table 5.3 lists ACI values reported in peer literatures over past two decades. Values in bold are presented as published. For the purpose of easy comparison, all values have been converted to the form of $d \ln N_d / d \ln \tau_a$ (i.e., a1) termed as ACI_N, which is basically three times of ACI values defined in Eqn. (5.7), since it is the matrix that we focus on in this study. ACI_N values based on in situ measurements, ground-based remote sensing as well as satellites shown in Table 5.3 nearly cover an entire range between 0 to 1, indicating there is quite a wide spread among observations. The uncertainties inherent in various instruments which observations are made as well as retrieval algorithm may contribute to this spread. In general, ACI values reported from in situ and ground-based observations are higher and close to the typical

value (i.e., around 0.7 or 0.8) from the aerosol activation theory than those from satellites. Hence, using empirical constraints to parameterize the model may be problematic (McComiskey and Feingold, 2009). This discrepancy, to some extent, explains the fact that pure satellite-based estimates (Quaas et al., 2008) or GCM-estimated aerosol indirect forcing with satellite–based empirical constraints (Lohmann and Lesins, 2002; Quaas et al., 2004) are consistently lower than those that use prognostic variables such as droplet number, aerosol mass concentration as well as updraft velocity to represent aerosol-cloud interactions by using a parameterization based on the theory of aerosol activation.

Table 5.3: ACI values reported in literatures[a].

Reference	ACI			Platform
	$\frac{\partial \ln \tau_d}{\partial \ln \alpha}$	$-\frac{\partial \ln r_e}{\partial \ln \alpha}$	$\frac{d \ln N_d}{d \ln \alpha}$	
Kaufman et al. (1991)			**0.7**	aircraft
Leaitch et al. (1992)			**0.257**	aircraft
Raga and Jonas (1993)			**0.26**	in situ airborne
Martin et al. (1994)			**0.75**	in situ airborne
Gulltepe et al. (1996)			**0.67**	in situ airborne
O'Dowd et al. (1999)			**0.60**	in situ airborne
Ramanathan et al. (2001)			**0.64-1**	in situ airborne
McFarquhar and Heymsfield (2001)			**0.34**	in situ airborne
Twohy et al. (2005)			**0.81**	in situ airborne
Feingold et al. (2003)		**0.02 to 0.06**	(0.06 to 0.18)	surface RS[b]
Garrett et al. (2005)		**0.13 to 0.19**	(0.39 to 0.57)	surface RS
McComisky et al. (2009)			**0.18 to 0.69**	surface RS
Nakajima et al. (2001)			**0.5 (ocean)**	AVHRR
Sekiguchi et al. (2003)[c]			**0.388 (ocean)**	AVHRR
Chamiedes et al. (2002)[d]	**0.13 to 0.19**		(0.39 to 0.57)	ISCCP
Breon et al. (2002)		**0.085(ocean); 0.04(land)**	0.255 (ocean); 0.12 (land)	POLDER
Quaas et al. (2004)		**0.042(ocean); 0.012(land)**	0.126 (ocean); 0.036 (land)	POLDER
Quaas and Boucher (2005)[e]			**conv: 0.45(ocean); 0.3(land)** **strat: 0.25(ocean); 0.2(land)**	POLDER
			conv: 0.25 **strat: 0.15**	MODIS
Quaas et al. (2006)			**0.3 (ocean)**	MODIS
Menon et al. (2008)		**0.11**	(0.33)	MODIS
		0.17	(0.51)	CERES
Bulgin et al. (2008)		**0.10 to 0.16**	(0.30 to 0.48)	ATSR-2
Quaas et al. (2009)			**0.256(ocean); 0.083 (land)**	MODIS Terra
			0.251(ocean); 0.078 (land)	MODIS Aqua

[a]Values in bold are presented as published. All values have been converted to the form $d \ln N_d / d \ln \tau_a$ for comparison purpose.

[b]RS, remote sensing.

[c]Only considered to be that of sulfate aerosols using 2.5ºx2.5º data.

[d]The coverage of the study (Chamiedes et al., 2002) is over Chine-MAP domain.

[e]conv, convective clouds; strat, stratiform clouds.

5.3.2 Statistical relationship following satellite-based method

Following the method described in the study (Quaas et al., 2008), the simulated cloud droplet number concentration and cloud droplet effective radius at cloud top were diagnosed in the radiative transfer model using the ISCCP cloud simulator (Klein and Jacob, 1999; Webb et al., 2001) which emulates the way nadir-looking satellites measure clouds and facilitates the comparison of the modeled data with satellite observations. The simulated data including cloud droplet number concentration, aerosol optical depth as well as Ångström exponent are sampled daily at 1:30 PM local time to match the Aqua satellite overpass time. The study is limited to liquid water clouds and the cloud droplet number concentration is calculated from the cloud droplet effective radius and cloud optical thickness assuming adiabatic clouds (Quaas et al., 2008; Quaas et al., 2009). Note that cloud and aerosol properties calculated from this method differ from those satellites measure since observations include feedbacks between aerosols and clouds (i.e., the change of cloud droplet number concentration is not only due to changes of aerosol concentrations, but also due to changes from sedimentation, precipitation and coagulation). Hence the offline method is used as default to avoid these feedbacks in order to calculate the IPCC-defined climate forcing. For the purpose of the comparison, results for instantaneous values of cloud droplet number concentration, aerosol optical depth and Ångström exponent predicted from our inline model that only partially include these feedbacks are reported here as well (see Figure 5.18 and Table 5.6). For this simulation, we only read in the cloud droplet number concentration calculated from the inline model and fix the cloud liquid water path and cloud fraction by using the PD

meteorological fields. The adiabatic clouds are also assumed here (i.e., the cloud droplet number concentration is assumed constant from the surface to the cloud top).

Following Feingold et al. (2001, 2003), the strength of the aerosol-cloud interactions are quantified as relative change in cloud droplet number concentration (N_d) with relative changes of τ_a or AI, i.e., $ACI_N(AOD) = \frac{d \ln N_d}{d \ln \tau_a}$ or $ACI_N(AI) = \frac{d \ln N_d}{d \ln AI}$. In this way, the strength of the aerosol-cloud interaction can be obtained by a linear regression between $\ln(N_d)$ and $\ln(\tau_a)$ or $\ln(AI)$.

In order to be consistent with the satellite-based estimate of aerosol indirect forcing, considering separately different regimes of aerosol types and meteorological conditions to some extent, we used the same 14 regions and all 4 seasons defined in Quaas et al. (2008) to estimate the relationship between $\ln(N_d)$ and $\ln(\tau_a)$ or $\ln(AI)$. Figure 5.2 presents the choice of 14 different regions and Table 5.4 lists the abbreviations for regions and seasons used in this study. High latitudes (polewards of 60º) in which satellite retrievals may not be reliable are excluded for the purpose of computing the relationships.

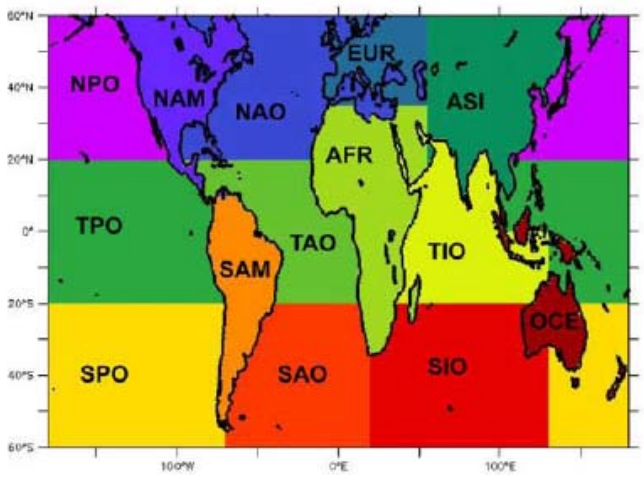

Figure 5.2: Choice of the fourteen different regions (Quaas et al., 2008).

Table 5.4: Abbreviations for regions and seasons (Quaas et al., 2008).

DJF	Dec–Jan–Feb
MAM	Mar–Apr–May
JJA	Jun–Jul–Aug
SON	Sep–Oct–Nov
NPO	North Pacific Ocean
NAM	North America
NAO	North Atlantic Ocean
EUR	Europe
ASI	Asia
TPO	Tropical Pacific Ocean
TAO	Tropical Atlantic Ocean
AFR	Africa
TIO	Tropical Indian Ocean
SPO	South Pacific Ocean
SAM	South America
SAO	South Atlantic Ocean
SIO	South Indian Ocean
OCE	Oceania

The present day slopes are obtained by a linear regression between $\ln(N_d)$ and $\ln(\tau_a)$ (or $\ln(AI)$) using the values in the PD condition. To quantify the error using present day slopes, we also estimated the slope using centroid values of $\ln(N_d)$ and $\ln(\tau_a)$ (or $\ln(AI)$) from PD and PI simulations as follows:

$$\frac{d\ln N_d}{d\ln \tau_a} = \frac{\frac{1}{N}\sum_{i=1}^{N}\ln N_{d,PD} - \frac{1}{N}\sum_{i=1}^{N}\ln N_{d,PI}}{\frac{1}{N}\sum_{i=1}^{N}\ln \tau_{a,PD} - \frac{1}{N}\sum_{i=1}^{N}\ln \tau_{a,PI}}, \tag{5.9}$$

and

$$\frac{d\ln N_d}{d\ln AI} = \frac{\frac{1}{N}\sum_{i=1}^{N}\ln N_{d,PD} - \frac{1}{N}\sum_{i=1}^{N}\ln N_{d,PI}}{\frac{1}{N}\sum_{i=1}^{N}\ln AI_{PD} - \frac{1}{N}\sum_{i=1}^{N}\ln AI_{PI}}, \tag{5.10}$$

where N is the number of grid points for a given season within each region.

5.4 Global aerosol mass budgets in PD and PI simulations

The anthropogenic sulfur emission from Smith et al. (2001, 2004) for the year 2000 with the source of 61.3 Tg S per year are used for the PD simulation, similar to the AeroCom models with the mean of 59.67 Tg S per year (Textor et al., 2004). The emission from the year 1850 with the source of 1.51 Tg S per year is for the PI simulation. Anthropogenic emissions of fossil fuel and biomass burning carbonaceous aerosol for the PD simulation are from the year 2000 of Ito and Penner (2005) with some adjustments, including fossil fuel BC and OM (5.8 Tg BC and 15.8 Tg OM per year) and biomass burning BC and OM (5.7 Tg BC and 47.4 Tg OM per year). The emission data from the year 1870 are used for the PI simulation with 23.0 Tg per year for OM and 2.52 Tg per year for BC. Both fossil fuel and bio-fuel aerosols are assumed to be emitted into the surface layer while aerosols with the origin from the open biomass burning are emitted uniformly into the boundary layer. Mineral dust emissions with sources of 2356 Tg per year is based on Ginoux et al. (2004) for the year 1998 while sources of sea salt are around 2545 Tg per year that were calculated in the coupled CAM/IMPACT model following the method (Gong et al., 1997). The emission and burden of sea salt used in this study are lower compared to mean values of AeroCom models. Global aerosol mass budgets used for PD and PI conditions in this study are given in Table 5.5.

Table 5.5: Aerosol emissions and burdens in the present day and preindustrial simulations used in this study[a].

Aerosol types	Sources (Tg/yr or Tg S/yr)		Burden (Tg or Tg S)	
	PD	PI	PD	PI
Sulfate	59.93 *(59.67, 22)*	24.35	0.86 (*0.66, 25*)	0.36
Black carbon	10.51 (*11.90, 23*)	2.52	0.13 (*0.24, 42*)	0.03
Organic carbon	77.52 (*96.60, 26*)	37.44	1.00 (*1.70, 27*)	0.47
Dust size[b] (μm)				
0.05-0.63	76.57	76.57	1.59	1.71
0.63-1.25	291.54	291.54	5.89	6.66
1.25-2.50	662.59	662.59	10.59	11.48
2.50-10.0	1325.20	1325.20	4.24	4.46
0.05-10.0	2355.90 (*1840.00, 49*)	2355.90	22.30 (*19.20, 20.50*)	24.31
Sea Salt size[b] (μm)				
0.05-0.63	112.15	112.86	0.43	0.43
0.63-1.25	429.79	432.37	1.57	1.57
1.25-2.50	929.18	934.75	2.54	2.56
2.50-10.0	1073.90	1080.60	0.45	0.46
0.05-10.0	2545.02 (*166000.00, 199*)	2560.58	4.99 (*7.52, 54*)	5.01

[a]The values given in the parenthesis in the PD column for sources and burden are mean (1st value) and standard deviation (2nd value) from available models in AeroCom [see Textor et al., 2006, Table 10].
[b]radius.

5.5 Results of PD and PI simulations

5.5.1 Statistical relationship between CDNC and AOD/AI

Following the methods described in Section 5.3.2, two statistical relationships based on the spatial variation of aerosols and clouds in the PD simulation along with those varied temporally between the PI and PD are computed. Figure 5.3ab show a scatter plot between ln(N_d) versus ln(AOD) in JJA and DJF over North America while Figure 5.3de show a similar set of scatter plots for ln(N_d) and ln(AI). PD values are in mainz and PI values are in blue. If including AOD and N_d values from the PI simulation, the slopes

computed only based on the spatial variation of aerosols and clouds from the PD simulation in Figure 5.3(a) and 5.3(b) would be larger since the spatial variation of AOD and N_d from the PD simulation does not include values as comparably small as those from the PI simulation. The scatter plot in Figure 5.3de shows that the values for AI and N_d have larger contrast between PI and PD simulations than the values for AOD and N_d in the PD condition. If including AI and N_d from the PI simulation, the computed slope based on the PD condition could be both underestimated (Figure 5.3d) or overestimated (Fig. 5.3e). The black line illustrates that the slope can be larger if the average of the actual PI values are used compared with that extrapolated from PD slopes (i.e., the red line).

Figure 5.3(c) and (f) show a similar set of scatter plots for the regions in Asia (ASI) in March, April and May (MAM). This region demonstrates what occurs with the relationships between aerosols and cloud properties when dust is present. Both the slope between $\ln(N_d)$ and ln(AOD) and the slope between $\ln(N_d)$ and ln(AI) calculated using AOD, AI and N_d values in the PD condition are negative in this season because dust has significant influence on aerosol loadings and further the magnitude of AOD, but it does not strongly contribute to the increases in droplet concentration due to its low hygroscopicity. Dust must be coated with hygroscopic aerosols such as sulfate or nitrate in the model before it can act effectively as good cloud condensation nuclei. Similar explanation applies when BC/OM aerosols dominate the aerosol optical depth but not the activation of N_d. This negative response is also observed by the MODIS satellite over Eastern Asia and Western Sahara shown in the study by Storelvmo et al. (2006) who ascribed varying correlation and low statistical significance of aerosol-cloud interactions

within those regions to the influence of hydrophobic black carbon or hydrophilic dust or the so called "competition effect" (i.e., the addition of large particles suppress the maximum supersaturation at the early stage of activation by providing larger surface area and enhancing condensation, thus inhibiting the activation of smaller CCN so that the total number of activated CCN get reduced by the large CCN) proposed by Ghan et al. (1998). Actually, Feingold et al. (2001) observed this "competition effect" over Brazilian biomass burning regions for smoke particles as well. This mechanism also explains the negative slopes of for Europe (EUR) in MAM, JJA, and SON and for Oceania (OCE) during SON in Figure 5.4.

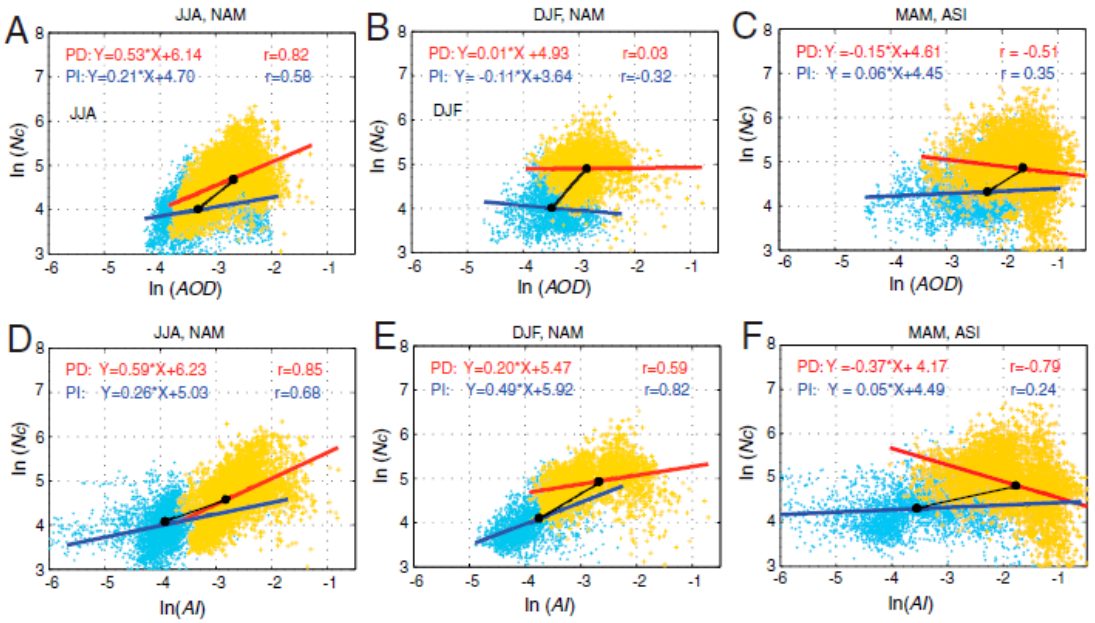

Figure 5.3: Scatter plot of the slope $\ln(N_d)$ vs ln(AOD) and ln(Nd) vs ln(AI) for North America (NAM) in JJA and DJF and for Asia (ASI) in MAM. The linear regressions for both the PD and PI simulation are shown. The black line shows the fit computed using the difference in the average of PD and PI values (i.e., Eqn. (5.9) and Eqn. (5.10)) (Figure 3, Penner et al, 2011).

Figure 5.4 (a) and (b) show the slopes calculated based on the PD simulations for all regions and seasons for (a) $\ln(N_d)$ versus ln(AOD) and for (b) $\ln(N_d)$ versus ln(AI) while Figure 5.5 (a) and (b) give similar slopes computed using the difference in average values of $\ln(N_d)$ and ln(AOD) or ln(AI) between PI and PD conditions (see Equation 5.9 and 5.10). Note that the range of slopes in Figure 5.5a goes from -1.5 to 2.0 while that in Figure 5.4a is only from -0.4 to 1.0. The slopes calculated from the difference in average values of $\ln(N_d)$ versus ln(AOD) for the PD and PI simulations are larger than those only using PD values for most regions although there are a number of regions and seasons with negative slopes when the actual PD and PI values of $\ln(N_d)$ and ln(AOD) or ln(AI) are used. The slopes computed for $\ln(N_d)$ versus ln(AI) based on the temporal variation from PI to PD are only slightly larger than those only accounting for spatial variation in PD values. Note that the slopes of $\ln(N_d)$ versus ln(AI) using PD and PI values for the regions NPO, TIO, SPO, SAO, SIO are smaller than those calculated only using PD values. These regions might be expected to have a smaller negative forcing when the actual PD and PI values of $\ln(N_d)$ and ln(AOD) or ln(AI) are used. This statement is only an approximation because the interaction between aerosols and clouds is non-linear (Ramaswamy et al., 2001). In addition, the slopes only using PD values are generally larger over the ocean than over the land, which is consistent with findings in the satellite data (Quaas et al., 2008). Whereas the slopes of $\ln(N_d)$ versus ln(AI) in Fig. 5.5 (b), clearly present larger ACI_N over the land than over the ocean, which were usually found in most GCMs (Quaas et al., 2009). This reverse of the land-ocean contrast observed by satellites might be problematic since the ACI_N is theoretically expected to be smaller over the ocean based on following three factors (Rosenfeld and Feingold, 2003):

i. Continental regions are generally more convective than oceans and hence have greater ACI_N in light that ACI_N increases strongly with updrafts (Feingold et al., 2003);

ii. Large sea salt particles that exits over the ocean preventing the activation some of smaller CCN by suppressing cloud supersaturation (Ghan et al., 1998), tending to reduce ACI_N over the oceans;

iii. The addition of salt particles over the ocean contributes to enhance droplet coalescence (e.g., Woodcock, 1953; Rosenfeld et al., 2002) that increases drop size, resulting in a lower ACI_N over the ocean.

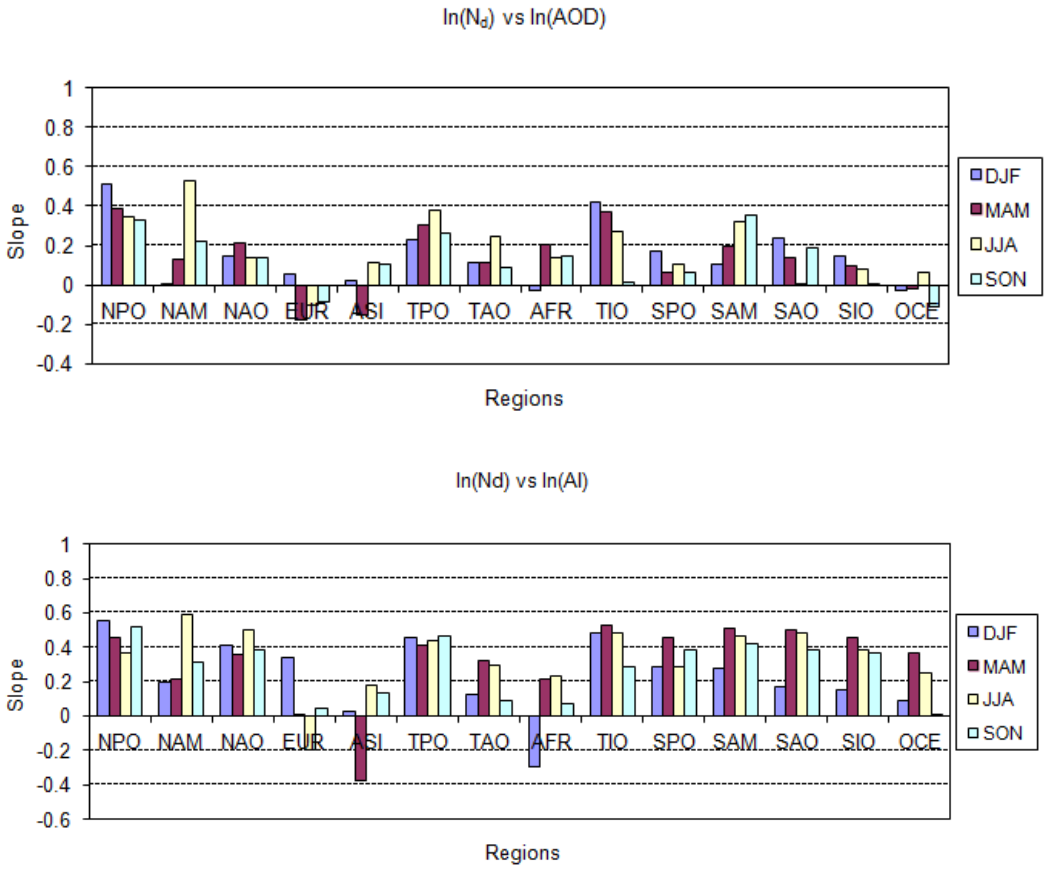

Figure 5.4: Slope of the regression between $\ln(N_d)$ and τ_a (i.e., AOD) (a) and ln(AI) (b) for the PD simulations for all seasons for the 14 regions in the analysis of Quaas et al. (2008).

The slopes shown in Figure 5.4 may be compared to the analysis for the MODIS satellite shown in Figure 3 of Quaas et al. (2008) to the variability shown in Figure 2(a) for AEROCOM models in Quaas et al. (2009). Nevertheless, by comparing estimated slopes shown in Figure 5.4 with those using average values of aerosol (AOD) and cloud (N_d) properties based on model-generated PD and PI conditions (Figure 5.5), we have established the fact that the estimates of the change in N_d with AOD only based on the PD condition are unlikely to be accurate.

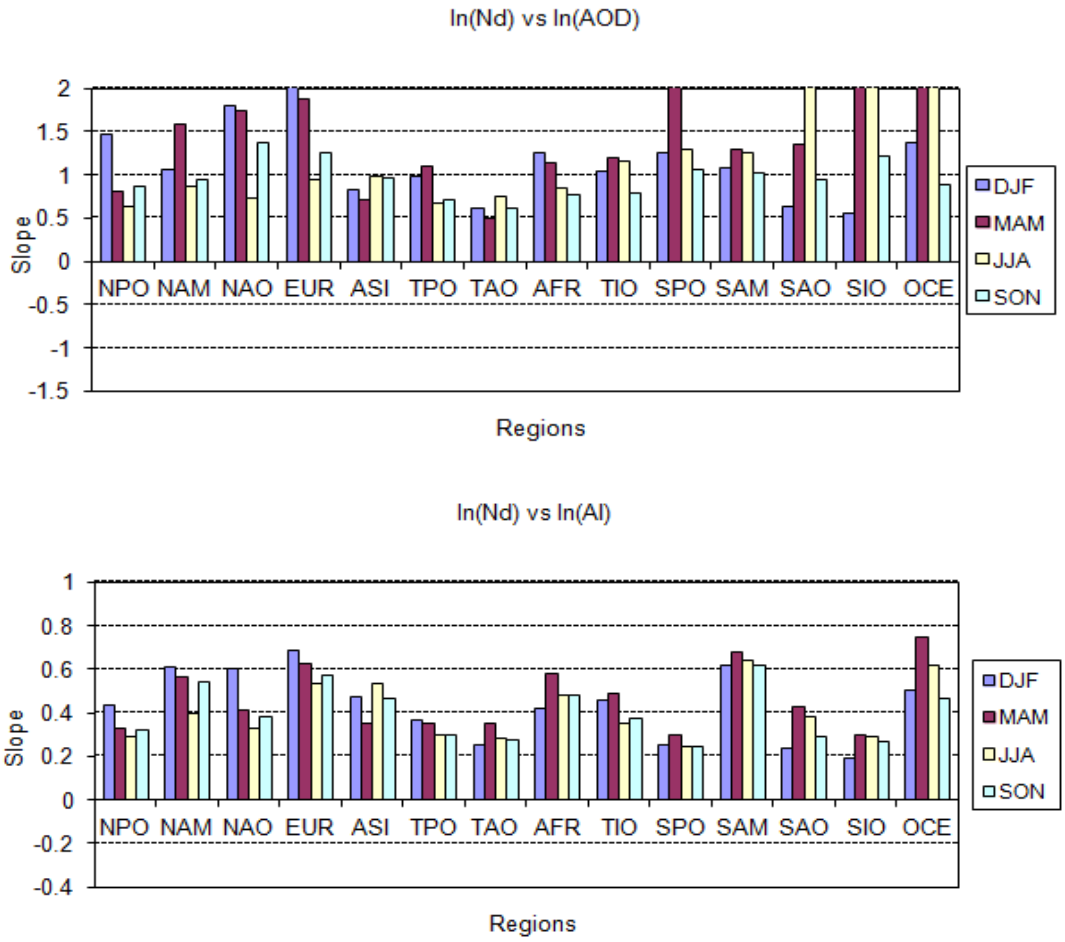

Figure 5.5: The slope calculated from the difference in the average values of ln(N_d) and ln(AOD) (top) and ln(AI) (bottom) between the PD and PI simulations for all seasons for the 14 region in the analysis of of Quaas et al. (2008).

5.5.2 Sensitivity study of CCN activation with the change of aerosol concentration

Shown in Figure 5.4a, some negative slopes (i.e., decreases of cloud droplet number with increases of aerosol amount) are computed over Europe (EUR) for nearly all seasons, Asia (ASI) for the season MAM as well as Australia (OCE) for the season SON. In general, the negative slopes for Europe generated from the use of only PD values are caused by mineral dust attributable to high values of AOD but low values of N_d due to its low hygroscopicity. On the other hand, for Europe during almost all seasons in the PD condition, higher values of AOD result from higher amount of mineral dust (and sometimes also fossil fuel OM/BC) where sulfate concentration are low. The increase of sulfate is usually accompanied with the increase of N_d as expected since the cloud droplet number is found mainly sensitive to the fine fraction of aerosols (such as pure sulfate) but sulfate does not control the change in AOD as much as does dust and OM/BC. Hence, even if sulfate aerosols increase, with the presence of mineral dust particles, the negative relationship between aerosol and cloud properties is still possible. Similar considerations apply in ASI during MAM and in OCE during SON.

In order to sort out the contribution of individual aerosol components to the aerosol activation, the sensitivity is conducted in EUR during MAM and in ASI during MAM since the comparably largest negative slopes over these two regions given the season MAM are computed in Figure 5.4. For each region given the season (e.g., MAM), as we compute PD slopes, we separate seasonal mean aerosol mass concentrations in the surface level, cloud top temperature and pressure for grids which fulfill following the criteria into two groups:

i. the “lowAODhighNd” case: AOD<0.08 and N_d>250 cm^{-3};

ii. the “highAODlowNd” case: AOD>0.15 and N_d<120 cm^{-3};

Basically, the “lowAODhighNd” case represents the case with lower aerosol loadings while “highAODlowNd” case represents the case with comparably higher aerosol loadings since aerosol optical depth is closely tied with column integrated aerosol mass concentrations. We assume that aerosols are well mixed within the boundary layer so that surface concentrations are characteristic of those at cloud base. In all simulations, when calculating the activated number concentration, the cloud top temperature and pressure for each grid are used while updraft velocities vary from 0.05 to 1 m/s with an increment of 0.05 m/s. The supersatuation of 0.2% is assumed in the parameterization of the aerosol activation. For the calculation of aerosol optical depth, cloud fraction and relative humidity are assumed to be 0.5 and 80%, respectively. The adjustments of clear-sky relative humidity are made if a clear-sky fraction exists. Note the aim of this sensitivity test is to explore variations of number concentration of particles activated with variation of composition along with updrafts. The averaged cloud and aerosol optical properties given region and season are reported here.

Figure 5.6 shows cloud droplet number concentrations activated as a function of updraft velocity for two base aerosol concentrations: lowAODhighNd (solid line) and highAODlowNd (dash line) in the Asia (ASI) during the season MAM. The colored lines are corresponding to the runs with doubling specific aerosol component indicated in the legend. For instance, “2xSO_4m1” and “2xSO_4m2” stands for the simulated results with doubling pure sulfate at the nucleation/Aitken and accumulation mode, respectively while “2xSO4-FFOMBC”, “2xSO_4-BBOMBC”, “2xSO_4-Dust” and “2xSO_4-Sslt” represent the

simulations with doubling fossil fuel, biomass burning, dust and sea salt aerosols compared to the base case. Two regimes are evident in Figure 5.6 given specific seasonal mean aerosol mass concentrations in ASI. For the high updraft velocity (i.e., w>0.15 m/s), cloud droplet number concentrations increase with an increase of total aerosol optical depth (i.e., aerosol mass) as expected. In contrast, for the low updraft velocity (i.e., w<0.15 m/s), the negative response of cloud droplet number concentrations occur with the increase of aerosol mass going from the case "lowAODhighNd" to the case "highAODlowNd". As given for the averaged aerosol optical depth calculated for two base aerosol concentrations (i.e., corresponding to aerosol loadings of two black lines in Fig. 5.6) in Figure 5.7, aerosols originated from biomass burning and fossil fuel combustion mixed with wind-blown dust and sulfate particles are dominant over the Asia during the season MAM. The presence of smoke aerosols as well as fossil fuel organic matter and black carbon mainly contribute to the deduction of activated cloud droplet number with the so-called "competition effect" for the available water vapor (Ghan et al., 1998; Feingold et al., 2001; Chen and Penner, 2005). At higher updraft velocity, this competition effect may not be important since higher updraft velocity promotes the activation of small particles such as sulfate. This "competition effect" is also clearly shown in sensitivity runs that decreases of activated aerosol number are accompanied with increasing accumulation mode sulfate (i.e., the case "2xSO4m2") as well as increasing biomass burning aerosols (i.e., the case "2xSO4-BBOMBC") at the updraft velocity up to 0.5 m/s for the case of "highAODlowNd". However, visible decreases of cloud droplets with increases of aerosols are only seen at very low updraft velocity (i.e., around 0.05 m/s) for the case of "lowAODhighNd", indicating this "competition effect"

becomes weaker as the total aerosol loading are smaller. This negative response of cloud droplet number with aerosols for the case "highAODlowNd" is correspondingly shown in the regime where large AOD (i.e., AOD>0.13) along with low N_d (i.e., $N_d < 50$ cm^{-3}) are present at the lower right panel in the Figure 5.3(c).

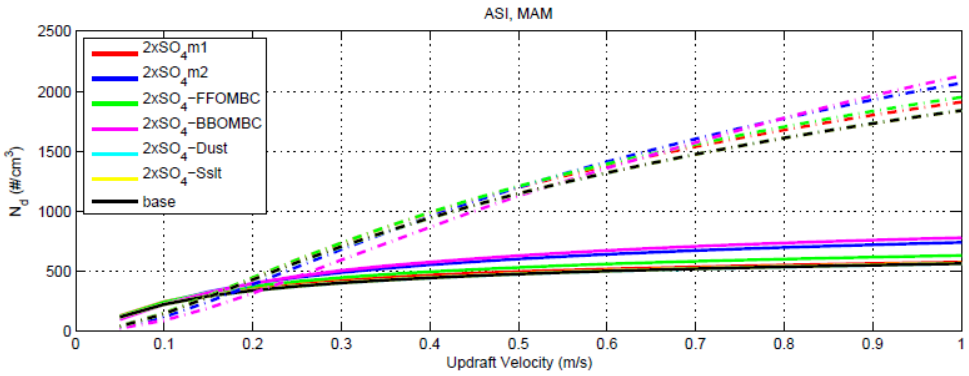

Figure 5.6: Cloud droplet number concentrations activated as a function of updraft velocity for two base aerosol concentrations: lowAODhighNd (solid line) and highAODlowNd (dash line) in the Asia (ASI) during the season (MAM). The colored lines are corresponding to the runs with doubling specific aerosol component indicated in the legend. "2xSO_4m1" and "2xSO_4m2" stands for the run with doubling pure sulfate at the aiken and accumulation mode, respectively while "2xSO4-FFOMBC", "2xSO_4-BBOMBC", "2xSO_4-Dust" and "2xSO_4-Sslt" represent the runs with doubling fossil fuel, biomass burning, dust and sea salt aerosols based on the base case.

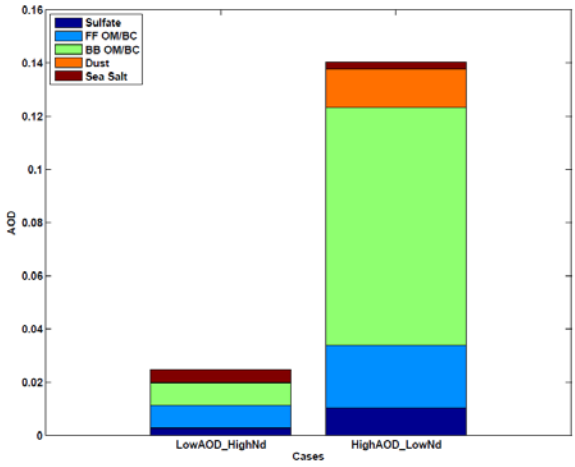

Figure 5.7: Aerosol optical depth for two base aerosol concentrations in ASI during the season MAM.

Figure 5.8 shows cloud droplet number concentrations activated as a function of updraft velocity for two base aerosol concentrations: lowAODhighNd (solid line) and highAODlowNd (dash line) in the Europe (EUR) during the season MAM. The legend is same as described in Figure 5.6. In general, the decrease of cloud droplet number occurs with the increase of aerosol mass (i.e., going from the case "lowAODhighNd" to "highAODlowNd"). Different with the aerosol composition in ASI during the season MAM, mineral dust dominates over the EUR in the spring show in Figure 5.9 (left panel). As discussed above, the hydrophobic dust is not good cloud condensation nuclei, thereby the presence of dust particles contribute to the enhancement of aerosol optical depth but not for the cloud droplet number. On the other hand, the presence of giant dust particles may inhibit the activation of small particles such as sulfate (Ghan et al., 1998). Because the competition for water limits the maximum supersaturation in an updraft, the activation of each CCN particle is dependent upon the presence of other CCN (Ghan et al., 1998, Feingold et al., 2001). This effect of dust suppressing cloud formation is observed from satellite and aircrafts (Rosenfeld et al., 2001). Hence, because of this competition, the cloud droplet number concentrations do not necessarily increase with the increase of aerosol loadings as opposed to what occurs in a conventional manner, i.e., the increase of aerosol mass leads to the increase of cloud droplets. Noticed that one interesting phenomenon is that the increase of nucleation mode of pure sulfate inversely results in the decrease of cloud droplet number almost for an entire range of updraft velocities (i.e., see the difference between the red solid and dash line in Figure 5.8). This is because the addition of sufficient great amount of tiny sulfate particles in the

nucleation mode may enhance condensation and reduce the maximum supersaturation (shown in Figure 5.9(right panel)) by added particle surfaces, which thereby inhibit the activation of other small CCN (e.g., accumulation mode sulfate) so that the total number of cloud droplets will be reduced eventually.

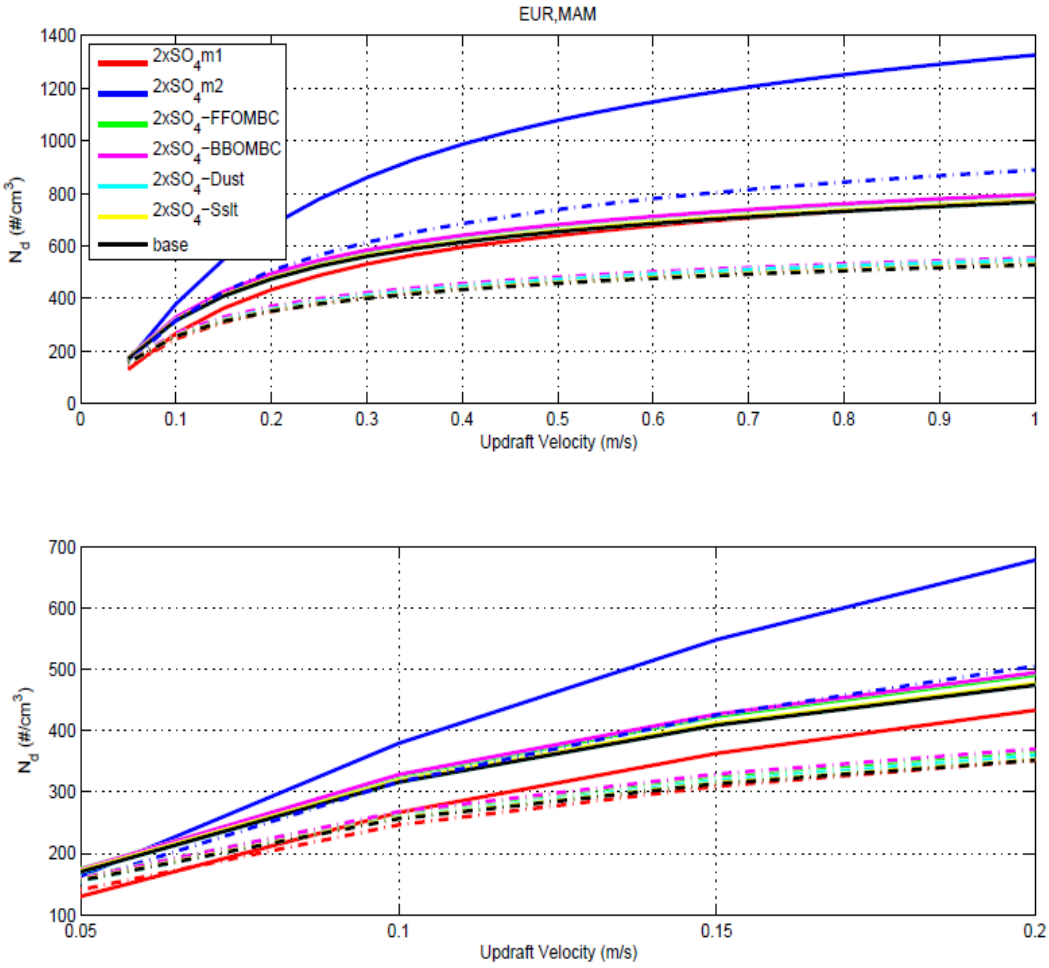

Figure 5.8: Same as in Figure 5.6, but for the Europe (EUR) during the season (MAM).

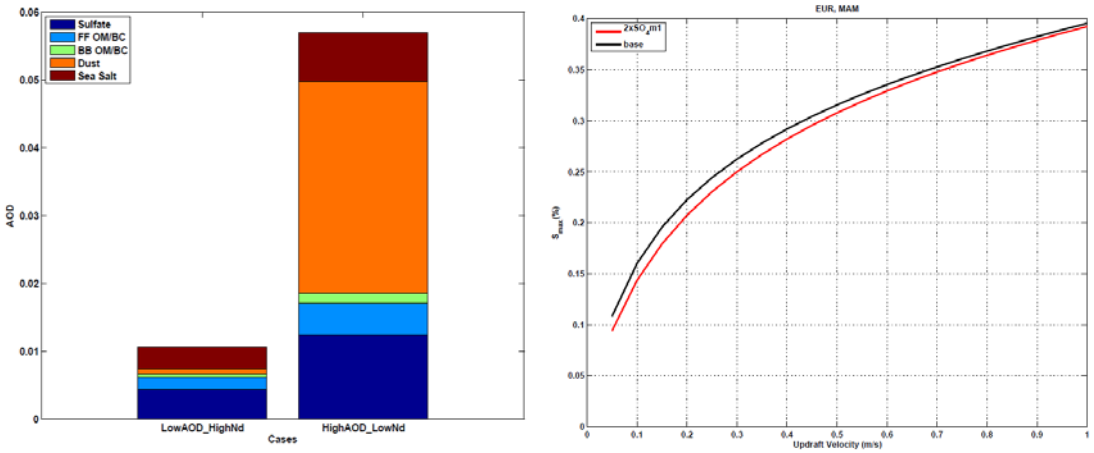

Figure 5.9: Same as in Figure 5.7, but for the Europe (EUR) during the season (MAM) (left panel); maximum supersaturation as a function of updraft velocity for the Europe (EUR) during the season (MAM) (right panel).

The use of the difference in average values of $\ln(N_d)$ and ln(AOD) for PD and PI simulations to compute slopes in Europe (EUR) results in a very large negative slope in DJF while the PD slope is positive for that season. On the other hand, the PD slopes for MAM, JJA and SON in EUR are all negative as compared to the positive slopes computed for the PD and PI conditions for same seasons. We have examined individual points contributing to the negative slope using the PD and PI values in Europe in DJF. The number concentration from dust and fossil fuel BC/OM decreases from the PI to the PD condition due to the increase in sulfate deposition on these aerosol types causing their stronger removable rate from precipitation. This decrease leads to a slight decrease in AOD so that the slope computed with the difference in average value of $\ln(N_d)$ and ln(AOD) for PD and PI simulations is negative even though the overall cloud droplet number concentration increase. This also explains the negative slope in SIO and OCE for MAM and the negative slope in NAO and NAM for DJF when values from PD and PI conditions are used.

5.5.3 Cloud droplet number concentration and cloud effective radius

The simulated cloud top droplet number concentrations in the PD and PI condition are shown in Figure 5.10. For the PD simulations, the simulated cloud droplet number concentration is larger over the land than over the ocean because of the larger anthropogenic emission over land. For the PI simulation, the simulated cloud droplet number concentration is much smaller over the land than that in the PD simulation, which results in the very small land/ocean contrast. The cloud droplet number concentration decreases about 36% going from the PD condition to the PI condition.

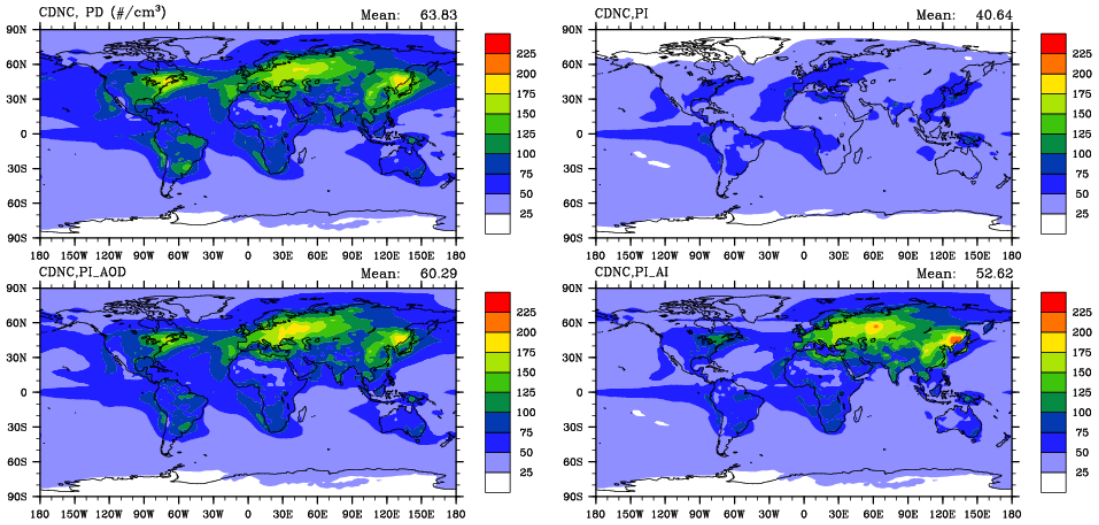

Figure 5.10: Annual averaged cloud droplet number concentration at cloud top for PD and PI condition (top two panels), for the derived PI using the statistical relationship between CDNC and AOD (left in the bottom panel) and using the statistical relationship between CDNC and AI (right in the bottom panel) and the CDNC ratio between the derived PI and the true PI (bottom two panels).

In the bottom panel of Fig. 5.10, the simulated cloud droplet number concentration for the derived PI condition using the statistical relationship (i.e., $ACI_N(AOD)$ and $ACI_N(AI)$) is also shown. Note that for a given season at each region,

$$N_{d,PI\_AOD}\,|_{region} = \exp(\ln N_{d,PD} + slope_{PD,AOD}\big|_{region} * (\ln \mathrm{AOD}_{PD} - \ln \mathrm{AOD}_{PI})), \qquad (5.11)$$

and

$$N_{d,PI\_AI}\,|_{region} = \exp(\ln N_{d,PD} + slope_{PD,AI}\big|_{region} * (\ln AI_{PD} - \ln AI_{PI})), \qquad (5.12)$$

where $slope_{PD,AOD}\big|_{region}$ and $slope_{PD,AI}\big|_{region}$ are present day slopes presented in Figure 5.4a.

The derived "PI" cloud droplet number concentration using the present day slope of AOD (i.e., $N_{d,\ PI\_AOD}$) share similar spatial pattern to that in the PD condition for both land and ocean. Slight increase of could droplet number concentration are found over the Europe due to negative slopes (i.e., $slope_{PD,AOD}$) calculated over that region. Overall the decrease of N_d from the PD condition to this derived "PI" condition is about 6%. The derived "PI" cloud droplet number concentration using the present day slope of AI (i.e., $N_{d,\ PI\_AI}$) show very similar spatial variation over the ocean as that in the true PI condition (top right panel in Figure 5.10) and has larger values over land compared to the original PI condition, especially over the Europe and Asia, due to negative slopes (i.e., $slope_{PD,AI}$) calculated over these regions shown in Fig. 5.4b. The decrease of cloud droplet number concentration is about 18% compared to the PD condition. Figure 5.11 provides the cloud droplet number concentration ratio between the derived PI and the true PI condition. As compared to the true PI condition, the derived $N_{d,\ PI\_AOD}$ shows higher values almost over an entire globe except some areas over the southern ocean while the derived $N_{d,\ PI\_AI}$ share similar spatial pattern over ocean but overestimates over the land. This is also seen in the annual zonal mean cloud droplet number concentration in Figure 5.12. Smaller difference between the derived "PI" cloud droplet number based on the relationship of $ACI_N(AI)$

exists over the southern hemisphere while the large discrepancy is present over the northern hemisphere, indicating that AI could be a good proxy of aerosol loadings only over the ocean.

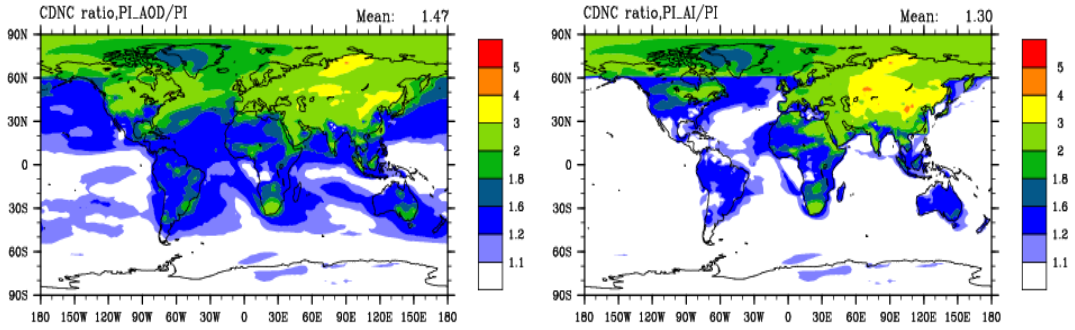

Figure 5.11: Annual averaged cloud droplet number concentration ratio at cloud top between the derived PI and the true PI condition.

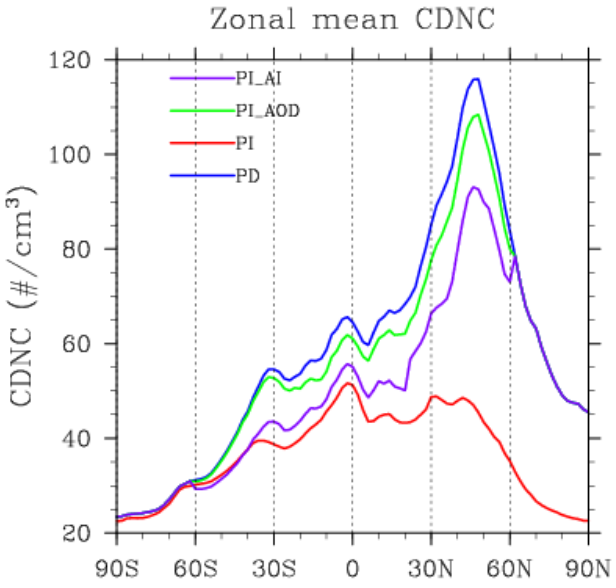

Figure 5.12: Annual zonal mean cloud droplet number concentration at cloud top. The case labels are same as in Figure 5.6.

By assuming constant liquid water content, the cloud effective radius can be diagnosed (Rostayn and Liu, 2003). Note that the cloud effective radius is inversely proportional to cloud droplet number concentration with fixed cloud liquid water content. Figure 5.13 shows annual average cloud top effective radius for the PD, PI, derived PI_AOD and PI_AI conditions. Similar to the cloud droplet number concentration, the cloud top effective radius derived from the PI_AOD case increases about 1% while that derived from the PI_AI case increases about 6%, which is closer to the true augment of 9% due to the difference of the true PD and PI conditions on the global scale. Figure 5.14 gives annual averaged cloud top effective radius ratio between the derived PI and the true PI conditions. The derived $R_{e,\ PI\_AOD}$ is apparently underestimated over an entire global except some areas in the southern ocean while the cloud effective radius derived from the PI_AI condition (i.e., $R_{e,\ PI\_AI}$) shows slight overestimation over most ocean regions except some areas in the Atlantic Ocean and similarly underestimation over land as $R_{e,\ PI\_AOD}$. This is consistent with the pattern in the cloud droplet number concentrations.

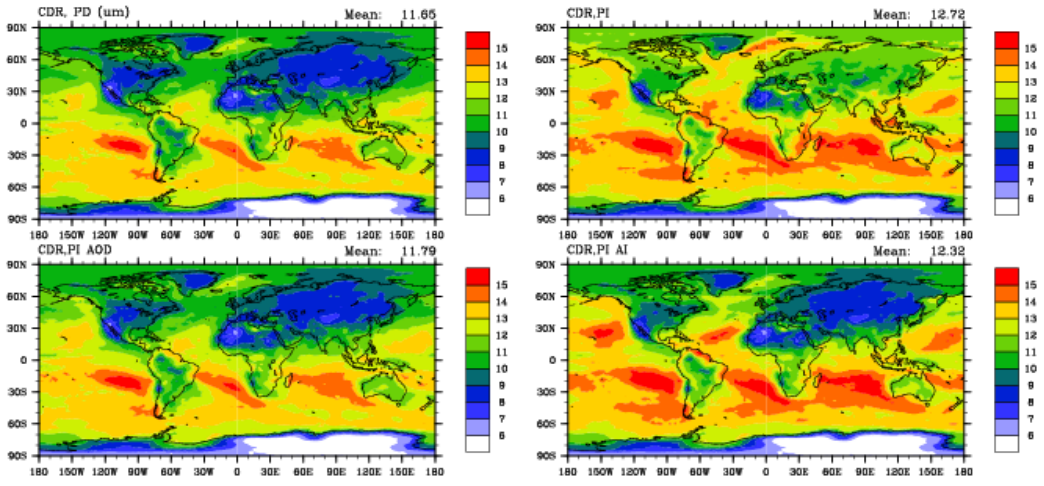

Figure 5.13: Annual averaged cloud effective radius at cloud top. The case labels are same as in Figure 5.6.

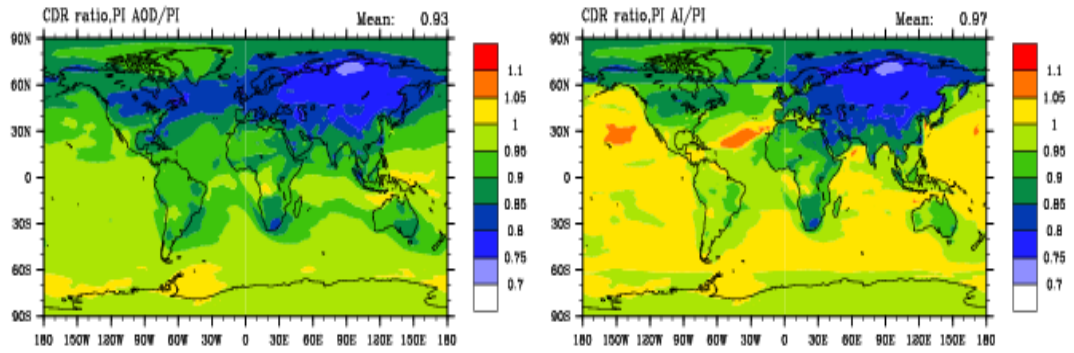

Figure 5.14: Annual averaged cloud top effective radius ratio between the derived PI and the true PI condition. The case labels are same as in Figure 5.6.

5.5.4 Aerosol optical depth and Aerosol index

Figure 5.15 gives aerosol optical depth, Ångström exponent and aerosol index for PD and PI conditions. In general, aerosol optical depth is highest over the Sahara for both PD and PI conditions, which indicates that the tremendous contribution of dust loadings to the total aerosol optical depth. By comparing the aerosol optical depth between the PI and the PD condition, larger differences occur over North America, Europe and East Asia, which are major industrial regions, as well as over the South America and South Africa, which are major biomass burning regions. The smaller the aerosol, the larger the Ångström exponent. The middle panel of Figure 5.15 shows that the smaller Ångström exponents are found over the North Africa where mineral dust are dominant particles and over the Southern Ocean where sea salt are predominant while larger values are located over North America and East Asia (where anthropogenic sulfate and carbonaceous particles dominate), South America and South Africa (where biomass burning aerosols dominate). Hence, the aerosol index (i.e., aerosol optical depth times Ångström exponent) account for the combined information of both aerosol loadings and sizes. The large discrepancy between the PD and the PI condition occurs in the industrial regions (North

America, Europe and East Asia) and biomass burning regions (South America and South Africa) due to anthropogenic activities since the PI era. Besides, the larger land/ocean contrast is found in the aerosol index for the PD condition than that for the PI condition. This is consistent with the spatial pattern of the cloud droplet number concentration for PD and PI conditions. Moreover, the peak regions (i.e., Asia, Europe and North America) shown in the spatial distribution of AI in the northern hemisphere is also in accordance with those for cloud droplet number concentration. This may explain why the use of aerosol index as proxy of aerosols in replace of aerosol optical depth is better for the representation of aerosol particles that are activated to cloud droplets.

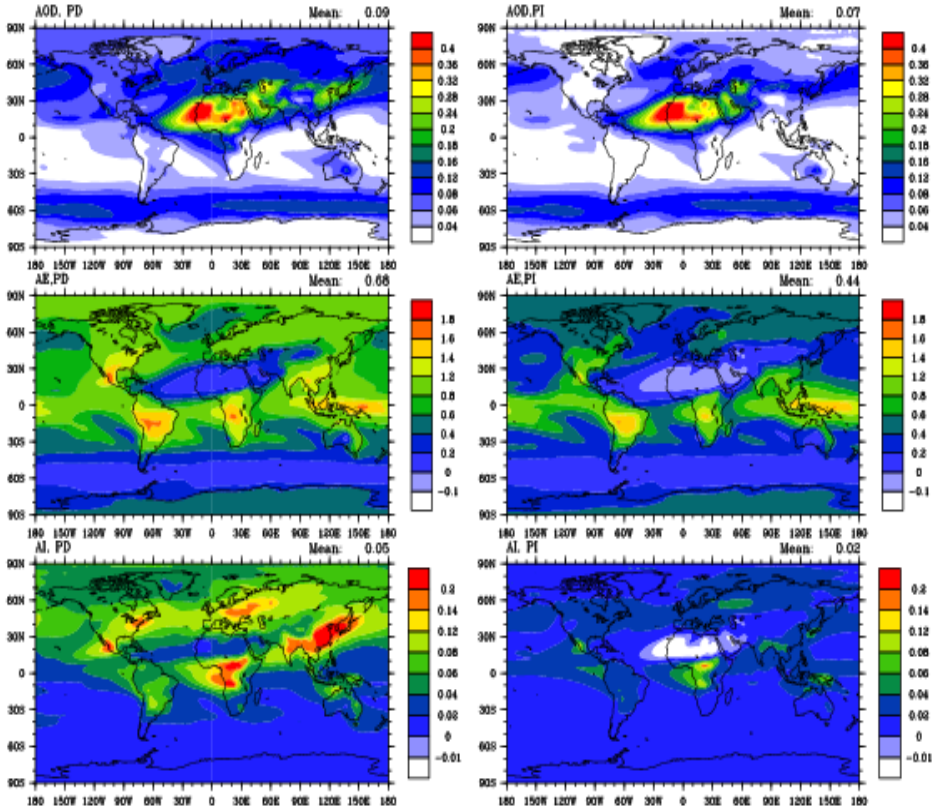

Figure 5.15: Annual averaged aerosol optical depth (top), Ångström exponent (middle) and aerosol index (bottom) for the PD (left) and PI (right) simulation.

5.5.5 Aerosol indirect forcing

The offline radiative transfer model is used to evaluate the use of the slope of ACI_N(AOD) or ACI_N(AI) to estimate aerosol first indirect forcing. IPCC has defined the aerosol indirect radiative forcing as the forcing obtained by holding all values constant except the estimated change in N_d (Ramaswamy et al., 2001; Forster et al., 2007), thereby requiring the feedbacks associated with droplet coalescence and precipitation not be included. This is the definition used here.

Figure 5.16 shows the TOA shotwave forcing using the true PI (N_d) (a) and that using the derived PI N_d based on the regression of ACI_N(AOD) (b) or ACI_N(AI) (c). The global average indirect forcing using both PD and PI values for N_d is -1.69 W/m^2 as apposed to that using the satellite method based on the relationship of ACI_N(AOD) is only -0.27 W/m^2. The forcing using the satellite-based regression is smaller in every region than the true model estimated value. If the regression with AI is used rather than AOD, the forcing is significantly larger, -1.09 W/m^2, but is still smaller than the value based on the true model estimate of PI N_d, even if we restrict the true model estimate to the region between 60°S and 60°N. As noted above, there are regions where the estimated forcing actually more negative using the satellite method based on AI, most notably in the regions NPO, TOP and SPO. However, in most regions, the satellite method underestimates the negative forcing.

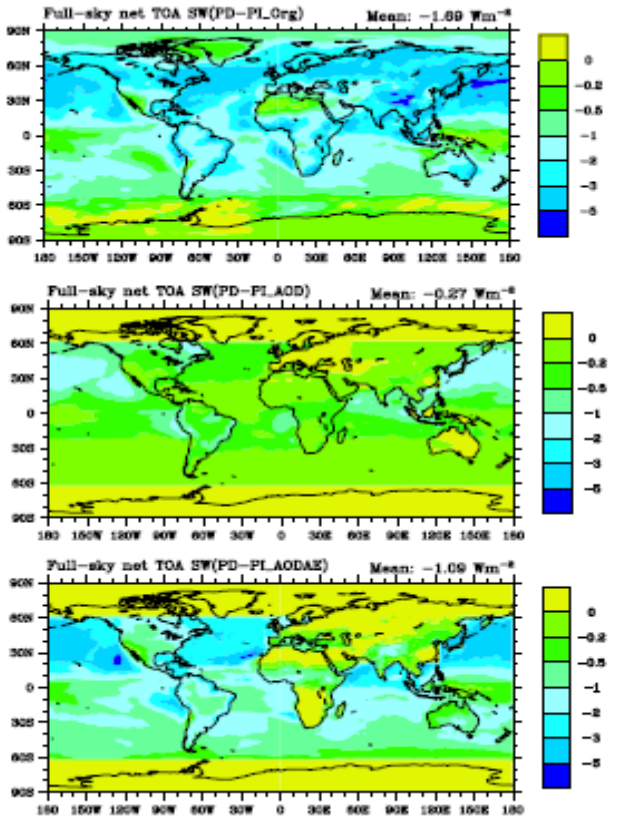

Figure 5.16: Shortwave indirect forcing from the PD and PI values of Nd (top), from the PD value of Nd and the estimate of the PI Nd based on the regression between Nd and AOD (middle), and from the PD value of Nd and the estimate of the PI Nd based on the regression between Nd and AI (bottom). The satellite estimates of forcing do not include the forcing outside the region from 60S to 60N. If the true model forcing is restricted to this region, the total forcing is -1.56 W m^{-2}.

Figure 5.17 shows annual averaged first aerosol indirect effect at the top of atmosphere over 19 regions for three cases (PD-PI, PD-PI_AOD, and PD-PI_AI). The legend is same as that defined in Figure 5.16. In general, the forcing based on estimating the PI concentration of N_d from the regression of ACI_N(AOD) is much smaller than that using the true PI values for all 19 regions studied here. The forcing based on estimating the PI concentration of N_d from the regression of ACI_N(AI) is close to that using the true PI values over all 9 ocean regions, resulting in only 7% difference over an entire ocean

basin. However, similar to the case using the regression of ACI_N(AOD), it also show smaller values over land. This is probably because the chemical composition of aerosols is more uniform over ocean than over land. Over ocean, sulfate and sea salt particles are dominant, both of which are good cloud condensation nuclei although the competition between sulfate and sea salt as CCN exist (Ghan et al. 1998). Over land, aerosol is usually found as the mixture of sulfate, organic matter, black carbon and mineral dust and thereby its capability to be activated as cloud droplets highly dependent on the hygroscopicity of the mixture and relative mass loadings of each aerosol components. As discussed above, black carbon and mineral dust are not good CCN due to their low hygroscopitiy but their abundance have significant impact on the magnitude of total aerosol optical depth. Note the increase of total aerosol optical depth due to the increase of aerosols like black carbon and dust particle may not contribute to the increase of cloud droplet number concentrations.

The values for the slope of ACI_N(AOD) or ACI_N(AI) shown in the study (Quaas et al., 2009) and those from satellite observations include the effects of change to N_d that results from the feedbacks between aerosol loadings and cloud droplet number concentrations. In the above, we emphasized the use of an offline model to calculate N_d in order to report results that are consistent with the IPCC definition of the first aerosol indirect effect forcing. Figure 5.18 gives the annual averaged first aerosol indirect effect at the top of atmosphere over 19 regions for three cases (PD-PI, PD-PI_AOD, and PD-PI_AI) from the coupled CAM/IMPACT inline model. Similar to the offline calculation, the forcing based on estimating the PI concentration of N_d from the regression of ACI_N(AOD) is much smaller than that using the true PI values for all 19 regions studied here. The

forcing based on estimating the PI concentration of N_d from the regression of $ACI_N(AI)$ is larger than that using the true PI values for the regional basis of an entire globe and for both northern hemisphere and southern hemisphere while it is larger and smaller over the ocean and the land, respectively. The forcing based on estimating the PI concentration of N_d from the regression of $ACI_N(AI)$ agrees well with that using the true PI values in both North America and South America.

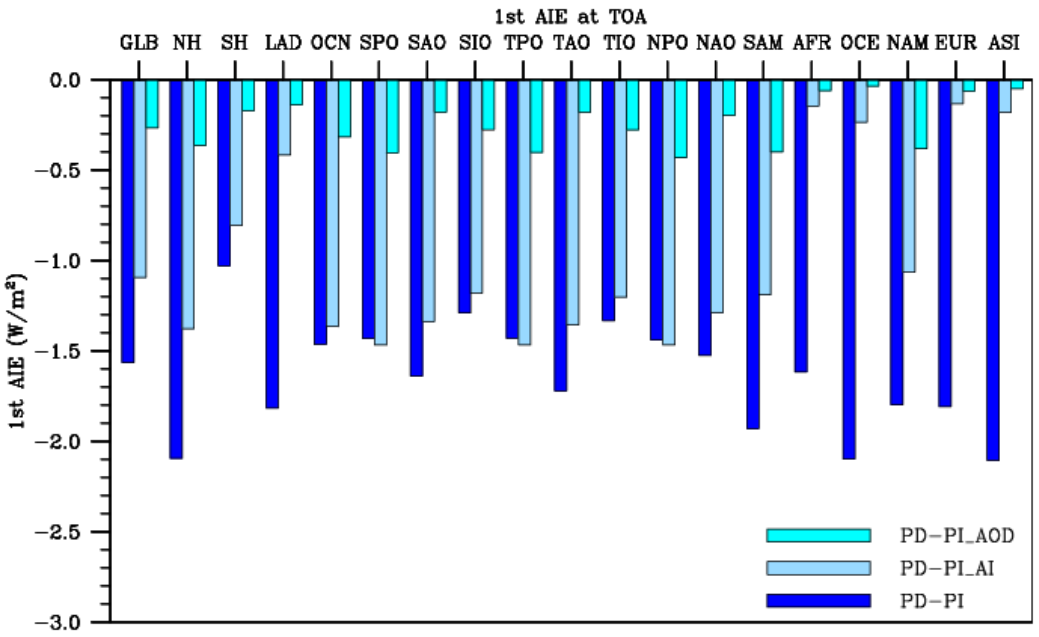

Figure 5.17: Annual averaged 1st aerosol AIE at the top of atmosphere over 19 regions for three cases (PD-PI, PD-PI_AOD, and PD-PI_AI). GLB stands for the region average within 60°S and 60°N, NH and SH are average over the northern and southern hemisphere, LAD and OCN are average over the land and ocean, and the rest of 14 regions are same as that defined in Figure 5.2.

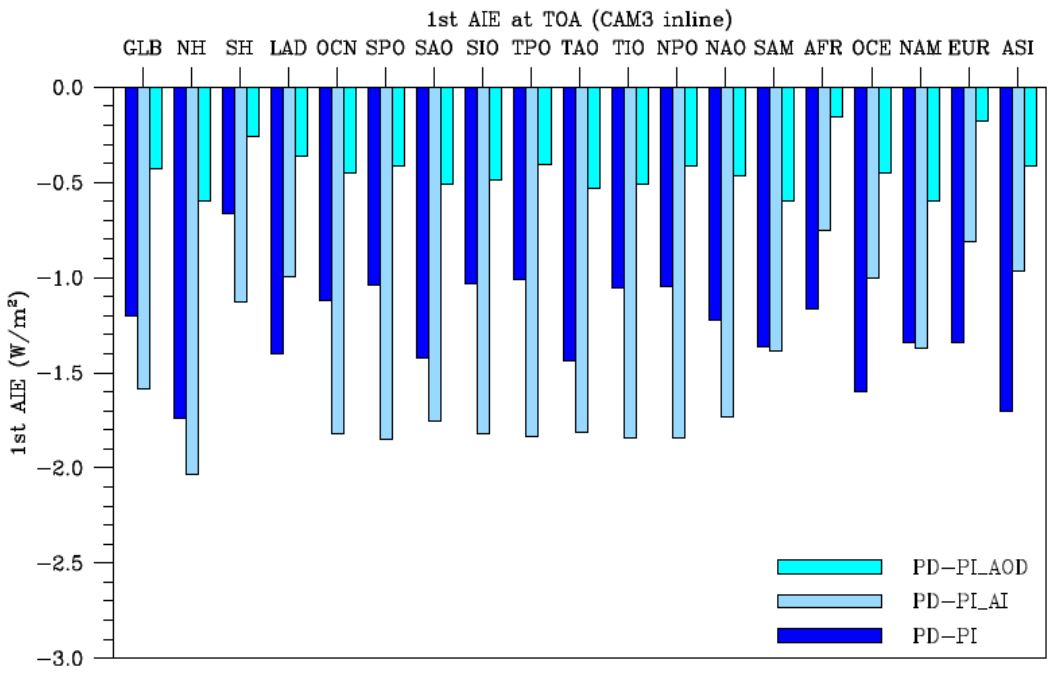

Figure 5.18: Same as in Figure 5.17 from the coupled CAM/IMPACT inline model.

Table 5.6 summarizes forcings calculate from the offline model as well as using inline values of N_d, AOD and AI from the coupled CAM/IMPACT model by holding cloud liquid water content and cloud fraction constant at PD values. The estimated forcing based on the derived PI concentrations of N_d from the regression of ACI_N(AOD) is smaller (in absolute value) than that using the true PI value because the neglect of temporal variations causes this method to underestimate the forcing for the off-line calculations. The forcing based on the CAM/IMPACT inline-calculated N_d from PD and PI simulations (-1.29 W m^{-2}) is somewhat smaller than that deduced from the method based on the IPCC defined forcing (-1.69 W m^{-2}). The forcing from the regression of ACI_N(AOD) and of ACI_N(AI) using the inline model is almost twice that of the offline model. Values for the slope of ACI_N(AOD) and for the slope of ACI_N(AI) from the inline model are, in general, larger than those from the offline model. This leads to the smaller

derived PI droplet number concentrations and hence the larger forcings (in absolute value) compared to those from the offline calculations. Larger slopes in the inline model compared to those computed from the offline model are mainly caused by the decreases loss of cloud droplets when aerosols increase because more aerosols lead to less sedimentation and precipitation, thereby reducing the sink of cloud droplets and resulting in relatively higher droplet number concentrations for a given aerosol concentrations.

Table 5.6: Forcing (W/m^2) based on PD and true PI model results for droplet number concentrations as well as for PI estimates using the regression of ACI_N(AOD) and of ACI_N(AI).

	PD – PI	PD – PI based on ACI_N(AOD)	PD – PI based on ACI_N(AI)
Inline N_c from CAM/IMPACT[a]	-1.29	-0.43	-1.59
Off-line N_c	-1.69	-0.27	-1.09

[a]Inline model results for PD and PI droplet number concentrations include changes from the initial concentration due to sedimentation, coagulation, and precipitation.

The PD slopes estimated from satellites actually include the feedbacks between aerosols and clouds, so this example also shows that the satellite-estimated indirect forcing by use of slopes of either ACI_N(AOD) or ACI_N(AI) could not be expected to match with the IPCC-defined first aerosol indirect forcing. We also note that the forcing based on the derived PI N_d from the regression of ACI_N(AI) in the inline model is larger than that using the modeled true PI values of N_d whereas it is smaller in the offline model. This is caused by the larger slopes using inline values as apposed to the slopes computed using offline values as discussed above.

5.6 Discussion and conclusions

This study is motivated by the large discrepancy in estimates of the aerosol first indirect forcing between satellites and global models. In the present work, we use an offline radiative transfer model combined with statistical slopes of $\ln(N_d)$ versus ln(AOD) or slopes of $\ln(N_d)$ versus ln(AI) based on either only PD values of aerosol and cloud properties or PD and PI values to explore the reason why satellite-based estimates of aerosol first indirect forcing are consistently smaller than model-based estimates. Moreover, the feedbacks between aerosol loadings and cloud droplet number concentrations are also taken into account by using inline calculations of N_d, AOD and AI from the coupled CAM/IMPACT model by holding cloud liquid water path and cloud fraction constant at the PD condition. Furthermore, we also investigated why the cloud droplet number does not necessarily increase with the increase of aerosol loadings as the conventional wisdom (i.e., the number of activated CCN increases with the number of CCN in a rising air parcel (Twomey, 1959)).

Our study shows that statistical slopes based on the temporal variation of PD and PI values of N_d and AOD would be steeper than those only based on spatial variation of PD values because the spatial variation of PD values does not include magnitude of AOD and N_d as small as those in the PI simulation. Statistical slopes of ACI_N(AI) based on PD and PI simulations can be steeper (Figure 5.3e) or flatter (Figure 5.3d) than those based on the PD simulation. By using slopes of ACI_N(AOD) or ACI_N(AI) to estimate aerosol indirect forcing, we found that the forcing based on the estimated N_d in the PI condition from the regression of ACI_N(AOD) is smaller than that using the true PI values of N_d over an entire globe and all regions (shown in Figure 5.17) while that based on slopes of

ACI_N(AI) is closer to the true model-estimated forcing over the ocean than that over the land. It turns out that the global average indirect forcing using true PD and PI values is -1.69 W m^{-2} while that using the satellite-based method is in general smaller, only -0.27 W m^{-2} for the slope of ACI_N(AOD), and -1.09 W m^{-2} for the slope of ACI_N(AI). Note that the estimated forcing using the satellite-based method with the slope of AI in some regions, specifically in the Pacific Ocean (NPO, SPO and TPO), is more negative than the true indirect forcing, but it underestimates the negative forcing in most regions. In accordance with previous analyses based on box-model results (Feingold, 2003), we conclude that the associated error in aerosol indirect forcing can be between a factor of 3 to more than a factor of 6 on a global average basis if one uses ACI_N(AOD) to estimate PI N_d or about ±25-35% if one uses ACI_N(AI). Besides, we also notice that the estimated aerosol indirect forcing using AI is closer to the true indirect forcing than that using AOD, indicating that AI is better served as the proxy of aerosol loadings than AOD because it is sensitive to the fine mode aerosol that is more likely to served as CCN (Nakajima et al., 2001; Bréon et al., 2002; Quaas et al., 2004).

In above, the findings are based on the study of initial cloud droplets variation with aerosol perturbations using an offline radiative transfer model in order to be consistent with the IPCC-defined first aerosol indirect forcing. In reality, the values of N_d "seen" from satellites actually include the effects of changes of N_d due to sedimentation, coagulation and precipitation. By using inline values of N_d, AOD and AI from the coupled CAM/IMPACT model, the forcing from the regression of ACI_N(AOD) or ACI_N(AI) is larger by a factor of 2 than that of offline calculations. That is because statistical slopes from inline calculations are, in general, larger than those computed in

offline calculations. This leads to smaller derived PI droplet number concentrations and hence larger negative forcing. The larger slopes from inline calculations possibly result from the reduction of sink of cloud droplets with the enhancement of aerosol loadings. That means, relatively larger changes of cloud droplet number for a given variation of aerosol concentration leads to increases of slopes of ACI_N(AOD) or ACI_N(AI). We also note that the increase in slopes using inline calculations causes the forcing estimated with the slope of ACI_N(AI) to be larger than the true forcing as opposed to relatively smaller value computed in the offline model.

In this study, when calculating statistical relationship between N_d and AOD or AI, negative response from the cloud droplets with the increase of aerosol loadings are found in some regions/seasons, such as Asia and Europe during the season MAM. Over the Asia during the spring time, on one hand, insoluable black carbon and organic matter originated from fossil fuel combustion are not excellent CCN; on the other hand, smoke aerosols exerts the competition with sulfate as CCN for the available water vapor. Over the Europe, the dominant mineral dust particles blown from the Sahara play a significant role, either similar as fossil fuel black carbon in Asia served as bad CCN, or served as giant CCN to inhibit the activation of small particles such as sulfate. This is contrast to the conventional way that the cloud droplet number increases with the increase of aerosol loadings.

In summary, we demonstrate that the use of PD values of N_d and statistical slopes of ACI_N(AOD) or ACI_N(AI) to estimate derived PI values of N_d is unlikely correct. This is because the use of regression techniques based on the spatial variation of aerosol and cloud properties in the PD condition in which satellite data are available hides the true

temporal variation of aerosols and clouds going from the PI to PD condition since there is no grantee that the relationship between N_d and AOD for the PD condition would be the same as that based on true PI and PD values (Figure 5.3). Satellite estimates of aerosol indirect forcing are expected to be improved in conjunction with the use of models to quantify the source of errors. On the other hand, model estimates of aerosol indirect forcing are also suspected since no one is able to reproduce the PD slopes between N_d and AOD inferred from the satellites in different regions (Quaas et al., 2009). Therefore, we hope improvements of both satellite and model based approaches could eventually bring satellite-based and model-based estimates of aerosol first indirect forcing closer, helping to advance our understandings of aerosol effects on clouds.

CHAPTER VI

SUMMARY AND FUTURE WORK

6.1 Summary

This dissertation includes two focuses. The first one is to simulate nitrate and ammonium in a global model and evaluate their direct and indirect effect. The second one is to evaluate the difference between the satellite-based estimates of aerosol indirect forcing and model-based estimates.

The first half of this dissertation focuses on the prediction as well as the treatment of nitrate and ammonium aerosols in both the box and global model. Due to the semi-volatile feature of nitrate and ammonium, both nitrate and ammonium can exist in gas and aerosol phase. The amount of nitrate and ammonium in the fine aerosol mode with diameter less than 1.25 μm is typically determined by a thermodynamic model. The instantaneous thermodynamic equilibrium with gas phase can be established for small particles within a few minutes under typical atmospheric conditions (Wexler and Seinfeld, 1990; Dassios and Pandis, 1999). The choice of thermodynamic model is critical for the partitioning of nitrate and ammonium for small particles between aerosol phase and their precursor gases HNO_3 and NH_3. In contrast to small particles, the

diffusion of semi-volatile gases to large particles is generally slow, especially under cold temperatures and low species concentrations, with a timescale on the order of several hours or even several days (Meng and Seinfeld, 1996; Seinfeld and Pandis, 1998). The non-equilibrium phenomenon between gases and aerosols with larger sizes exists, which has been observed for coarse particles during the Southern California Air Quality Study (SCAQS) (John et al., 1989). Therefore, the appropriate representation of the partitioning of semi-volatile species (e.g., HNO_3, HCl and NH_3) between their gas and particle phase for both fine and coarse aerosol modes is essential to accurately predict aerosol chemical compositions. Moreover, aerosol nitrate and ammonium are formed on the surface of pre-existing aerosol particles through the partitioning of gaseous HNO_3 into the aerosol phase and through the hydrolysis of N_2O_5. The amount of nitrate and ammonium formed on particle surfaces may depend on how these pre-existing aerosols are mixed.

In Chapter II, a comprehensive comparison between EQUISOLV II and EQSAM4 models for various relative humidities and chemical compositions was conducted assuming thermodynamic equilibrium for small particles. EQUISOLV II is one of the most reliable and widely used equilibrium models while EQSAM4 is based on parameterizations that improve computational efficiency and flexibility regarding the large number of aerosol species that can be considered (currently 100 compounds per solid or liquid phase per aerosol mode or size bin). Our major objective is to gain an improved understanding of the similarities and differences between these two models for the representation of the gas/liquid/solid partitioning of the aerosols under various thermodynamic regimes. In general, the particulate nitrate concentration predicted by two models agrees satisfactorily, except for the conditions around the deliquescence relative

humidity (about 60%). At higher relative humidity, EQSAM4 predicts similar or for a few cases somewhat more nitrate because the EQSAM4 parameterizations result in a slightly larger activity coefficient for NH_4NO_3. The largest discrepancies occur at a relative humidity regime between 50-60% due to the differences in the prediction of the mixed phase transition, which affects the associated water concentration. Similar to particulate nitrate, both models agree under most conditions for particulate ammonium, especially in the sulfate rich and neutral regimes. A comparison of the prediction of nitrate and ammonium using these two models with observed atmospheric conditions was also conducted. The nitrate and ammonium concentrations during the MINOS campaign were simulated for the summer of 2001 from July 28th to August 21st in Crete, Greece, a location characterized by high solar intensity and polluted air from Europe. Overall, both EQSAM4 and EQUSOLV II underestimate particulate ammonium as compared to the observations by 32% and 25% on average, respectively. The predictions of particulate nitrate by both models deviate significantly from the observations only for the dry period. This is related to the fact that the concentration of total nitrate is very low and most of total nitrate is observed in the gas phase. Because of the very low nitrate concentrations, the impact of these differences on the prediction of total particulate matter as well as aerosol water is minor. Both EQSAM4 and EQUISOLV II are able to reproduce the gaseous nitric acid and particulate matter to within a factor of 1.5 in 98% of the observations and to within a factor of 2 in more than 90% of the observations, respectively. Our comparisons show that the results of EQSAM4 and EQUISOLV II are comparable under most conditions. However, debates on the validation of concepts of the EQSAM4 arise when we submitted the manuscript based on this part of work (Xu et al.,

2009) to the Atmospheric Chemistry and Physics Discussion (ACPD). Two accompanying paper (Metzger et al., 2011a, b) were then submitted to clarify EQSAM4 as a parameterization module. EQUISOLV II is used for the rest of the dissertation.

In Chapter III, we study the heterogeneous formation of nitrate and ammonium aerosols in a box model of EQUISOLV II. Two mixing states are considered assuming either completely internally mixed (IM) or externally mixed (EM) with partial internal mixing for pre-existing aerosol particles using the hybrid dynamic method (HDYN). We also compare two different treatments for mass transfer between gas and aerosol (i.e., a simple kinetic-limited equilibrium (KEQ) method versus the HDYN method) in order to gain some insights for future implementation in the global chemistry transport model. Considering three types of pre-existing aerosols (i.e., sulfate, dust and sea salt), the prediction of nitrate and ammonium using two mixing states (i.e., IM versus EM) is evaluated for three different aerosol backgrounds: continental, marine as well as comprehensive mixed condition with varying dust and sea salt concentrations. For both continental and marine cases, the differences in the use of these two treatments are negligible for the predicted NH_4^+ concentrations while large differences occur in the prediction of NO_3^- concentration. The IM treatment favors the condensation of gaseous HNO_3 on larger particles through the diffusion limited mass transfer while the EM treatment predicts higher NO_3^- in the smaller size of aerosols. The reason is that the additional aerosol surface provided by dust and sea salt aerosols allows the heterogeneous reaction between HNO_3 and cations (e.g., Ca^{2+}, Na^+, K^+ and Mg^{2+}) tied to dust and the cation Na^+ tied to sea salt and forms more metal nitrate salts, which results in comparably higher nitrate formed in the fine mode. For the mixed case, two sequential orders (i.e.,

first for sulfate, then dust and sea salt versus first for sulfate, then sea salt and dust) among three aerosol types have been examined and the relative difference is less than 10% calculated for a wide range of dust (i.e., 0.1~100 μg m^{-3}) and sea salt (0.01~50 μg m^{-3}) concentrations. In the second part of Chapter III, a simple kinetic-limited equilibrium (KEQ) method (Pringle et al., 2010) that is more computationally efficient is examined against the hybrid dynamic (HDYN) method that is theoretically more accurate. The idea behind the KEQ method is to calculate the amount of volatile species that is kinetically able to condense onto aerosol particles at the first stage and then to re-distribute this amount of volatile gases between gas and aerosol phase with a thermodynamic equilibrium model. For both continental and marine cases, the KEQ method predicts higher amount of nitrate occurring in the aerosol phase than does the HDYN method but it predicts lower nitrate formed on small particles and consequently higher amount of nitrate formed on larger particles, which results in the large discrepancy in the representation of aerosol nitrate size distribution between these two methods. The prediction of nitrate and nitric acid by the KEQ method is very close to that by the EQ method for both continental and marine cases. That is because the KEQ method does not explicitly constrain the mass fraction of volatile species 'kinetically' able to condense onto aerosol particles for any aerosol with the radius larger than 0.0036 μm in the first stage shown in the Chapter III. Therefore, for the aerosol radius range from 0.05 to 10 μm considered in this study, the KEQ method is actually reduced to the pure equilibrium method at the second stage. Additionally, the KEQ method is problematic on several aspects discussed in detail in the Chapter III, for instance, assuming zero equilibrium partial pressure of volatile species (e.g., HNO_3, NH_3 and HCl) at the particle surface as

same as H_2SO_4 gas with low volatility, applying the diffusion coefficient of H_2SO_4 gas for all semi-volatile species, using a crude time step to solve mass transfer equations.

Based on the results in Chapter II and III, the hybrid dynamic (HDYN) method assuming that all the pre-existing aerosols are externally mixed (EM) with partial internally mixed sulfate is implemented into the global chemical transport model to study nitrate and ammonium aerosols in Chapter IV. The simulated results with this implementation are presented together with their radiative effects. In general, the model with this implementation predicts similar spatial distribution of total nitrate and ammonium as those in pioneer studies (Feng and Penner, 2007; Liao et al., 2003; Adams et al., 1999) for the PD scenario. In most industrialized regions such as eastern United States, Europe and China, nitrate aerosols mainly exceed 1 ppbv with the form of ammonium nitrate in an amount determined by a thermodynamic equilibrium. Nitrate over continents generally exceeds 300 pptv while marine mixing ratio of nitrate is comparably lower in the range of 1-100 pptv except in coastal regions. At regions with high dust and sea salt aerosols, more than 50% of total nitrate are present in aerosol phase, indicating the formation of nitrate in these regions is limited by the availability of gas-phase HNO_3. The predicted mixing ratios of ammonium are mainly determined by both ammonia emission and uptake by sulfate and nitrate. The highest ammonium mixing ratios are found closely tied with sulfate concentrations in industrialized regions. Continental ammonium mixing ratios exceed 300 pptv almost everywhere while marine mixing ratios of ammonium are in the range of 100-300 pptv. The predicted NO_3^- lifetime in this work is 4.2 days while it is 5.1 days in the simulation following the IM treatment similar as Feng and Penner (2007). The shorter lifetime can be ascribed to two aspects:

larger sources (or sinks) and smaller predicted burden of NO_3^-. By explicitly accounting for the interaction between nitric acid and all five types of aerosols, the total chemical production of aerosol nitrate are increased by about 11% compared with the IM treatment because mineral dust and sea salt provide more particle surfaces that allow more nitrate to be condensed. Hence, this work predicts 60% higher fine model aerosol nitrate through gas-to aerosol conversion. Due to different deposition strategies employed in these two treatments, the IM treatment removes nitrate from the atmosphere less efficiently than does the EM treatment in this work. This leads to a predicted lower nitrate burden in this work, despite that the higher gas-to-particle conversion is predicted compared with the IM treatment. For example, comparing the nitrate burden in the fine mode in the EM treatment with the IM treatment, it is enhanced by 6% in contrast to the 60% increase in the nitrate production in the fine mode. Compared to the IM treatment, the difference in the removal rate between these two treatments also causes lower burden and shorter lifetime of aerosol ammonium predicted in this work. In the second part of Chapter IV, we estimate the direct and indirect effects of nitrate and ammonium and their anthropogenic contributions. Nitrate and ammonium are found to exhibit two counteracting effects with respect to the direct effect on pre-existing aerosol particles in this work. The inclusion of ammonium and nitrate can boost scattering efficiency of scattering aerosols such as sulfate and organic matter from biomass burning since nitrate is generally more hygroscopic than sulfate and organic matter in terms of the cooling effect. On the other hand, nitrate contributes a warming effect when they are internally mixed with sea salt, by lowering scattering efficiency of sea salt aerosol particles due to its lower hygroscopicity than that of sea salt. The direct effect of nitrate and ammonium

at the top of atmosphere (TOA) for the present-day in this work is estimated to be -0.12 W m^{-2}, within the range of -0.07 W m^{-2} estimated by Jacobson et al. (2001) to -0.30 W m^{-2} by Adams et al. (2001). It is close to -0.11 W m^{-2} from Bauer et al. (2007) and -0.14 W m^{-2} from Liao et al. (2004). Smaller effect is estimated for the PI scenario due to smaller burden of ammonium and nitrate. The anthropogenic forcing of nitrate and ammonium is estimated to be -0.21 W m^{-2} and -0.25 W m^{-2} at TOA and the surface for the clear-sky condition, respectively. It is -0.11 W m^{-2} and -0.15 W m^{-2} at TOA and the surface for the cloudy-sky condition, respectively. Strong cooling of up to -3 W m^{-2} is found over Easter Asia, North America and Europe, which is consistent with areas where nitrate and ammonium aerosols are highest. The anthropogenic nitrate and ammonium direct forcing at the surface of -0.15 W m^{-2} calculated here is comparable to the -0.15 W m^{-2} estimated by Liao et al. (2005). The simulated results using monthly, daily and hourly aerosol fields indicate that the frequency of aerosol fields does not change the direct effect of nitrate and ammonium so much, i.e., within 5%. The indirect effect induced by total nitrate and ammonium is also examined based on the substitution method proposed by Chen (2006) who found that both aqueous phase nitrate and gas phase nitric acid have effect on aerosol activation. During an uplifting process in a parcel model, most of gas phase nitric acid was found to be redistributed to aerosol phase in the fine mode. In this work, we first calculate cloud droplet number without accounting for gas phase nitric acid effect and then distribute nitric acid gas to each aerosol type in the fine mode according to their relative activation fraction to the total cloud droplet number calculated in the first step. The cloud droplet number is updated with this new aerosol distribution following the same procedure in the first step. The total nitrate effect on aerosol activation is found to

have two counteracting effects. On one hand, the addition of nitrate and nitric acid enhances the activation of cloud condensation nuclei (CCN) by lowering critical supersaturation and increasing hygroscopicity when smaller particles collect comparably more gases. This increasing effect is dominant over continents. On the other hand, the addition of nitrate and ammonium could also decrease cloud drops when the ambient maximum supersaturation is suppressed. In general, the cloud droplet number increases with the addition of nitrate and ammonium on the global basis. Cloud optical properties may not change with a similar magnitude as the cloud droplet number because the addition of nitrate and ammonium also contributes to the broaden cloud droplet spectrum as it increases cloud droplet number. Hence, relative changes in cloud effective radius and cloud optical depth are predicted to be comparably smaller than relative changes in cloud droplet number due to the addition of nitrate and ammonium in this work. This is consistent with the findings in Xue and Feingold (2004). In summary, the first aerosol indirect effect of total nitrate and ammonium for the PD and PI simulation is estimated to be -0.24 W m^{-2} and -0.14 W m^{-2} at TOA, respectively, leading to the first aerosol indirect forcing of -0.1 W m^{-2} at TOA induced by anthropogenic nitrate and ammonium. Anthropogenic nitrate and ammonium aerosols have higher influence on clouds in the northern hemisphere than in the southern hemisphere and higher effects over the land than over the ocean. The anthropogenic aerosol first indirect forcing of total nitrate and ammonium is mainly determined by the nitric acid gas effect, which is -0.09 W m^{-2} on a global basis. This is the first estimate for the nitric acid gas effect in literature. The simulated results using monthly, daily and hourly average aerosol fields indicate that the

frequency of aerosol fields contributes to changing the direct effect of nitrate and ammonium within 5% while the change of aerosol indirect forcing is less than 10%.

In the second half of this dissertation, we focus on the study on the large discrepancy of aerosol indirect forcing estimated by satellites and global models. The aerosol indirect effect is recognized as one of the largest uncertainties in our understanding of climate change since its magnitude can be comparable to the warming effects due to greenhouse gases. Although there has been a large number of studies on the development of understanding the aerosol indirect effects on the global climate system over the past decade, uncertainties in the estimation of the indirect aerosol forcing is still large. The IPCC Fourth Assessment Report (AR4) gives a best estimate of -0.7 W m^{-2} as the median with a 5% to 95% confidence interval range of -0.3 to -1.8 W m^{-2} (Forster et al., 2007), whereas the lower end of this range stems from three model estimates constrained by satellites in contrast to comparably higher estimates from free-running global models. For model-based estimates, the aerosol indirect effect is usually assessed using prognostic variables such as cloud droplet number, aerosol mass and number concentration as well as updraft velocity to represent aerosol-cloud interactions by use of a parameterization based on the classical theory of aerosol activation. On the other hand, for the satellite-based estimates, the aerosol indirect effect is quantified by incorporating empirical statistical relationships between a proxy of column aerosol loadings (e.g., aerosol optical depth (AOD), aerosol index (AI), etc) and a proxy of column cloud properties (e.g., cloud droplet number concentration (N_d), cloud effective radius, cloud fraction, liquid water path, etc) derived from satellite observations. In Chapter V, we used an offline radiative transfer model combined with statistical slopes of $\ln(N_d)$ versus ln(AOD) (hereafter

referred as ACI_N(AOD)) or slopes of ln(N_d) versus ln(AI) (hereafter referred as ACI_N(AI)) based on either only present-day (PD) values of aerosol and cloud properties or PD and pre-industrial (PI) values to explore the reason why the satellite-based estimates of the first aerosol indirect forcing are generally smaller than model-based estimates. Our study shows that statistical slopes based on the temporal variation of PD and PI values of N_d and AOD would be steeper than those only based on spatial variation of the PD simulation because the spatial variation of PD values does not have magnitude of AOD and N_d as small as those in the PI simulation. Statistical slopes of ACI_N(AI) based on PD and PI simulations can be steeper or flatter than those based on the PD simulation. By using the slope of ACI_N(AOD) or ACI_N(AI) to estimate aerosol indirect forcing, we found that the forcing based on the estimated N_d in the PI condition from the regression of ACI_N(AOD) is smaller than that using the true PI values of N_d over entire globe and all regions while that based on the slope of ACI_N(AI) is closer to the true model-estimated forcing over the ocean than that over the land. It turns out that the global average indirect forcing using true PD and PI values is -1.69 W m^{-2} while that using the satellite-based method is in general smaller, only -0.27 W m^{-2} for the slope of ACI_N(AOD), and -1.09 W m^{-2} for the slope of ACI_N(AI). In summary, we conclude that the associated bias in aerosol indirect forcing can be between a factor of 3 to more than a factor of 6 on a global average basis if one uses ACI_N(AOD) to estimate PI N_d or about ±25-35% if one uses ACI_N(AOD). In addition to the findings based on initial cloud droplets variation with aerosol perturbations by using an offline radiative transfer model summarized above, inline values of N_d, AOD and AI from the CAM/IMPACT coupled model are evaluated in accordance with the scenario of N_d practically “seen” from

satellites that includes the change of N_d due to sedimentation, coagulation and precipitation. The forcing from the regression of ACI_N(AOD) using inline values is larger by a factor of 2 than that of offline calculations, leading to smaller derived PI droplet number concentrations and hence larger negative forcing. In summary, the use of PD values of N_d and the statistical slopes of ACI_N(AOD) or ACI_N(AI) to estimate derived PI values of N_d that satellites based on is unlikely to be correct. This is because the use of regression techniques based on the spatial variation of aerosol and cloud properties in the PD condition in which satellite data are available hides the true temporal variation of aerosols and clouds going from the PI to PD condition since there is no grantee that the relationship between N_d and AOD for the PD condition would be the necessarily same as that based on true PI and PD values. Satellite estimates of aerosol indirect forcing are expected to be improved in conjunction with the use of models to quantify the source of errors. On the other hand, unfortunately, model estimates of aerosol indirect forcing are also suspected since no one is able to reproduce the PD slopes between N_d and AOD inferred from satellites in different regions (Quaas et al., 2009). Therefore, we hope improvements of both satellite and model based approaches could eventually bring satellite-based and model-based estimates of aerosol first indirect forcing closer, which is helpful to advance our understandings of aerosol effects on clouds.

6.2 Future work

The study in this dissertation lays the foundation for further work discussed below.

First of all, one of most interesting directions is to couple the current nitrate model with the model including full tropospheric chemistry and to study heterogeneous interactions between tropospheric gases and aerosols. On one hand, aerosols impact gas-

phase chemistry by providing particle surfaces for heterogeneous conversion of gas-phase species (Dentener and Crutzen, 1993; Andreae and Crutzen, 1997; Jacob, 2000) and by altering photolysis rates (Dickerson et al., 1997; Jacobson, 1998; Liao et al., 1999, 2003; Martin et al., 2003; Bian and Zender, 2003). Liao et al. (2003) reported that the global effect of aerosols on gas-phase chemistry through altered photolysis rates is small. The changes in global O_3 concentrations due to aerosols are less than 1 ppbv (Liao et al., 2003). However, heterogeneous processes are found to have significant effects on ozone chemistry. Dentener et al. (1996) found a yearly average decrease of ozone up to 8% by including the heterogeneous interaction of N_2O_5 on mineral dust. Bauer et al. (2004) also confirmed the results from Dentener et al. (1996) and they found that the global tropospheric ozone mass can be reduced by 5% through the interactions of gas-phase species with mineral dust. Liao et al. (2005) summarized that anthropogenic ozone forcing is less by 20-45% in present-day and by 20-32% in the year 2100 when accounting for heterogeneous reactions compared with when they are absent. On the other hand, gas-phase species in the troposphere influence the formation of aerosols. For example, as discussed Chapter IV, the partitioning of HNO_3 between gas and aerosol phase determines the production of nitrate aerosols; the concentrations of O_3 and H_2O_2 have impact on the oxidation of SO_2 to form sulfate aerosols. Therefore, two issues might be of great importance in the future assessment of global radiative forcing of atmospheric chemical constitutes. One is how gas phase chemistry and aerosols intertwines each other; the other is how this gas-phase chemistry-aerosol interaction influences the direct radiative forcing of both anthropogenic O_3 and aerosols in the troposphere.

Secondly, in Chapter V, we also identified that the estimated aerosol indirect forcing using AI as a proxy of aerosol properties is closer to the true indirect forcing than that using AOD, especially over oceans, indicating that AI is better served as a proxy of aerosol properties than AOD. One reason is because it is sensitive to the fine mode aerosol that is more likely to served as CCN (Nakajima et al., 2001; Bréon et al., 2002; Quaas et al., 2004). Another reason is because human activities do not influence aerosols compositions over the ocean as much as they do over the land. Hence, the AI based on PD values might include similar magnitude of values in the PI condition as we shown in Chapter V. In light of that, this land-ocean contrast might, to some extent, serve as an indicator of anthropogenic activities. Probably, we could use AI values over pristine oceans as a proxy of PI aerosol properties whereas AI values over polluted regions regarded as a proxy of PD aerosol properties to infer aerosol effects on clouds in future. More tests and analysis need to be conducted on a trial-and-error basis in different regions of oceans and lands to provide more detail information about this hypothesis.

BIBLIOGRAPHY

Andreae, M. O., R. J. Charlson, F. Bruynseels, H. Storms, R. V. Grieken, and W. Maenhaut: Internal mixture of sea salt, silicates, and excess sulfate in marine aerosols, Science, 232, 1620–1623, 1986.

Andreae, M.O., et al.: Smoking rain clouds over the Amazon. Science, 303, 1337–1342, 2004.

Abdul-Razzak, H., and Ghan, S. J.: A parameterization of aerosol activation 2. Multiple aerosol types, Journal of Geophysical Research, 105, 6837-6844, 2000.

Abdul-Razzak, H., and Ghan, S. J.: A parameterization of aerosol activation - 3. Sectional representation, Journal of Geophysical Research, 107, 4026, doi:10.1029/2001JD000 483, 2002.

Adams, P. J., Seinfeld, J. H., and Koch, D. M.: Global concentration of tropospheric sulphate, nitrate and ammonium aerosol simulated in a general circulation model, J. Geophys. Res., 104, 13791-13823, 1999.

Adams, P. J., Seinfeld, J. H., Koch, D. M, Mickley, L., and Jacob, D.: General circulation model assessment of direct radiative forcing by the sulphate-nitrate-ammonium-water inorganic aerosol system, Journal of Geophysical Research, 106, 1097-1111, 2001.

Albrecht, B. A.: Aerosols, cloud microphysics, and fractional cloudiness, Science, 245, 1227-1230, 1989.

Andres, R. J., and Kasgnoc, A. D.: A time-averaged inventory of subaerial volcanic sulfur emissions, Journal of Geophysical Research, 103, 25251-25261, 1998.

Ansari, A. S., and S. N. Pandis: Response of inorganic PM to precursor concentrations, Environ. Sci. Technol., 32, 2706-2714, 1998.

Ansari, A.S. and Pandis, S.N.: Prediction of multicomponent inorganic atmospheric aerosol behavior, Atmos. Environ., 33, 745-757,1999a.

Ansari, A.S. and Pandis, S.N.: An analysis of four models predicting the partitioning of semivolatile inorganic aerosol components, Aeros. Sci. Tech., 31, 129-153,1999b.

Ansari, A.S. and Pandis, S.N.: The effect of metastable equilibrium states on the partitioning of nitrate between the gas and aerosol phases, Atmos. Environ., 34, 157-168, 2000.

Amundson, N.R., Caboussat, A., He, J.M., Martynenko, A.V., Savarin, V.B. and Seinfeld, J.H.: A new inorganic atmospheric aerosol phase equilibrium model (UHAERO), Atmos. Chem. Phys., 6(4), 975-992, 2006.

Bassett, M.E. and Seinfeld, J.H.: Atmospheric equilibrium models of sulfate and nitrate aerosol II, Particle size analysis, Atmos., Environ., 18, 1163-1170, 1983.

Bassett, M.E. and Seinfeld, J.H.: Atmospheric equilibrium models of sulfate and nitrate aerosol, Atmos. Environ., 17, 2238-2252, 1984.

Bauer, S. E., Y. Balkanski, M. Schulz, D. A. Hauglustaine, and F. Dentener: Global modeling of heterogeneous chemistry on mineral aerosol surfaces: Influence on tropospheric ozone chemistry and comparison to observations, J. Geophys. Res., 109, D02304, doi:10.1029/2003JD003868, 2004.

Bauer, S.E., D. Koch, N. Unger, S.M. Metzger, D.T. Shindell, and D.G. Streets: Nitrate aerosols today and in 2030: Importance relative to other aerosol species and tropospheric ozone. Atmos. Chem. Phys., 7, 5043-5059, doi:10.5194/acp-7-5043-2007, 2007.

Binkowski, F.S. and U. Shankar: The regional particulate matter model, 1. mode desription and preliminary results, Journal of Geophysical research, 100, 26191-26209, 1995.

Bollasina, M. A., Y. Ming, and V. Ramaswamy: Anthropogenic aerosols and the weakening of the South Asian summer monsoon, Science, 334, 502, 2011.

Bond, T. C., G. Habib, and R. W. Bergstrom: Limitations in the enhancement of visible light absorption due to mixing state, J. Geophys. Res., 111, D20211, doi:10.1029/2006JD007315, 2006.

Boucher, O., and U. Lohmann: The sulfate-CCN-cloud albedo effect: a sensitivity study using two general circulation models. Tellus, 47B, 281–300, 1995.

Bouwman, A. F., D. S. Lee, W. A. H. Asman, F. J. Dentener, K. W. Van Der Hoek, and J. G. J. Olivier: A global high-resolution emission inventory for ammonia, Global Biogeochem. Cycles, 11, 561–588, 1997.

Boville, B. A., P. J. Rasch, J. J. Hack, and J. R. McCaa: Representation of clouds and precipitation processes in the Community Atmosphere Model version 3 (CAM3), J. Clim., 19(11), 2184–2198, doi:10.1175/JCLI3749.1, 2006.

Brenguier, Jean-Louis, Hanna Pawlowska, Lothar Schüller, Rene Preusker, Jürgen Fischer, Yves Fouquart: Radiative Properties of Boundary Layer Clouds: Droplet

Effective Radius versus Number Concentration. J. Atmos. Sci., 57, 803–821, 2000.

Brenguier, J.L., H. Pawlowska, and L. Schuller: Cloud microphysical and radiative properties for parameterization and satellite monitoring of the indirect effect of aerosol on climate. J. Geophys. Res., 108(D15), 8632, doi:10.1029/2002JD002682, 2003.

Bréon, F.-M., D. Tanré, and S. Generoso: Aerosol effect on cloud droplet size monitored from satellite. Science, 295, 834–838, 2002.

Bromley, L.A.: Thermodynamic properties of strong electrolytes in aqueous solutions. AI. Ch. E. Journal 19, 313-320, 1973.

Cantrell, B. K., and Whitby, K. T.: Aerosol size distributions and aerosol volume formation for a coal-fired power-plant plume, Atmospheric Environment, 12, 323-333, 1978.

Capaldo, K., Pilinis, C., and Pandis, S. N.: A computationally efficient hybrid approach for dynamic gas/aerosol transfer in air quality models, Atmos. Environ., 34, 3617–3627, 2000.

Chameides, W. L., C. Luo, R. Saylor, D. Streets, Y. Huang, M. Bergin, and F. Giorgi: Correlation between model-calculated anthropogenic aerosols and satellite-derived cloud optical depths: Indication of indirect effect?, J. Geophys. Res., 107(D10), 4085, doi:10.1029/2000JD000208, 2002.

Charlson, R. J., J. E. Lovelock, M. O. Andreae, and S. G. Warren: Oceanic phytoplankton atmospheric sulphur, cloud albedo and climate, Nature, 326, 655-661, 1987.

Chen, Y., and J.E. Penner: Uncertainty analysis of the first indirect aerosol effect. Atmos. Chem. Phys., 5, 2935–2948, 2005.

Chen, Y.: Aerosol indirect effects on clouds and global climate, PhD, Department of Atmospheric, Oceanic, and Space Sciences, University of Michigan, Ann Arbor, MI, 218 pp., 2006.

Chuang, C.C., et al.: An assessment of the radiative effects of anthropogenic sulfate. J. Geophys. Res., 102(D3), 3761–3778, 1997.

Chuang, C.C., et al.: Cloud susceptibility and the first aerosol indirect forcing: Sensitivity to black carbon and aerosol concentrations. J. Geophys. Res., 107(D21), 4564, doi:10.1029/2000JD000215, 2002.

Clegg, S.L., Pitzer, K.S. and Brimblecombe, P.: Thermodynamics of multicomponent, miscible, ionic solutions. II. Mixture including unsymmetrical electrolytes. Journal of Physical Chemistry, 96, 9470–9479, 1992.

Clegg, S.L., Pitzer, K.S. and Brimblecombe, P.: (additions and corrections for their published papers). Journal of Physical Chemistry, 98, 1368, 1994.

Clegg, S.L., Pitzer, K.S. and Brimblecombe, P.: (additions and corrections for their published papers). Journal of Physical Chemistry, 99, 6755, 1995.

Clegg, S.L., Brimblecombe, P. and Wexler, A.S.: A thermodynamic model of the system H^+–NH_4^+–Na^+–SO_4^{2-}–NO_3^-–Cl^-–H_2O at 298.15 K, Journal of Physical Chemistry, 102, 2155–2171, 1998a.

Clegg, S.L., Brimblecombe, P. and Wexler, A.S.: A thermodynamic model of the system H^+–NH_4^+–Na^+– SO_4^{2-}–NO_3^-–Cl^-–H_2O at tropospheric temperatures. Journal of Physical Chemistry, 102, 2137–2154, 1998b.

Collins, W. D., P. J. Rasch, B. A. Boville, J. J. Hack, J. R. McCaa, D. L. Williamson, B. P. Briegleb, C. M. Bitz, S. J. Lin, and M. H. Zhang: The formulation and atmospheric simulation of the Community Atmosphere Model version 3 (CAM3), J. Clim., 19(11), 2144 – 2161, doi:10.1175/JCLI3760.1, 2006a.

Collins, W. D., et al.: The Community Climate System Model version 3 (CCSM3), J. Clim., 19(11), 2122– 2143, doi:10.1175/JCLI3761.1, 2006b.

Dassios, K. G., and S. N. Pandis: The mass accommodation coefficient of ammonium nitrate aerosol, Atmos. Environ., 33, 2999– 3003, 1999.

Dall'Osto, M., Harrison, R. M., Coe, H., Williams, P. I., and Allan, J. D.: Real time chemical characterization of local and regional nitrate aerosols, Atmos. Chem. Phys., 9, 3709-3720, doi:10.5194/acp-9-3709-2009, 2009.

de Reus, M., F. Dentener, A. Thomas, S. Borrmann, J. Ström, and J. Lelieveld: Airbone observations of dust aerosol over the North Atlantic Ocean during ACE 2: Indication for heterogeneous ozone destruction, J. Geophys. Res., 105, 15263-15275, 2000.

Dentener, F. J., and P. Crutzen: A three-dimensional model of the global ammonia cycle, J. Atmos. Chem., 19, 331– 369, 1994.

Dufresne, L.L., et al.: Contrasts in the effects on climate of anthropogenic sulfate aerosols between the 20th and the 21st century. Geophys. Res. Lett., **32**, L21703, doi:10.1029/2005GL023619, 2005.

Ehhalt, D., and J.W Drummond, The tropospheric cycle of NOx: chemistry of the unpolluted and polluted troposphere, W.J Georgii, Editor, Proc. NATO Adv. Study Inst.,Corfu, Greece, 28 Sept.–10 Oct., 1981 Reidel, Dordrecht, pp. 219–251, 1982.

Feingold, G., Remer, L. A., Ramaprasad, J., and Kaufman, Y. J.: Analysis of smoke impact on clouds in Brazilian biomass burning regions: an extension of Twomey's approach, J. Geophys. Res., 106, 22907–22922, doi:10.1029/2001JD000732, 2001.

Feingold, G., 2003: Modelling of the fi rst indirect effect: Analysis of measurement requirements. Geophys. Res. Lett., 30(19), doi:10.1029/2003GL017967, 1997.

Feng, Y.: Global modeling of nitrate and ammonium aerosol: radiative effect and interaction with gas-phase chemistry and aerosols, PhD, Department of Atmospheric, Oceanic, and Space Sciences, University of Michigan, Ann Arbor, MI, 265 pp., 2005.

Feng, Y., J. E. Penner, S. Sillman, and X. Liu: Effects of cloud overlap in photochemical models, J. Geophys. Res., 109, D04310, doi:10.1029/2003JD004040, 2004.

Feng, Y and Penner, J.E.: Global modeling of nitrate and ammonium: Interaction of aerosols and tropospheric chemistry, J. Geophys. Res., 112, D01304, doi: 10.1029/2005JD006404, 2007.

Ferek, R., D. Hegg, P. Hobbs, P. Durkee, and K. Nielsen: Measurements of ship‐induced tracks in clouds off the Washington coast, J. Geophys. Res., 103(D18), 23199-23206, 1998.

Fountoukis, C. and Nenes, A.: ISORROPIA II: a computationally efficient thermodynamic equilibrium model for K^+-Ca^{2+}-Mg^{2+}-NH_4^+-Na^+-SO_4^{2-}-NO_3^--Cl^--H_2O aerosols, Atmos. Chem. Phys., 7, 4639-4659, 2007.

Forster, P., V. Ramaswamy, P. Artaxo, T. Berntsen, R. Betts, D.W. Fahey, J. Haywood, J. Lean, D.C. Lowe, G. Myhre, J. Nganga, R. Prinn, G. Raga, M. Schulz and R. Van Dorland: Changes in Atmospheric Constituents and in Radiative Forcing. In: Climate Change 2007:The Physical Science Basis. Contribution of Working Group I to the Fourth Assessment Report of the Intergovernmental Panel on Climate Change [Solomon, S., D. Qin, M. Manning, Z. Chen, M. Marquis, K.B. Averyt, M.Tignor and H.L. Miller (eds.)]. Cambridge University Press, Cambridge, United Kingdom and New York, NY, USA, 2007.

Fuchs, N. A., and Sitigom, A. G.: High dispersed aerosols, in Topics in Current Aerosol Research (Part 2), edited by G. M. Hidy and J. R. Brock Pergamon, New York, pp.1-200, 1971.

Garrett, T. J., C. Zhao, X. Dong, G. G. Mace, and P. V. Hobbs: Effects of varying aerosol regimes on low-level Arctic stratus, Geophys. Res. Lett., 31, L17105, doi:10.1029/2004GL019928, 2004.

Ghan, S. J., G. Guzman, and H. Abdul-Razzak, Competition between sea salt and sulfate particles as cloud condensation nuclei, J. Atmos. Sci., 55, 3340-3347, 1998.

Ghan, S., et al.: Evaluation of aerosol direct radiative forcing in MIRAGE. J. Geophys. Res., 106(D6), 5295–5316, 2001.

Ghan, S., and Schwartz, S. E.: Aerosol properties and processes, Bulletin of the American Meteorological Society, 88, 1059-1083, 2007.

Ginoux, P., Chin, M., Tegen, I., Prospero, J. M., Holben, B., Dubovik, O., and Lin, S. J.: Sources and distributions of dust aerosols simulated with the GOCART model, Journal of Geophysical Research, 106, 20255-20273, 2001.

Ginoux, P., Prospero, J. M., Torres, O., and Chin, M.: Long-term simulation of global dust distribution with the gocart model: Correlation with north atlantic oscillation, Environ. Model. Software, 19, 113–128, 2004.

Gong, S. L., Barrie, L. A., and Blanchet, J. P.: Modeling sea-salt aerosols in the atmosphere .1. Model development, J. Geophys. Res., 102, 3805–3818, 1997.

Goodman, A. L., G. M. Underwood, and V. H. Grassian: A laboratory study of the heterogeneous reaction of nitric acid on calcium carbonate particles, J. Geophys. Res., 105, 29,053–29,064, 2000.

Guazzotti, S. A., J. R. Whiteaker, D. Suess, K. R. Coffee, and K. A. Prather: Real-Time Monitoring of Individual Atmospheric Aerosol Particles: Establishing Correlations Between Particle Size and Chemical Speciation, Atmos. Environ., 35, 3229– 3240, 2001.

Guenther, A., Hewitt, C. N., Erickson, D., Fall, R., Geron, C., Graedel, T., Harley, P., Klinger, L., Lerdau, M., Mckay, W. A., Pierce, T., Scholes, B., Steinbrecher, R., Tallamraju, R., Taylor, J., and Zimmerman, P.: A global-model of natural volatile organic-compound emissions, Journal of Geophysical Research, 100, 8873-8892, 1995.

Gultepe, I., et al.: Parameterizations of marine stratus microphysics based on in-situ observations: Implications for GCMs, J. Clim., 9, 345– 357, 1996.

Hansen, J., M. Sato, and R. Ruedy: Radiative forcing and climate response. Journal of Geophysical Research, 102, 6831-6864., 1997.

Harned, H.S. and Owen, B.B.: The Physical Chemistry of Electrolyte solutions, New York, Reinhold, Chapter 8, 1958.

Haywood, J.M. and Ramaswamy, V.: Global sensitivity studies of the direct radiative forcing due to anthropogenic sulfate and black carbon aerosols. Journal of Geophysical Research 103(D6): doi: 10.1029/97JD03426. issn: 0148-0227, 1998.

Heintzenberg and Coauthors: Characteristics of haze, mist and fog. Contrib. Atmos. Phys., 71, 21–30, 1998.

Herzog, M., D. K. Weisenstein, and J. E. Penner: A dynamic aerosol module for global chemical transport models: Model description, J.Geophys. Res., 109, D18202, doi:10.1029/2003JD004405, 2004.

Hofmeister, F.: Zur Lehre von der Wirkung der Salze, Arch. Exp. Pathol. Pharmakol, (Leipzig) 24 (1888) 247–260; translated in: Zur Lehre von der Wirkung der Salze

(about the science of the effect of salts: Franz Hofmeister's historical papers, edited by: Kunz, W., Henle, J., and Ninham, B. W., Curr. Opin. Coll. Interface Sci., 9, 19–37, 2004.

Hoose, C., Kristj´ansson, J. E., Iversen, T., Kirkev°ag, A., Seland, Ø., and Gettelman, A.: Constraining cloud droplet number concentration in GCMs suppresses the aerosol indirect effect, Geophys. Res. Lett., 36, L12807, doi:10.1029/2009GL038568, 2009.

Intergovernmental Panel on Climate Change (IPCC), Climate change 1994: Radiative Forcing of Climate Change and an Evaluation of the IPCC IS92 Emission Scenarios [Houghton, J. T., L. G. Meria Filho, J. Bruce, H. Lee, B. A. Callander, E. F. Haites, N. Harris, and K. Maskell (eds.)], Cambridge Univ. Press, Cambridge, United Kingdom and New York, NY, USA, 1994.

IPCC: Climate change 2007: The physical science basis. Contribution of working group I to the fourth assessment report of the intergovernmental panel on climate change, edited by: Solomon, S., D. Qin, M. Manning, Z. Chen, M. Marquis, K.B. Averyt, M. Tignor and H.L. Miller, Cambridge University Press, 996 pp., 2007.

Ito, A. and Penner, J. E.: Historical emissions of carbonaceous aerosols from biomass and fossil fuel burning for the period 1870-2000, Global Biogeochem. Cycles, 19, GB2028, doi:10.1029/2004GB002374, 2005.

Ito, A. and Akimoto, H.: Seasonal and interannual variations in CO and BC emissions from open biomass burning in Southern Africa during 1998–2005, Global Biogeochem Cycle, 21, 2, GB2011, 2007.

Ito, A: Lightning emissions fro NO_x, NO_2 from gas-phase IMPACT, Mar. 21, 2008.

Iversen, T., and O. Seland: A scheme for process-tagged SO4 and BC aerosols in NCAR CCM3: Validation and sensitivity to cloud processes. J. Geophys. Res., 107(D24), 4751, doi:10.1029/2001JD000885, 2002.

Jacob, D. J., and S. C. Wofsy: Budgets of reactive nitrogen, hydrocarbons, and ozone over the Amazon forest during the wet season, J. Geophys. Res., 95, 16,737–16,754, 1990.

Jacobson, M.Z., Tabazadeh, A., and Turco, R.: Simulating equilibrium within aerosols and nonequilibrium between gases and aerosols, J. Geophys., Res., 101, No. D4, 9079-9091, 1996.

Jacobson, M. Z.: Development and application of a new air pollution modeling system-II: Aerosol module structure and design, Atmos. Environ., 31A, 131-144, 1997a.

Jacobson, M. Z.: Numerical techniques to solve condensational and dissolutional growth equations when growth is coupled to reversible reactions, Aerosol Sci. Techinol., 27, 491-498, 1997b.

Jacobson, M.Z.: Studying the effects of calcium and magnesium on size-distributed nitrate and ammonium with EQUISOLV II, Atmos. Environ., 33, 3635-3649, 1999.

Jacobson, M. Z.: Global direct radiative forcing due to multicomponent anthropogenic and natural aerosols, J. Geophys. Res., 106, 1551–1568, 2001a.

Jacobson, M. Z., Strong radiative heating due to the mixing state of black carbon in atmospheric aerosols, Nature, 409, 695– 697, 2001b.

Jacobson, M.Z.: Fundamentals of Atmospheric Modeling, Cambridge University Press, 2005.

Jacobson, M. Z.: Effects of Externally-Through-Internally-Mixed Soot Inclusions within Clouds and Precipitation on Global Climate". J Phys Chem A, 110(21):6860-6873, 2006.

Jayaraman, A., Lubin, D., Ramachandran, S., Ramanathan, V., Woodbridge, E., Collins, W.D. and Zalpuri, K.S.: Direct observations of aerosol radiative forcing over the tropical Indian Ocean during the January--February 1996 pre-INDOEX cruise. Journal of Geophysical Research 103(D12): doi: 10.1029/98JD00559. issn: 0148-0227, 1998.

John,W., S. M.Wall, J. L. Ondo, and W. Winklmayr: Acidic-aerosol size distributions during SCAQS (Southern California Air Quality Study), final report, Rep. CA/DOH/AIHL/SP-51, Calif. Air Resour. Board, Sacramento, 1989.

Kaufman, Y.J., C.J. Tucker, and R.L Mahoney: Fossil fuel and biomass burning effect on climate: Heating or cooling? J. Clim., 4, 578–588, 1991.

Kaufman, Y. J., and R. S. Fraser, The effect of smoke particles on clouds and climate forcing, Science, 277, 1636-1639, 1997.

Kaufman, Y.J., and I. Koren: Smoke and pollution aerosol effect on cloud cover. Science, 313, 655–658, doi:10.1126/science.1126232, 2006.

Kettle, A. J., Andreae, M. O., Amouroux, D., Andreae, T. W., Bates, T. S., Berresheim, H., Bingemer, H., Boniforti, R., Curran, M. A. J., DiTullio, G. R., Helas, G., Jones, G. B., Keller, M. D., Kiene, R. P., Leck, C., Levasseur, M., Malin, G., Maspero, M., Matrai, P., McTaggart, A. R., Mihalopoulos, N., Nguyen, B. C., Novo, A., Putaud, J. P., Rapsomanikis, S., Roberts, G., Schebeske, G., Sharma, S., Simo, R., Staubes, R., Turner, S., and Uher, G.: A global database of sea surface dimethylsulfide (DMS) measurements and a procedure to predict sea surface DMS as a function of latitude, longitude, and month, Global Biogeochemical Cycle, 13, 399-444, 1999.

Khain, A.P., D. Rosenfeld, and A. Pokrovsky: Aerosol impact on the dynamics and microphysics of convective clouds. Q. J. R. Meteorol. Soc., 131(611), 2639–2663, 2005.

Kiehl, J. T. and Trenberth, K. E.: Earth's Annual Global Mean Energy Budget, , Bulletin of the American Meteorological Society, 78, 197-208, 1997.

Kiehl, J.T., et al.: Radiative forcing due to sulfate aerosols from simulations with the National Center for Atmospheric Research Community Climate Model, Version 3. J. Geophys. Res., 105(D1),1441–1457, 2000.

Kim, Y.P., Seinfeld, J.H. and Saxena, P.: Atmospheric gas aerosol equilibrium, I: thermodynamic model. Aerosol Science and Technology 19, 157–181, 1993a.

Kim, Y.P., Seinfeld, J.H. and Saxena, P.: Atmospheric gas aerosol equilibrium, II: analysis of common approximations and activity coefficient calculation methods. Aerosol Science and Technology 19, 182–198, 1993b.

Kim, Y.P. and Seinfeld, J.H.: Atmospheric gas-aerosol equilibrium III: thermo-dynamics of crustal elements Ca^{2+}, K^{+}, and Mg^{2+}. Aerosol Science and Technology, 22, 93–110, 1995.

King, M., Y. Kaufman, D. Tanre, and T. Nakajima: Remote sensing of tropospheric aerosols: Past, present and future, Bull. Amer. Meteor. Soc., 80, 2229–2259, 1999.

Kinne, S., et al.: An AeroCom initial assessment: optical properties in aerosol component modules of global models. Atmos. Chem. Phys. **6**, 1815–1834, 2006.

Kirchstetter, T. W., Novakov, T., and Hobbs, P. V.: Evidence that the spectral dependence of light absorption by aerosols is affected by organic carbon, J. Geophys. Res.-Atmos., 109, D21208, doi:10.1029/2004JD004999, 2004.

Kleeman, M. K., G.R. Cass and A. Elderin: Modeling the airborne particle complex as a source-oriented external mixture. Journal of Geophysical Research, 102, pp. 21355–21372, 1997.

Klein, S. A. and Jakob, C.: Validation and sensitivities of frontal clouds simulated by the ecmwf model, Mon. Weather Rev., 127, 2514–2531, 1999.

Koren, I., Y.J. Kaufman, L.A. Remer, and J.V. Martins: Measurements of the effect of smoke aerosol on inhibition of cloud formation. Science, 303, 1342–1345, 2004.

Koren, I., J.V. Martins, L.A. Remer and H. Afarganc: Smoke invigoration versus inhibition of clouds over Amazon, Science, 321, 946-949, 2008.

Kouvarakis, G. and Mihalopouls, N., Seasonal variation of dimethylsulfide in the gas phase and of methanesulfonate and non-sea-salt sulfate in the aerosol phase measured in the Eastern Mediterranean atmosphere, Atmos. Environ., 36, 929-938, 2002.

Kristjánsson, J.E., A. Staple, J. Kristiansen, and E. Kaas: A new look at possible connections between solar activity, clouds and climate. Geophys. Res. Lett., 29, doi:10.1029/2002GL015646, 2002.

Kristjánsson, J.E., et al.: Response of the climate system to aerosol direct and indirect forcing: Role of cloud feedbacks. J. Geophys. Res., 110, D24206, doi:10.1029/2005JD006299, 2005.

Kulmala, M., Laaksonen, A., Korhonen, P., Vesala, T., Ahonen, T., and Barrett, J. C.: The Effect of Atmospheric Nitric-Acid Vapor on Cloud Condensation Nucleus Activation, J. Geophys. Res.-Atmos., 98, 22 949–22 958, 1993.

Kulmala, M., Toivonen, A., Mattila, T., and Korhonen, P.: Variations of cloud droplet concentrations and the optical properties of clouds due to changing hygroscopicity: A model study, J. Geophys. Res.-Atmos., 103, 16 183–16 195, 1998.

Kulmala, M., K. E. J. Lehtinen, and A. Laaksonen: Cluster activation theory as an explanation of the linear dependence between formation rate of 3nm particles and sulphuric acid concentration, Atmos. Chem. Phys., 6, 787–793, 2006.

Lammel, G., and T. Novakov: Water nucleation properties of carbon black and diesel soot particles, Atmos. Environ., 29, 813–823, 1995.

Leaitch, W. R., G. A. Isaac, J. W. Strapp, C. M. Banic, and H. A. Wiebe, The relationship between cloud droplet number concentrations and anthropogenic pollution: Observations and climatic implications, J. Geophys. Res., 97, 2463-2474, 1992.

Lefer, B. L., and R. W. Talbot: Summertime measurements of aerosol nitrate and ammonium at a northeastern U.S. site, J. Geophys. Res., 106, 20,365–20,378, doi:10.1029/2000JD900693, 2001.

Lelieveld, J., Berresheim, H., Borrmann, S., Crutzen, P.J., Dentener, F.J., Fischer, H., Feichter, J., Flatau, P.J., Heland, J., Holzinger, R., Korrmann, R., Lawrence, M. G., Levin, Z., Markowicz, K. M., Mihalopoulos, N., Minikin, A., Ramanathan, V., de Reus, M., Roelofs, G. J., Scheeren, H. A., Sciare, J., Schlager, H., Schultz, M., Siegmund, P., Steil, B., Stephanou, E.G., Stier, P., Traub, M., Warneke, C., Williams, J., and Ziereis, H.: Global Air Pollution Crossroads over the Mediterranean, Science, 298, 794–799, 2002.

Levin, Z. L., E. Ganor, and V. Gladstein, The effects of desert particles coated with sulfate on rain formation in the eastern Mediterranean, J. Appl. Meteorol., 35, 1511 – 1523, 1996.

Li, X., Larson DE, Gliberic M, Oaks A.: Effects of nitrogen metabolites on the induction of maize nitrate reductase. Plant Physiology 102, Supplement, 37, 1993.

Liao, H. and J.H. Seinfeld: Effect of Clouds on Direct Aerosol Radiative Forcing of Climate, J. Geophysical Research 103, 3781-3788, 1998.

Liao, H., Adams, P.J., Chung, S.H., Seinfeld, J.H., Mickley, L.J. and Jacob, D. J.: Interactions between tropospheric chemistry and aerosols in a unified general

circulation model. J. Geophys. Res., 108(D1), 4001, doi:10.1029/2001JD001260, 2003.

Liao, H., J. H. Seinfeld, P. J. Adams, and L. J. Mickley: Global radiative forcing of coupled tropospheric ozone and aerosols in a unified general circulation model, J. Geophys. Res., 109, D16207, doi:10.1029/2003JD004456, 2004.

Liao, H., and J.H. Seinfeld: Global impacts of gas-phase chemistry aerosol interactions on direct radiative forcing by anthropogenic aerosols and ozone. J. Geophys. Res., **110**, D18208, doi:10.1029/2005JD005907, 2005.

Liao, H., W.-T. Chen, and J. H. Seinfeld: Role of climate change in global predictions of future tropospheric ozone and aerosols, J. Geophys. Res., 111, D12304, doi:10.1029/2005JD006852, 2006.

Lin, S.-J., and R. B. Rood: Multidimensional flux-form semi-Lagrangian transport schemes, Mon. Weather Rev., 124, 2046– 2070, 1996.

Liousse, C., J. E. Penner, C. Chuang, J. J. Walton, H. Eddleman, and H. Cachier: A global three-dimensional model study of carbonaceous aerosols, J. Geophys. Res., 101, 19,411-19,432, 1996.

Liu, H. Y., Jacob, D. J., Bey, I., and Yantosca, R. M.: Constraints from pb-210 and be-7 on wet deposition and transport in a global three-dimensional chemical tracer model driven by assimilated meteorological fields, Journal of Geophysical Research, 106, 12109-12128, 2001.

Liu, X., and J. E. Penner: Effect of Mount Pinatubo H2SO4/H2O aerosol on ice nucleation in the upper troposphere using a global chemistry and transport model, J. Geophys. Res., 107(D12), 4141, doi:10.1029/2001JD000455, 2002.

Liu, X. H., J. E. Penner, and M. Herzog: Global modeling of aerosol dynamics: Model description, evaluation, and interactions between sulfate and nonsulfate aerosols, J. Geophys. Res., 110, D18206, doi:10.1029/2004JD005674, 2005.

Liu, X., J. Penner, S. Ghan, and M. Wang: Inclusion of ice microphysics in the NCAR Community Atmospheric Model Verision 3 (CAM3), J. Clim., 20, 4526– 4547, 2007.

Loeb, N.G., and S. Kato: Top-of-atmosphere direct radiative effect of aerosols over the tropical oceans from the Clouds and the Earth's Radiant Energy System (CERES) satellite instrument. J. Clim., **15**, 1474–1484, 2002.

Lohmann, U., and J. Feichter: Global indirect aerosol effects: A review. Atmos. Chem. Phys., 5, 715–737, 2005.

Lohmann, U., J. Feichter, J.E. Penner, and W.R. Leaitch: Indirect effect of sulfate and carbonaceous aerosols: a mechanistic treatment. J. Geophys. Res., 105(D10), 12193–12206, 2000.

Lohmann, U., and G. Lesins: Stronger constraints on the anthropogenic indirect aerosol effect. Science, 298, 1012–1016, 2002.

Lurmann, F. W., A.S Wexler, S.N Pandis, S Musarra, N Kumar and J.H Seinfeld: Modeling urban and regional aerosols. Atmospheric Environment, 31A, pp. 2695–2715, 1997.

Mahowald, N.M., and L.M. Kiehl: Mineral aerosol and cloud interactions. Geophys. Res. Lett., 30, doi:10.1029/2002GL016762, 2003.

Malm, W.C., et al.: Spatial and monthly trends in speciated fine particle concentration in the United States. J. Geophys. Res., **109**, D03306, doi:10.1029/2003JD003739, 2004.

Markar, P.A., Bouchet, V.S., and Nenes, A.: Inorganic chemistry calculations using HETV – a vectorized solver for the SO_4^{2-}-NO_3^--NH_4^+ system based on the ISORROPIA algorithms, Atmos. Environ., 37, 2279-2294, doi:10.1016/S1352-2310(03)00074-8.510, 2003.

Mari, C., Jacob, D. J., and Bechtold, P.: Transport and scavenging of soluble gases in a deep convective cloud, Journal of Geophysical Research, 105, 22255-22267, 2000.

Martin, G. M., et al.: The measurement and parameterization of effective radius of droplets in warm stratocumulus clouds, J. Atmos. Sci., 51, 1823– 1842, 1994.

McComiskey, A. and Feingold, G.: Quantifying error in the radiative forcing of the first aerosol indirect effect, Geophys. Res. Lett., 35, L02810, doi:10.1029/2007GL032667, 2008.

McComiskey, A., G. Feingold, A. S. Frisch, D. D. Turner, M. A. Miller, J. C. Chiu, Q. Min, and J. A. Ogren: An assessment of aerosol - cloud interactions in marine stratus clouds based on surface remote sensing, J. Geophys. Res., 114, D09203, doi:10.1029/2008JD011006, 2009.

McFarquhar, G. M., and A. J. Heymsfield: Parameterizations of INDOEX microphysical measurements and calculations of cloud susceptibility: Applications for climate studies, J. Geophys. Res., 106, 28,675–28,698, 2001.

Meng, Z., Seinfeld, J.H., Saxena, P. and Kim, Y.P.: Atmospheric gas-aerosol equilibrium, IV: thermodynamics of carbonates. Aerosol Science and Technology, 23, 131–154, 1995.

Meng, Z. and Seinfeld, J.H.: Time Scales to Achieve Atmospheric Gas-Aerosol Equilibrium for Volatile Species, Atmos. Environ., 30, 2889-2900, 1996.

Meng, Z., D. Dabdub, and Seinfeld, J.H.: Size-resolved and chemically resolved model of atmospheric aerosol dynamics, J. Geophys. Res., 103, 3419-3435, 1998.

Menon, S., A.D. Del Genio, D. Koch, and G. Tselioudis: GCM simulations of the aerosol

indirect effect: sensitivity to cloud parameterization and aerosol burden. J. Atmos. Sci., 59, 692–713, 2002a.

Menon, S., J. Hansen, L. Nazarenko, and Y. Luo: Climate effects of black carbon aerosols in China and India. Science, 297, 2250–2252, 2002b.

Menon, S., and A. Del Genio: Evaluating the impacts of carbonaceous aerosols on clouds and climate. In: An Interdisciplinary Assessment: Human-Induced Climate Change [Schlesinger, M., et al. (eds.)]. Cambridge University Press, Cambridge, UK, in press, 2007.

Menon, S., Del Genio, A. D., Kaufman, Y. J., Bennartz, R., Koch, D., Loeb, N., and Orlikowski, D.: Analyzing signatures of aerosol-cloud interactions from satellite retrievals and the GISS GCM to constrain the aerosol indirect effect, J. Geophys. Res., 113, D14S22, doi:10.1029/2007JD009442, 2008.

Metzger, S., Dentener, F.J., Lelieveld, J., and Pandis, S.N.: Gas/aerosol partitioning I: A computationally efficient model, J. Geophys. Res., 107(D16), ACH 16-1-24, doi:10.1029/2001JD001102, 2002a.

Metzger, S., F. Dentener, M. Krol, A. Jeuken, and J. Lelieveld: Gas/aerosol partitioning: 2. Global modeling results, J. Geophys. Res., 107(D16), 4313, doi:10.1029/2001JD001103, 2002b.

Metzger, S., Mihalopoulos, N., and Lelieveld, J.: Importance of mineral cations and organics in gas-aerosol partitioning of reactive nitrogen compounds: case study based on MINOS results, Atmos. Chem. Phys., 6, 2549–2567, 2006,

Metzger, S. and Lelieveld, J.: Reformulating atmospheric aerosol thermodynamics and hygroscopic growth into fog, haze and clouds, Atmos. Chem. Phys., 7, 3163–3193, 2007.

Metzger, S., Steil, B., Xu, L., Penner, J. E., and Lelieveld, J.: Aerosol hygroscopic growth parameterization based on a solute specific coefficient, Atmos. Chem. Phys. Discuss., 11, 24813-24855, doi:10.5194/acpd-11-24813-2011, 2011a.

Metzger, S., Steil, B., Xu, L., Penner, J. E., and Lelieveld, J.: Description of EQSAM4: gas-liquid-solid partitioning model for global simulations, Geosci. Model Dev. Discuss., 4, 2791-2847, doi:10.5194/gmdd-4-2791-2011, 2011b.

Moore, W. J.: Physical chemistry, 3rd edition, Prentice Hall, Englewood Cliffs, NJ, pp 238, 1962.

Morrison, H., Curry, J. A., and Khvorostyanov, V. I.: A new doublemoment microphysics parameterization for application in cloud and climate models. Part i: Description, J. Atmos. Sci., 62, 1665–1677, 2005.

Moya, M., Ansari, A. S., Pandis, S.N., Partitioning of nitrate and ammonium between the gas and particulate phases during the 1997 IMADA-AVER study in Mexico City, Atmos. Environ., 35, 1791-1804, 2001.

Murphy, D. M., J. R. Anderson, P. K. Quinn, L. M. McInnes, F. J. Brechtel, S. M. Kreidenweis, A. M. Middlebrook, M. Po´ sfai, D. S. Thomson, and P. R. Buseck, Influence of sea-salt on aerosol radiative properties in the Southern Ocean marine boundary layer, Nature, 395, 62– 65, 1998.

Myhre, G., Grini, A., and Metzger, S.: Modelling of nitrate and ammonium-containing aerosols in presence of sea salt, Atmos. Chem. Phys., 6, 4809–4821, doi:10.5194/acp-6-4809-2006, 2006.

Myhre G.: Consistency Between Satellite-Derived and Modeled Estimates of the Direct Aerosol Effect. Science 325, 187; DOI: 10.1126/science.1174461, 2009.

Nakajima, T., A. Higurashi, K. Kawamoto, and J. Penner: A possible correlation between satellite-derived cloud and aerosol microphysical parameters. Geophys. Res. Lett., 28, 1171–1174, 2001.

Nakicenovic, N., et al.: Emission Scenarios: A Special Report of Working Group III of the Intergovernmental Panel on Climate Change, 599 pp., Cambridge Univ. Press, New York, 2000.

Naoe, H., and K. Okada, Mixing properties of submicrometer aerosol particles in the urban atmosphere: With regard to soot particles, Atmos. Environ., 35, 5765–5772, 2001.

Nenes, A., Pilinis, C. and Pandis, S.N.: ISORROPIA: a new thermodynamic equilibrium model for multiphase multicomponent marine aerosols. Aquatic Geochemistry, 4, 123–152, 1998.

Nenes, A., Pilinis, C. and Pandis, S.N.: Continued development and testing of a new thermodynamic aerosol module for urban and regional air quality models. Atmos. Environ., 33, 1553–1560, 1999.

Nenes, A., and J.H. Seinfeld: Parameterization of cloud droplet formation in global climate models. J. Geophys. Res., 108, doi:10.1029/2002JD002911, 2003.

O'Dowd, C. D., et al.: The relative importance of sea-salt and nsssulphate aerosol to the marine CCN population: An improved multicomponent aerosol-droplet parameterization, Q. J. R. Meteorol. Soc., 125, 1295– 1313, 1999.

Okada, K., and R. Hitzenberger: Mixing properties of individual submicrometer particles in Vienna, Atmos. Environ., 35, 5617– 5628, 2001.

Parrish, D., Norton,R., Bollinger, M., Liu, S., Murphy, P., Albritton.D., and Fehsenfeld,F.: Measurements ofHNO_3 and NO_3^- particulates at a rural site in the Colorado mountains. J. Geophys. Res. 91, 5379-5393, 1986.

Penner, J. E., R. Dickinson, and C. O'Neill: Effects of aerosol from biomass burning on the global radiation budget. Science,**256**, 1432-1434, 1992.

Penner, J. E., H. Eddleman, and T. Graedel: Towards the developemtn of a global inventory of black carbon emissions, Atmos. Environ., Part A, 27,1277-1295, 1993.

Penner, J. E., C. A. Atherton, and T. E. Graedel: Global emissions and models of photochemically active compounds, in Global Atmospheric-Biospheric Chemistry, edited by R. Prinn, pp. 223 – 248, Springer, New York, 1994.

Penner, J. E., C. C. Chuang, and K. Grant, Climate forcing by carbonaceous and sulfate aerosols, Clim. Dyn., 14, 839– 851, 1998.

Penner, J. E., et al., Aerosols, their direct and indirect effects, in In Climate Change 2001: The Scientific Basis, edited by J. T. Houghton et al., 289–348, Cambridge Univ. Press, 2001.

Penner, J.E., X. Dong, and Y. Chen: Observational evidence of a change in radiative forcing due to the indirect aerosol effect. Nature, 427, 231–234, 2004.

Penner, J.E., et al.: Model intercomparison of indirect aerosol effects. Atmos. Chem. Phys. Discuss., 6, 1579–1617, 2006.

Penner, J.E., Y. Chen, M. Wang, and X. Liu: Possible influence of anthropogenic aerosols on cirrus clouds and anthropogenic forcing, Atmos. Chem. Phys, 9, 879-896, 2009.

Penner, J. E., L. Xu, and M. Wang: Satellite methods underestimate indirect climate forcing by aerosols, PNAS,1018526108v1-5, 2011.

Petters, M.D., and Kreidenweis, S.M., A single parameter representation of hygroscopic growth and CNN activity, Atmos. Chem. Phys., 7,1961-1971, 2007.

Pilinis, C. and Seinfeld, J.H.: Continued development of a general equilibrium model for inorganic multicomponent atmospheric aerosols, Atmos. Environ., 32, 2453-2466, 1987.

Pilinis, C., Pandis, S.N. and Seinfeld, J.H.: Sensitivity of direct climate forcing by atmospheric aerosols to aerosol size and composition, J. Geophys. Res., 100, 18, 739-18,754, 1995.

Pilinis, C., K. P. Capaldo, A. Nenes, and S. N. Pandis: MADM-A new multicomponent aerosol dynamics model, Aerosol Sci. Technol., 32, 482, 2000.

Pitzer, K.S. and Mayorga, G., Thermodynamics of electrolytes, II, Activity and osmotic coefficients for strong electrolytes with one or both ions univalent. Journal of Physical Chemistry, 77, 2300-2308, 1973.

Pósfai, M., J. R. Anderson, P. R. Buseck, and H. Sievering, Soot and sulfate aerosol particles in the remote marine troposphere, J. Geophys. Res., 104, 21,685–21,693, 1999.

Pringle, K. J., Tost, H., Message, S., Steil, B., Giannadaki, D., Nenes, A., Fountoukis, C., Stier, P., Vignati, E., and Lelieveld, J.: Description and evaluation of GMXe: a new aerosol submodel for global simulations (v1), Geosci. Model Dev., 3, 391-412, doi:10.5194/gmd-3-391-2010, 2010.

Pruppacher,H . R., and J. D. Klett, Microphysics of Clouds and Precipitation, Kluwer Acad., 954 pp., 1997.

Putaud, J.-P., et al.: A European aerosol phenomenology; physical and chemical characteristics of particulate matter at kerbside, urban, rural and background sites in Europe. European Commission, Report nr. EUR 20411 EN, 2003.

Pye, H. O. T., Liao, H., Wu, S., Mickley, L. J., Jacob, D. J., Henze, D. K., and Seinfeld, J. H.: Effect of changes in climate and emissions on future sulfate-nitrate-ammonium aerosol levels in the United States, J. Geophys. Res.-Atmos., 114, D01205+, doi:10.1029/2008JD010701, 2009.

Reid, R. C., J. M. Prausnitz, and T. K. Sherwood: The properties of Gases and Liquids, pp 554-560, 1977.

Rodriguez, M. A., and D. Dabdub: IMAGES-SCAPE2: A modeling study of size- and chemically resolved aerosol thermodynamics in a global chemical transport model, J. Geophys. Res., 109, D02203, doi:10.1029/2003JD003639, 2004.

Quaas, J., Boucher,O., and Br´eon, F.-M.: Aerosol indirect effects in POLDER satellite data and in the LMDZ GCM, J. Geophys. Res., 109, D08205, doi:10.1029/2003JD004317, 2004.

Quaas, J., and O. Boucher: Constraining the first aerosol indirect radiative forcing in the LMDZ GCM using POLDER and MODIS satellite data. Geophys. Res. Lett., 32, L17814, doi:10.1029/2005GL023850, 2005.

Quaas, J., O. Boucher, and U. Lohmann, Constraining the total aerosol indirect effect in the LMDZ and ECHAM4 GCMs using MODIS satellite data, Atmos. Chem. Phys., 6, 947–955, 2006.

Quaas, J., Boucher, O., Bellouin, N., and Kinne, S.: Satellite-based estimate of the direct and indirect aerosol climate forcing, J. Geophys. Res., 113, D05204, doi:10.1029/2007JD008962, 2008.

Quaas, J., Ming, Y., Menon, S., Takemura, T., Wang, M., Penner, J. E., Gettelman, A., Lohmann, U., Bellouin, N., Boucher, O., Sayer, A. M., Thomas, G. E., McComiskey, A., Feingold, G., Hoose, C., Kristj´ansson, J. E., Liu, X., Balkanski, Y., Donner, L. J., Ginoux, P. A., Stier, P., Grandey, B., Feichter, J., Sednev, I., Bauer, S. E., Koch, D., Grainger, R. G., Kirkev°ag, A., Iversen, T., Seland, Ø., Easter, R., Ghan, S. J., Rasch, P. J., Morrison, H., Lamarque, J.-F., Iacono, M. J., Kinne, S., and Schulz, M.: Aerosol indirect effects – general circulation model intercomparison and evaluation with satellite data, Atmos. Chem. Phys., 9, 8697–8717, doi:10.5194/acp-9-8697-2009, 2009.

Quinn, P.K., and T.S. Bates: Regional aerosol properties: comparisons from ACE 1, ACE 2, Aerosols99, INDOEX, ACE Asia, TARFOX, and NEAQS. J. Geophys. Res., **110**, D14202, doi:10.1029/2004JD004755, 2005.

Quinn, P. K., D. J Coffman, V. N. Kapustin, T. S. Bates and D. S. Covert: Aerosol optical properties in the marine boundary layer during the First Aerosol Characterization Experiment (ACE 1) and the underlying chemical and physical aerosol properties, J. Geophys. Res., 103, 547-563, 1998.

Raga, G. B., and P. R. Jonas: On the link between cloud-top radiative properties and sub-cloud aerosol concentrations, Q. J. R. Meteorol. Soc., 119, 1419–1425, 1993.

Ramanathan, V., P.J. Crutzen, J.T. Kiehl, and D. Rosenfeld: Atmosphere: aerosols, climate, and the hydrological cycle. Science, 294, 2119–2124, 2011.

Ramaswamy, V., et al., Radiative forcing of Climate Change, in In Climate Change 2001: The Scientific Basis, edited by J. T. Houghton et al., 349–416, Cambridge Univ. Press, 2001.

Riipinen, I., et al.: Connections between atmospheric sulphuric acid and new particle formation during QUEST III-IV campaigns in Heidelberg and Hyyti, Atmos. Chem. Phys., 7, 1899–1914, 2007.

Rodriguez, M.A., and D. Dabdub: IMAGES-SCAPE2: A modeling study of size- and chemically resolved aerosol thermodynamics in a global chemical transport model, J. Geophys. Res., 108(D4), 4144, doi:10.1029/2002JD002436, 2004.

Rosenfeld, D.: TRMM observed first direct evidence of smoke from forest fires inhibiting rainfall. Geophys. Res. Lett., 26(20), doi:10.1029/1999GL006066, 1999.

Rosenfeld, D., and W.L. Woodley: Deep convective clouds with sustained supercooled liquid water down to –37.5 °C. Nature, 405, 440–442, 2000.

Rosenfeld, D., Y. Rudich, and R. Lahav: Desert dust suppressing precipitation: a possible desertifi cation feedback loop. Proc. Natl. Acad. Sci. U.S.A., 98, 5975–5980, 2001.

Rosenfeld, D., R. Lahav, A. Khain, and M. Pinsky: The role of sea spray in cleansing air pollution over the ocean via cloud processes. Science, 297, 1667–1670, 2002.

Rosenfeld, D., and G. Feingold: Explanation of discrepancies among satellite observations of the aerosol indirect effects. Geophys. Res. Lett., 30(14), 1776, doi:10.1029/2003GL017684, 2003.

Rotman, D. A., et al.: IMPACT, the LLNL 3-D global atmospheric chemical transport model for the combined troposphere and stratosphere: Model description and analysis of ozone and other trace gases, J. Geophys. Res., 109, D04303, doi:10.1029/2002JD003155, 2004.

Rotstayn, L.D., and Y. Liu: Sensitivity of the first indirect aerosol effect to an increase of the cloud droplet spectral dispersion with droplet number concentration. J. Clim., 16, 3476–3481, 2003.

Russell et al., 1988 A.G. Russell, K.F. McCue and G.R. Cass: Mathematical modeling of the formation of nitrogen-containing air pollutants. 1. Evaluation of an Eulerian photochemical model. Envir. Sci. Technol., 22 , pp. 263–271, 1988.

Salisbury, G., Williams, J., Holzinger, R., Gros, V., Mihalopoulos, N., Vrekoussis, M., Sarda-Est`eve, R., Berresheim, H., von Kuhlmann, R., Lawrence, M., and Lelieveld, J.: Ground-based PTR-MS measurements of reactive organic compounds during the MINOS campaign in Crete, July–August 2001, Atmos.Chem. Phys., 3, 925–940, 2003.

Savoie, D. L., and J. M. Prospero: Particle size distribution of nitrate and sulfate in the marine atmosphere, Geophys. Res. Lett., 9(10), 1207–1210, doi:10.1029/GL009i010p01207, 1982.

Saxena, P., Seigneur, C., Hudischewskyj, A.B. and Seinfeld, J.H.: A comparative study of equilibrium approaches to the chemical characterizations of secondary aerosols, Atmos. Environ., 20, 1471-1484, 1986.

Schaap, M., et al.: Secondary inorganic aerosol simulations for Europe with special attention to nitrate. Atmos. Chem. Phys., **4,** 857–874, 2004.

Schultz, M. G., et al.: On the origin of tropospheric ozone and NOx over the tropical South Pacific, J. Geophys. Res., 104, 5829–5844, 1999.

Schlesinger, W. H., and A. E. Hartley: A global budget for atmospheric NH3, Biogeochemistry, 15, 191– 211, 1992.

Schulz, M., et al.: Radiative forcing by aerosols as derived from the AeroCom present-day and pre-industrial simulations. Atmos. Chem. Phys. Discuss., **6**, 5095–5136, 2006.

Schwartz, S. E., & Benkovitz, C. M.: Influence of anthropogenic aerosol on cloud optical depth and albedo shown by satellite measurements and chemical transport modeling. Proceedings of the National Academy of Sciences of the United States of America, 99(4), 1784-1789, 2002.

Sekiguchi, M., et al.: A study of the direct and indirect effects of aerosols using global

satellite datasets of aerosol and cloud parameters. J. Geophys. Res., 108(D22), 4699, doi:10.1029/2002JD003359, 2003.

Seinfeld, J.H. and Pandis, S.N.: Atmospheric Chemistry and Physics: From Air Pollution to Climate Change, John, Wiley & Sons, Inc., 1998.

Sihto, S. L., et al.: Atmospheric sulphuric acid and aerosol formation: Implications from atmospheric measurements for nucleation and early growth mechanisms, Atmos. Chem. Phys., 6, 4079– 4091, 2006.

Shine, K. P., J. Cook, E. J. Highwood, and M. M.Joshi: An alternative to radiative forcing for estimating the relative importance of climate change mechanisms, Geophys. Res. Lett., 30 (20), doi:10.1029/2003GL018,141, 2003.

Silva, P. J., R. A. Carlin, and K. A. Prather, Single particle analysis of suspended soil dust from southern California, Atmos. Environ., 34, 1811– 1820, 2000.

Singh, H., et al.: Distribution and fate of selected oxygenated organic species in the troposphere and lower stratosphere over the Atlantic, J. Geophys. Res., 105, 3795–3806, 2000.

Singh, H. B., et al.: Latitudinal distribution of reactive nitrogen in the free troposphere over the Pacific Ocean in late winter/early spring, J. Geophys. Res., 103, 28,237–28,247, 1998.

Smith, C.A., J.D. Haigh, and R. Toumi: Radiative forcing due to trends in stratospheric water vapor. Geophys. Res. Lett., 28(1), 179–182, 2001.

Smith, S.J., E. Conception, R. Andres, and J. Lurz: Historical Sulphur Dioxide Emissions 1850-2000: Methods and Results. Research Report No. PNNL-14537, Joint Global Change Research Institute, College Park, MD, 16 pp, 2004.

Spann, J.F. and Richardson, C.B.: Measurement of the water cycle in mixed ammonium acid sulfate particles, Atmos. Environ., 19(5), 819-825, 1985.

Stelson, A.W. and Seinfeld, J.H.: Relative humidity and pH dependence of the vapor pressure of ammonium nitrate–nitric acid solutions at 25 degrees C. Atmos. Env. 16, 993–1000, 1982.

Stokes, R.H. and Robinson, R.A.: Interactions in aqueous nonelectrolyte solutions, I. Solute-solvent equilibria, Journal of Physical Chemistry, 70, 2126-2130, 1966.

Storelvmo, T., Kristj´ansson, J. E., Myhre, G., Johnsrud, M., and Stordal, F.: Combined observational and modeling based study of the aerosol indirect effect, Atmos. Chem. Phys., 6, 3583–3601, 2006.

Sun, Q., and A. S. Wexler: Modeling urban and regional aerosols near acid neutrality application to the 24-25 June SCAQS episode, Atmos. Environ., 32, 3533-3545,

1998a.

Sun, Q., and A. S. Wexler: Modeling urban and regional aerosol-condensation and evaporation near acid neutrality, Atmos. Environ., 32, 3527-3531, 1998b.

Takemura, T., et al.: Simulation of climate response to aerosol direct and indirect effects with aerosol transport-radiation model. J. Geophys. Res, 110, doi:10.1029/2004JD00502, 2005.

ten Brink, H. M., J. P. Veefkind, A. Waijers-Ijpelaan, and J. C. van der Hage: Aerosol light-scattering in the Netherlands, Atmos. Environ., 30, 4251–4261, 1996.

ten Brink, H. M., C. Kruisz, G. P. A. Kos, and A. Berner: Composition/size of the light-scattering aerosol in the Netherlands, Atmos. Environ., 31, 3955-3962, 1997.

Textor, C., et al.: Analysis and quantification of the diversities of aerosol life cycles within AeroCom, Atmos. Chem. Phys., 6, 1777–1813, 2006.

Toon, O. B. and Ackerman, T. P., Algorithms for the calculation of scattering by stratified spheres, Appl. Opt., vol. 20, no. 20, pp. 3657-3660, 1981.

Topping, D.O., Mcfiggans, G.B., and Coe, H.: A curved multicomponent aerosol hygroscopicity model framework: Part 2: Including organic compounds, Atmos. Chem. Phys., 5, 1223-1242, 2005.

Trenberth, K.E., J.T. Fasullo, and J. Kiehl: Earth's Global Energy Budget, Bulletin of the American Meteorological Society, Vol 90, No 2, pp 311–323, 2009.

Trebs, I., Metzger, S., Meixner, F., Helas, G., Hoffer, A., Rudich, Y., Falkovich, A., Moura, M., Da Silva, R., Artaxo, P., Slanina, J. and Andreae, M.: The NH4+-NO3--Cl--SO42--H2O aerosol system and its gas phase precursors at a pasture site in the Amazon Basin: How relevant are mineral cations and soluble organic acids?. Journal of Geophysical Research 110(D7): doi: 10.1029/2004JD005478. issn: 0148-0227, 2005.

Twomey, S.: The nuclei of natural cloud formation. Part II: The supersaturation in natural clouds and the variation of cloud droplet concentration, Geophys. Pure Appl., 43, 243–249, 1959.

Twomey, S., Pollution and the planetary albedo, Atmos. Environ., 8, 1251-1256, 1974.

Twomey, S., The influence of pollution on the short wave albedo of clouds, J. Atmos. Sci., 34, 1149-1152, 1977.

Twohy, C. H., M. D. Petters, J. R. Snider, B. Stevens, W. Tahnk, M. Wetzel, L. Russell, and F. Burnet: Evaluation of the aerosol indirect effect in marine stratocumulus clouds: Droplet number, size, liquid water path, and radiative impact, J. Geophys. Res., 110, D08203, doi:10.1029/2004JD005116, 2005.

van Dorland, R., F. J. Dentener, and J. Lelieveld: Radiative forcing due to tropospheric ozone and sulphate aerosols, J. Geophys. Res., 102, 28,079–28,100, 1997.

van Aardenne, J.A., Dentener, F.J., Olivier, J.G.J., Klein Goldewijk, C.G.M. and J. Lelieveld: A 1 x 1 degree resolution dataset of historical anthropogenic trace gas emissions for the period 1890-1990. Global Biogeochemical Cycles,15(4), 909-928, 2001.

Vehkamäki, H., Kulmala, M., Napari, I., Lehtinen, K. E. J., Timmreck, C., Noppel, M., and Laaksonen, A.: An improved parameterization for sulfuric acid-water nucleation rates for tropospheric and stratospheric conditions, Journal of Geophysical Research, 107, 4622, doi:10.1029/2002JD002184, 2002.

Vignati, E., Wilson, J., and Stier, P.: M7: An efficient size-resolved aerosol microphysics module for large-scale aerosol transport models, J. Geophys. Res., 109, D22202, doi:10.1029/2003JD004485, 2004.

Walcek, C. J., R. A. Brost, and J. S. Chang: SO_2, sulfate and HNO_3 deposition velocities computed using regional land use and meteorological data, Atmos. Environ., 20, 949–964, 1996.

Walton, J. J., Maccracken, M. C., and Ghan, S. J.: A global-scale lagrangian trace species model of transport, transformation, and removal processes, Journal of Geophysical Research, 93, 8339-8354, 1988.

Wang, J.S., et al.: A 3-D model analysis of the slowdown and interannual variability in the methane growth rate from 1988 to 1997. Global Biogeochem. Cycles, 18, GB3011, doi:10.1029/3003GB002180, 2004.

Wang, M. and Penner, J. E.: Aerosol indirect forcing in a global model with particle nucleation, Atmos. Chem. Phys., 9, 239-260, doi:10.5194/acp-9-239-2009, 2009.

Wang, M., J. E. Penner, and X. Liu: Coupled IMPACT aerosol and NCAR CAM3 model: Evaluation of predicted aerosol number and size distribution, J. Geophys. Res., 114, D06302, doi:10.1029/2008JD010459, 2009.

Warneck, P.: Chemistry of the Natural Atmosphere, 757 pp., Elsevier, New York, 1988.

Webb, M., Senior, C., Bony, S., and Morcrette, J. J.: Combining erbe and isccp data to assess clouds in the hadley centre, ecmwf and lmd atmospheric climate models, Clim. Dynam., 17, 905–922, 2001.

Wesely, M. L.: Parameterization of surface resistances to gaseous dry deposition in regional-scale numerical models, Atmos. Environ., 23, 1293– 1304, 1989.

Wexler, A.S. and Seinfeld, J.H.: The distribution of ammonium salts among a size and composition dispersed aerosol. Atmos. Environ., 24A, 1231–1246, 1990.

Wexler, A.S. and Seinfeld, J.H.: Second-generation inorganic aerosol model. Atmos. Environ., 25A, 2731–2748, 1991.

Wexler, A.S. and Clegg, S.L.: Atmospheric aerosol models for systems including the ions H^+, NH_4^+, Na^+, SO_4^{2-}, NO_3^-, Cl^-, Br^- and H_2O, J. Geophys. Res., 107 (D14), 4207, doi:10.1029/2001JD000451.593, 2002.

Whitby, K. T.: Physical characteristics of sulfur aerosols, Atmospheric Environment, 12, 135-159, 1978.

Wolff, G.T.: On the nature of nitrate in coarse continental aerosols. Atmospheric Environment, 18 (1984), pp. 977–987, 1984.

Woodcock, A. H., Salt nuclei in marine air as a function of altitude and wind force, J. Meteorol., 10, 362-371, 1953.

Wyslouzil, B. E., K. L. Carleton, D. M. Sonnenfroh, and W. T. Rawlins: Observation of hydration of single, modified carbon aerosols, Geophys. Res. Lett., 21, 2107– 2110, 1994.

Xu, L., Penner, J. E., Metzger, S., and Lelieveld, J.: A comparison of water uptake by aerosols using two thermodynamic models, Atmos. Chem. Phys. Discuss., 9, 9551-9595, doi:10.5194/acpd-9-9551-2009, 2009.

Xue, H. and Feingold, G.: A modeling study of the effect of nitric acid on cloud properties. Journal of Geophysical Research 109(D18): doi: 10.1029/2004JD004750. issn: 0148-0227, 2004.

Yu, S., Dennis, R., Roselle, S., Nenes, A., Walker, J., Eder, B., Schere, K., Swall, J. and Robarge, W.: An assessment of the ability of three-dimensional air quality models with current thermodynamic equilibrium models to predict aerosol NO_3^-, J. Geophys. Res., 110, D07S13, doi:10.1029/2004JD004718, 2005.

Zaveri, R.A., Easter, R.C. and Peters, L.K.: A computationally efficient Multicomponent Equilibrium Solver for Aerosols (MESA), J. Geophys. Res., 110, D24203, doi: 10.1029/2004JD005618, 2005a.

Zaveri, R.A., Easter, R.C. and Wexler, A.S.: A new method for multicomponent activity coefficients of electrolytes in aqueous atmospheric aerosols, J. Geophys. Res., 110, D02201, doi: 10.1029/2004JD004681, 2005b.

Zhang, D., Y. Iwasaka, G. Shi, J. Zhang, A. Matsuki, and D. Trochkine: Mixture state and size of Asian dust particles collected at southwestern Japan in spring 2000, J. Geophys. Res., 108(D24),4760, doi:10.1029/2003JD003869, 2003.

Zhang, Y., Seigneur, C., Seinfeld, J H., Jacobson, M.Z., Clegg, S.L., and Binkowski, F.: A comparative review of inorganic aerosol thermodynamic equilibrium modules: similarities, differences, and their likely causes, Atmos. Environ., 34, 117-137, 2000.

Zhang, L., S. L. Gong, J. Padro, and L. Barrie: A size-segregated particle dry deposition scheme for an atmospheric aerosol module, Atmos. Environ., 35(3), 549–560, 2001.

Zhang, D., Y. Iwasaka, G. Shi, J. Zang, A. Matsuki, and D. Trochkine: Mixture state and size of Asian dust particles collected at southwestern Japan in spring 2000, J. Geophys. Res., 108(D24), 4760, doi:10.1029/2003JD003869, 2003.

Zhang, S., Penner, J. E., and Torres, O.: Inverse modeling of biomass burning emissions using total ozone mapping spectrometer aerosol index for 1997, Journal of Geophysical Research, 110, D21306, doi:10.1029/2004JD005738, 2005.